An Investigation of Carbon Cycle Dynamics since the Last Glacial Maximum Using a Climate Model of Intermediate Complexity

By

Christopher Thomas Simmons

Department of Atmospheric and Oceanic Sciences
McGill University, Montréal
August 2013

A thesis submitted to the Faculty of Graduate Studies and Research in partial fulfillment of the requirements of the degree of Doctor of Philosophy

I dedicate this thesis to "the spirit of passion that aroused and excited this universe and all it contains."
--Jalal ad-Din Muhammad Balkhi (Rumi), trans. Deepak Chopra

Abstract

The University of Victoria Earth System Climate Model (UVic ESCM) v. 2.9 is used in this thesis to investigate two important topics in paleoclimate research: the glacial-to-interglacial rise in CO_2 and the Holocene carbon cycle. The UVic ESCM belongs to a class of models known as Earth system Models of Intermediate Complexity (EMICs) (Claussen et al. 2002) and provides a simplified yet comprehensive representation of the climate system and carbon cycle dynamics, including a three-dimensional ocean model, a dynamic-thermodynamic sea ice model, a dynamic global vegetation model, ocean sediments, and a fully-interactive inorganic and organic carbon cycle in the ocean.

First, a suite of transient simulations were conducted to cover the period from the Last Glacial Maximum (LGM) to the present (2000 A.D). Simulations including only prescribed orbital forcing and continental ice sheet changes failed to produce an increase in atmospheric CO_2 for the simulation period, although they demonstrated significant long-term sensitivity (10-15 ppm) to small (1.9 Tmol yr^{-1}) variations in the weathering rate. Modelling experiments incorporating the full CO_2 radiative forcing effect since the Last Glacial Maximum, however, resulted in much higher CO_2 concentrations (a 20 ppm increase over those without CO_2 radiative forcing) due to a greater ventilation of deep-ocean DIC and decreased oceanic CO_2 uptake, related in part to a larger decrease in southern hemisphere sea ice extent. The more thorough ventilation of the deep ocean in simulations with CO_2 radiative forcing also caused a larger net alkalinity decrease during the late deglacial and interglacial, allowing atmospheric CO_2 to increase by an additional 10 ppm in the simulations presented here. The inclusion of a high latitude terrestrial carbon reservoir provided a net release of carbon to the atmosphere, mostly

during the early deglacial, increasing atmospheric CO_2 levels to 240-250 ppm. This terrestrial release also provided better agreement with observed changes in carbonate concentrations in the deep ocean since the LGM (Yu et al. 2010). The addition of freshwater fluxes from ice sheet melting in North America added emphasis on the importance of a lower weathering rate during the LGM and early deglacial and indicated that deep water in the North Pacific may become more positively buoyant during freshwater fluxes in the Atlantic due to greater diffusion of heat to the deep ocean by enhanced Pacific intermediate water formation.

Second, our results for the Holocene carbon cycle indicate that atmospheric CO_2 should decrease between 6000 B.C. and 2000 A.D. without some kind of external forcing not represented in the model. However, the amount of the decrease (8-15 ppm) varied for different ocean circulation states. Furthermore, our simulations demonstrated significant sensitivity to Antarctic marine ice shelves, and these results indicate that more extensive marine ice shelves during the Holocene (relative to previous interglacials) may increase atmospheric CO_2 levels by ~5 ppm (from purely physical mechanisms) and as much as 10 ppm when different ocean circulation states or alkalinity changes are included. Adding various anthropogenic land use scenarios to the Holocene carbon cycle were unable to explain the CO_2 trend, accounting for only a third of the ice core CO_2 increase by 1 A.D. in our most extreme scenario. However, the results imply that external mechanisms leading to a decrease in alkalinity during the Holocene (such as declining weathering rates, more extensive marine ice shelves, terrestrial uptake, more calcifiers, coral reef expansion, etc.) may prevent the ocean from absorbing more of the anthropogenic terrestrial release, allowing the deforestation flux to balance a greater fraction of the Holocene peatland uptake (not modelled) and permitting CO_2 to increase from oceanic processes that are normally overwhelmed by northern peatlands.

Abrégé

Cette thèse détaille l'application du modèle du système climatique terrestre de l'Université de Victoria (version 2.9) dans le cadre de deux importants champs de recherche en modélisation paléoclimatique : l'augmentation du niveau de dioxyde de carbone (CO_2) dans l'atmosphère durant la plus récente transition glaciaire-interglaciaire, ainsi que l'évolution du cycle du carbone durant l'Holocène. Le modèle utilisé dans cette étude est répertorié comme modèle de complexité intermédiaire (Claussen et al. 2002), offrant un traitement à la fois simplifié et exhaustif de la dynamique du système climatique terrestre et du cycle du carbone. Celui-ci comprend un modèle océanique tridimensionnel, un modèle de glace marine dynamique/thermodynamique, un modèle dynamique et global de la végétation, les sédiments océaniques ainsi qu'un traitement interactif du cycle du carbone organique et inorganique.

Premièrement, une série de simulations transitoires sont effectuées afin de couvrir la période s'étendant du plus récent maximum glaciaire (LGM) jusqu'à aujourd'hui (2000 apr. J.-C.). Les simulations fondées uniquement sur une prescription des paramètres orbitaux et des calottes glaciaires ne reproduisent pas l'augmentation du CO_2 dans l'atmosphère durant la période transitoire tel que mentionné ci-haut, mais exposent toutefois une certaine sensibilité (10-15 ppm) à de faibles (1.9 Tmol/an) variations dans le taux d'érosion. Dans le cas de simulations prenant en compte la gamme complète des effets radiatifs associés au CO_2, par contre, la concentration du CO_2 dans l'atmosphère s'avère beaucoup plus élevée (une augmentation de 20 ppm par rapport à celles sans effets radiatifs). Cette différence est causée par une plus importante ventilation de carbone inorganique dissous en eaux profondes ainsi qu'une diminution du taux d'absorption de CO_2 par l'océan, qui s'explique en partie par une fonte accélérée de la glace marine dans l'hémisphère Sud. Le changement du régime de

ventilation en profondeur a également pour effet de diminuer l'alcalinité marine à partir de la fin de la période de déglaciation, augmentant de 10ppm la concentration de CO_2 dans l'atmosphère. La présence d'un réservoir de carbone terrestre an hautes latitudes fournit une source additionnelle de carbone, principalement durant les stages initiaux de la période de déglaciation, permettant ainsi aux niveaux de CO_2 dans l'atmosphère d'atteindre les 240-250 ppm. En outre, ceci facilite la validation de nos résultats par rapport aux changements dans la concentration de carbonate observées depuis le dernier maximum glaciaire dans les profondeurs marines (Yu et al. 2010). Le faible taux d'érosion terrestre durant le maximum glaciaire et la période de déglaciation qui a suivi est d'autant plus significatif en raison d'un apport accru d'eau douce de fonte en provenance des calottes glaciaires Nord-Américaines. L'addition d'eau douce dans l'hémisphère Nord pourrait également être indicateur d'eaux profondes plus dynamiques dans le Pacifique Nord, ce qui est causé par une plus importante diffusion thermique en profondeur associée au rehaussement de la formation d'eaux intermédiaires dans l'Océan Pacifique.

Deuxièmement, nos résultats quant au cycle du carbone durant l'Holocène pointent vers une certaine diminution du niveau de CO_2 dans l'atmosphère se manifestant vers 6000 av. J.-C. et qui, en l'absence de forçage externe au modèle, devrait se maintenir jusqu'à aujourd'hui ; celle-ci semble toutefois varier (8-15 ppm) en fonction du mode de circulation océanique. De plus, la concentration atmosphérique de CO_2 dans nos simulations démontre une importante sensibilité à l'étendue des barrières de glace en Antarctique, d'où notre conclusion qu'une présence accrue de glace marine durant l'Holocène (par rapport aux autres périodes interglaciaires) pourrait augmenter le niveau de CO_2 atmosphérique de près de 5 ppm (effets physiques directs), et de pas moins de 10 ppm en considérant la gamme de modes de circulation océanique ainsi que les changements dans l'alcalinité marine. L'inclusion d'une multitude de

scénarios anthropogéniques quant à l'occupation terrestre durant l'Holocène et son impact sur le cycle du carbone s'est avérée insuffisante pour expliquer la tendance du niveau de CO_2 dans l'atmosphère telle qu'obtenue dans les carottes glaciaires, contribuant à peine un tiers de l'augmentation totale vers l'an 1 apr. J.-C. dans notre scénario le plus extrême. Cependant, tout porte à croire que les mécanismes externes menant à une diminution de l'alcalinité marine durant l'Holocène (p. ex., un taux d'érosion plus faible, une plus grande étendue de glace marine, absorption terrestre accrue, davantage de calcifiants, l'expansion des récifs coralliens, etc…) pourraient ralentir l'absorption par les océans du surplus de CO_2 causé par l'activité humaine. Ceci permettrait non seulement aux flux de CO_2 en provenance de changements à l'occupation terrestre (i.e., la déforestation) de contrebalancer une plus grande fraction de l'absorption de CO_2 par les tourbières durant l'Holocène (non modélisé), mais également d'augmenter la concentration atmosphérique de CO_2 par des processus océaniques normalement accablés par les mécanismes biogéochimiques des tourbières nordiques.

Contribution of Authors

Three authors were engaged in the writing of this thesis. Lawrence A. Mysak both proposed and provided the primary supervision and financial support for the current project described here, while H. Damon Matthews served as a co-supervisor and provided essential technical support on the model and the scientific basis behind the simulations. Both Damon Matthews and Lawrence Mysak helped brainstorm ideas for some of sensitivity experiments, such as agricultural soil management, a high latitude terrestrial release during deglaciation, and weathering sensitivity experiments. All of the technical work, including designing and launching experiments as well as introducing changes to the model code, was carried out by the thesis author. The papers in this thesis (and the auxillary text) were also written by Christopher Simmons as the first author, with comments, improvements, and editorial changes provided by both Lawrence Mysak and Damon Matthews.

Statement of Originality

The University of Victoria Earth System Climate Model (UVic ESCM) is used in this study to explore changes in the carbon cycle since the Last Glacial Maximum, with particular emphasis on processes causing and maintaining increases in atmospheric CO_2. This model, classified as an EMIC, has been used for a variety of studies in the past to explore various aspects of deglaciation and the LGM climate (e.g., Schmitner et al. 2002; Meissner et al. 2003b; Meissner 2007; Schmittner and Galbraith 2008; Huiskamp and Meissner 2012; Handiani et al. 2012a). Our simulations used the latest version of the model, including ocean-sediment interactions, to simulate the entire period from the Last Glacial Maximum to the present. Most previous studies using the UVic ESCM focused on a more restricted period (for example, the LGM, Heinrich Event 1, or the Younger Dryas). The longer modeling experiments (23000 model years) discussed in this thesis required as many as six months to complete, and they are rare in the current literature (Menviel et al. (2012) is one recent example using an EMIC). We also explore the response of the model to a variety of different factors, including CO_2 radiative forcing, weathering rate, freshwater fluxes, and a prescribed high-latitude terrestrial carbon release. By conducting a significant number of factorial experiments, we determine the relative role of each forcing.

The inclusion of sediments allowed us to compare the simulated evolution of carbonate concentrations and alkalinity in the deep ocean with the general trends suggested from proxy data (Yu et al. 2010; Rickaby et al. 2010). This provided insights into possible scenarios that could lead to alkalinity changes in the ocean that fit the available data. Furthermore, in this study we included a simple parameterization of a high latitude terrestrial carbon release and found that it played an important role in the early deglacial period. The contribution of a passive carbon

reservoir to the deglacial carbon cycle is very topical (Ciais et al. 2012). We found that such a terrestrial release could provide a better fit for the carbonate concentrations changes suggested by the proxy data. This is a significant result that we expect will motivate future research into the role of permafrost in glacial-interglacial changes in atmospheric CO_2. Another notable finding is the demonstration that weathering rates in our simulations can strongly affect the amplitude of the atmospheric CO_2 increase. This suggests that more proxy data are needed to pin down weathering rates during deglaciation in order to adequately resolve the deglacial rise in CO_2. In addition, we also identified a significant positive feedback between the initial post-glacial increase in CO_2 and further increases in atmospheric CO_2 via southern hemisphere sea ice. These all represent original contributions to the glacial-interglacial carbon cycle debate.

Furthermore, this thesis addresses the Holocene carbon cycle, both with and without deforestation. We did not resolve the observed Holocene rise in CO_2 with our simulations, but our modeling experiments do suggest that atmospheric CO_2 would decrease slightly after 6000 B.C. without the effect of changes in ocean alkalinity. Our results indicate that the extent of marine ice shelves in Antarctica has a relatively large impact on atmospheric CO_2 (5-10 ppmv for constant alkalinity experiments, higher in some simulations where alkalinity is allowed to vary) by determining the relative distributions of Antarctic-generated deep waters and North-Atlantic generated deep waters in the oceans. To our knowledge, we are the first to model such an important role for marine ice shelves and hope that this will provide impetus for future research in this area. Regarding the role of deforestation, our results represent the first modeling study that addresses this topic for the entire period from 6000 B.C. to 2000 A.D. with the TRIFFID model (most other studies have used the Lund Potsdam-Jena Dynamic Global Vegetation Model). We also include a new parameterization of soil management in these

simulations. Our results join the chorus of modeling studies that indicate that the deforestation by itself played a relatively minor role in the Holocene rise in CO_2 (maximum of 5 ppmv of the 16 ppmv observed rise between 6000 B.C. and 1 A.D.). Correspondingly, we suggest that a decrease in ocean alkalinity would be necessary to provide a potentially greater role of deforestation to counterbalance the terrestrial uptake from northern peatlands. These finding represent original contributions to the current debate on the role of early Holocene deforestation in global carbon cycle dynamics.

Acknowledgments

I would like to thank my supervisor, Prof. Lawrence Mysak, for his support, understanding and guidance over the course of this project, without which the present work would not have been possible. His flexibility and creativity with respect to the scientific process provided a very positive and rewarding work environment as well as the basis for many innovative modeling experiments. Lawrence Mysak also helped facilitate many useful collaborations with the leading scientists in the field, who provided us with important feedback over the years. I am also very thankful to Damon Matthews, my co-supervisor, who contributed vital support on the underpinnings and coding of the model as well as the scientific significance of the results. His ideas regarding the importance of terrestrial processes (soil management and high latitude carbon) and weathering greatly enriched the work presented here. In addition, I would like to acknowledge Michael Eby, who provided very down-to-earth responses to our many technical questions, including details regarding the model's marine ice shelves and various aspects of the sediment module. His very clear, direct, and comprehensive responses allowed us to present a more complete interpretation of our modeling results. I also thank Marc-Olivier Brault for the opportunity to collaborate with him on a separate project, for his friendship, for always lending an ear and for providing the translation of the abstract into French. I also thank Michael Havas for his broad knowledge and swift, attentive help on all computer-related issues. In addition, I am grateful to Eric Galbraith, Victor Brovkin, Jerry McManus, Navin Ramankutty, and Yi Wang for their interest in my research and helpful suggestions.

Most of all, I would like to thank my family: Teresa Simmons (my mother), Serena Simmons (my grandmother), Robert Simmons (my grandfather), Tante Missia, Diane Bernahl (my adopted aunt), and Maxi (Maxuela) and Bobbola T. Simmons (my cats) for their

unconditional love, patience and emotional support as I completed this thesis. I would like to thank those who have enriched my life since I began my doctoral studies, including (in no particular order) David Brady, Jessica Hample, Chadée Deen, Zeng (Jackie) Yip, Catherine Thauer, Gaëlle Combeau, Philippe Chambon, Antoine Boudet, Chase Pelletier, Diana Welch, Morgan McBride, Nikolay Damyanov, Rabah Aider, David Carozza, François Delisle, Therese Trotochaud, Ericene Contreras, Alissa Razy, Thomas Williams, Kevin Traser, Jeannine and Christina Bryant, Ayako Yamamoto, Alexandra Jahn, Jasmine Rémillard, Veronique Meunier, Bruno Laliberté, Eric Noel, Marc Normandeau, Kimberly Wong and Ahmed Rabhi. In addition to my friends, I am also very grateful to the administrative staff who provided a positive work and social environment at McGill over the years; they include (in no particular order) Ornella Cavalière, Jennifer Marleau, Vaughan Thomassin, Paula Domingues, Emily Yang, Joseph Varcirca, Angela Mansi and Rachel Reynen.

For financial support, I would also like to acknowledge Lawrence Mysak's Discovery Grant from the Natural Science and Engineering Research Council of Canada (NSERC). In addition, I am particularly grateful to the Global Environmental and Climate Change Centre (GEC3) for funding assistance and for providing a useful, local collaborative research environment.

Table of Contents

List of Abbreviations

$[CO_3^{2-}]$: Carbonate concentration in seawater (estimated in our modelling results as alkalinity minus dissolved inorganic carbon)

AABW: Antarctic bottom water (global abyssal ocean waters generated at the surface near Antarctica)

ALCC: Anthropogenic land cover change

ACC: Antarctic circumpolar current

A.D.: Years "Anno Domini," or Common Era (C.E.)

AGCM: Atmospheric general circulation model (three-dimensional atmospheric model)

Alk: Ocean alkalinity approximation used in the UVic ESCM (bicarbonate concentration plus two times the carbonate concentration: $[HCO_3^-] + 2[CO_3^{2-}]$)

AMOC: Atlantic meridional overturning circulation

AOGCM: Atmosphere-ocean general circulation model (three-dimensional for both the atmosphere and the oceans)

B.C.: Years "Before Christ" or Before Common Era (B.C.E.)

BE: "Before Event", initial conditions taken just before a flush of DWNP in the 6000 B.C. equilibrium simulation (EQ_1, Chapter 4)

BP: Before present (years before 1950 A.D.)

C_3: C_3 photosynthetic pathway

C_4: C_4 photosynthetic pathway

CA : Constant alkalinity (weathering flux set equal to sedimentation flux)

CO2rad: CO_2 radiative forcing calculated from Petit et al. (1999) from 0 Watts m^{-2} at 19004 B.C.

DIC: Dissolved inorganic carbon

DE: "During Event", initial conditions taken just after a flush of DWNP in the 6000 B.C. equilibrium simulation (EQ_1, Chapter 4)

DGVM: Dynamic global vegetation model

DWNP: Deep water in the North Pacific (as opposed to NPDW, deep water generated in the surface ocean of the North Pacific)

EMIC: Earth system Model of Intermediate Complexity

FC : Free carbon (no prescribed changes to atmospheric CO_2 or CO_2 radiative forcing)

Forams: Foraminifera

FW: Freshwater fluxes

GNAIW: Glacial North Atlantic intermediate water (implying a shallower circulation than the NADW)

ha: hectares

HE1 : Heinrich Event 1 (defined here using freshwater fluxes from 17050 B.C. to 12720 B.C.)

HIGH:: Deforestation scenario (Chapter 5) imposing a scale factor to cause land area use per person to decrease from 4.5 ha/person at 6000 B.C. to ~1 ha/person at 2000 A.D.

HLC: High latitude carbon (terrestrial release of 600 Pg C)

HW: Constant high weathering rate (~12 Tmol yr^{-1})

HYDE: Deforestation scenario (Chapter 5) from Klein Goldewijk et al. (2011) interpolated to the UVic Model resolution.

IC: initial conditions

LGM: Last Glacial Maximum

LW: Constant low weathering rate (~10.1 Tmol yr^{-1})

MOC: Meridional overturning circulation

MOSES: Met Office Surface Exchange Scheme

NADW: North Atlantic deep water (global deep waters generated at the surface in the North Atlantic)

NH: Northern Hemisphere

NPZD: Nutrient-phytoplankton-zooplankton-detritus model

OGCM: Ocean general circulation model (three-dimensional ocean model)

PC: Prescribed carbon

Pg C: Petagrams (10^{15} g) of carbon, equivalent to Gt C (gigatons of carbon)

ppm : Short form for ppmv in this thesis

RUEL: Deforestation scenario (Chapter 5) imposing a scale factor to cause land area use per person to decrease from 4.5 ha/person at 6000 B.C. to ~1 ha/person at 2000 A.D.

SAT: Surface air temperature

SH : Southern Hemisphere

SST: Sea surface temperature

Tg C: Teragrams (10^{12} g) of carbon

TRIFFID: Top-Down Representation of Interactive Foliage and Flora Including Dynamics model

UVic ESCM (or "UVic model"): University of Victoria Earth System Climate Model

YD: Younger Dryas (here defined using freshwater fluxes between 10950 B.C. and 9950 B.C.)

Chapter 1: Introduction

1.1 Thesis Motivation and Project History

This thesis uses the University of Victoria Earth System Climate Model (UVic ESCM) v.2.9 to investigate the evolution of the model's carbon cycle during deglaciation and the Holocene. The UVic ESCM belongs to a class of models called Earth system Models of Intermediate Complexity (Claussen et al. 2002), which allow long-term climate simulations with reasonable computational efficiency. To date, there are an abundance of hypotheses but no single accepted theory on how glacial-interglacial changes in CO_2 occur, or why atmospheric CO_2 increased during the Holocene instead of decreasing as in previous interglacials. Understanding these important processes may also be quite significant for evaluating future climate and carbon cycle trends due to anthropogenic forcing. While this thesis does not provide simple answers to these important questions in paleoclimate research, it proposes a series of mechanisms which could contribute to both the glacial-interglacial rise in CO_2 and the Holocene increase in CO_2, including a new mechanism for the Holocene CO_2 rise related to Antarctic marine ice shelf extent.

This research project began with a focus on the Holocene carbon cycle, including both natural and anthropogenic contributions to its changes. We started with an exploration of the natural carbon cycle during the Holocene, beginning from an equilibrium simulation for 6000 B.C. (~7950 BP), the date for which atmospheric CO_2 began to increase into the middle and late Holocene according to the ice core record (Indermühle et al. 1999; Monnin et al. 2001; Ahn et al. 2004). The results for this research in the early stages of the project are given in Chapter 4 and have already been published. In attempting to find an equilibrium state, the model demonstrated

significant instability in response to fixed atmospheric CO_2, land ice and orbital forcing at 6000 B.C. In particular, the model produced quasi-periodic flushes of deep waters in the North Pacific. We took different initial conditions from this equilibrium simulation (i.e., a North Pacific with different ventilation states) to launch transient simulations in order to test the model's sensitivity to winds, marine ice shelves, and ocean circulation state from 6000 B.C. to 2000 A.D. These simulations produced decreases in atmospheric CO_2 from 260 ppm to ~245-252 ppm. However, these CO_2 reductions also coincided with a significant change in marine ice shelves in Antarctica. In particular, the interpolated model ice sheet dataset (ICE-4G from Peltier (2002)) shows a nearly complete disappearance of marine ice shelves between 4000 B.C. and 3000 B.C. This transition eliminated the Ross and Ronne-Filchner ice shelves, which are still in existence today, motivating us to conduct transient simulations to test the model response to more extensive marine ice shelves. These experiments produced much smaller decreases in atmospheric CO_2 (a few ppm). Together, these results suggested an approximately 5 ppm contribution (slightly greater for some simulations) to Holocene CO_2 levels from more extensive marine ice shelves. As it turns out, Antarctic ice shelves might have also been more extensive during the Holocene than during previous interglacials (Pollard and DeConto 2009).

In addition to resolving the model's natural (unforced) carbon cycle for the Holocene, the original objective of this study was to address the Holocene carbon cycle debate by including anthropogenic land use scenarios in the UVic model to address the early anthropogenic hypothesis of Ruddiman (2003). However, as we were exploring model sensitivity to the Holocene carbon cycle in our first paper (Chapter 4), the estimated anthropogenic contributions to the pre-industrial Holocene CO_2 levels were scaled back in the literature (Ruddiman et al. 2011). Furthermore, other modeling studies (Oloffson and Hickler 2008; Pongratz et al. 2009;

Stocker et al. 2011) that emerged over the course of this project suggested that human land use could have only contributed a few ppmv to the 16 ppmv rise in CO_2 experienced by 1 A.D. Our simulations (Chapter 5) also suggested that anthropogenic land use could only provide a relatively minor contribution to atmospheric CO_2 before the Middle Ages. Challenges to the early anthropogenic hypothesis also arose from proxy evidence, and in particular the high-resolution atmospheric $\delta^{13}C$ record from ice cores in Elsig et al. (2009) and Schmitt et al. (2012), which document a relatively small decrease in $\delta^{13}C$ (by 0.05‰) after 4000 B.C. This $\delta^{13}C$ change suggests a relatively minor net terrestrial release over the period, whereas the 40 ppmv increase in atmospheric CO_2 due to deforestation, as originally proposed by Ruddiman (2003), would have shown up as a larger decrease in the $\delta^{13}C$ record. Our preliminary simulations on methane (not presented in this thesis) also indicated that methane radiative forcing led to relatively small changes in temperature and provided only a 1-2 ppmv impact on CO_2 relative to the simulations described in Chapter 4.

Without a substantial imprint on the carbon cycle from methane radiative forcing and deforestation, the focus of our project gradually drifted into paleoclimate's holy grail : an attempt to use the model to explore glacial-to-interglacial CO_2 changes. Our work on this topic (covered in Chapter 3 to provide a better chronological order for the scope of the modeling experiments) began with an equilibrium simulation for the Last Glacial Maximum, which arrived at a steady state solution, unlike our first series of simulation using time-independent forcing at 6000 B.C. We initially planned to use the LGM equilibrium simulation to launch transient simulations to test the UVic model's sensitivity to the CO_2-alkalinity feedback proposed in Broecker et al. (1999) and Broecker (2006) as important for the Holocene increase in CO_2. These papers hypothesized that the terrestrial uptake from the early Holocene removed CO_2 from the surface

ocean, causing downwelling waters to have relatively higher concentrations of carbonate. The downwelling of waters with high carbonate concentrations, Broecker et al. (1999) argued, would have shifted the Carbonate Compensation Depth (CCD) to greater depths and allowed more sediment preservation (described in Broecker et al. (2001) in the western tropical Pacific). As greater sedimentation removes alkalinity from the ocean, atmospheric CO_2 concentrations would have increased from this effect. While Broecker et al. (1999) estimated that the entire Holocene CO_2 increase (20 ppmv) could be attributed to this CO_2-alkalinity feedback, various modeling studies have attributed modest increases in CO_2 due to this effect, including a 4-11 ppm rise computed from Joos et al. (2004) and a 6 ppm rise calculated from Elsig et al. (2009). Our results indicated that the application of the original ICE-4G database in the model led to no change in CO_2 in response to a removal of DIC from the oceans during the early Holocene, whereas more extensive ice shelves caused the effect to be as high as 7-10 ppm (Chapter 3, Section 3.1.7).

Technically, the vegetation-induced CO_2-alkalinity feedback could also be addressed by starting with an equilibrium simulation with time-independent prescribed forcing for 9000 B.C. (intended to find a steady-state equilibrium in modeled climate and carbon cycle variables for this date), before the decline in atmospheric CO_2 associated with terrestrial uptake. This simulation could then be transiently-run with prescribed atmospheric CO_2 to 6000 B.C (forcing CO_2 to decrease according to the ice core trend and thus reallocating model carbon to the terrestrial reservoir) before being "freed" from the ice core trend at 6000 B.C. However, the assumption that sediments were in a steady-state equilibrium at 9000 B.C. (10950 BP) is not tenable due to observed significant ventilations of the deep ocean during the deglacial period and the long time adjustment of sediments (on the order of 5000-10000 years). Thus, we opted to use an equilibrium simulation just prior to the LGM (21000 B.C. or 22950 BP as a starting point) to

explore the CO_2-alkalinity feedback associated with terrestrial uptake. At that time, it is more reasonable to assume that the ocean sediments are in near-equilibrium. In the transient simulations starting from this equilibrium state, we ran the model from the LGM to the present with prescribed atmospheric CO_2 (in Chapter 3, the PC CA and PC HW simulations). We further investigated the model's carbon cycle with free atmospheric CO_2 (i.e., not forced to follow the ice core trend), called henceforth a "free carbon" simulation.

These free carbon simulations (FC CA and FC HW) produced decreases in atmospheric CO_2 during deglaciation and the Holocene instead of the expected increase. This result perplexed us and inspired a series of transient simulations to determine what physical processes could lead to CO_2 increases during deglaciation and the interglacial. We discovered through these factorial experiments that both the initial weathering rate and the warming effect of CO_2 (CO_2 radiative forcing) enhanced the contribution of the oceans to the CO_2 rise, with lower weathering rates during the deglacial period supporting a substantially higher CO_2. As attention in the literature turned to the disappearance of a large passive carbon reservoir from the LGM to the present (Zimov et al. 2012; Ciais et al. 2012; Zech 2012), we simulated a high latitude terrestrial carbon release for this period, which was paced to the retreat of ice sheets. While the UVic model does not currently contain northern peatlands, we found that most of the net release to the atmosphere from this passive carbon reservoir occurred during the deglacial period (before the acceleration of peatland uptake in nature). This deglacial release led to substantially higher CO_2 concentrations in the model and provided a better match for the carbonate record from Yu et al. (2010). While none of our experiments reproduce the full magnitude of glacial-interglacial CO_2 changes, the results provide significant impetus for future experiments with a lower early-deglacial weathering rate, a forced recovery from freshwater fluxes (through a salt flux as in

Huiskamp and Meissner 2012), and a high-latitude terrestrial carbon release, which may together offer a conceptual model for deglacial CO_2 changes.

2 Thesis Outline

While the chronology of this research started with Chapter 4 (natural Holocene carbon cycle) and Chapter 5 (Holocene carbon cycle with deforestation) and terminated with Chapter 3 (deglacial changes in CO_2), we structured the articles in this thesis in terms of the paleoclimate chronology, presenting the results from the Last Glacial Maximum and the deglacial carbon cycle first (Chapter 3) before moving onto the Holocene carbon cycle (chapters 4 and 5). Chapter 2 provides a detailed review of the hypotheses related to the glacial-interglacial carbon cycle changes, with particular emphasis on the deglacial rise in CO_2 (which Chapter 3 attempts to simulate). A similar review of the Holocene carbon cycle was published in the journal *Atmosphere-Ocean* (Chapter 4, Section 1), and the details regarding this scientific debate were left in the original paper rather than moved to the literature review in Chapter 2. The reader should note that Chapter 3, Section 1.1 is simply a reduced version of the more comprehensive literature review for the deglacial carbon cycle debate found in Chapter 2.

Chapters 3, 4, and 5 are topical papers presented in article format. The results in Chapter 4 have already been published in the journal *Atmosphere-Ocean* (Simmons et al. 2013), whereas chapters 3 and 5 will be reduced for a future submission to other journals (such as *Climate of the Past* and *Climate Dynamics*). To summarize the topics of each article, Chapter 3 contains our results for the deglacial carbon cycle, describing our transient simulations covering the period from 21000 B.C. to 2000 A.D. These include experiments (1) using prescribed atmospheric carbon dioxide (ice core trend), (2) allowing for a free carbon cycle, and (3) imposing prescribed CO_2 radiative forcing. These simulations were repeated to test the sensitivity of our results to a

net release of terrestrial carbon during the early deglacial as well as to freshwater forcing from ice sheet melt. In Chapter 4, the natural carbon cycle during the mid-to-late Holocene was addressed with a series of sensitivity simulations to test model's response to different winds (modern winds and the model's internal wind feedback) as well as the initial circulation state of the ocean. The simulations in Chapter 4, unlike in Chapter 3 and Chapter 5, begin from an equilibrium simulation conducted for 6000 B.C. Finally, Chapter 5 presents our results for deforestation experiments conducted for the middle and late Holocene, followed by Chapter 6, which summarizes the main conclusions.

Structurally, the thesis is composed of independent articles, and figure numbering starts over at the beginning of each chapter. All dates in this thesis are reported in years B.C. and A.D., which correspond to the B.C.E. (Before the Common Era) and C.E. (Common Era) respectively. This was our solution to addressing the different time scales used for different literatures; published articles and data on deforestation scenarios tend to present results in B.C./A.D., whereas the literature on glacial-interglacial change prefers years or kilo-years before present (i.e., number of years before 1950 A.D.). Because deforestation data from Klein Goldewijk et al. (2011) are provided in years B.C. and A.D., which makes the presentation of the main results cleaner in Chapter 5, we opted to maintain a B.C./A.D. scale throughout the thesis to maintain consistency. While this is unconventional for studies of deglacial CO_2 change (Chapter 3), in the literature review (Chapter 2) we describe major features of glacial/interglacial change on the B.C./A.D. scale in order to provide context for important date ranges in the literature. In addition to using a B.C./A.D. time scale, another convention used in this thesis is the abbreviation of the units for CO_2 concentrations, measured in parts per million per volume (ppmv). All future reference to CO_2 concentrations in this thesis will be simply labeled "ppm", which here

represents nothing more than an abbreviation for ppmv that is more familiar to non-experts in the field. A fuller list of other important abbreviations in this thesis is also provided on p. xv.

Chapter 2: A summary of the Glacial-Interglacial Carbon Cycle Debate

While abrupt Quaternary post-glacial increases in atmospheric CO_2 are well-established features in the Vostok and EPICA Dome C ice core records, identifying the mechanisms that led to this predictable trend has proven more difficult. Proxy studies provide no definitive answers, and carbon cycle models have been unable to independently reproduce the abrupt nature of the deglacial CO_2 rise without some form of prescribed forcing (for example, the CO_2 radiative forcing used in Brovkin et al. (2012) and Menviel et al. (2012)). At present, there are three contributors that have been identified as major carbon sources to the atmosphere during deglaciation: (1) the oceans, (2) the passive fraction of the terrestrial carbon pool (permafrost and other deep-soil carbon pools), and (3) volcanic activity. There are problems with each hypothesis, which are summarized below. For a more a comprehensive discussion concerning the mechanisms behind low glacial CO_2 concentrations and the deglacial rebound in atmospheric CO_2, we refer the reader to Sarmiento and Gruber (2006, Ch. 10.4) and Sigman et al. (2010) for further discussion on ocean processes and Zimov et al. (2009) and Ciais et al. (2012) for details on potential terrestrial biosphere contributions.

1 Ocean Carbon during Deglaciation

The oceans represent the largest carbon reservoir that can fully exchange CO_2 with the atmosphere on millennial time scales, and thus they have naturally been assumed to play an important role for the increase observed in the ice core record. Some considerations include physical changes in basic ocean properties, such as salinity and temperature, which influence the solubility of CO_2 in ocean water, i.e., warmer and high-salinity water hold less CO_2 than colder

and low-salinity water. Assuming a 2°C colder high-latitude sea surface temperature (SST) and 5°C colder tropical SST between the LGM and the Holocene, Sigman and Boyle (2000) provided a mid-range estimate of a 30 ppm release during deglaciation (and ocean uptake during glaciation) due to temperature effects alone. However, because the ocean was approximately 3% saltier during the LGM due to greater freshwater storage in continental ice sheets, Sigman and Boyle (2000) further calculated that today's fresher oceans hold approximately 6.5 ppm more CO_2 due to this effect. The combination of these two factors would lead to a 23.5 ppm increase in CO_2 during deglaciation (Sigman and Boyle, 2000). Kohfeld and Ridgwell (2009) compiled a broader range of estimates, suggesting 21-30 ppm more CO_2 in the atmosphere due to deglacial/interglacial temperature increases (driving lower CO_2 solubility) and a partially-compensatory loss of atmospheric carbon (from 12 to 16 ppm) due to a freshening of the ocean. Model studies also give a diverse range of contributions related to solubility. Recently, Brovkin et al. (2012) found a 10 ppm net solubility effect (from a 2°C SST variation with freshening) and Menviel et al. (2012) provide a 16.5 ppm solubility effect (from a 2.6°C warming with freshening), while Chikamoto et al. (2012) obtained a much larger sensitivity (29 ppm). It has often been assumed that this oceanic release to the atmosphere would be entirely compensated for by the uptake of CO_2 in expanded bogs, peatlands and forests appearing in previously ice-covered terrain (Sigman and Boyle 2000; Sarmiento and Gruber 2006), but these estimates neglect terrestrial releases from other sources (see Section 2).

In addition to physical temperature and salinity controls on CO_2 solubility, the amount of carbon stored in the ocean may also be linked to (1) the rate at which deep water is ventilated and replaced by new deep water (Section 1.1), (2) the sedimentation of $CaCO_3$ (Section 1.2), and (3) the biological pump (which extracts carbon from the atmosphere/surface ocean and

transports it to the ocean interior) (Section 1.3). Each of these contributors and some of the hypotheses surrounding them are discussed below.

1.1. Physical Changes in Ocean Circulation

Ocean transport and mixing profiles during the LGM were likely much different than during the present interglacial, and it has often been proposed that some glacial deep water masses circulated or mixed at a slower rate during the LGM than they do today. If so, deep waters would theoretically have longer residence times before being ventilated at the surface, and thus more time to accumulate carbon through biological pump mechanisms. Modelling marine productivity alone, Kwon et al. (2011) determined a 44-88 ppm closed-system decrease in atmospheric CO_2 when NADW overturning was reduced by 13% and AABW overturning was reduced by 55% due to trapping of respired carbon in the ocean interior. Similarly, Tschumi et al. (2011) attributed the deglacial CO_2 rise to greater ventilation of the deep ocean through the Southern Ocean (the Southern Ocean Ventilation Hypothesis) and corresponding changes in phosphate inventory and sedimentation. These results imply that a change in the rate of overturning might fundamentally alter both the partitioning and exchange of carbon between the atmosphere and the ocean.

Related to ocean circulation state, the extent of deep water masses from different source regions can also have important implications for the carbon cycle. The $\delta^{18}O$ profiles of benthic formaninifera (acting as tracer for temperature and salinity, a conservative quantity except through mixing) suggest that Antarctic Bottom Water (AABW) likely filled the Atlantic basin up to 2000 m depth during the LGM, a significant increase in volume compared to today's lid at approximately 4000 m depth (Lund et al. 2011). Similarly, Negre et al. (2010) demonstrated, using a core in the South Atlantic at 2440 m depth dominated today by North Atlantic Deep

Water (NADW), that the $^{231}Pa/^{230}Th$ (a proxy for deep water flow rate) gradient between the North Atlantic and South Atlantic was reversed during the LGM. These results imply a northward flow of Southern Ocean-source waters at about half the Holocene southward flow rate of NADW at 2000-3000 m depth. Due to the apparent lack of an extensive North Atlantic Deep Water mass during the LGM, the more limited sinking water mass in the glacial North Atlantic is often referred to as Glacial North Atlantic Intermediate Water (GNAIW). The lack of strong overturning in the North Atlantic may have led to a poorer ventilation of this basin (more similar to the current North Pacific basin) and a greater global prominence of Southern Ocean-generated deep waters (Thornalley et al. 2011). Modeling studies disagree on the relative importance of this effect, however, with Brovkin et al. (2012) attributing 30 ppm to the changing distribution of NADW and AABW (the 'standing volume' effect), whereas Chickamoto et al. (2012) produced little change in atmospheric CO_2 from deep water reorganization due to the increased downwelling of preformed nutrients near Antarctica when AABW formation dominates (weakening the biological pump in the Southern Ocean).

1.1.1. Model-Proxy Comparisons

Modeling studies generally support the idea that the circulation and ventilation of the glacial ocean was significantly different than today. Ganopolski and Rahmstorf (2001) proposed that the stable mode of glacial thermohaline circulation involved a southward-shifted (40°N-50°N), weakened, and shallower overturning in the North Atlantic. Ganopolski and Rahmstorf (2001) also suggested that the reduced freshwater fluxes from northern ice sheets under cold, stable conditions may have allowed the locus of heat transport and overturning to shift northward and increase in intensity into a stronger (but unstable) subArctic overturning scenario more analogous to today's NADW overturning. The depth and intensity of glacial North Atlantic

overturning is still a subject of debate, with some models suggesting that the GNAIW was characterized by both shallow overturning and strong transport (Weber et al. 2007; Oliver and Edwards 2008).

With regard to Southern Ocean dynamics, Watson and Naveira Garabato (2006) suggested that enhanced seasonal sea ice production and colder temperatures during the glacial period led to much denser AABW and greater vertical stratification of the oceans globally. Proxy evidence of ocean temperature from $\delta^{18}O$ (benthic foraminifera) and salinity (sediment pore-water chlorinity) seems to suggest that most LGM deep waters below 2500 m were less than 0°C, and the salinity of deep waters was as high as 37.08±0.17 psu (compared to the global LGM mean of ~35.85 psu) (Duplessy et al. 2002; Adkins et al. 2002). Furthermore, these cold, salty deep waters were especially concentrated in the Southern Ocean (Duplessy et al. 2002; Adkins et al. 2002). Highly saline deep waters would require, through total ocean conservation of salinity, that overlying surface and intermediate waters be substantially fresher (Watson and Naveira Garabato 2006). In turn, these large vertical density gradients support the idea of reduced deep mixing in the glacial ocean and a greater residence time of abyssal waters (Watson et al. 2006). The transport-to-mixing ratios determined from the Atlantic basin $\delta^{18}O$ tracer budget in Lund et al. (2011) also indicate that vertical mixing was probably significantly lower than today, corresponding well to the conjectures in Watson and Naveira Garabato (2006). Similarly, Watson and Naveira Garabato (2006) argued that greater seasonal sea ice coverage and colder Antarctic atmospheric temperatures would have reduced the buoyancy gain of upwelling waters along the ACC (i.e., less the warming of the surface ocean through air-sea heat fluxes and subsequent mixing into outcropping deeper water masses), thus further reducing the rate of upwelling in the Southern Ocean and isolating deep waters.

In order to quantify these salinity-driven changes in ocean circulation, Bouttes et al. (2011) found that the brine rejection associated with increased LGM sea ice production probably isolated the abyssal ocean (and associated carbon reservoir), accounting for as much as 42 ppm of the CO_2 difference between separate simulations of the LGM and the pre-industrial period (the related increase in ocean stratification contributed another 8 ppm). A transient simulation of a full glacial-interglacial cycle in Brovkin et al. (2012) similarly modeled a greater dominance of Southern ocean-generated waters at depth with higher DIC storage (their Fig. 6) following the last glacial inception (~115000 B.C.). This, along with the increased solubility of CO_2 in water and weakened NADW formation, drove most of the 50 ppm decrease in the early glacial period in Brovkin et al. (2012), generally consistent with the results from the LGM - preindustrial comparison in Bouttes et al. (2011).

Linked to this change in ocean circulation, greater Antarctic sea ice extent during the glacial period may have by itself increased upper ocean stratification by acting as a cap and reducing air-sea gas exchange in important ventilation regions (for more on the feedbacks surrounding this process in the UVic model, see Meissner et al. 2008). The box model results in Stephens and Keeling (2000) suggested that greater seasonal sea ice extent in the Southern Ocean during the LGM may have played an important role in regulating glacial-interglacial CO_2 changes by increasing the efficiency of the biological pump without affecting productivity or significantly modifying the ocean's lysocline. Using diatoms and radiolaria as a proxy, Gersonde et al. (2005) show that there was ~10°-latitude greater Southern Ocean sea ice coverage during the LGM winter than in today's ocean but relatively little difference between the LGM summer and present summer sea ice extent. Thus, recent proxy evidence (Gersonde et al. 2005; Roche et al. 2012) appears to limit the cap argument to a cold-season enhancement. Using AOGCM time

slices, Chikamoto et al. (2012) found that the greater sea ice coverage in the Southern Ocean reduced atmospheric CO_2 by 6.2 ppm, but more LGM North Atlantic sea ice opposed this trend by reducing the oceanic uptake of CO_2 in this region.

In addition to a seasonal sea ice cap and reduced buoyancy in the Southern Ocean, the position of the Southern Hemisphere (SH) westerlies has also been proposed as a possible control on glacial-interglacial CO_2 changes. A poleward shift in the westerlies during an interglacial period could reinforce the Antarctic Circumpolar Current (ACC) and increase upwelling of deep water associated with Ekman divergence, whereas conversely an equatorward shift of westerlies during a glacial period would reduce the upwelling of CO_2-rich deep waters near Antarctica (Toggweiler et al. 2006). Furthermore, glacial-interglacial changes in buoyancy may serve as a positive feedback, with interglacial dynamically-forced upwelling enhanced by the relatively greater buoyancy (from air-sea exchange and mixing) of interglacial deep waters (Toggweiler et al. 2006; Watson and Naveira Garabato 2006). Some limited proxy evidence does suggest significant shifts in the westerlies during the warm and cold periods of the Holocene. In particular, glacial moraine expansion in New Zealand indicate that Antarctic cooling (in particular for the Antarctic Cold Reversal ~11000 B.C.) caused a northward shift in the SH westerlies and glacial expansion in New Zealand (Putnam et al. 2010), while a sediment core in Patagonia (52°S) shows greater long-distance pollen transport (stronger westerlies) during a period of more SH sea ice (~ 7150 B.C.), with weaker winds due southward-shifted westerlies before that date during the early Holocene Climatic optimum (Mayr et al. 2007). Using the UVic Model, Huiskamp and Meissner (2012) tested this hypothesis for the period from 15500 B.C. to 12500 B.C. for a variety of sensitivity experiments with SH westerlies shifted 9° latitude to the north and south from its present (NCEP) position. The simulations with a 9° northward shift of

the SH westerlies produced more AABW and North Pacific overturning, whereas a simulation with a weakening-then-strengthening Atlantic MOC and SH westerlies shifted south 9° latitude from its present position (an extreme scenario) produced a fast 21 ppm increase over the early part of the simulation interval (58% of the observed increase from ice cores). Huiskamp and Meissner (2012) concluded, however, that most of the amplitude in CO_2 variations were due to the restrengthening of the overturning circulation after freshwater fluxes, with latitudinal shifts may provide for a slightly faster rate of CO_2 increase.

Despite its conceptual strengths, significant uncertainty surrounds the SH westerlies hypothesis. Lamy et al. (2010) combined several peat and sediment Chilean proxy records and proposed an expansion of the northern margin of the westerlies during cold periods and a contraction/ intensification of the core westerlies (50-55°S) to the south during warm periods (i.e., the early Holocene) rather than an explicit latitudinal translation of the wind field. In an inter-model comparison study of SH westerlies, Rojas et al. (2009) also demonstrated little change in latitudinal position between LGM and pre-industrial simulations. However, the authors did show that most models simulated weaker near-surface SH westerlies during the LGM (implying reduced wind stress for dynamical upwelling). Latitudinal shift simulations in Tschumi et al. (2008) suggested that northward shifts in the SH westerlies actually expand the spatial extent of upwelling over the ocean and increased atmospheric CO_2 by as much as 2-14 ppm in the Bern3D ocean model, whereas a 50% decrease in wind speed produced a 3-33 ppm reduction in CO_2. The UVic model also confirms the importance of wind speed over latitudinal shifts, with D'Orgeville et al. (2010) indicating major difference between between strong (2× NCEP wind stress) SH westerlies (a 36 ppm increase in atmospheric CO_2) and weak (0.5× NCEP wind stress) SH westerlies (a 20 ppm decrease in atmospheric CO_2) but no major change with

latitudinal shifts. In addition, some modeling studies also indicate that an increase in marine biological productivity associated with greater dynamical upwelling could counteract an increase in atmospheric CO_2 and thus serve as a negative feedback (Menviel et al. 2008a; Chikamoto et al. 2012).

1.1.2. $\delta^{13}C$ Arguments

Evidence related to non-conservative tracer $\delta^{13}C$ generally supports the hypothesis that the overturning circulation of the oceans during the glacial period was significantly different (especially for the deep ocean) than during the pre-industrial period, giving evidence to the ventilation hypothesis for explaining changes in the carbon cycle. While marine biology can alter remineralization rates in the deep ocean and thus benthic $\delta^{13}C$, slowly-ventilating deep waters may have more time to accumulate respired organic carbon and thus contain significantly lower $\delta^{13}C$; this process is called "^{13}C aging" (Curry and Oppo 2005). Many studies addressing the topic of glacial-versus-interglacial ocean circulation have concentrated on the $\delta^{13}C$ gradient between benthic foraminifera at different ocean depths.

Reconstructions providing an Atlantic Ocean cross-section of modern and LGM $\delta^{13}C$, provided in Duplessy et al. (2002, their Fig. 6), indicates that a deep tongue of Southern Ocean-generated deep waters (with naturally reduced $\delta^{13}C$ due to nutrient limitations and incomplete surface photosynthesis in this region) was extremely rich in ^{12}C ($\delta^{13}C$ up to 0.9‰ lower than present-day AABW). This water mass also dominated the deep ocean up to 40°N. Curry and Oppo (2005) updated and confirmed these general results for the western Atlantic, indicating a strongly negative $\delta^{13}C$ associated with southern ocean-generated deep waters below 2000 m depth. Furthermore, their data indicated that downwelling water in the North Atlantic was reasonably shallow, concentrated around 1500 m depth and aging considerably as it was

transported southward due to mixing with the deep water below it. Curry and Oppo (2005) also attributed the much larger gradient in $\delta^{13}C$ (compared to today) to stronger horizontal advection than deep vertical mixing. In the Southern Ocean, Hodell et al. (2003) similarly concluded (from sediment cores documenting the last 600,000 years on the north flank of the Agulhas Ridge) that poorly-ventilated waters existed below 2500 m depth during the last four glacial periods, with well-ventilated waters constrained to the upper 2100 m of the ocean. Their Fig. 12a demonstrates that glacial periods, characterized by strongly negative $\delta^{13}C$ (and large vertical $\delta^{13}C$ gradients), give way to high deep-ocean $\delta^{13}C$ and small vertical gradients during interglacial periods, suggesting a thick, poorly-ventilated deep water mass in the Southern Ocean that disappeared during interglacials (Hodell et al. 2003). Bringing much of the sediment evidence for the Atlantic Ocean together, Marchal and Curry (2008) concluded (with statistical significance) that the $\delta^{13}C$ from benthic forams indicates that circulation during the LGM is 'dynamically incompatible' with the modern and Holocene ocean circulation states. Similarly, Hesse et al. (2011) used a carbon cycle model to show that the present-day AMOC is incompatible with glacial $\delta^{13}C$ observations; the authors obtained a more realistic profile of glacial Atlantic $\delta^{13}C$ observations when Southern Ocean sea ice formation was enhanced, suggesting that greater AABW formation and a weaker NADW could potentially explain $\delta^{13}C$ observations from sediment cores.

A broader synthesis of benthic $\delta^{13}C$ for all ocean basins for the past 150000 years was provided in Oliver et al. (2009); these data indicated greater $\delta^{13}C$ during temperature maxima and decreased $\delta^{13}C$ during temperature minima (for example, the LGM). Quantitatively, this was manifested in an increase of 0.4–1.0 ‰ from the LGM to the late Holocene in the Atlantic and an increase of 0.1–0.4 ‰ in the Indian and Pacific (Oliver et al. 2009). Complementing these trends, Schmitt et al. (2012) demonstrated an abrupt decrease in atmospheric $\delta^{13}C$ by 0.3‰ from

~15400 B.C. to 14000 B.C. at the same time as a 35 ppm increase in CO_2 (followed by a prolonged $\delta^{13}C$ minimum to 9000 B.C., their Fig. 2) and increasing $\delta^{13}C$ during the early interglacial. Because atmospheric $\delta^{13}C$ is ultimately dominated by ocean surface DIC, the authors of this study concluded that the increasingly well-ventilated ocean led to an upwelling of old carbon formerly isolated at depth. The implication is that during deglaciation, a substantial proportion of the $\delta^{13}C$ increase in ocean deep waters may be explained by a ventilation of comparatively stagnant glacial deep waters. Complicating this picture, however, Yu et al. (2010) indicated that $\delta^{13}C$ only increased in the deep waters of several ocean basins toward the end of deglaciation.

1.1.3. $\Delta^{14}C$ Proxy Data

To support the circulation-change hypothesis without some of the limitations that $\delta^{13}C$ from foraminifera present, several recent studies (Marchitto et al. 2007; Bryan et al. 2010; Skinner et al. 2010; Thornalley et al. 2011; Burke and Robinson 2012) have forged a link between cosmogenic ^{14}C and changes in ocean circulation. Because ^{14}C (formed through the interaction of cosmic rays with ^{14}N in the upper troposphere and stratosphere) is well-mixed in the atmosphere and introduced into the ocean through air-sea gas exchanges, poorly-circulated deep waters that have been isolated from atmosphere for prolonged periods of time tend to have very low ^{14}C concentrations due to the radioactive decay of this isotope back into inert ^{14}N (Burke and Robinson 2012). In general, waters frequently exposed to the surface will have ^{14}C concentrations following those of the atmosphere, whereas water masses isolated longer from the atmosphere will have much lower ^{14}C concentrations and greater ^{14}C ventilation ages (relative to the atmosphere), leading to an increasingly reduced ^{14}C to ^{12}C ratio ($\Delta^{14}C$). The radioactive fractionation quantity $\Delta^{14}C$ is thus independent of the complex, sometimes competing biological

sources limiting the interpretation of non-conservative $\delta^{13}C$, but it is also a notoriously difficult quantity to measure with precision in sediments and requires accounting for changes in the Earth's magnetic sphere and cosmic ray fluxes to the atmosphere (Burke and Robinson 2012).

North Pacific intermediate waters (near Baja California) profiled in Marchitto et al. (2007) since the LGM generally followed the reconstructed atmospheric $\Delta^{14}C$, except for a substantial part of deglaciation (~16000-10000 B.C.), during which the $\Delta^{14}C$ of this water mass dropped sharply below the atmospheric $\Delta^{14}C$ (their figure 1c). These data imply the entrainment of a highly ^{14}C-depleted water mass into intermediate waters at this time. The two most prominent decreases in intermediate water $\Delta^{14}C$ occur between 16000 B.C. and 12600 B.C. (Heinrich Event 1) and then later between 11500 B.C. and 9600 B.C. (the Younger Dryas), both coincident with prominent atmospheric CO_2 increases.

Other studies using $\Delta^{14}C$ have also suggested a link between rising CO_2 and the ventilation of lower-$\Delta^{14}C$ waters. For example, using $\Delta^{14}C$ ages in separate core from the deep Southern ocean (3770 m depth), Skinner et al. (2010) estimated that the glacial Circumpolar Deep Water (CDW) at the LGM was between 1.6 and 3 times 'older' than present (with some water masses up to 4000 years in ventilation age) and provided a conceptual model (their Fig. 4) for the entrainment of much older abyssal waters into CDW being ventilated in the Southern Ocean during the last deglaciation. Pulses of ^{14}C-depleted deep water into intermediate waters was also confirmed by sediment cores (1237-2303m depth) in the North Atlantic (~60°N) near Iceland, where rapid changes in ventilation age between modern values (400-500 years) and much greater ages (3500-5200 years) were determined (Thornalley et al. 2011, their Fig. 4). Echoing results from Marchitto et al. (2007), older ventilation ages in the North Atlantic were especially common during from ~15500 B.C. and ~13000 B.C. and the Younger Dryas (~10800-

9500 B.C.). Bryan et al. (2010) also documented decreasing $\Delta^{14}C$ between ~17000 B.C. and ~13000 B.C. in the Arabian Sea, with the water mass at 13000 B.C. being over two times more depleted in ^{14}C than the most carbon-depleted water in today's ocean. A shallower (500-1800 m depth) record from seamount corals in the Drake Passage also suggested a ^{14}C-depleted water mass, but with more modest ventilation ages (just over 2000 years) during the LGM (Burke and Robinson 2012). Because the intermediate-ocean $\Delta^{14}C$ anomaly occurred during the Heinrich Stadial, a time of increased ice rafted debris and a shutdown in North Atlantic overturning from ~15000-13000 B.C. (McManus et al. 2004), a change in circulation in the Southern Ocean (and not an intensification of the North Atlantic gyre) was likely responsible for the deglacial pulse in low $\Delta^{14}C$ to shallower depths. Modelling work in Hain et al. (2011), however, suggested that ^{14}C-depleted signatures should dissipate and diffuse rapidly when they circulate out through intermediate depths. It is thus difficult to reproduce a large $\Delta^{14}C$ decrease in the North Pacific due to abyssal ventilation using models, especially when a Southern Ocean source is assumed (Hain et al. 2011; Huiskamp and Meissner 2012).

The scope of ^{14}C-depleted deep water may have been rather limited in spatial extent, however, especially in the Pacific. Broecker et al. (2008) failed to find any major changes in $\Delta^{14}C$ since the LGM from a sediment core at 2800 m depth in the westernmost tropical Pacific (near Indonesia), and Broecker and Clark (2010) also found ventilation ages at much greater depths (4400 m) in the Central Pacific comparable to the Holocene. In the North Pacific, Keigwin et al. (2006) in cores up to 3200 m deep in the Okhotsk Sea found only slightly greater ventilation ages than today, whereas Galbraith et al. (2007) documented 1.3-1.5 times greater ventilation ages than present at 3647 m depth in the Gulf of Alaska. Perhaps most surprisingly, a sediment core from 1000 m off the coast of central Chile, an area strongly influenced by the

modern AAIW, demonstrated no major change in ventilation age during deglaciation (De Pol-Holz et al. 2010). However, a sediment core near the Galapagos Islands at 617 m depth (in the equatorial upwelling region) recorded an excessively old 8000 year ^{14}C ventilation age for Heinrich Event 1 (Stott et al. 2009). Similarly, the deep Equatorial Eastern Pacific (3600-3700 m depth, 2800-6000 years ventilation age) and southwestern Pacific (near New Zealand, 2700 m, 3000-5040 years ventilation age) also show evidence of strong ^{14}C-depletion (Keigwin et al. 2006 ; Sikes et al. 2000). This Pacific variability has raised the possibility of more than one source region for Antarctic intermediate waters during deglaciation, or perhaps an important abyssal source for ^{14}C-depleted waters outside of the Southern Ocean (Bryan et al. 2010; Burke and Robinson 2012; Rose et al. 2010). Another recent proposal suggests that these global $\Delta^{14}C$ excursions (and oceanic CO_2 releases) may be related to a destabilization of CO_2-rich fluid hydrates flanking hydrothermal vents during deglacial warming (Stott and Timmermann 2011).

The sediment cores that do demonstrate a decrease in $\Delta^{14}C$ in intermediate waters during the Heinrich Event 1 and Younger Dryas correspond to similar trends in atmospheric/surface ocean $\Delta^{14}C$ records (confirmed in separate stalagmite, coral, and planktonic foraminifera data), which all show an abrupt and unprecedented decrease of 190±10‰ between ~15500 B.C. and ~12500 B.C., a period coined the "Mystery Interval" (Denton et al. 1999; Broecker and Barker 2007). It is likely that just less than 20% (~ 37‰) could be accounted for by geomagnetic changes, thus requiring a substantial carbon source to the atmosphere that is strongly depleted in ^{14}C, arguably from the deep ocean (Broecker and Barker 2007; Burke and Robinson 2012). The search for an excessively-aged abyssal reservoir capable of creating the Mystery Interval $\Delta^{14}C$ signal in the atmosphere and intermediate waters has afforded significant limitations (Broecker and Clark 2010; Hain et al. 2011). However, Burke and Robinson (2012) has recently supplied a

mid-range calculation (based on their own more moderate ventilation ages) demonstrating that the upwelling of only 3% of deep ocean carbon is required to produce a 190‰ excursion in atmospheric $\Delta^{14}C$ when intermediate-deep water masses have ventilation ages of only 2000-3000 years (i.e., less than double that of today). This potential explanation of the Mystery Interval provides that the atmosphere holds much less ^{14}C than the ocean and can be relatively easily overpowered by the upwelling of ^{14}C-depleted waters.

1.1.4. Opal Proxies

Opal fluxes in the Southern Ocean provide another proxy of ocean circulation, free from a few of the analytical difficulties afforded by $\delta^{13}C$ and $\Delta^{14}C$. Anderson et al. (2009) examined biogenic opal production, which is strongly dependent on the upwelling of dissolved nutrients (Silicon) from deepwater masses, from three widely-separated sediment cores near the Antarctic Polar Front. Their results indicate a strong increase in opal flux after 15000 B.C., gradually decreasing back to values more comparable to glacial production during the Holocene. This provides independent evidence for greater upwelling in the Southern Ocean during the Mystery Interval. Anderson et al. (2009) also linked periods of elevated CO_2 during glacial Heinrich events to increased upwelling (opal production) in the Southern Ocean.

1.2 Alkalinity and Biological Pump Mechanisms

While changes in ocean circulation and vertical mixing can alter the distribution of DIC in the ocean, thus isolating the ocean carbon reservoir (the glacial ocean) or ventilating it to the atmosphere (deglaciation), chemical transformations of the ocean carbon reservoir, related to increases and decreases in total ocean alkalinity, can also lead to significant secondary changes in atmospheric CO_2 concentrations. Changes in the balance between alkalinity sources (weathering and sediment/$CaCO_3$-shell dissolution) and alkalinity sinks (the sedimentation of

$CaCO_3$) in the ocean thus has the potential to strongly influence glacial-interglacial variations in atmospheric CO_2.

1.2.1: Proxy Evidence for Deglacial Changes in Ocean Chemistry

Many hypotheses of glacial-interglacial carbon cycle changes rely strongly on transformations of ocean chemistry to explain part of the CO_2 drawdown during glacial periods and the corresponding CO_2 rebound during deglaciations. Proxy evidence (Yu et al. 2010; Rickaby et al. 2010; Catabig et al. 1998, and references therein) of past concentrations of carbonate ion concentration ($[CO_3^{2-}]$) in seawater are often based on the strong empirical relationship between B/Ca in benthic formaninifera and carbonate ion concentration in seawater or the weight percent in $CaCO_3$ at different depths. Observational constraints on the scale of alkalinity change were provided by Catubig et al. (1998) from a compilation of cores that together suggest that fluxes of $CaCO_3$ to the sediments, and thus the global-average Carbonate Compensation Depth (CCD), might not have changed significantly between the LGM and the Holocene.

More recently, Yu et al. (2010) brought together five high-resolution sediment cores that provided evidence for carbonate ion concentrations for the Atlantic, Pacific, and Indian basins for the past 50000 years (their Fig. 1). The cores representing very deep waters between 3400 m and 4147 m depth indicate lower $[CO_3^{2-}]$ during the LGM in all three ocean basins, followed by a deglacial increase (by 10-18 μmol/kg) to an early-Holocene maximum in carbonate ion concentration (Yu et al. 2010). The two cores that represent the intermediate/upper deep-waters in the Pacific (2310 m) and Carribean (3623 m below a 1900 m sill) basins show no change since the LGM or a greater carbonate ion concentration during the LGM, thus indicating that the larger carbonate ion gradient during the LGM between the surface and deep ocean likely existed.

Because CO_2 concentrations and carbonate concentrations are inversely related, the rise in [CO_3^{2-}] during deglaciation in the three ocean basins, at the same time as a drop in [CO_3^{2-}] in intermediate waters, suggests an entrainment or ventilation of a deep reservoir of CO_2 into intermediate waters and the atmosphere (Yu et al. 2010). Furthermore, greater sedimentation (an alkalinity sink) in response to a downwelling of high-[CO_3^{2-}] waters in the Atlantic and parts of the Indian and Pacific could contribute to alkalinity removal from the oceans during deglaciation. Rickaby et al. (2010), on the other hand, documented elevated alkalinity (high [CO_3^{2-}]) in the deep Weddell Sea during glacial periods (and abrupt decreases following glacial termination), thus indicating that there was substantial spatial complexity to glacial-interglacial changes in deep [CO_3^{2-}].

1.2.2: The Sea Level Change Hypothesis

Early hypotheses pointed to the fact that one consequence of glacial-interglacial rises is a change in sea level, in particular, approximately 140 m since the LGM. This would have brought vast expanses of continental shelves above sea level, increasing land area by approximately 15.7 to 17.3 x 10^{12} m^2 in ice-free regions (Montenegro et al. 2006). The change in sea level would have also resulted in the death and exposure of large expanses of shallow tropical coral reefs (composed of $CaCO_3$) along these continental shelves to weathering and also possibly reducing global reef habitats (fourfold) by limiting coral growth to steeper oceanic ledges (Ridgwell and Zeebe 2005). More ice-rafted debris in the North Atlantic basin during glacial periods may also be unfavourable to cold-water corals as well, although the response of deep and cold-water corals to glacial conditions on a global scale has yet to be explored (Dorshel et al. 2005). The reduction in the areal extent of shallow seas and ocean basins would also

potentially lead to less shallow water sedimentation (that is, sedimentation of $CaCO_3$ shells above the lysocline), amplifying the alkalinity signal associated with coral reef decline.

Conversely, over the course of deglaciation, the flooding of continental shelves would have led to a gradual expansion of coral reefs, equivalent to a permanent $CaCO_3$ precipitation, a factor that by itself should force the pCO_2 in the ocean and atmospheric CO_2 to rise. Thus, the reestablishment of barrier reefs since the LGM may have potentially had a significant impact on ocean chemistry (Ridgwell and Zeebe 2005). However, a prominent role for coral reef deposition in the atmospheric carbon budget has been difficult to prove, as Broecker and Henderson (1998) established that the greatest deglacial increases in atmospheric CO_2 significantly predated the most substantial sea level rise. Furthermore, given the slow pace of ocean circulation, the chemical response to precipitation would occur with a lag time of several thousand years after the reestablishment of coral reefs. Addressing this delay, Ridgwell et al. (2003) and Brovkin et al. (2012) have suggested through modeling studies that shallow water sedimentation (most notably coral reefs) should account for the more gradual and modest interglacial rise in atmospheric CO_2 during the Holocene (20 ppm). However, similar CO_2 rises during previous interglacials due to this effect have not been observed despite comparable continental shelf flooding during deglaciation (Ruddiman et al. 2011). Furthermore, higher (lower) chemical weathering rates during the interglacial (glacial) period may have, in fact, diminished or overpowered the effect of shallow water sedimentation (or glacial shelf carbonate weathering) on ocean alkalinity (Foster and Vance 2006; Lupker et al. 2013).

Countering the alkalinity effect of sea level rise on increasing atmospheric CO_2, another proposal suggests that the greater tidal mixing along continental shelves conversely increased the efficiency of oceanic CO_2 uptake as sea level rise rose (the continental shelf CO_2 pump,

Tsunogai et al. 1999). Rippeth et al. (2008) provided that the sea level rise between ~15000 B.C. and ~6000 B.C. would have increased CO_2 uptake (i.e., the air-sea exchange of CO_2 through greater tidal mixing) by a factor of 3-4, with a larger influence in the early Holocene (between ~9000 B.C. and ~6000 B.C., 0.01 ppmv yr^{-1}) corresponding to an~30 ppm oceanic drawdown. Rippeth et al. (2008) argue, in turn, that this uptake could potentially contribute to the early Holocene decline in atmospheric CO_2 as indicated by the ice core record.

1.2.3: Remineralization Storage and Depth

The biological pump to the deep ocean has also been suggested as an important factor modifying the carbonate chemistry of glacial deep waters. From a compilation of cores in the equatorial Pacific (from 1900 m – 3091 m depth), Bradtmiller et al. (2010) demonstrate that authigenic Uranium (aU) in sediments (inversely related to the oxygen (O_2) content of bottom waters) was greater during the LGM than the Holocene, and furthermore opal fluxes in these cores (providing a measure of the flux of organic matter to the deep ocean) was unchanged or substantially lower during the LGM compared to the Holocene. Together, these two proxies reveal that the respiration of falling organic matter consumed more completely the O_2 in deep waters during the LGM than during the Holocene, despite the fact that the flux of organic carbon into deep waters was actually greater during the Holocene and preformed O_2 content was reduced (due to the lower O_2 solubility in warmer Holocene deep waters). In keeping with the ventilation hypothesis, this would indicate that the suboxia of the LGM deep ocean was likely due to a greater accumulation of respired CO_2 rather than a larger influx of organic carbon in the tropical Pacific.

Jaccard et al. (2009) found similar results in the North Pacific (3244 m depth), with higher aU in sediments and lower opal fluxes during the LGM indicating poorly-oxygenated

(though not anoxic) deep waters with a high CO_2 content. Integrating these values over the entire ocean, the authors estimated a 60 ppm decrease in atmospheric CO_2 due to this transfer of carbon to the deep ocean. Furthermore, poorly-ventilated deep waters accumulating remineralized CO_2 would decrease carbonate ion concentrations, leading to event greater carbonate undersaturation at depth, a greater dissolution of carbonate in sediments and falling carbonate shells, and thus an increase in alkalinity. These sediment considerations would provide an enhanced long-term oceanic removal of CO_2 from the atmosphere (Jaccard et al. 2009; Bradtmiller et al. 2010; Sigman et al. 2010). Jaccard et al. (2009) estimated this alkalinity effect to be 15-20 ppm, suggesting thus that the transfer of respired biological carbon to the deep ocean may account for nearly all of the glacial-interglacial CO_2 variation.

Also related to greater CO_2 accumulation in the deep ocean, a change in the mean depth of organic carbon remineralization has also been suggested as an important factor determining glacial-interglacial CO_2 differences. While nutrient availability tends to limit marine biological processes more than temperature considerations, temperature may be a critical factor in determining the respiration rate of organic carbon carried out by bacteria, whose metabolism is partly temperature-dependent (see Menviel et al. (2012) for a thorough review of this topic). In particular, the colder ocean temperatures during the LGM might have slowed the respiration of falling detritus, such that more organic carbon was respired in poorly-ventilated deep waters and less carbon respired in faster-circulating intermediate waters (Kwon et al. 2009). This effect could also increase ocean alkalinity by increasing sediment dissolution.

A downward shift in remineralization depth has been explored in a few recent modeling studies. Using a biogeochemical model, Kwon et al. (2009) determined that a 24 m shift toward deeper remineralization potentially led to a 10-27 ppm decrease in atmospheric CO_2, with larger

implied decreases between glacial and interglacial climates possibly associated with a 30-77 ppm decrease in atmospheric CO_2 (without accounting for a positive alkalinity feedback). Menviel et al. (2012) also modeled changes in respired carbon storage and found a 31 ppm decrease in atmospheric CO_2 during glaciation and a 21 ppm increase during deglaciation for a low latitude ~12 m shift and a high latitude ~26 m shift in remineralization depth.

Beyond respiration rate considerations, certain coccolithophores actually develop different physiological characteristics under glacial low-CO_2 conditions that may allow their shells to fall much faster through the ocean than they do under contemporary high upper ocean and atmospheric CO_2 concentrations (Biermann and Engel 2010). More ballast minerals (dust) in the glacial ocean may have also increased the sinking speed of organic matter (Armstrong et al. 2002). Furthermore, Henson et al. (2012) shows that low-latitude ecosystems tend to transfer organic matter to the deep ocean more efficiently than high-latitude ecosystems. These factors provide additional contributions and spatial complexity to changes in remineralization depth since the LGM.

1.2.4: Calcium Carbonate : Organic Carbon Rain Ratio

The hard tissue pump has also been invoked as opposing the effects of remineralization on ocean chemistry. Strictly speaking, the slower ventilation which allows more respired CO_2 to accumulate at depth should also be accompanied by more $CaCO_3$ shell accumulation in the deep ocean, a process which consumes ambient deep-water CO_2 and leads to an increase in carbonate ion concentration at depth. Thus, accounting for the ratio of calcium carbonate or particulate inorganic matter (PIC) to particulate organic matter (POC) at the sediment level is important in order to resolve important ocean chemistry changes during glacial-interglacial cycles.

In order to explain greater deep-water CO_2 concentrations during the LGM, Archer and Maier-Reimer (1994) proposed that the rain ratio of calcium carbonate to organic carbon may have been less during glacial periods. In particular, diatoms and radiolaria, which use silicon instead of calcium carbonate for shell production, may have been more abundant, thus reducing the $CaCO_3$:POC rain ratio and maximizing the efficiency of CO_2 transfer to the deep ocean. Greater iron deposition (discussed more thoroughly in Section 1.3.1) likely stimulated more nitrate use in the Southern Ocean, reducing silicon uptake by marine organisms near Antarctica and thus allowing more unused $Si(OH)_4$ to be transported equatorward (Brzezinski et al. 2002). This "Si leak" seems to be reflected by sediment proxies near Antarctica, which show greater nitrate utilization and reduced silicon utilization during glacial periods and greater silicon utilization and reduced nitrate utilization during interglacials (Brzezinski et al. 2002). The resulting increase in silicon availability at lower latitudes may have allowed diatoms to outcompete $CaCO_3$-shell making coccolithophorids in upwelling regions, thus reducing the $CaCO_3$:POC rain ratio for glacial periods (Matsumoto et al. 2002).

Box models suggest that the rain ratio mechanism may also have important consequences on atmospheric CO_2: a 40 ppm drawdown in atmospheric CO_2 is associated with a 60% reduction in rain ratio in Matsumoto et al. (2002) and a 40% reduction in rain ratio in Munhoven (2007). When Munhoven (2010) lowered rain ratio changes over very deep basins to avoid unrealistic excursions in the modeled calcite saturation horizon, the rain ratio mechanism accounted for a lower 25 ppm decrease in atmospheric CO_2. Serious criticism to the rain ratio hypothesis has stemmed from global sediment flux data suggesting that denser $CaCO_3$-producing organisms transport organic carbon to the deep ocean much more efficiently than diatoms (Klaas and Archer 2002). Thus, the ballasting effect of $CaCO_3$ in transferring POC to the deep ocean

may "buffer" sediments from surface changes in the rain ratio (Ridgwell 2003). However, Ragueneau et al. (2006) argued that diatoms provide important contributions to the deep-ocean POC flux, propelling the rain ratio mechanism back into the spotlight along with related changes in remineralization depth during glacial-interglacial cycles.

1.3 Changes in Nutrient Availability

1.3.1 Iron Fertilization

While terrestrial biology is strongly tied to changes in temperature, primary production in the oceans is largely controlled by nutrient availability in the photic zone. Preformed nutrients, such as phosphates, nitrates, and iron, are upwelled from the deep ocean (which tends to be rich in nutrients owing to the remineralization of falling detritus) or transported from the land to the surface ocean through wind or runoff. Glacial-interglacial changes in processes controlling nutrient availability may, in turn, have important implications for marine production and thus for the carbon cycle. For example, Martin (1990) proposed that phytoplankton blooms near Antarctica experience "iron deficiency," with as little as 10% of the available nutrients being used in the Drake Passage due to the lack of iron inputs in this region (and iron serving as an important catalyst for photosynthesis). Furthermore, Petit et al. (1999) demonstrated that the dust flux from terrestrial sources to Antarctica was much greater during glacial periods and substantially lower during interglacials, indicating the same general pattern of abrupt transitions following glacial termination as in CO_2 and temperatures derived from ice cores. Greater glacial dust fluxes over Antarctica (and the Southern Ocean more generally) may have fertilized the ocean with iron and increased photosynthesis in this region. The abrupt decrease in dust fluxes after glacial terminations, in turn, may have increased atmospheric CO_2 by rapidly reducing the iron necessary for enhanced marine productivity.

These observations stimulated the Iron Fertilization Hypothesis, which posits that greater desertification and/or stronger winds during the glacial period transported more iron to the ocean. This would, in turn, increase the efficiency of the biological pump. Recent evidence from sediment cores suggest that tropical regions may have had a 2.5 times greater dust flux than today (Winckler et al. 2008), whereas the EPICA Dome C ice core suggests a 25 times greater ice flux near Antarctica (Lambert et al. 2008). Furthermore, greater sea ice melting in the summer and shallow bathymetry around Antarctica could have provided additional iron sources during the glacial periods (Sigman et al. 2010). Enhanced iron fertilization may also help explain the greater nitrate utilization in the Southern Ocean during glacial periods (Brzezinski et al. 2002). In addition, a combination of iron fertilization, greater sea ice, and colder temperatures may have also lead to the formation of larger Southern Ocean diatoms during some glacial periods, with implications for the biological pump (Cortese et al. 2012).

A variety of modeling studies have addressed the iron fertilization hypothesis to explore the potential impact on atmospheric CO_2, with conflicting results regarding the relative importance of iron fluxes during glacial periods. The box model in Watson et al. (2000) suggested that iron fluxes could explain as much as 40 ppm atmospheric CO_2 decrease during glaciation, whereas a three dimensional model in Bopp et al. (2003) suggested a more modest decrease of 15 ppm due to this effect. In general, models with greater high latitude sensitivity produce greater atmospheric CO_2 changes with iron fertilization, whereas models with low high latitude sensitivity demonstrate smaller changes (Sarmiento and Gruber 2006). More recently, Bouttes et al. (2011) showed that brine rejection and iron fertilization together could account for low CO_2 and accurate $\delta^{13}C$ profiles for the LGM, whereas transient simulations with the same model for an entire glacial-interglacial cycle in Brovkin et al. (2012) indicate that the inclusion

of iron fertilization effects in the model decreased CO_2 by 10-15 ppm by the LGM relative to the same simulation without iron fertilization. Similarly, the three dimensional model used in Menviel et al. (2012) performed several different iron fertilization experiments and found only 10-12 ppm lower atmospheric CO_2 due to greater iron fertilization. These correspond with the results of Parekh et al. (2008), which produced only a 10 ppm drawdown in CO_2 in response to a 1000-year-long flux of 100x greater iron to the ocean. At the same time, Parekh et al. (2008) also argued that the effect of iron ligand concentrations (dissolved iron which has a longer residence time in the surface ocean and thus is more available to organisms) is relatively large, amplifying the effect of more modest EPICA Dome C dust fluxes by 5-10 ppm.

1.3.2 Oceanic Phosphate Inventory

As some models are unable to produce large changes in atmospheric CO_2 related to iron fluxes, attention has increasingly turned to phosphate availability as an additional contributor to atmospheric CO_2 changes over glacial-interglacial cycles. First proposed by Broecker (1982) as the Shelf-Nutrient Hypothesis, the disappearance of continental shelves during glaciation transferred oceanic phosphate cycling to deeper ocean basins. The weathering of previously-sedimented phosphates from continental shelves to the oceans may have further increased the oceanic phosphate inventory. Perhaps more importantly, the transfer of oceanic phosphates to deeper basins also increased the distance that reactive phosphate must fall in order to be sedimented, thus likely increasing the residence time of phosphate in the water column and allowing a more efficient recycling back to the surface ocean through intermediate waters (Tamburini and Föllmi 2009). From a compilation of sediment cores, Tamburini and Föllmi (2009) estimated that glacial phosphate burial in the deep ocean was approximately 8% lower than during interglacial periods, further calculating that the total oceanic phosphate inventory

may have been 17-40% greater during glacial periods. With more abundant oceanic nitrates during the LGM, phosphates were also likely the most important limiting nutrient for primary production under glacial conditions (Eugster et al. 2013).

In order to quantify the effects of phosphate inventory on atmospheric CO_2, Menviel et al. (2012) imposed a gradual 10% increase in oceanic phosphate inventory (with iron fertilization) in the Bern3D model, which produced a substantial 50 ppm atmospheric CO_2 decrease over the course of glaciation. However, changes in phosphate inventory (which generally occur over very long timescales) were only able to explain 5 ppm of the deglacial CO_2 rise in Menviel et al. (2012), with the authors concluding that deglacial CO_2 increase is primarily due to changes in remineralization depth and physical forcings (temperature, sea ice, meridional overturning). By contrast, in a new twist to the Shelf Nutrient Hypothesis, Ushie and Matsumoto (2012) argued that phosphate weathering from continental shelf weathering actually increased CO_2 concentrations during glacial periods by 5-14 ppm rather than decreasing it. This is based on the idea that dissolved organic matter weathered from exposed continental shelves already has much lower phosphate content (due to quick phosphate removal during the initial stages of respiration) than organic carbon content (which respires more slowly). Thus, the authors argue that the flux of shelf material to the ocean leads to more substantial CO_2 inputs into surface waters from the remineralization of organic carbon than CO_2 removal due to primary production stimulated by the flux of phosphate (Ushie and Matsumoto 2012). Menviel et al. (2012) maintained, however, that the acidification of the oceans from such a pulse of CO_2 should partially counter this effect by raising ocean alkalinity.

2 Terrestrial Carbon Contributions during Deglaciation

While changes in ocean circulation, alkalinity, remineralization depth, and nutrient inventory have typically dominated the literature on glacial-interglacial CO_2 change, several recent studies have pointed to the terrestrial carbon reservoir as a potential source of atmospheric CO_2 during deglaciation. This proposition seems contradictory to reconstructions, which indicate that LGM terrestrial carbon stocks were as much as 1900 Pg C lower than during the Holocene (Zeng 2003, their table 1). Similarly, recent modeling results also suggest a smaller but substantial terrestrial uptake of 550-694 Pg C between the LGM and pre-industrial Holocene (Prentice et al. 2011). Broadly, lower terrestrial carbon storage during the LGM compared to the Holocene would suggest that the terrestrial reservoir removed CO_2 from the atmosphere over the course of deglaciation rather than contributed to a deglacial CO_2 rise.

However, vegetation-centered estimates of changes in terrestrial carbon storage exclude a potentially crucial part of the terrestrial carbon reservoir: extensive mid-latitudes permafrost in a glacial climate (Zimov et al. 2006). Under cooling (glacial) conditions, tundra litter may freeze into the soil (permafrost), becoming essentially passive until extensive thawing (e.g., during deglaciation) allows the carbon to be respired again. Many of the aforementioned modeling studies of glacial-interglacial CO_2 change do not account for the accumulation of non-peatland permafrost carbon in their simulations, which could provide an important fraction of the glacial CO_2 drawdown (Brovkin et al. 2012). Although most of this ice age tundra has disappeared, surviving glacial yedoma permafrost in Alaska allows broad estimates of past permafrost carbon storage (Zimov et al. 2006). From these calculations, Zimov et al. (2009) argued that over 1000 Pg C was released from melting permafrost during the Pleistocene-Holocene transition as ice sheets retreated and large expanses of steppe-tundra permafrost biomes were converted to boreal

forests. Similarly, Prentice and Harrison (2009) also argued that peatlands during the glacial period cannot be neglected, as low-latitude glacial wetlands (now disappeared) may account for more than 200 Pg C. Furthermore, there is some evidence of increased fire activity in the Holocene compared to the LGM, which may have provided an additional flux of terrestrial carbon to the atmosphere over the course of deglaciation (Justino et al. 2010).

Related to the permafrost release hypothesis, Zeng (2003) also proposed that organic matter may not be directly respired to the atmosphere with the approach of land ice sheets but rather buried under snow and ice or trapped in glacial moraines for long periods of time. Using a model to simulate the trapped carbon storage due to wood burial, Zeng (2003) proposed that the LGM had 547 Pg C greater storage than during the Holocene and that much of this vegetation carbon was respired during deglaciation (contributing up to 30 ppm to the deglacial CO_2 rise). Zeng (2007) further suggested that some of this organic material may have been flushed beneath ice sheets early during deglaciation along with ice-rafted debris (e.g. Heinrich Event 1), thus contributing to part of the Mystery Interval negative excursion in atmospheric $\delta^{13}C$.

An independent estimate on the difference between glacial and interglacial terrestrial carbon stocks was recently given by Ciais et al. (2012), who provide constraints on the figures provided in Zeng (2003) and Zimov et al. (2009). This study takes advantage of the fact that photosynthesis preferentially extracts $^{16}O_2$ and leaves $^{18}O_2$ in the atmosphere (the Dole Effect), and that the relative abundances of these oxygen molecules preserved in ice cores (as compared to the oceanic record) provide a measure of past photosynthetic activity. These data indicate that photosynthetic activity was ~50% less during the LGM compared to the Holocene, although estimates of terrestrial stocks from carbon isotopes suggest that this reservoir during the LGM (3640 ± 400 Pg C) held only ~330 Pg less carbon than during the pre-industrial Holocene (Ciais

et al. 2012). Taking the relatively small difference in terrestrial carbon stocks between the LGM and Holocene into account, low photosynthetic activity would suggest that ~700 Pg C of the LGM terrestrial carbon reservoir was inert (i.e., not photosynthetically active), providing an independent estimate of the total permafrost, peatland, and glacial burial carbon storage during the LGM that was released to the atmosphere during deglaciation and the early Holocene (Ciais et al. 2012).

Within the photosynthetically-active portion of the LGM carbon stocks, another terrestrial source of CO_2 to the atmosphere stems from the 140 m rise in sea level over the course of deglaciation. This sea level rise resulted in a 7% increase in ocean surface area, inundating large areas of continental shelves and destroying the terrestrial ecosystems that had been established on this land during the glacial period (Smith et al. 2011; Rippeth et al. 2008). Montenegro et al. (2006) provided reconstructions based on mean continental carbon storages, which estimated inundated carbon stocks at 182-220 Pg C, as well as results from an inter-model comparison, which produced a higher carbon storage estimates at 219-266 Pg C for the inundated region. These emissions considered alone (i.e. without accounting for subsequent oceanic or terrestrial resequestration of this flux) could translate to an 88-128 ppm increase in CO_2. In addition to releasing CO_2 to the atmosphere, the flooding of continental shelves has also been proposed as a partial (~60 ppb) contributor to deglacial rises in methane (CH_4) (Ridgwell et al. 2012).

While it represents a potentially major contribution to the deglacial rise in CO_2, significant criticism to the terrestrial release hypothesis stems from observational constraints in oceanic and atmospheric $\delta^{13}C$ (discussed in more detail in Section 1.1.2). In particular, Schmitt et al. (2012) demonstrated that a low atmospheric $\delta^{13}C$ excursion occurred between 15400 B.C.

and 9000 B.C., which may include the ventilation of respired organic carbon from the deep ocean as well as inputs from the terrestrial carbon reservoir (both sources could contribute to lower atmospheric $\delta^{13}C$). However, Schmitt et al. (2012) show that a low atmospheric $\delta^{13}C$ excursion occurred between 15400 B.C. and 9000 B.C. and coincided with the low $\Delta^{14}C$ anomaly in the atmosphere and the intermediate ocean, evidence that together supports the ventilation of respired organic carbon from the deep ocean. In addition, significant continental inundation and permafrost melting likely continued into the early Holocene as $\delta^{13}C$ was increasing in the atmosphere (Schmitt et al. 2012; Zimov et al. 2009). Greater marine productivity in the Pacific Ocean during deglacial ventilations (for example, Bradtmiller et al. 2010) might have partially masked a $\delta^{13}C$ signal associated with a terrestrial release, leading to little net change in atmospheric $\delta^{13}C$ according to Zimov et al. (2009). In addition, permafrost and inundation releases of terrestrial carbon after 9000 B.C. may have been partially balanced by the uptake of atmospheric CO_2 from expanding Holocene peatlands (~500±100 Pg C since the early Holocene according to Yu (2012)) and northward-advancing boreal forests (Prentice et al. 2011). Such a balance, however, would lead to small net changes in atmospheric CO_2 due to the terrestrial carbon after 9000 B.C. (Zimov et al. 2009), thus challenging the terrestrial uptake-carbonate compensation hypothesis for explaining the later 20 ppm increase in CO_2 after the mid-Holocene (Broecker 2006; Kleinen et al. 2010). In general, accounting for the timing and magnitude of terrestrial carbon releases and uptake within the atmospheric and oceanic $\delta^{13}C$ budgets provide the most significant challenge to determining the role of terrestrial releases to the deglacial rise of CO_2.

3 Volcanic CO_2 Inputs during Deglaciation

Another recent hypothesis concentrates on a possible lithospheric control of CO_2 during glacial-interglacial cycles (Smith et al. 2011). Huybers and Langmuir (2009) compiled data indicating that volcanic emissions of CO_2 were two to six times greater than present emissions between 10000 B.C. and 5000 B.C., mostly in high-latitude regions and likely related to mantle decompression as ice sheets began to melt (as well as potentially other related factors, including changing mantle pressure due to sea level rise). The authors of this study concluded that increased volcanic activity was concident with the rise to the early Holocene peak in CO_2 and perhaps accounted for 40 ppm of the observed deglacial CO_2 rise. Using a spectral analysis of Pacific Ring of Fire volcanism (measured by ash layers in marine sediment cores), Kutterolf et al. (2013) also demonstrated a statistically-significant spectral peak at the Milankovitch obliquity period, which also suggests volcanic pacing with changes in ice mass.

Using the Bern3D model to explore the effect of volcanic emissions on the deglacial rise in atmospheric CO_2, Roth and Joos (2012) applied a mid-range estimate of volcanic emissions and found a 40 ppm simulated CO_2 increase due to volcanic emissions. With this increase combined with an enhanced terrestrial uptake starting in the early Holocene (analogous to peatlands and forest expansion), the model produced a dampened early Holocene CO_2 decrease (3 ppm) roughly similar to the observed ice core trend (5 ppm decrease). The authors concluded that observational constraints could allow for volcanic emissions just below their mid-range estimate as a possible explanation for the late-deglacial rise in CO_2, although this release does not account for the possible balance between terrestrial uptake (peatlands/forest expansion) and a terrestrial release (inundated terrestrial carbon stocks and permafrost) as discussed in Section 2. The volcano hypothesis also suffers the same setbacks as other sea level rise hypothesis in that

the timing of the event is only able to explain a small portion of the deglacial atmospheric CO_2 increase.

Chapter 3: Carbon Cycle Dynamics since the Last Glacial Maximum: An Investigation with an Intermediate Complexity Climate Model

Within the context of the debate over deglacial changes in CO_2 summarized in Chapter 2, the UVic ESCM was used to produce several long-term simulations to determine processes important for the deglacial CO_2 increase since the Last Glacial Maximum. All simulations presented in this chapter covered the period from the LGM to the present and included land ice and Milankovitch (orbital forcing) changes. The relative importance of CO_2 radiative forcing (i.e., feedbacks related to the warming effect of CO_2) are also highlighted, and a high latitude respiration of terrestrial carbon was included in several simulations as a rough approximation to a paced permafrost release (as discussed above in Chapter 2, Section 2).

Some potentially important processes discussed in Chapter 2 above are also excluded in the simulations presented here. For example, we do not include changes in iron availablility or mineral or $CaCO_3$ ballasting, neither of which are included in the current version of the model. Unlike Menviel et al. (2012), we also do not impose changes in the ocean phosphate inventory or remineralization depth; these are allowed to evolve freely with the climate variables (and remineralization depth does decrease over the course of the simulation period due to warming). To address the contribution of shallow water sedimentation and coral reefs, we suggest that a simple manipulation of the model's weathering rate may lead to the same end result (as weathering counterbalances shallow water sedimentation and upslope coral reef growth). Volcanic emissions were not considered, although the results from simulations with prescribed

carbon (carbon injected directly into the atmosphere in order to balance the demands of other reservoirs to produce the observed CO_2 increase) could be considered analogous to a volcanic release explaining the CO_2 trend.

Abstract

The effort to explain glacial-interglacial variations in the global carbon cycle has led to one of the most stimulating debates in paleoclimate research. In this paper, we used the University of Victoria Earth System Climate Model v. 2.9 to simulate the deglacial and interglacial carbon cycle from the Last Glacial Maximum (LGM) to the present. In particular, we evaluate the model's sensitivity to a changing continental ice sheet configuration, Milankovitch forcing, CO_2 radiative forcing, different constant weathering rates, high latitude terrestrial carbon storage, and freshwater fluxes (Heinrich Event 1 and the Younger Dryas in the North Atlantic). The simulations with only orbital, ice sheet, and CO_2 radiative forcing produced a set of results with variations in atmospheric CO_2 ranging ~35 ppmv. In these simulations, CO_2 radiative forcing was the dominant factor allowing for a ventilation of deep-ocean DIC. In addition, a corresponding ventilation-alkalinity feedback related to a flush of deep-ocean DIC allowed CO_2 to continue to increase throughout the deglacial period and into the interglacial. While CO_2 radiative forcing produced the largest ventilation of the Atlantic and Indian basins, the inclusion of freshwater fluxes led to an earlier warming, destabilization and flushing of deep waters in the North Pacific. Our modeling experiments also suggest that lower weathering rates might help explain early deglacial rises in CO_2, due in part to the slow effect of carbonate compensation that is ultimately overwhelmed by the ventilation-alkalinity feedback. Regarding the terrestrial biosphere, these simulations suggest that virtually all of the net global vegetation carbon uptake since the LGM is attributable to CO_2 fertilization and not to greater land availability and warmer temperatures. Furthermore, a respiration of high latitude terrestrial carbon storage (600 Pg C) indicates that the carbon released during the early and mid-deglacial has the largest net effect on the carbon cycle, causing atmospheric CO_2 to increase up to 250 ppm in the model.

1 Introduction

Abrupt increases in atmospheric CO_2 during the Quaternary period following glacial terminations are well-established features in the Vostok and EPICA Dome C ice core records (Petit et al. 1999; Monnin et al. 2001), although identifying a reliable chain-of-events that lead to this predictable trend has proven more difficult. Much of the debate surrounding glacial-interglacial variations in atmospheric CO_2 has centered on the relative role of terrestrial, oceanic, and volcanic contributions to these variations. However, current estimates of relatively small changes in the calcite compensation depth (CCD) (Catubig et al. 1998) provide caveats for an oceanic release and small changes in atmospheric $\delta^{13}C$ limit the scope of a terrestrial release (Schmitt et al. 2012; Elsig et al. 2009). While proxy studies allow few simple, definitive answers, carbon cycle models have also been unable to independently reproduce the abrupt nature of the deglacial CO_2 rise without some form of prescribed forcing (such as CO_2 radiative forcing) or imposing changes on ocean diffusivity or the way marine detritus is cycled through the ocean (Brovkin et al. 2012; Menviel et al. 2012). In this paper, the University of Victoria Earth System Climate Model (UVic ESCM) is used to investigate the last deglaciation and present interglacial climate (23000 BP to present, or 21000 B.C. to 2000 A.D.). These include sensitivity experiments to explore the impacts of a high latitude carbon release and freshwater forcing on the carbon cycle.

1.1 A Summary of the Glacial-Interglacial Carbon Cycle Debate

Most of the current literature agrees that the oceans play a vital role in the deglacial rise of atmospheric CO_2. Simple physical changes in basic ocean properties, such as a gradually lower salinity and warmer sea surface temperatures over the course of deglaciation, altered the solubility of CO_2 in sea water. Kohfeld and Ridgwell (2009) compiled a range of estimates,

suggesting that an increase in ocean temperature could provide 21-30 ppm of the deglacial CO_2 increase (driving lower CO_2 solubility); however, this would be partially compensated by an oceanic uptake of atmospheric CO_2 on the order of 12 to 16 ppm due to a freshening of the ocean. Model studies also give a diverse range of contributions related to solubility. Recently, Brovkin et al. (2012) found a 10 ppm net solubility effect (from a 2°C SST variation with freshening) and Menviel et al. (2012) provide a 16.5 ppm solubility effect (from a 2.6°C warming with freshening), while Chikamoto et al. (2012) estimated a much larger sensitivity (29 ppm).

In addition to the physical controls on CO_2 solubility, ocean transport and mixing profiles during the Last Glacial Maximum (LGM) were likely much different than during the present interglacial, and it has often been proposed that some glacial deep waters masses circulated or mixed at a slower rate during the glacial period than they do today. The strongly negative $\delta^{13}C$ in Atlantic deep waters (Duplessy et al. 2002; Curry and Oppo 2005; Marchal and Curry 2008) during the LGM suggests a more stratified ocean with poorly-ventilated deep waters that had a high remineralized carbon content. In the Southern Ocean, Hodell et al. (2003) similarly concluded that poorly-ventilated waters existed below 2500 m depth in the Southern Ocean during the last four glacial periods, with well-ventilated waters constrained to the upper 2100 m of the ocean. To characterize deglaciation, Spero and Lea (2002) analyzed planktic (thermocline-dwelling) foraminifera from tropical marine sediments, which suggested a substantial low $\delta^{13}C$ excursion in near-surface waters consistent with a significant upwelling of low- $\delta^{13}C$ deepwater. A flush of glacial deep waters to the surface during the early deglacial was also documented in the Southern Ocean, where Anderson et al. (2009) suggests significantly greater upwelling (opal fluxes) during the deglacial period near the Antarctic Polar Front between ~15000 B.C. and ~8000 B.C. Similarly, Galbraith et al. (2007) show a flush of glacial deep waters in the North

Pacific around 12600 B.C., coincident with a reinvigoration of the NADW after Heinrich Event 1 and a 10 ppm increase in atmospheric CO_2.

Measurements of $\Delta^{14}C$ also appear to support a ventilation of carbon-rich deep waters. Several sediment core studies document either highly depleted $\Delta^{14}C$ in glacial deep waters or an incursion of low $\Delta^{14}C$ anomalies into intermediate waters during deglaciation in the Atlantic, Indian, and parts of the Southern and Pacific oceans (Marchitto et al. 2007; Bryan et al. 2010; Skinner et al. 2010; Thornalley et al. 2011; Burke and Robinson 2012). The very low $\Delta^{14}C$ values obtained in these studies suggest that glacial deep waters had been isolated from the atmosphere or did not mix with intermediate waters for prolonged periods of time. The incursion of low $\Delta^{14}C$ values into intermediate waters during deglaciation also coincided with an abrupt and unprecedented decrease of 190±10‰ $\Delta^{14}C$ during the Mystery Interval (~15500 B.C. and ~12500 B.C.), which implies a significant release of carbon from the ocean to the atmosphere due to the ventilation of carbon-rich deep waters. However, several cores in the Pacific have failed to find any major changes in $\Delta^{14}C$ since the LGM (Broecker et al. 2008; Broecker and Clark 2010; Keigwin et al. 2006; De Pol-Holz et al. 2010), whereas others show evidence of significant ^{14}C-depletion (Sikes et al. 2000; Keigwin et al. 2006; Marchitto et al. 2007; Galbraith et al. 2007; Stott et al. 2009). Pacific variability has raised the possibility of more than one source region for low- $\Delta^{14}C$ waters during deglaciation, or perhaps an important abyssal source for ^{14}C-depleted waters outside of the Southern Ocean (Bryan et al. 2010; Burke and Robinson, 2012; Rose et al. 2010). Another recent proposal suggests that the complex pattern of $\Delta^{14}C$ excursions (and oceanic CO_2 releases) may be related to a destabilization of CO_2-rich fluid hydrates flanking hydrothermal vents during deglacial warming (Stott and Timmermann 2011).

Related to the ocean circulation state, the spatial extent and depth of deep water masses from different source regions might also have important implications for the carbon cycle. The $\delta^{18}O$ profiles of benthic formaninifera (acting as tracer for temperature and salinity, a conservative quantity except where mixing occurs) suggest that Antarctic Bottom Water (AABW) likely filled the Atlantic basin up to 2000 m depth during the LGM, a significant increase in volume compared to today's lid at approximately 4000 m depth (Lund et al. 2011). Similarly, Negre et al. (2010) indicated a northward flow of Southern Ocean-source waters in the Atlantic at about half the southward flow rate of NADW at 2000-3000 m depth during the Holocene. The weaker overturning in the North Atlantic (McManus et al., 2004) may have led to a poorer ventilation of this basin and a greater global prominence of Southern Ocean-generated deep waters (Thornalley et al. 2011), which tend to have higher DIC content. Modeling studies disagree on the relative importance of this effect, however, with Brovkin et al. (2012) attributing 30 ppm to the changing distribution of NADW and AABW (the 'standing volume' effect), whereas Chikamoto et al. (2012) produced little change in atmospheric CO_2 from deep water reorganization due to the increased burial of preformed nutrients near Antarctica when AABW formation is enhanced (weakening the biological pump in the Southern Ocean).

With regard to Southern Ocean dynamics, proxy evidence of ocean temperature from $\delta^{18}O$ (benthic foraminifera) and salinity (sediment pore-water chlorinity) seems to suggest that most LGM deep waters below 2500 m were less than 0°C, and the salinity of deep waters was as high as 37.08±0.17 psu in the Southern Ocean (compared to the global LGM mean of ~35.85 psu) (Duplessy et al. 2002; Adkins et al. 2002). Large vertical density gradients implied by these salinity and temperature differences support the idea of reduced deep mixing in the glacial ocean and a greater residence time of abyssal waters, with more sea ice coverage limiting the

downward mixing of positive buoyancy by winds (Watson and Naveira Garabato 2006). The transport-to-mixing ratios determined from the Atlantic basin $\delta^{18}O$ tracer budget in Lund et al. (2011) also indicate that vertical mixing was probably significantly lower than today. Bouttes et al. (2011) demonstrated that the brine rejection associated with increased LGM sea ice production could account for as much as 42 ppm of the CO_2 difference between the LGM and the pre-industrial period, whereas a transient simulation of a full glacial-interglacial cycle in Brovkin et al. (2012) similarly modeled a 50 ppm decrease in CO_2 from the interglacial to glacial climate due to this effect as well as a weaker NADW.

The physical presence of more Antarctic sea ice extent during the glacial period may have by itself increased upper ocean stratification by acting as a cap and reducing air-sea gas exchange in important ventilation regions. Stephens and Keeling (2000) first suggested (using a box model) that greater seasonal sea ice extent in the Southern Ocean during the LGM played a crucial role in regulating glacial-interglacial CO_2 changes. Using diatoms and radiolaria as a proxy, Gersonde et al. (2005) show that there was ~10°-latitude greater Southern Ocean sea ice coverage during the LGM winter than in today's ocean but relatively little difference between the LGM summer and present summer sea ice extent. Thus, recent proxy evidence (Gersonde et al. 2005; Roche et al. 2012) appears to limit this argument to a cold-season enhancement. Using AOGCM time slices, Chikamoto et al. (2012) determined the effect of increased sea ice extent in the Southern Ocean to be 6.2 ppm, with greater LGM North Atlantic sea ice opposing this trend by reducing the oceanic uptake of CO_2 in this region.

Also related to air-sea exchanges, a poleward shift in the westerlies during an interglacial period could reinforce the Antarctic Circumpolar Current (ACC) and increase the upwelling of deep water associated with Eckman divergence, whereas conversely an equatorward shift of

westerlies during a glacial period may reduce the upwelling of CO_2-rich deep waters near Antarctica (Toggweiler et al. 2006). Some limited proxy evidence using glacial moraines in New Zealand (Putnam et al. 2010) and sediment cores in Patagonia suggest a strengthening of winds and/or northward shifts in the westerlies during warm periods of the Holocene (Mayr et al. 2007; Lamy et al. 2010). An inter-model comparison study of SH westerlies (Rojas et al. 2009) demonstrated little change in the latitudinal position of westerlies between LGM and pre-industrial simulations but indicated that most models simulated weaker near-surface SH westerlies during the LGM (implying reduced dynamical upwelling). Using the Bern3D ocean model, Tschumi et al. (2008) found that northward shifts in the SH westerlies actually expanded the spatial extent of upwelling (and marine productivity) over the ocean and decreased atmospheric CO_2 by as much as 14 ppm. Huiskamp and Meissner (2012) tested this hypothesis for the Mystery Interval (~ 15500 B.C. to 12500 B.C.) in the UVic model but suggested that changes in freshwater forcing dominated the total magnitude of the release more than latitudinal shifts in the SH westerlies. However, D'Orgeville et al. (2010) modeled significant atmospheric CO_2 increases in conjunction with (large) intensifications of the SH westerlies (up to 36 ppm) but found there was relatively little change in CO_2 due to latitudinal shifts.

In addition to ventilation and the distribution of different water masses, many hypotheses concerning deglacial carbon cycle changes also rely on transformations of ocean chemistry, in which alkalinity decreases in the ocean (forcing atmospheric CO_2 to increase on multi-millennial time scales). Early research pointed to the 140 m sea level rise since the LGM, which would provide for greater shallow water sedimentation and coral reef expansion on continental shelves (alkalinity sinks in the ocean). Broecker and Henderson (1998), however, established that the greatest deglacial increases in atmospheric CO_2 significantly predated the most substantial sea

level rise. Addressing this delay, Ridgwell et al. (2003), Kleinen et al. (2010) and Brovkin et al. (2012) have suggested that shallow water sedimentation and coral reefs should account for the more gradual and modest interglacial rise in atmospheric CO_2 during the Holocene (20 ppm). However, similar CO_2 rises during previous interglacials due to this effect have not been observed despite similar continental shelf flooding during deglaciation (Ruddiman et al. 2011), and higher (lower) weathering rates during the interglacial (glacial) period may have, in fact, diminished or overpowered the effect of shallow water sedimentation (or glacial shelf carbonate weathering) on ocean alkalinity (Foster and Vance 2006; Lupker et al. 2013).

In order to document changes in ocean chemistry since the LGM, Yu et al. (2010) brought together five sediment cores that provided data on carbonate ion concentrations ($[CO_3^{2-}]$) for the Atlantic, Pacific, and Indian basins. Cores representing very deep waters suggest lower $[CO_3^{2-}]$ during the LGM (especially pronounced in the Atlantic), followed by a deglacial increase (in the Atlantic 10-18 μmol/kg) to an early-Holocene maximum in $[CO_3^{2-}]$ (Yu et al. 2010). Greater sedimentation (an alkalinity sink) in response to a downwelling of high-$[CO_3^{2-}]$ waters in the Atlantic and parts of the Indian and Pacific could thus contribute to alkalinity removal during deglaciation. Rickaby et al. (2010), on the other hand, documented elevated alkalinity (high $[CO_3^{2-}]$) in the deep Weddell Sea during glacial periods and decreases during deglaciation, indicating that there was substantial spatial complexity to glacial-interglacial changes in $[CO_3^{2-}]$ and alkalinity. Observational constraints on the scale of alkalinity change were provided by Catubig et al. (1998) from a compilation of cores that suggest that (globally) the CCD might not have changed significantly between the LGM and the Holocene.

The soft and hard tissue biological pumps to the deep ocean, as well as their impact on alkalinity, have also been proposed as an important factor modifying the carbonate chemistry of

glacial deep waters. For example, colder ocean temperatures during the LGM might have slowed the respiration of falling detritus, such that more organic carbon was respired in poorly-ventilated deep waters and less carbon respired in faster-circulating intermediate waters (Bradtmiller et al. 2007; Kwon et al. 2009). This change in remineralization depth has been explored in several recent modeling studies, with a 24 m shift toward deeper remineralization leading to a 10-27 ppm decrease in atmospheric CO_2 in Kwon et al. (2009). Menviel et al. (2012) also modeled changes in respired carbon storage and found a 31 ppm decrease in atmospheric CO_2 during glaciation and a 21 ppm increase during deglaciation for a low latitude ~12 m shift and a high latitude ~26 m shift in remineralization depth.

Another potential contributor to changes in the biological pump includes the availability of preformed nutrients (iron, phosphate and nitrates). Evidence from sediment cores suggest that during the LGM tropical regions may have experienced a 2.5 times greater dust flux than today (Winckler et al. 2008). EPICA Dome C ice core also suggests a 25 times greater dust flux near Antarctica (Lambert et al. 2008). Box models with stronger high latitude sensitivity tend to produce large changes due to this effect (40 ppm in Watson et al. 2000), whereas OGCMs and Earth System models of intermediate complexity attribute glacial-interglacial variations in atmospheric CO_2 of only 10-20 ppm due to iron fertilization (Bopp et al. 2003; Parekh et al. 2008; Brovkin et al. 2012; Menviel et al. 2012).

In addition to iron fluxes, changes in phosphate inventory have also been proposed as potential contributors to glacial-interglacial CO_2 variations. In particular, the flooding of continental shelves during deglaciation may have encouraged more (shallow-water) sedimentation of phosphate (i.e., removal from the oceans), thus weakening the biological pump. As such, Tamburini and Föllmi (2009) estimated that total oceanic phosphate inventory may

have been 17-40% greater during glacial periods. Menviel et al. (2012) imposed a gradual 10% increase in oceanic phosphate inventory in the Bern3D model, which produced (along with iron fertilization) a substantial 50 ppm atmospheric CO_2 decrease over the course of glaciation. However, changes in phosphate inventory (which generally occur over very long timescales) were only able to explain 5 ppm of the deglacial CO_2 rise in Menviel et al. (2012), with the authors concluding that the deglacial CO_2 increase is primarily due to changes in remineralization depth and physical forcings (temperature, sea ice, meridional overturning). By contrast, Ushie and Matsumoto (2012) argued that phosphate weathering from continental shelf weathering actually increased CO_2 concentrations during glacial periods (5-14 ppm) because weathered content on continental shelves contains more unrespired organic carbon than unrespired phosphate.

Another recent hypothesis to explain atmospheric CO_2 variations concentrates on a possible lithospheric control of CO_2 during glacial-interglacial cycles. Huybers and Langmuir (2009) compiled data indicating that volcanic emissions of CO_2 were two to six times greater than present emissions between 10000 B.C. and 5000 B.C. These emissions were mostly in high-latitude regions and likely related to mantle decompression as ice sheets began to melt. Using a spectral analysis of Pacific Ring of Fire volcanism (measured by ash layers in marine sediment cores), Kutterolf et al. (2013) also demonstrated a statistically-significant spectral peak at the Milankovitch obliquity period, which suggests volcanic pacing with changes in ice mass. In a modeling study, Roth and Joos (2012) concluded that observational constraints could allow for volcanic emission (coupled to terrestrial uptake) just below their mid-range estimate as a possible explanation for the late-deglacial rise in CO_2. However, the volcano hypothesis also

suffers the same setbacks as the sea level rise hypothesis in that the timing of the event is only able explain only a small portion of the deglacial atmospheric CO_2 increase.

While changes in ocean circulation, calcium carbonate compensation, remineralization depth, and nutrient inventory have typically dominated the literature on glacial-interglacial CO_2 change (Sigman et al. 2010), several recent studies have pointed to the terrestrial carbon reservoir as a potential source of atmospheric CO_2 . Traditionally, the terrestrial reservoir has been considered a sink of CO_2 during deglaciation, with LGM terrestrial carbon stocks estimated as much as 1900 Pg C lower than during the Holocene (Zeng 2003, their table 1).

Opposing this uptake, greater permafrost storage at mid-latitudes in a glacial climate may have provided a net release of carbon to the atmosphere over the course of deglacation (Zimov et al. 2006). Zimov et al. (2009) argued that over 1000 Pg C was released from melting permafrost during the Pleistocene-Holocene transition as ice sheets retreated and large expanses of steppe-tundra permafrost biomes were converted to boreal forests. Prentice and Harrison (2009) also argued that low-latitude glacial wetlands and peatlands (which disappeared during deglaciation) may account for more than 200 Pg C. Furthermore, Montenegro et al. (2006) indicated that the deglacial flooding of continental shelves may have contributed an additional 182-220 Pg C release to the ocean and atmosphere. At the same time, Yu (2012) estimated that expanding peatlands during the interglacial period absorbed ~500±100 Pg C from the atmosphere.

An independent assessment of the difference between glacial and interglacial terrestrial carbon stocks was recently provided by Ciais et al. (2012), providing constraints on the magnitude of both terrestrial uptake and release during deglaciation. The Dole Effect (in $\delta^{18}O$ measurements) indicate that photosynthetic activity was ~50% less during the LGM compared to the Holocene, although estimates of total terrestrial stocks from carbon isotopes suggest that

this reservoir held only 330 Pg C less carbon than during the pre-industrial Holocene (Ciais et al. 2012). This implies that ~700 Pg C of the LGM terrestrial carbon reservoir was inert (i.e., not photosynthetically active), providing an independent estimate of the total permafrost, peatland, and glacial burial carbon storage during the LGM that was released to the atmosphere during deglaciation and the early Holocene.

While it represents a potentially major contribution to the deglacial rise in CO_2, significant criticism to the terrestrial release hypothesis stems from observational constraints in oceanic and atmospheric $\delta^{13}C$. In particular, Schmitt et al. (2012) demonstrates that a low atmospheric $\delta^{13}C$ excursion occurred between 15400 B.C. and 9000 B.C. and coincided with the low $\Delta^{14}C$ anomaly in the atmosphere and the oceans, evidence that together supports the ventilation of respired organic carbon from the deep ocean. To counter this argument, Zimov et al. (2009) suggested that an increase in marine productivity in the Pacific Ocean following glacial termination (for example, Bradtmiller et al. 2010) might have partially masked a $\delta^{13}C$ signal associated with a terrestrial release, leading to little net change in atmospheric $\delta^{13}C$ as provided in the ice core record. In general, accounting for a terrestrial carbon release in the atmospheric and oceanic $\delta^{13}C$ and $\Delta^{14}C$ budgets provide a significant challenge to the terrestrial release hypothesis.

1.2 Contributions of this Paper to the Glacial-Interglacial CO_2 Debate

In this paper we apply the UVic ESCM v. 2.9 to the entire period from the LGM to the present to determine the relative importance of temperature, ocean circulation, sedimentation, and terrestrial changes in producing a deglacial and Holocene increase in atmospheric CO_2. Strengths of the UVic ESCM include the application of a three-dimensional ocean general circulation model (OGCM) at a spatial resolution of 1.8° x 3.6° for long transient simulations.

The results presented here build on past work using the UVic model to explore glacial (Schmittner et al. 2007a,b; Schmittner and Galbraith 2008) and deglacial changes in CO_2 in response to freshwater forcing and wind shifts (Meissner 2007; D'Orgeville et al. 2010; Huiskamp and Meissner 2012). However, longer transient simulations of the entire deglacial period allow for a more complete exploration of alkalinity impacts on the deglacial CO_2 rise due to the recent incorporation of sediments in the model (Archer et al. 1996; Eby et al. 2009). In particular, a series of sensitivity experiments were carried out to explore deglacial and interglacial changes with two different (constant) weathering rates. These simulations were compared with other modeling experiments where alkalinity was held constant (weathering set equal to sedimentation) to isolate the contributions of alkalinity to CO_2 changes.

In addition, unlike in most previous modeling studies, which impose ice core CO_2 radiative forcing on the model climate, we present both (1) simulations that allow the model's climate and carbon cycles to respond to the changes in the model-calculated CO_2 and (2) simulations including (solely) the CO_2 radiative forcing from ice cores. The distinction between the two types of modelling experiments helps distinguish important processes related to CO_2 warming (beyond ocean solubility considerations) that contribute to an increase in atmospheric CO_2. Furthermore, the sensitivity simulations provide further exploration of the influence of freshwater forcing (Meissner 2007; Liu et al. 2009) and Southern Ocean processes on glacial-interglacial change. Additionally, several simulations include a high latitude terrestrial carbon reservoir (very roughly analogous to permafrost) that is allowed to respire in concert with the retreat of ice sheets in order to evaluate the active terrestrial biosphere's capacity to re-sequester carbon releases from a passive carbon reservoir.

In the following sections, we provide a brief description of the model (Section 2.1), with attention to processes considered important for glacial-interglacial changes, as well as details on our equilibrium simulation for the LGM (Section 2.2). The experimental design for transient simulations of the period is given in Section 2.3-2.6. Then, in Section 3, we discuss important results for simulations without high latitude terrestrial carbon storage (Section 3.1), with such high latitude carbon (Section 3.2), and with freshwater fluxes (Section 3.3). A summary of the major conclusions is provided in in Section 4.

2 Model and Methodology

2.1 Model Description

The University of Victoria Earth System Climate Model (UVic ESCM, or simply UVic model) v. 2.9 provides a simplified but comprehensive representation of the Earth's climate system and carbon cycle and is classified as an Earth system Model of Intermediate Complexity (EMIC) (Claussen et al. 2002). All components of the model operate on a grid of 1.8° latitude by 3.6° longitude, a reasonable spatial resolution for long-term paleoclimate simulations. The core of the model is a three-dimensional primitive equation ocean general circulation model (the Modular Ocean Model v. 2.0, see Pacanowski (1995)) with 19 vertical levels, coupled to a dynamic-thermodynamic sea ice module (Weaver et al. 2001). Eddy transport is parameterized according to Gent and McWilliams (1990), and diapycnal ocean (vertical) mixing is accomplished through a time-independent horizontally-constant diffusivity profile (approximately 0.3 10^{-4} m^2 s^{-1} at the pycnocline). In its present configuration, the model's ocean regime is defined by unchanging present-day bathymetry and sea level, and thus some important features of LGM and deglacial topography, such as continental shelves above sea level, are not featured in the simulations discussed here. However, a closed Bering Strait is a feature of the present simulations

Concerning ocean properties, inorganic carbon chemistry and air-sea exchanges of CO_2 (controlled by temperature, salinity, DIC, alkalinity, wind speed, and sea ice cover) are described in Ewen et al. (2004). Contributions of the biological pump to the ocean carbon cycle are calculated by a Nutrient-Phytoplankton-Zooplankton-Detritus (NPZD) module, which includes both nitrates and phosphates as well as nutrient recycling through microbial respiration and

differential treatment of dissolved and particulate organic carbon (POC) (Schartau and Oschlies 2003; Schmittner et al. 2005; Schmittner et al. 2008).

An important update to the 2.9 version of the UVic ESCM is the inclusion of an oxic-only sediment module from Archer et al. (1996), which allows the model to evaluate secondary changes in ocean chemistry and atmospheric CO_2 due to sediment respiration and calcium carbonate compensation (albeit without the effect of shallow water sedimentation and coral reefs) (Eby et al. 2009). In thismodel, the dissolution of $CaCO_3$ in falling detritus occurs with an e-folding depth of 3500 m (Schmittner et al. 2008). Once reaching the ocean floor, total $CaCO_3$ dissolution depends on the respired CO_2 content of overlying waters and the $CaCO_3$:POC rain ratio at the sediment level (which is calculated as the amount of unrespired organic carbon to calcite content of falling detritus that reaches the ocean floor). Changes in the rain ratio are constrained in the model to lie between 0.55 and 1.82 due to the buffering capacity of sediments (Ridgwell 2003) and the neglect of $CaCO_3$ ballasting effects in the current version of the model. In our simulations, however, the rain ratio does not actually vary significantly (1.05-1.27) (see Section 3.1.4). It should be noted that all sedimentation occurs at or below a depth of 1240 m, and thus variations in shallow water sedimentation (with increasing sea level) are not parameterized in these simulations.

The model atmosphere is simplified to a two-dimensional Energy-Moisture Balance Model (EMBM) that generates its own surface temperature and humidity in response to prescribed incoming solar radiation (only orbitally-forced changes in insolation in the present simulations) and radiative forcing from CO_2. Included in the EMBM equations are contributions from latent and sensible heat fluxes as well as evapotranspiration (Fanning and Weaver 1996; Weaver et al. 2001). Surface wind fields must be prescribed in order to drive horizontal moisture

advection and the wind stress over the ocean. All simulations in this paper use a dampened version of the "wind feedback" in Weaver et al. (2001), which provides a thermal-wind adjustment to 20thcentury reanalysis winds (Kalnay et al. 1996) based on the model-generated spatial temperature gradient at each time step. The atmospheric $\Delta^{14}C$ was kept constant at 0‰ for all simulations, and thus the oceanic $\Delta^{14}C$ profiles generated by the model are mostly a function of ocean ventilation changes. The fractionation ratio $\delta^{13}C$ is not traced in the current version of the model for either the atmosphere or the ocean, although the implications of $\delta^{13}C$ observational constraints are discussed in Section 3.3.3.

Vegetation changes on land are driven by the Top-down Representation of Interactive Foliage and Flora Including Dynamics (TRIFFID) Module, which represents five plant functional types (PFTs) : C_3-photosynthesis grasses (manifested as mid-latitude prairie/steppe and very high latitude tundra in the model), C_4-photosynthesis grasses (mostly tropical and subtropical savannah in the model), broadleaf trees (tropical and subtropical forest), needleleaf trees (predominately boreal and high-elevation forest), and shrubs (tropical/Mediterranean bushy vegetation and tundra-boreal forest transition regions) (Cox 2001; Meissner et al. 2003a; Matthews et al. 2004). The distribution of PFTs is determined by temperature and soil moisture, and in regions where several types of vegetation can grow, Lotka-Volterra equations (predator-prey interspecies competition based ultimately on a tree-shrub-grass dominance hierarchy and net primary production) determine a dominant species for each grid cell. The soil model (MOSES) stores and respires terrestrial carbon litter in a single layer with 1 m depth (Cox et al. 1999). Special treatment of peatland processes are not currently included in the UVic model, although Chapter 4 shows that TRIFFID's C_3 tundra yielded similar land carbon uptake results as more-developed high-latitude peatland modules for the late Holocene period.

The UVic model also incorporates prescribed continental ice sheets and non-conducting marine ice shelves. Their thickness and areal coverage at the LGM and over the course of deglaciation are determined by the ICE-4G dataset (Peltier 2002). The geographical coverage and retreat of these ice sheets is prescribed every 1000 years according to the above data, with no ice melting (except of accumulated snow on or near the ice sheets) as a result of insolation or temperature changes generated by the model. The UVic ESCM also does not produce a freshwater flux to the ocean when land ice sheets disappear, and thus (prescribed) freshwater fluxes due to the retreat of these ice sheets are only present in the suite of freshwater sensitivity simulations described in sections 2.6 and 3.3. Marine ice shelves are represented as a "lid" over the ocean; their presence influences both temperature and precipitation over the surrounding ocean through the ice-albedo effect and eliminate air-sea fluxes where they are present (thus providing a strong influence on overturning near Antarctica; see Chapter 4 for more details). However, these simplified marine ice shelves neither exchange freshwater nor latent heat with the surrounding ocean. Also, they cannot be grounded against the ocean floor.

2.2 LGM Equilibrium Simulation

Slowly-varying atmospheric CO_2 and land ice cover make the LGM perhaps the most appropriate time period to generate a model equilibrium climate with constant forcing parameters, although there is some debate on whether the climate system and carbon cycle were truly in equilibrium at the LGM (e.g., Rickaby et al. 2010). A model spin-up start date of 21000 B.C. (~22950 BP) was selected, approximately 2000 years before the actual LGM in order to ensure that glacial conditions are adequately captured by the model in transient simulations. Initiated from pre-industrial conditions (the default restart file for the UVic ESCM v. 2.9), this equilibrium simulation was run for 9700 model years with time-independent prescribed CO_2

(191.1 ppm), orbital forcing (the Milankovitch forcing for 21000 B.C.), and land ice sheets (LGM extent at 19000 B.C.) with the model's wind feedback adjustment to NCEP reanalysis winds. The carbon content of the oceanic, terrestrial, and sediment reservoirs were equilibrated to maintain the constant atmospheric CO_2. No adjustments to the CO_2 radiative forcing were made to account for lower concentrations of other greenhouse gases (namely CH_4 and N_2O). Furthermore, to maintain the assumption of an equilibrium carbon cycle just prior to the LGM, the weathering flux was set equal to the sedimentation rate in the spin-up simulation (i.e., no nascent carbonate compensation at the beginning of transient simulations).

Virtually all model variables reached a steady state equilibrium without the instabilities documented in Chapter 4. From the pre-industrial starting point, global surface air temperatures decreased from 12.2°C to 9.2°C and the depth-integrated ocean potential temperature decreased from 3.7°C to 2.0°C. In addition, the meridional overturning circulation slowed down (the global maximum overturning streamfunction decreased from 21.4 Sv to 14.6 Sv) and the oceans became less well-ventilated (mean-ocean $\Delta^{14}C$ decreased from -155.2‰ to -196.8‰). At the end of the simulation, broadleaf trees maintained high vegetation fractions in the tropics and subtropics, whereas needleleaf trees (boreal forests) were restricted to the southern two-thirds of the United States, central China, Korea and mid-latitude portions of South America and Africa (not shown). Over the course of the simulation, a significant fraction of terrestrial carbon (~187 Pg C) south of the LGM-extent ice sheets was transferred into the ocean reservoir due to colder conditions and less fertilization from lower atmospheric CO_2. The high-latitude terrestrial carbon at the pre-industrial starting point that was transferred underneath the LGM ice sheets for the equilibrium simulation (~366 Pg C) was removed from the model rather than buried under the ice or forced into the atmosphere/oceans. This may have contributed to the model's

underestimation of the DIC content of the glacial oceans, as suggested in Huiskamp and Meissner (2012) for their modeling experiments of the Mystery Interval.

2.3 Transient Forcing

` This equilibrium simulation for 21000 B.C. was then used as the initial conditions for a series of transient simulations exploring deglaciation with time-evolving orbital (Milankovitch) forcing and retreating ice sheets (ICE-4G) from 21000 B.C. to the present (ice data was interpolated between data points every 1000 years). A complete list of these experiments is provided in Table 1. Incorporating changes in land ice and insolation, Free Carbon (FC) transient simulations allowed the model's carbon reservoirs to evolve freely without any other prescribed forcing beyond evolving ice sheets and insolation changes. The only CO_2 radiative forcing in these FC experiments was provided by model-generated atmospheric CO_2 concentration and not the observed record from ice cores. Prescribed Carbon (PC) simulations, however, forced the model's carbon reservoirs to equilibriate to the observed ice core record of atmospheric CO_2 concentrations, following the Vostok record (Petit et al. 1999) from 21000 B.C. to 6000 B.C., Taylor Dome (Indermühle et al. 1999) from 6000 B.C. to 1006 A.D. and from Law Dome (Etheridge et al. 1996) after 1006 A.D. This ice core record was used to maintain consistency with other prescribed carbon simulations performed with the UVic model (for example, see Chapter 4). In contrast to the FC experiments, carbon was injected into (or removed from) the atmosphere in the PC simulations to balance the net sources and sinks from other carbon reservoirs (oceans, biosphere, sediments) in order to maintain the interpolated ice core CO_2 concentration for that date. A third series of simulations, testing model sensitivity to deglacial CO_2 radiative forcing and denoted "CO2rad" in the results discussion, allowed the model carbon

Simulation Name	Milankovitch forcing	ICE-4G prescribed land ice	Ice core CO_2 radiative forcing starting at 19004 B.C.	Prescribed atmospheric CO_2 from ice cores	Weathering Rate =	Frozen Soil Carbon (600 Pg C)	Freshwater fluxes
Transient Simulations described in Section 3.1							
FC CA	X	X			sedimentation rate		
FC HW	X	X			144.0 Tg C/yr or 12.0 Tmol/yr		
FC LW	X	X			120.7 Tg C/yr or 10.1 Tmol/yr		
CO2rad CA	X	X	X		sedimentation rate		
CO2rad HW	X	X	X		144.0 Tg C/yr or 12.0 Tmol/yr		
PC CA	X	X		X	sedimentation rate		
PC HW	X	X		X	144.0 Tg C/yr or 12.0 Tmol/yr		
Transient Simulations described in Section 3.2 with a high latitude terrestrial carbon release							
FC CA HLC	X	X			sedimentation rate	X	
FC HW HLC	X	X			144.0 Tg C/yr or 12.0 Tmol/yr	X	
FC LW HLC	X	X			120.7 Tg C/yr or 10.1 Tmol/yr	X	
CO2rad CA HLC	X	X	X		sedimentation rate	X	
CO2rad HW HLC	X	X	X		144.0 Tg C/yr or 12.0 Tmol/yr	X	
CO2rad LW HLC	X	X	X		120.7 Tg C/yr or 10.1 Tmol/yr	X	
Transient Simulations described in Section 3.3.1 and 3.3.2 with freshwater fluxes							
FC CA FW	X	X			sedimentation rate		X
FC HW FW	X	X			144.0 Tg C/yr or 12.0 Tmol/yr		X
CO2rad CA FW	X	X	X		sedimentation rate		X
CO2rad HW FW	X	X	X		144.0 Tg C/yr or 12.0 Tmol/yr		X
Transient Simulations described in Section 3.3.3 with freshwater fluxes and a high latitude terrestrial carbon release							
FC CA FW HLC	X	X			sedimentation rate	X	X
FC HW FW HLC	X	X			144.0 Tg C/yr or 12.0 Tmol/yr	X	X
FC LW FW HLC	X	X			120.7 Tg C/yr or 10.1 Tmol/yr	X	X
CO2rad CA FW HLC	X	X	X		sedimentation rate	X	X
CO2rad HW FW HLC	X	X	X		144.0 Tg C/yr or 12.0 Tmol/yr	X	X
CO2rad LW FW HLC	X	X	X		120.7 Tg C/yr or 10.1 Tmol/yr	X	X

Table 1: A summary of the principal transient simulations discussed in this paper.

cycle to evolve freely but applied the radiative forcing (warming effect) of CO_2 according to the ice core record. The CO_2 radiative forcing increased from 0 Watts m^{-2} at 19004 B.C. and was calculated from the same ice core record (Vostok and Taylor/Law Domes) as in the PC simulations using the traditional formula ($\Delta F = 5.35 \times \ln(C/C_o)$, where C represents the linearly-interpolated CO_2 between data points from the ice core record and C_o represents the CO_2 value from Petit et al. (1999) at ~19004 B.C.). CO2rad simulations allowed the warming influence of the observed CO_2 increase to be isolated from secondary factors related exclusively to the atmospheric carbon reservoir content in the PC simulation, such as terrestrial sequestration.

2.4 Weathering Rates

Changes in weathering rates can have important implications for ocean alkalinity. Howver, modeling studies investigating the influence of weathering changes are limited (Brovkin et al. 2012). A comprehensive weathering module is not available in the 2.9 version of the model, but the effects of weathering can be tested indirectly by using different constant weathering rates or by setting the weathering rate equal to the ocean sedimentation rate. In the latter case where weathering equals sedimentation, denoted henceforth as CA for "constant alkalinity," there can be no carbonate compensation because weathering inputs directly balance precipitation to the sediments. Simulations with constant alkalinity allow for purely physical mechanisms (and their climate reponses) to be isolated from those related to chemical changes in the ocean (alkalinity changes and carbonate compensation). The UVic ESCM, however, does not remove carbon from the terrestrial carbon reservoir (soil erosion) in order to maintain this weathering flux but rather generates new bicarbonate to inject into the ocean. Thus, as the model is currently configured, total carbon conservation is not possible for the constant weathering simulations.

The most obvious choice for constant weathering experiments is the $CaCO_3$ sedimentation rate obtained at the end of the LGM equilibrium simulation (for 21000 B.C.), in which the global flux to the oceans had stabilized to a value of 12.0 Tmol (Alk)yr^{-1} (or 4566 kg C s^{-1}) to balance a nearly constant global sedimentation rate. The choice of 4566 kg C s^{-1} maintains the basic assumption of an equilibrium climate just prior to the LGM. However, in the first 2000 years of both the FC and PC transient simulations (leading up to the actual LGM at 19000 B.C.), the sedimentation rate dropped abruptly before stabilizing to a lower rate at 19000 B.C. of ~10.1 Tmol yr^{-1} (or 3824 kg C s^{-1}) in the PC CA transient simulation and 3828 kg C s^{-1} in

the FC CA transient simulation. Because the model ice sheets are unchanging during this period and atmospheric CO_2 is nearly constant in both the PC and FC simulations, orbital forcing might be responsible for changes in sedimentation and the large difference between the two equilibrium weathering rates (~4566 kg C s^{-1} and ~3828 kg C s^{-1}) calculated for the LGM period. Except for the freshwater sensitivity experiments (which have lower weathering rates approaching 2500 kg C s^{-1}), most CA transient simulations from 21000 B.C. to 2000 A.D. produce weathering rates within the range of 3500 kg C s^{-1} to 5000 kg C s^{-1} to balance sedimentation. Therefore, 3828 kg C s^{-1} (at 19000 B.C. in transient simulations) represents the lower end of this range and 4566 kg C s^{-1} (from 21000 B.C.) provides a high estimate. As a result, sensitivity simulations are presented in this paper in which the higher constant weathering rate (12.0 Tmol yr^{-1}, or 4566 kg C s^{-1}) was applied during the entire deglaciation period, denoted "high weathering rate" or "HW," and several experiments were repeated with the lower constant weathering rate (10.1 Tmol yr^{-1}, or 3828 kg C s^{-1}), denoted "low weathering rate" or "LW." On a global scale, these are relatively small differences in weathering rates, approximately equivalent to the glacial (10 Tmol yr^{-1}) to interglacial (12-13 Tmol yr^{-1}) cycles in silicate weathering as modeled in Brovkin et al. (2012).

2.5 High Latitude Terrestrial Carbon Storage

Because the calculations in Ciais et al. (2012) indicate that the terrestrial biosphere of the LGM was probably only ~330 Pg C smaller than the pre-industrial terrestrial carbon pool, it is likely that a ~650-700 Pg C passive soil carbon reservoir existing at the time of the LGM essentially disappeared after 19000 B.C. and was absorbed into a photosynthetically-active carbon pool. A series of experiments were designed to model the biosphere's sequestration response to the release of a large high-latitude passive soil carbon reservoir, as proposed by Ciais et al. (2012). As the passage from soil carbon back to vegetation carbon requires a pathway

through the atmosphere, this passive soil carbon, likely dominated by permafrost, represents a potentially large source of carbon to the atmosphere on multicentennial-to-millennial timescales during deglaciation (Zimov et al. 2009), although the $\delta^{13}C$ record in the atmosphere and ocean limits the timing and long-term impact of such a release (Schmitt et al. 2012). The goal of these experiments are to determine the response of the Earth system to a paced release of soil carbon, with particular interest in how this release impacts other important processes during deglaciation, such as alkalinity changes in the ocean.

In order to address the response time of terrestrial re-sequestration of this reservoir, we created an LGM inert high-latitude soil carbon pool of 600 Pg C inserted into the model with a carbon density of 34.434 kg C m^{-2} in experiments denoted "HLC" for "high latitude carbon." This pool amount is well within the range of uncertainty in Ciais et al. (2012) and with density comparable to that in Zimov et al. (2009). It was used because the maximum sequestration potential of the model from the LGM to pre-industrial is also 600 Pg C (See Section 3.1.2). A total re-sequestration of high latitude carbon would thus, in the model, produce no net change in terrestrial carbon. Northern peatlands are not currently represented in the model. However, the approximately 473-621 Pg C (Yu 2012) associated with northern peatland uptake beginning around 9000 B.C., partially compensated for by the disappearance and release of glacial and early deglacial peatlands (~200 Pg C, according to Prentice et al. (2009)), may explain the rest of the net terrestrial uptake implied in Ciais et al. (2012) that is not modeled in these simulations. As ice sheets retreated during deglaciation (at 1000-year time steps in the interpolated ICE-4G dataset), a corresponding fraction of this soil carbon pool (with the aforementioned density of 34.434 kg C m^{-2}) was brought to the surface in the newly ice-free regions and allowed to begin respiring, though in reality the release of terrestrial carbon from permafrost would have occurred

along the margins of the maximum-extent ice sheets rather over recently-cleared terrain Because the UVic model has a one soil layer, respiration likely occurred faster than under more realistic conditions of gradual permafrost melting and slow deep-soil respiration. At the same time, abrupt threshold releases of high latitude carbon have been proposed in the past (Zimov et al. 2009). The HLC experiments represent accordingly a fast release of the passive carbon reservoir from Ciais et al. (2012).

2.6 Freshwater Fluxes

As the prescribed ice sheets in the model do not exchange latent heat or freshwater with other model components, a separate series of simulations were conducted to test the sensitivity of the model's carbon cycle and ocean circulation to freshwater fluxes from Heinrich Event 1 and the Younger Dryas event. Freshwater forcing experiments are difficult to parameterize in this particular model, as the UVic ESCM demonstrates strong hysteresis behavior (Rahmstorf et al. 2005), and overturning in the North Atlantic does not readily recover from collapses in the thermohaline circulation. Previous studies on thermohaline circulation using the UVic model tend to focus on freshwater pulses of limited duration (Schmittner and Galbraith 2008), whereas the fluxes imposed here occur over a longer period of time. In order to overcome the hysteresis obstacle, Huiskamp and Meissner (2012) imposed an "unphysical salt flux" following the freshwater fluxes from Heinrich Event 1 in several simulations in order to achieve a realistic recovery in North Atlantic overturning as illustrated in McManus et al. (2004). However, on the longer time scales considered here, an unphysical salt flux could also lead to an unphysical increase in atmospheric CO_2, considering that the solubility of CO_2 in sea water decreases for increasing salinity in the model. Although this effect is likely quite small, we did not impose a salt flux in the present simulations. Furthermore, though unrealistic, the absence of a NADW

recovery also allowed us to isolate the role of Southern Ocean dynamics on atmospheric CO_2. Nevertheless, results from the Heinrich Event 1 and shortly thereafter are highlighted in this paper, as this is when the model results agree best with Liu et al. (2009) and proxy data (McManus et al. 2004).

The data for Heinrich Event 1 was taken directly from the DGL-A meltwater scheme defined in the supporting online material of Liu et al. (2009) in sea level equivalents, also used more recently in He et al. (2013). Due to large uncertainties surrounding Heinrich Event 1, these fluxes are couched to resemble Younger Dryas data and are perhaps larger than in reality (Jerry McManus, personal communication, 2013). In our simulations, the Gulf of Mexico meltwater was introduced to the ocean through the Mississippi River Valley, and the North Atlantic fluxes passed through the St. Lawrence Valley. All meltwater pulses were added on top of natural runoff from precipitation in the model, which Meissner (2007) found produced a stronger North Atlantic MOC shutdown in the UVic model for the Younger Dryas. Between 12720 B.C. and 10950 B.C., no meltwater was added to the model. Thereafter, between 10950 B.C. and 9550 B.C., we applied the meltwater scheme for the Younger Dryas in Carlson et al. (2007), which had been previously used in UVic model in Meissner (2007) with different initial conditions. As in Meissner (2007), the Younger Dryas pulse was injected into the North Atlantic through the St. Lawrence Valley rather than into the Arctic Ocean.. After 9550 B.C., no further meltwater pulses were introduced. All experiments with these fluxes are denoted "FW" for "freshwater." The model considers no other freshwater inputs from glacial melting beyond these two events and thus accounts for an 0.46 ‰ increase in salinity, only ~44% of the total glacial-interglacial change in oceanic salinity.

3 Results and Discussion

3.1 Simulations without High Latitude Carbon Storage

3.1.1 Atmospheric CO_2

While the simulations presented here do not result in abrupt increases in atmospheric CO_2 over the course of deglaciation, they do illustrate a range of CO_2 changes (35 ppm). Furthermore, the largest increase in CO_2 (~25 ppm) from the LGM to the late Holocene is comparable to that obtained in an AOGCM study with a free carbon cycle (20-23.7 ppm, Chikamoto et al. 2012). Fig. 1 illustrates the results for transient experiments with both the freely-evolving model carbon cycle (FC) without excess high latitude carbon storage or freshwater forcing. Atmospheric CO_2 (Fig. 1a) does not increase in any of the simulations without prescribed radiative forcing, indicating that the large changes in land ice (the ice-albedo feedback) and northern hemisphere insolation do not by themselves trigger mechanisms in the model to increase CO_2. In fact, for the simulation with constant alkalinity (FC CA) and the higher weathering rate (HW), atmospheric CO_2 declines 5-10 ppm from 19000 B.C. to 2000 A.D.

Looking in greater detail at the other carbon reservoirs, the decrease in atmospheric CO_2 in the FC CA simulation is fueled by a 200 Pg C net increase in the terrestrial carbon reservoir since the LGM (Fig 1b, blue line), a figure somewhat less than the 330 Pg C recently estimated by Ciais et al. (2012). In the same simulation, a compensating release (Fig. 1b, blue line) of ocean carbon (~195 Pg C) is partially hindered by an increase in model living marine biomass that occurs between the LGM and the mid-Holocene (Section 3.1.4). The lower constant weathering rate (LW), however, produced a slightly greater atmospheric CO_2 (195 ppm) by the mid-Holocene (Fig. 1a, green line). The simulation with the higher constant weathering

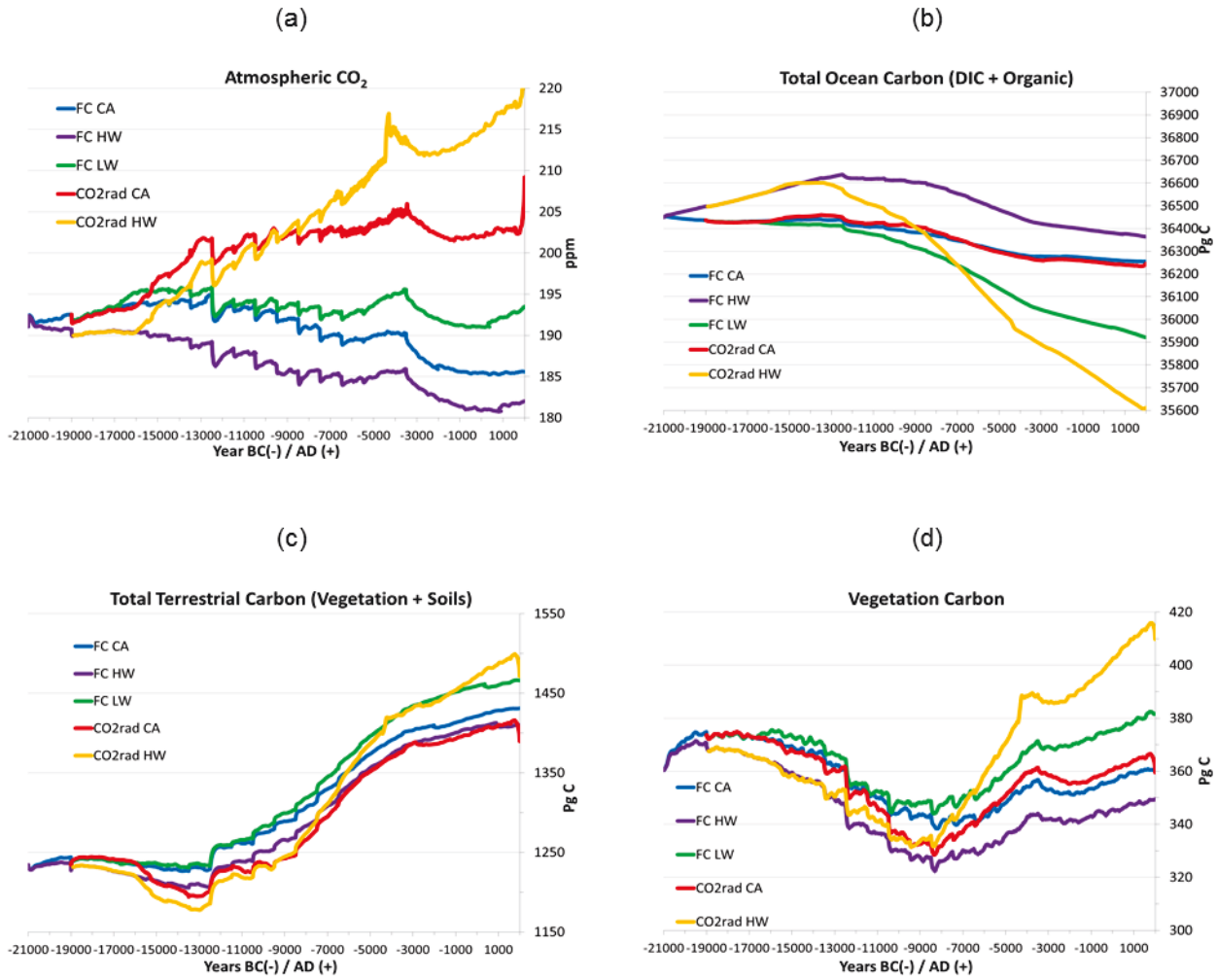

Fig. 1: Carbon reservoirs that exchange directly with the atmosphere, for simulations without high latitude carbon. These include (a) atmospheric carbon dioxide (ppmv, abbreviated ppm), (b) total terrestrial carbon (both vegetation and soils), (c) vegetation (above-ground) carbon, and (d) total ocean carbon (organic and inorganic carbon). All simulations represented in this figure have a freely-evolving carbon cycle. They include separate transient simulations with constant ocean alkalinity (FC CA, blue line), a higher (12 Tmol yr^{-1}) constant weathering rate (FC HW, purple line), and a lower (10.1 Tmol yr^{-1}) constant weathering rate (FC LW, green line). Two of these simulations, FC CA and FC HW, were repeated with CO_2 radiative forcing (denoted by warmer colours): CO2rad CA (red line) and CO2rad HW (orange line).

rate (HW) yielded, in turn, the lowest atmospheric CO_2 value just above 180 ppm at the end of the Holocene (Fig. 1a, purple line). The difference between the higher and lower weathering rate curves is somewhat intuitive: greater weathering is an alkalinity source to the oceans and causes atmospheric CO_2 to decrease unless sedimentation (the alkalinity sink) outpaces weathering, whereas lower weathering leads to a decrease in ocean alkalinity if sedimentation (an alkalinity sink) outpaces the combined effect of weathering and sediment dissolution (alkalinity sources).

Regardless of alkalinity differences between the simulations, the dip in CO_2 in most experiments after 4000 B.C. occurred in response to a large reduction in Antarctic marine ice shelves. In Chapter 4, the modelled disappearance of Antarctic marine ice shelves over the course of an interglacial stimulated more air-sea exchange and bottom water formation near the coast of Antarctica, which in turn led to a greater prominence of deep, high-DIC Antarctic bottom waters globally. These denser abyssal waters also lead to poorer abyssal ventilation, resulting inan accumulation of DIC at depth and a corresponding drawdown in atmospheric CO_2. The effect of the greater formation of slowly-ventilating AABW also appears to initiate a 5 ppm decrease in CO_2 in the many of the present simulations. In Chapter 4, it is also noted that this complete disappearance of marine ice shelves between 4000 and 3000 B.C. in the interpolated ICE-4G dataset is perhaps overemphasized, and that the comparatively greater marine ice shelf extent during the Holocene compared to most earlier interglacials (Pollard and DeConto 2009) might have resulted in a better-ventilated ocean and a 5-10 ppm higher CO_2 during the Holocene. A sensitivity study (not shown) of the FC LW simulation with more extensive ice shelves (as in Chapter 4) rose to 199 ppm between 4000 B.C. and 2000 A.D. rather than the decline shown here.

For the simulations including CO_2 radiative forcing, in which the warming effect of rising CO_2 is imposed on the modelled climate system without changing the evolution of the carbon cycle, a total post-glacial CO_2 rise of approximately 15 ppm (to 206 ppm before the ice shelf transition) occurred in the CO2rad CA simulation (Fig. 1a, red line). Compared to the same constant alkalinity simulation without radiative forcing (Fig. 1a, blue line), the net effect of this prescribed warming is 20 ppm more CO_2 in the atmosphere. Because CO_2 radiative forcing increases global temperature and leads to a better-ventilated ocean (Section 3.1.3), this 20 ppm

difference represents the combined effect of both outgassing and ventilation in the model's atmospheric CO_2 balance (Fig. 1b, red line). Furthermore, by allowing alkalinity to respond to these ventilation changes, the influence of CO_2 radiative forcing on the HW profile led to an even greater increase in CO_2 (to 215-220 ppm) due to a notable decrease in both DIC and alkalinity associated with a better-ventilated ocean (Fig. 1a, orange line).

3.1.2 Terrestrial Carbon

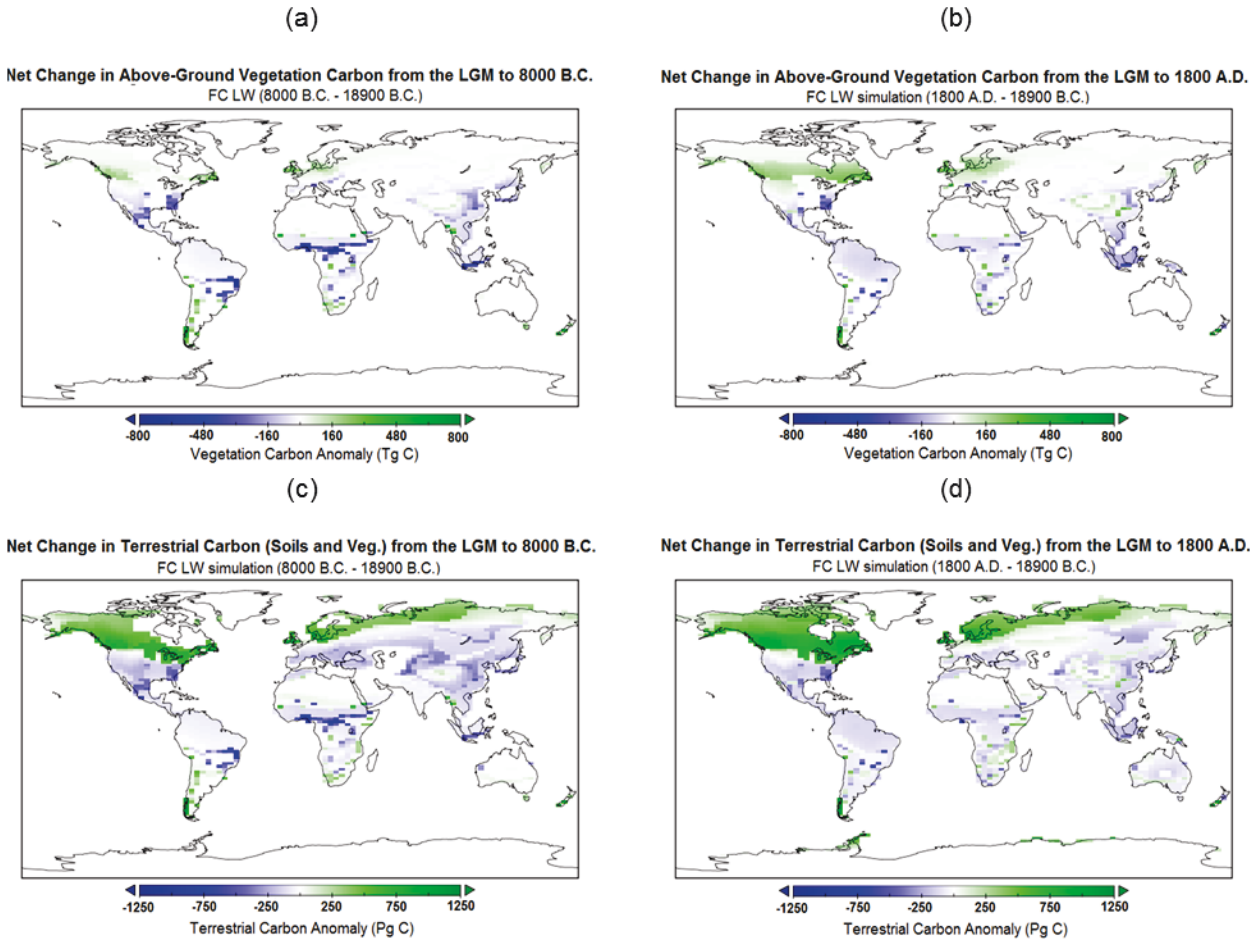

Fig. 2: The net change in the spatial distribution of above-ground vegetation carbon at (a) 8000 B.C. and (b) 1800 A.D. and the net change in total terrestrial carbon (vegetation and soils) at (c) 8000 B.C. and (d) 1800 A.D. since the LGM climate (defined as 18900 B.C.) for the FC LW simulation. Vegetation carbon anomalies are plotted on a scale of -800 Tg C to +800 Tg C, whereas terrestrial carbon anomalies are plotted from -1250 Tg C to +1250 Tg C.

While atmospheric CO_2 does not increase markedly in the simulations described above, a more detailed analysis of the changes in vegetation and terrestrial carbon yields some surprising finds. Terrestrial carbon (Fig. 1c) increased just over 200 Pg C in all FC simulations after 13000 B.C., although Fig. 1d demonstrates that vegetation carbon (above-ground biomass) actually decreased in many runs from the LGM to the early Holocene (9000 B.C.). A comparison of Figs. 1c and 1d also reveals that all simulations produced net decreases or slight increases in vegetation carbon from the LGM to the Holocene, indicating that the net terrestrial increase after 13000 B.C. was largely driven by a global increase in soil carbon as ice sheets retreated (Fig. 2c,d). Even the simulations with CO_2 radiative forcing (Fig. 1d, red and orange lines) produced a strong decline in vegetation carbon from the LGM through to the early Holocene. This decrease in global vegetation seems at first counterintuitive considering that ice sheets were retreating, the Earth was warming, and vegetation was expanding over formerly ice-covered areas in all of these simulations.

The spatial distribution of vegetation carbon stocks (Fig. 2a,b) provides additional insight into this pattern. The FC LW experiment is selected among the FC simulations for this illustration because it only slightly surpassed the original LGM vegetation carbon storage by the end of the period. The comparison indicates that terrestrial vegetation gains in mid and high-latitude regions were unable to outweigh larger losses in the tropics (until, at least, the end of the simulation in the FC LW case). The disappearance of ice sheets and related warming slowly destabilized some tropical and subtropical ecosystems. This is particularly true where boreal forests were reduced and replaced in subtropical regions (such as the present-day southeastern United States, Fig. 2a), resulting in new PFT distributions that accumulate biomass more slowly due to the low atmospheric CO_2 in these simulations. Even by the end of the HW simulation

(Fig. 2b,d), the model only yielded substantial vegetation and soil carbon gains in areas covered by ice sheets during the LGM, with other parts of the world demonstrating equivalent or slightly reduced carbon storage. It should be noted that the UVic's wind feedback is unable to generate a significantly-enhanced African monsoon vegetation (Fig. 2a); thus, the model likely overemphasized the vegetation loss in the Sahel region in the early Holocene. However, the net effect on vegetation carbon should be similar, as most of the African vegetation gains in the mid Holocene were likely lost by the late Holocene (Indermülhe et al. 1999). Although pollen reconstructions are sparse in northern Africa for the LGM (Prentice et al. 2000), other modeling results also suggest that African forests were replaced more readily by low-density forests and shrublands (Fig. 2a) under low glacial CO_2 conditions (Dominique and Haxeltine 1997; Street-Perrott et al. 1997). The sensitivity of subtropical and tropical vegetation to less CO_2 fertilization thus appears to have a significant impact on vegetation and terrestrial carbon losses in these simulations, implying that the greater CO_2 fertilization over the course of deglaciation was instrumental in maintaining high biomass density in the tropics.

The addition of CO_2 radiative forcing to the constant alkalinity experiment actually led to less vegetation carbon storage than some of the other FC simulations (Fig. 1d), indicating that the temperature rise associated with both retreating ice sheets and increasing CO_2 does not lead to more global vegetation. The PC simulation (Fig. 3) provides an important comparison, as it injects carbon into the model's carbon reservoirs to force the increase in CO_2, whereas no physical carbon reservoir changes are altered in the CO_2 radiative forcing experiments. The presence of more carbon in the atmosphere system causes substantial net increases in vegetation carbon stocks (by ~230 Pg C, see Fig. 3b), without the decrease in vegetation carbon

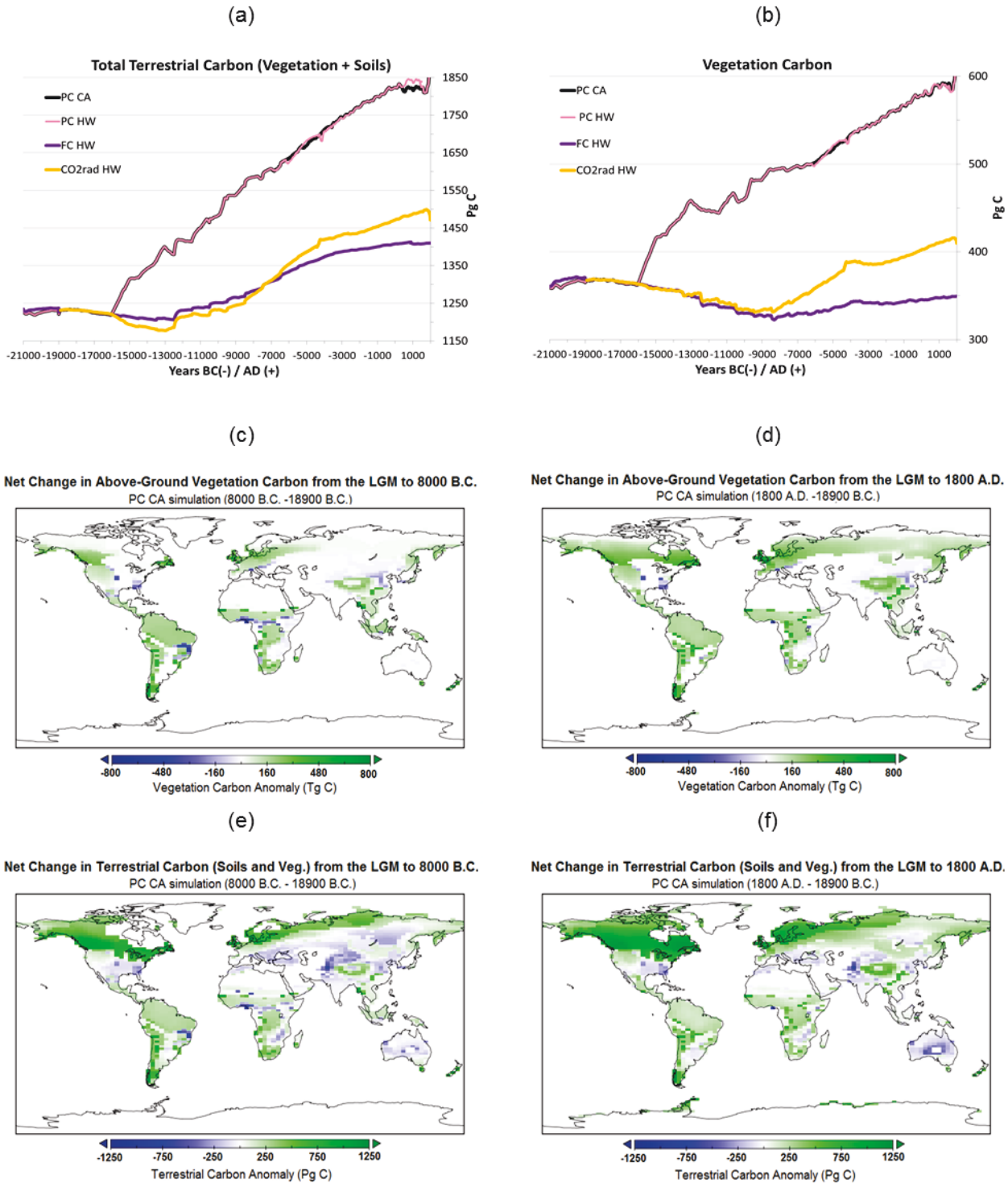

Fig. 3: Time series of (a) global terrestrial carbon (vegetation and soils) and (b) above-ground vegetation carbon for a Prescribed Carbon simulation with constant alkalinity (PC CA, black line) and Prescribed Carbon with the higher (12 Tmol yr^{-1}) weathering rate (PC HW, pink line). The FC HW and CO2rad HW results (from Fig. 1) are plotted for comparison. In (c-f), vegetation carbon and total terrestrial carbon anomalies from the LGM are mapped as in 2(a-d) for the PC CA simulation.

seen between the LGM and the early Holocene in the FC simulations (Fig. 1d). The total increase in terrestrial carbon of ~600 Pg C in the PC simulations (Fig. 3a) from the LGM to the late Holocene is also comparable in magnitude to that seen in other modeling studies (for example, 550-694 Pg C in Prentice et al. (2011)). The effect of CO_2 fertilization turned net terrestrial carbon losses in the tropics in the FC experiments (Fig 2c,d) into carbon gains (Fig 3e,f) and also enhanced carbon storage in subpolar regions. The decrease in vegetation carbon evidenced by the FC experiments, then, appears to be solely an artifact of the lower atmospheric carbon content (the CO_2 fertilization effect), with changes in temperature and land area availability having a much smaller impact on terrestrial carbon storage.

A secondary effect of the denser and more expansive vegetation afforded by the fertilization effect leads to greater absorption of incoming solar radiation, as seen in comparing the divergence in surface air temperature between the CO2rad HW and the PC HW simulations in Supplementary Fig. 1g (both of which have equivalent CO_2 radiative forcing). The biogeophysical impact of greater fertilization in the PC HW simulation appears to increase SAT globally by ~0.14°C (Supplementary Fig. 1g) and may contribute to processes leading to a higher depth-integrated ocean potential temperature (0.12°C) (Supplementary Fig. 1h). The denser tropical vegetation--particularly in South America, Africa, and Southeast Asia (as shown in Fig. 3d) appears to drive much of the fertilization-related increase in global temperature (up to 0.3°C locally, Fig. 4a), as these regions experience a substantial loss in vegetation density without CO_2 fertilization. Fig. 4b shows that the temperature difference between the PC CA and CO2rad CA simulations have significant variability in the high latitudes (related to different centennial-scale fluctuations in sea ice and the MOC) but demonstrate a consistent zonal-average tropical warming of 0.07-0.2°C.

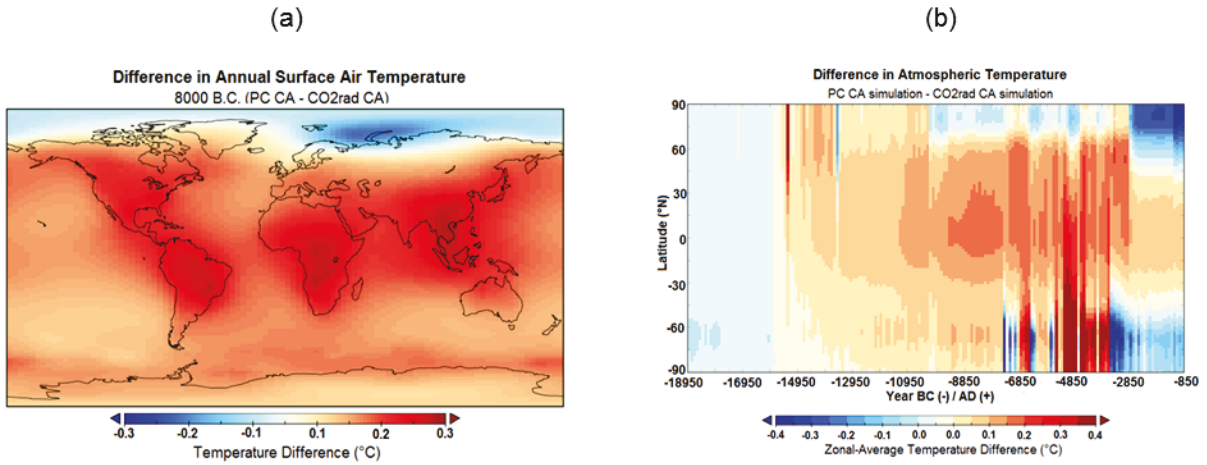

Fig. 4 : Surface air temperature differences between the PC CA simulation and the CO2rad CA simulation, both of which have equivalent CO_2 radiative forcing. In (a), a time slice is provided for 8000 B.C., which corresponds to the terrestrial and vegetation carbon stocks shown in Fig. 3 for the PC CA simulation). In (b), a Hovmöller diagram of the zonal-average surface air temperature difference between the two simulations with time.

Furthermore, because the tropics are important oceanic upwelling/outgassing regions, the additional warming of the tropics due to the fertilization effect may have a disproportionate influence on the outgassing of CO_2. The model's wind feedback also suggests that this warm anomaly driven by CO_2 fertilization increases zonal wind speeds in the subtropics (not shown), which adds to the wind stress and dynamical upwelling off the west coasts of South America and Africa (not shown). The implied deglacial strengthening of the Hadley Cell after the LGM is also suggested by the proxy record (Thompson et al. 1998) and could contribute to poleward shifts in the mid-latitude westerlies (Lamy et al. 2001; Toggweiler et al. 2006).

In summary, the FC simulations (including CO_2 radiative forcing) suggest that, without the full CO_2 fertilization associated with the observed ice core trend, modelled vegetation carbon stocks would be lower following deglaciation than they were during the LGM. This is contrary to the proxy evidence provided by the $\delta^{18}O$ Dole effect (discussed in detail in Prentice et al. (2011) and Ciais et al. (2012)), which reveals that photosynthetically-active terrestrial gross primary productivity doubled between the LGM and the late Holocene. The only simulations that support a substantial increase in vegetation carbon are the prescribed carbon dioxide (PC) simulations,

with a 50% increase in vegetation GPP and a ~64% increase in the photosynthetically-active vegetation carbon pool (Fig. 3a). These are well within the range of uncertainly offered by Ciais et al. (2012). As there is no significant net increase in vegetation when the warming effect of retreating ice shelves and CO_2 radiative forcing are included, these results imply that the physical presence of more carbon in the atmosphere available for biosphere sequestration (rather than temperature change or land availability) is crucial to explaining an increase in photosynthetically-active carbon during deglaciation and the Holocene. For slight CO_2 changes (~15 ppm) over the entire simulation period, vegetation does expand over formerly ice-covered areas. However, these small changes in atmospheric CO_2 are not sufficient to promote the woody thickening (Prentice et al. 2011) in tropical and subtropical regions necessary to increase global vegetation carbon stocks above the LGM value (Fig. 3c,d).

The results presented here strongly suggest that the carbon sequestration in response to the deglacial rise in CO_2 is probably the most important factor in increasing vegetation biomass between the LGM and present. It appears that vegetation carbon gains at the end of deglaciation and into the Holocene are driven by greater fertilization instead of ice sheet or temperature changes; without a major increase in atmospheric carbon content, vegetation actually decreases during deglaciation and the early Holocene in the UVic model. Regardless of the sequestration effect, total terrestrial carbon does increase (200-250 Pg C) in all free carbon simulations starting at the Pleistocene-Holocene transition, but this feature is largely driven by greater soil carbon storage at high latitudes.

3.1.3 Physical and Dynamical Ocean Changes

While the warming from CO_2 radiative forcing cannot explain an increase in vegetation carbon since the LGM, Fig. 1a reveals that the CO2rad CA simulation contained substantially greater atmospheric CO_2 concentrations (20 ppm by the mid-Holocene) than the FC CA simulation (without CO_2 radiative forcing). This substantial difference indicates that the net warming in the atmosphere and oceans (Fig. 5a-b) results in greater atmospheric CO_2. A comparison of these two simulations reveals that there is ~50 Pg C less terrestrial carbon during deglaciation in the simulation with CO_2 radiative forcing (Fig. 1c, red line vs. blue line), and only a small fraction of this is taken up by the oceans (Fig. 1b), which gradually become a net source of atmospheric CO_2 during the Holocene. The decreasing ability for the oceans to take up atmospheric CO_2 (greater outgassing than uptake) is modulated by warming ocean temperatures (Fig. 5b) by over 2˚C in the CO2rad CA simulation versus only 0.5˚C in the FC CA simulation. This warming is most pronounced at depth, as surface waters vary slightly less over the course of these simulations (1.5-1.6˚C for the CO2rad CA and 0.4-0.5˚C for the FC CA simulation) (Supplementary Figure 2). Solubility considerations (~9 ppm per 1°C warming) mandate that the net effect should be ~9-11 ppm of the ~20 ppm difference in atmospheric CO_2 between the FC and CO2rad simulations. These ocean properties do not incorporate the salinity effect favouring greater CO_2 uptake during deglaciation, as global salinity only decreased by 0.002 ppt as a result of precipitation changes in these experiments (freshwater fluxes are discussed in Section 3.3).

Complementing the CO_2 solubility effect, changes in ocean ventilation also appear to contribute to the higher CO_2 levels in the CO2rad simulations. Fig. 5c plots the global maximum overturning streamfunction, which provides here a general indicator of the strength of North

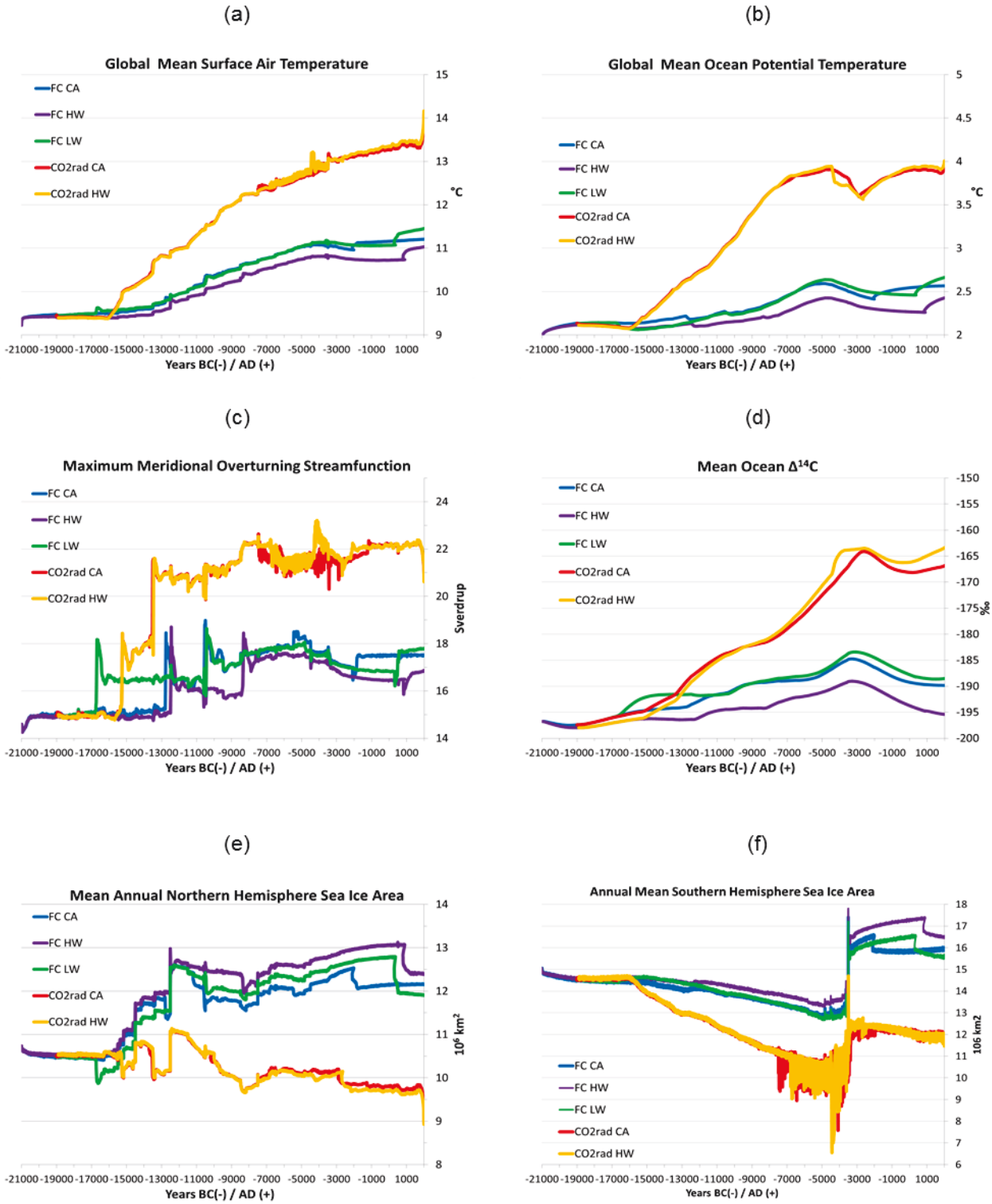

Fig. 5: Time series of (a) global mean surface air temperature (9°C to 15°C), (b) volume-weighted mean ocean potential temperature (2°C to 5°C), (c) global maximum ocean meridional overturning streamfunction value (14 Sv to 25 Sv), (d) volume-weighted mean ocean $\Delta^{14}C$ (-200‰ to -150‰), (e) mean annual Northern Hemisphere sea ice area (8 -14×10^6 km^2), and (f) mean annual Southern Hemisphere sea ice area (6-18×10^6 km^2). The colours representing each simulation are as in Fig. 1.

Atlantic overturning and NADW formation. The PC (Supplementary Fig. 1e) and CO2rad simulations equivalently produced a two-stage increase in the meridional overturning circulation (MOC) strength from LGM values (~15 Sv) to modern values (~21 Sv) by 13500 B.C., broadly consistent with an abruptly stronger NADW after the end of Heinrich Event 1 (also around 13000 B.C.) as demonstrated by Pa/Th proxy data (McManus et al. 2004). Thus, a more intense North Atlantic overturning was produced in the CO2rad simulations around the same time period as in nature despite the lack of freshwater fluxes. The unforced FC experiments also produced a somewhat stronger (17-18 Sv) meridional overturning circulation (MOC) around the same time period, but most of these experiments lag behind the CO2rad MOC recovery, and none of them achieve present-day overturning values. However, all the CO2rad simulations follow the MOC profile from the PC simulation (Supplementary Fig. 1e), indicating that the strength of the MOC rebound to the model's typical modern values is mostly a product of the temperature increase due to the radiative forcing effect of CO_2.

The divergence in the $\Delta^{14}C$ trend lines between the FC and CO2rad simulations (Fig. 5b), which lags the divergence in air temperature between the FC and CO2rad simulations by approximately 1000 years, provides further evidence of a link between CO_2 and ventilation changes. The initial increase in CO_2 (Fig. 1a) stimulated greater ventilation of (relatively) stagnant deep water from the glacial period, and the ventilation (and warming) of CO_2-rich deep waters subsequently lead to less oceanic absorption of atmospheric CO_2 and eventually a net release (achieved by 7000 B.C. according to Fig. 1b) from the ocean to the atmosphere from this effect. Fig. 6 illustrates the deep-ocean DIC change for the CO2rad HW simulation at 12500 B.C., the approximate timing of post-Heinrich event recovery and ventilation of the North

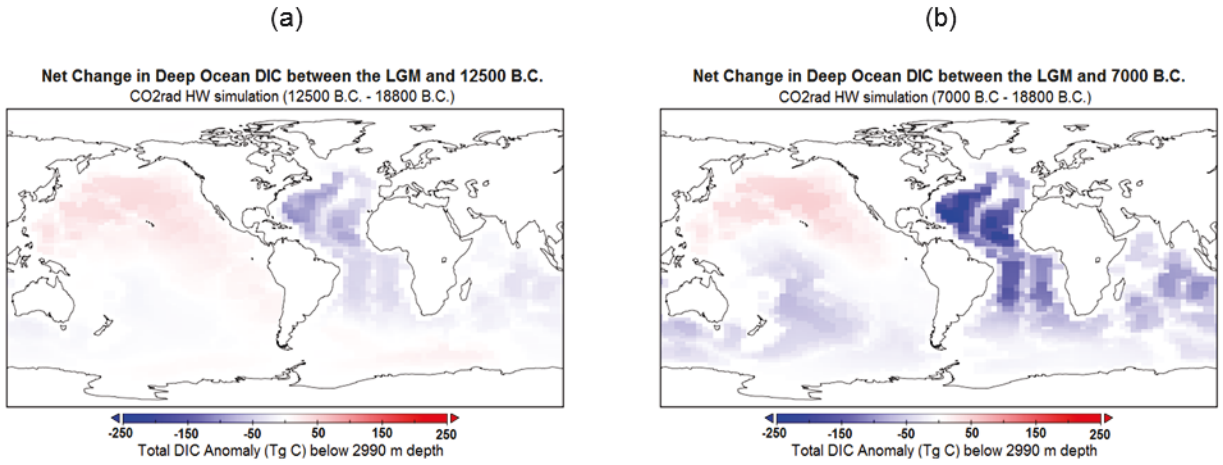

Fig. 6: The net change in deep-ocean DIC (below 2990, the deepest 31.2% of the model ocean) in Tg C between the LGM and (a) 12500 B.C. and (b) 7000 B.C. in the CO2rad HW simulation, both on a scale from -250 Tg C (blue) to +250 Tg C (red).

Pacific (Galbraith et al. 2007), and at 7000 B.C., by which time McManus et al. (2004) indicated that NADW transport essentially reached its peak and plateaued. The simulations correspondingly demonstrate a gradual decrease in the DIC content of the Atlantic Ocean relative to the LGM state, with the NADW becoming more prominent and promoting the decrease of DIC in the Indian and South Pacific with time (compare Fig. 6a to Fig. 6b). Related to this ventilation change, proxy evidence of low $\Delta^{14}C$ excursions during the Mystery Interval (~15500 B.C. to ~12500 B.C.) provide evidence of an important ventilation (or series of flushes) of the glacial deep ocean during the late Pleistocene. What is new here is that CO_2 warming appears to enhance this ventilation.

The model results thus reveal a potential positive feedback relevant to the deglacial rise in CO_2, in which an initial increase in temperature due to rising CO_2 stimulates more ventilation of carbon-rich deep waters, which causes an even greater increase in CO_2. One potential fast-response contributor to this feedback loop is sea ice, which is strongly sensitive to warming

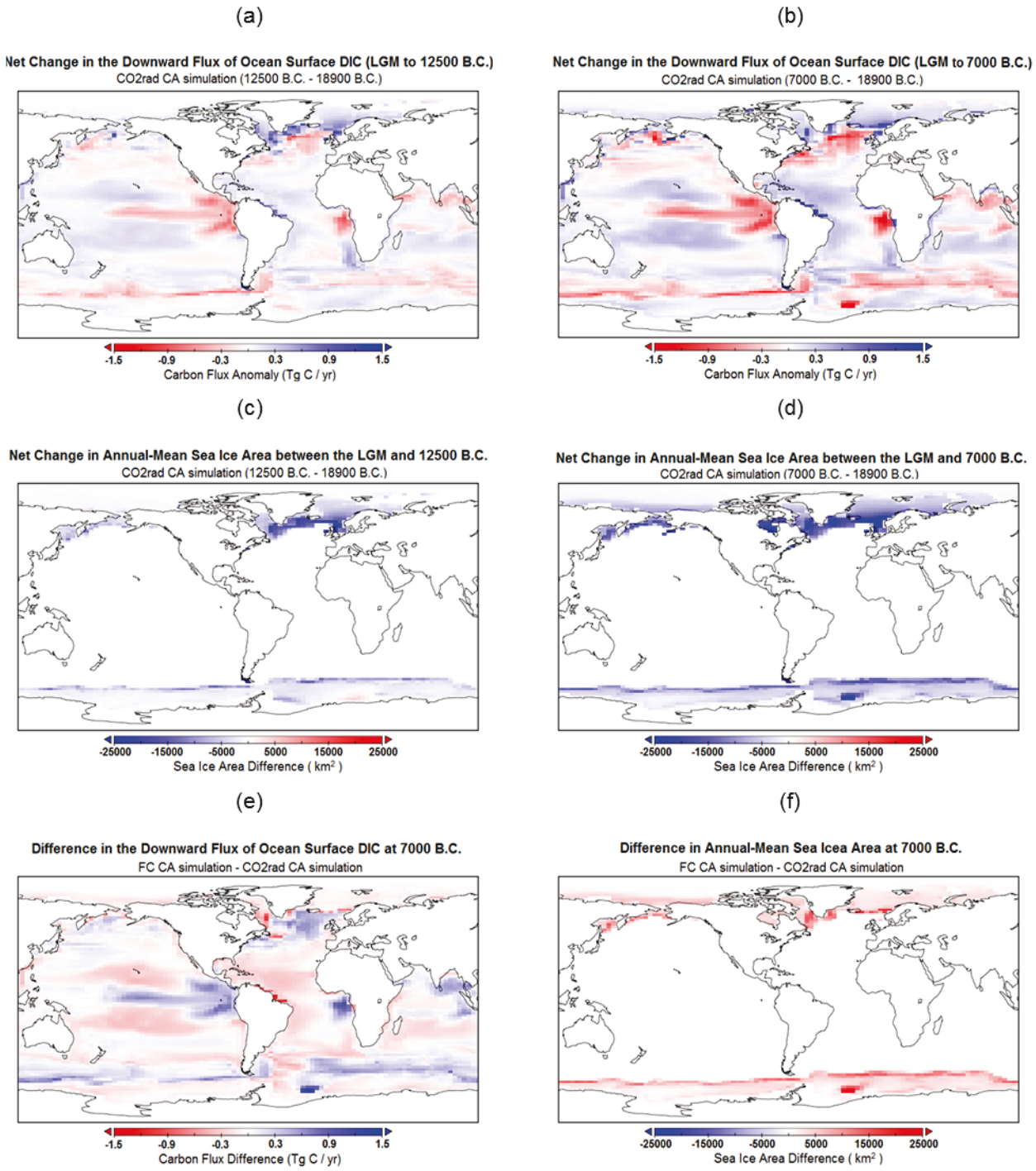

Fig. 7: The spatial distribution of the net change in the downward flux of inorganic carbon at the ocean surface between the LGM (-1.5 to +1.5 Tg C yr^{-1}) and (a) 12500 B.C. and (b) 7000 B.C. Regions with greater outgassing than the LGM are shaded in red, whereas areas with greater uptake are blue. These are compared to the net change in annual-mean sea ice area since the LGM (-25000 to +25000 km^2) at (c) 12500 B.C. and (d) 7000 B.C., with area losses relative to the LGM shaded in blue and gains shaded in red. In (e-f), the differences in (e) surface inorganic carbon flux and (f) sea ice area between the FC CA and CO2rad CA simulation at 7000 B.C. are given. Blue (red) shading represents less (more) outgassing in the FC CA simulation relative to the CO2rad CA simulation in (e) and red indicating greater sea ice area in the FC CA simulation relative to the CO2rad CA simulation at 7000 B.C. in (f).

temperatures (with less sea ice under higher CO_2 /temperature conditions). Furthermore, air-sea gas exchanges are not possible through sea ice in the UVic model, and therefore the much greater annual sea ice extent in both the northern and southern hemispheres (Fig. 5e-f) could limit convection in both regions (Fig 7). Even without freshwater fluxes, sea ice extent in the North Atlantic was more expansive in the FC simulations after the LGM compared to the CO2rad simulations (Fig 5e), which limited the strength of North Atlantic overturning and, therefore, the rate at which deep waters in the Atlantic were flushed to the surface in upwelling regions during deglaciation. The FC CA simulation in particular demonstrated less outgassing in tropical upwelling regions at 7000 B.C. (Fig. 7e), whereas the CO2rad CA simulation showed greater upwelling in the tropics due to stronger convection (Fig. 7b,e). Similarly, more sea ice in the Southern Ocean in the FC simulations limited the air-sea exchange of upwelling water masses near Antarctica (Fig. 7e-f).

Fig. 7 also shows that downwelling regions in the North Atlantic (Fig. 7a-b) shifted northeastward over the course of deglaciation in concert with reduced sea ice extent (Fig. 7c-d), whereas upwelling regions (carbon sources to the atmosphere) intensified in the Southern Ocean along retreating sea ice margins, particularly in the CO2rad experiments. In addition to controlling outgassing, Southern Ocean annual sea ice (Fig. 5f) demonstrated significant sensitivity to CO_2 radiative forcing, leading slightly the strengthening of the MOC in the CO2rad simulations. Proxy evidence also suggests that this region was likely critical during the upwelling of glacial deep water (Anderson et al. 2009). The abrupt increase in SH sea ice after 4000 B.C. in most simulations (Fig. 7f) is a response to a rapid decrease in Antarctic marine ice shelves in the database (discussed in Chapter 4). This transition was followed by a reduction in

atmospheric CO_2 associated with a weaker NADW, slowly-ventilating AABW and reduced upwelling (more sea ice) in the Southern Ocean.

In summary, these model results indicate that warming temperatures due to increasing CO_2 may contribute to a decrease in annual-mean sea ice in both hemispheres, which coincides with an enhanced MOC that flushes high-DIC glacial deep waters through the Southern Ocean and stimulates a further rise in CO_2. These findings could suggest that the Southern Ocean sea ice mechanism established in Stephens and Keeling (2000) may have some merit in enhancing an ongoing release of carbon from the deep ocean to the atmosphere, especially considering that proxy evidence (Gersonde et al. 2005; Roche et al. 2012) indicates that winter sea ice extent at the LGM was likely much greater than at present. After accounting for the warming of the ocean, the sensitivity of atmospheric CO_2 to Southern Ocean sea ice area seems similar in magnitude to the 6.2 ppm obtained in the AOGCM study of Chikamoto et al. (2012), ignoring the positive feedbacks of greater ventilation on alkalinity discussed below. Fletcher et al. (2007) discovered that most OGCMs in OCMIP-2 underestimate both the present-day outgassing of CO_2 in the high-latitude Southern Ocean by as much as 0.4 Pg C yr^{-1} and the CO_2 uptake in the mid-latitude Southern Ocean by -0.2 Pg C yr^{-1}. Therefore, the real-world effect of sea ice changes in this region may be larger than that modeled here. In particular, Brovkin et al. (2012) cite a 20 ppm sensitivity to SH sea ice after including increased diffusivity with their zonally-averaged ocean model.

3.1.4 Marine Productivity

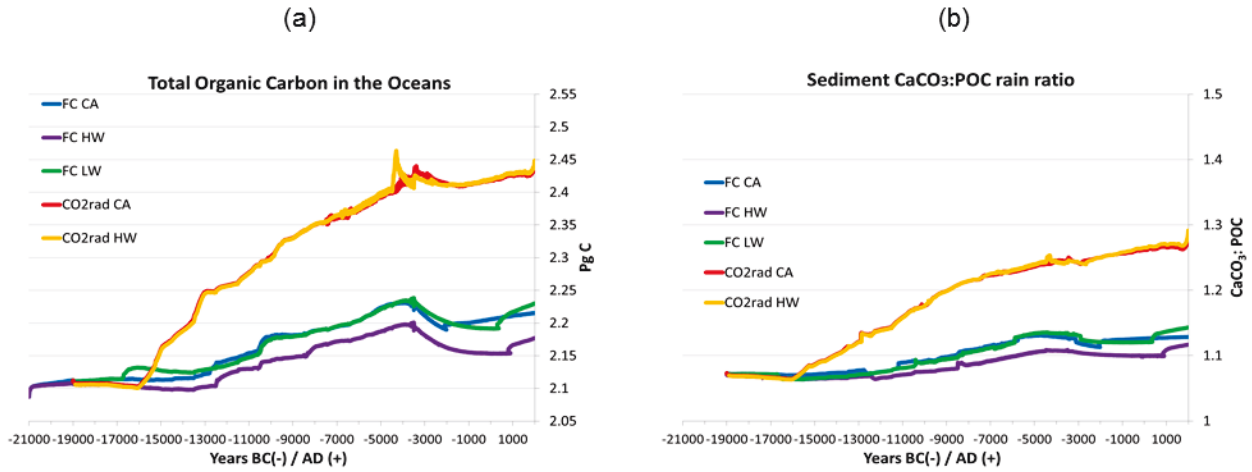

Fig. 8: Simulations are presented as in Fig. 1 and Fig. 5 for (a) the total living biomassof phytoplankton, zooplankton, diazotrophs, and detritus (Pg C) in the oceans (the scale ranges from 2.05 to 2.55 Pg C) and (b) the CaCO3:POC (particular organic carbon) ratio at the sediment level, indicating the relative preservation of (un-dissolved) particulate inorganic carbon (PIC) to (un-respired) particulate organic carbon (POC) when detritus reaches the bottom of the ocean (the scales range from 1.0 to 1.5).

One major consequence of increased ventilation, however, is greater living biomass in the oceans, not to be confused with remineralized DIC or export production. Other modeling studies (for example, Rojas et al. (2009)) have demonstrated that increases in ventilation also accompany greater biological productivity at the ocean surface, thus limiting atmospheric CO_2 gains. Our simulations show an increasein the living biomass in the CO2rad scenarios with greater ventilation (Fig. 8a), but the associated net downward flux of organic matter (not shown here) does not overwhelm the effect of ventilation on the DIC storage in the deep ocean. Fig. 8a also indicates that living biomass in the ocean is virtually the same in the CO2rad CA and CO2rad HW simulations (i.e., with and without alkalinity changes), indicating that more ventilation imposed by CO_2 warming is the dominant mechanism increasingthe availability of nutrients contributing to greater living biomass. Other distinctions, such as the differences in the

carbon content of the atmosphere and ocean, are relatively unimportant: see the PC simulations in Supplementary Fig. 1c. The fact that atmospheric CO_2 in the CO2rad CA rises above the FC CA simulation (Fig. 1a) reveals that the DIC change due to greater ventilation still dominated, producing a net source of CO_2 to the atmosphere.

While extremely important for the marine carbon cycle and ultimately atmospheric CO_2, a comparison of the living biomass plotted in Fig. 8a with proxy evidence is difficult, as organic carbon content is not a measure of export production to the deep ocean, and patterns of marine productivity are spatially quite complex (Kohfeld et al (2005), their Fig 2c) and species-dependent (coccolithophores vs. diatoms). Kohfeld et al. (2005) indicates that export production decreased between the LGM and late Holocene in many parts of Atlantic and Indian oceans north of the Antarctic Polar Front but increased in parts of the Pacific and much of the Southern Ocean south of the polar front. Despite the net decrease in marine productivity between LGM and late Holocene, many studies show a pulse of greater marine productivity during deglaciation in response to the ventilation of deep waters. For example, in the Eastern Equatorial Pacific, Bradtmiller et al. (2010) documents a marine productivity (opal fluxes) peak during the Pleistocene-Holocene transition and the early Holocene, likely in response to the ventilation of the Pacific Ocean around 12600 B.C. Similarly, Mohtadi et al. (2008) also documented greater marine productivity (opal fluxes) off southern Chile, also possibly linked to greater dynamical upwelling induced by stronger winds. In the Equatorial Atlantic, Bradtmiller et al. (2007) documented deglacial maxima in opal fluxes for several cores at ~13000 B.C., followed by a sharp decline in activity to late Holocene minima.

Overall, these studies generally suggest that peaks in marine productivity occurred during periods of enhanced ventilation, many around 13000-12000 B.C., similar to the timing of MOC

recovery in our CO2rad simulations. The increasing nutrient availability in surface waters (not shown) ventilation in our simulations may be relevant to real-world oceanic changes in response to deep convection. Furthermore, the increase in living biomass coincides with a larger sedimentation flux (calcite rain) (Fig. 9c) along with a modest (0.17) increase in the sediment $CaCO_3$:POC rain ratio (Fig. 8b) in our simulations. Because calcite is dissolved with a constant e-folding (3500 m) depth in the model before reaching the sediments, the change in rain ratio is mostly a function of faster organic carbon respiration with warmer ocean temperatures (i.e., a shallowing of the remineralization depth) (M. Eby, personal communication, 2013). Several proxy studies agree with the silicon leakage hypothesis (Brezinski et al. 2002) that diatoms (which require Silicic acid supply) outcompeted coccolithophores (calcifiers) during the LGM beyond the Southern Ocean. Richaud et al. (2007) in particular demonstrates a pronounced increase in $CaCO_3$ flux into the sediments in the Equatorial Pacific, reaching a peak in the late Holocene, whereas Bradtmiller et al. (2007) presents a few cores indicating unchanging or increasing $CaCO_3$ fluxes from the LGM to the Holocene in the Atlantic. Greater $CaCO_3$ fluxes in many regions associated with more calcifiers, coupled with more sedimentation above the lysocline in response to the flooding of continental shelves, would together mandate an increase in sedimentation flux (calcite rain) during deglaciation and parts of the Holocene. From this perspective, the model accurately produced an increase in the calcite rain to the sediments (Fig. 9c), a relatively plausible feature of the glacial-interglacial transition. Further discussion of these sediment fluxes are given in Section 3.1.6.

3.1.5 Ventilation-Alkalinity Feedbacks

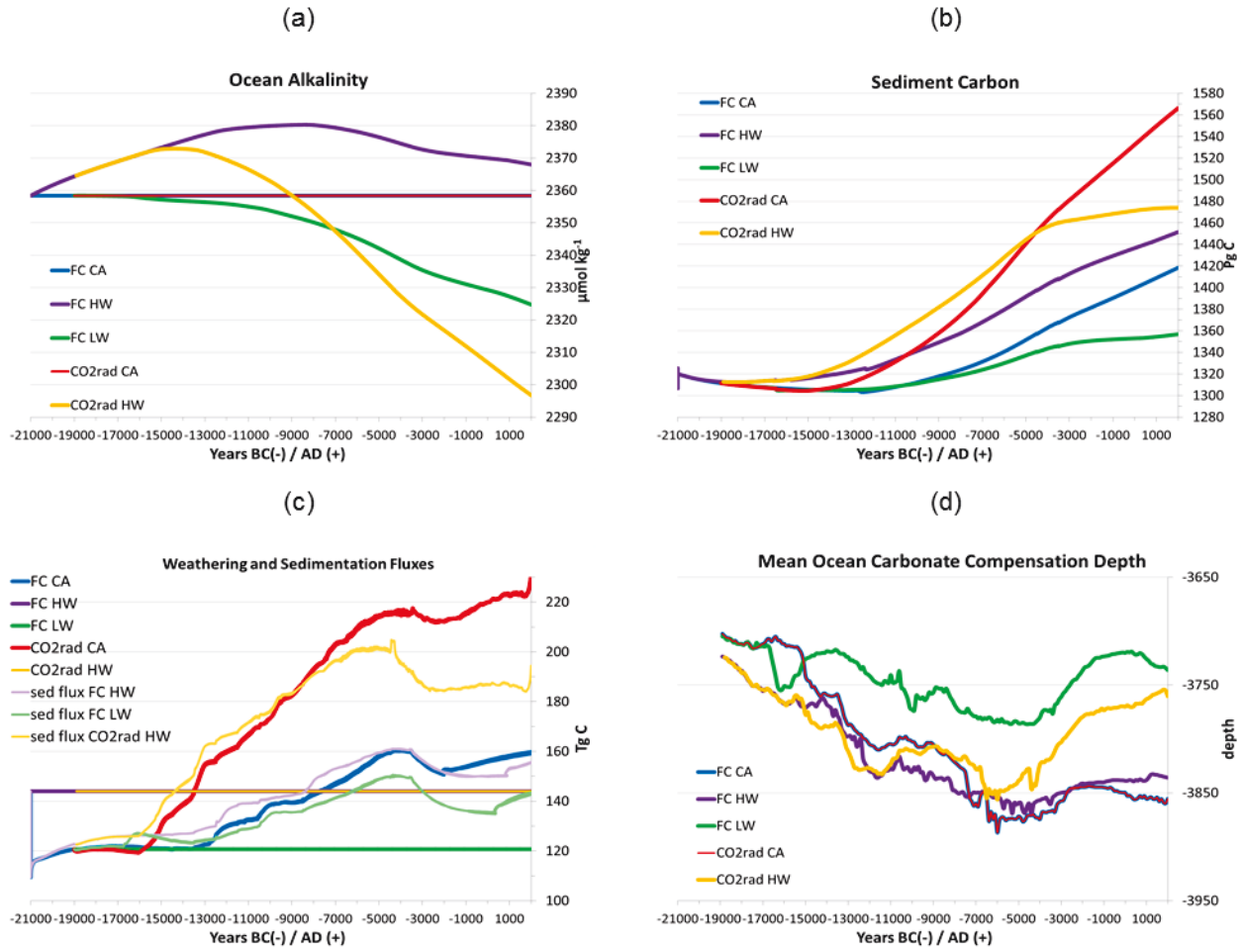

Fig. 9: As in Fig. 1, for variables related changes in ocean alkalinity. In (a), changes in total mean ocean alkalinity ($[HCO_3^-] + 2[HCO_3^{2-}]$) are given in µmol kg^{-1} (with a plot range from 2290 to 2390 µmol kg^{-1}). In (b), the total change in sediment carbon (Pg C) are provided on a different scale (1280 to 1580 Pg C) than in Supplementary Fig. 1d. In (b), weathering fluxes (thick darker lines) and sedimentation fluxes (thin, light-coloured lines) are provided. For the CO2rad CA and FC CA simulations, only the weathering rate is plotted, as by definition the weathering rate and sedimentation rates are exactly equal in these simulations. In (d), the carbonate compensation depth (CCD), calculated as the depth where sedimentation flux is equal to the dissolution flux (above which 99-100% of sedimentation occurs in the model) is provided with a scale range from 3950m to 3650 m depth.

Through a more vigorous ventilation of glacial deep water, CO_2 radiative forcing also promoted a shift in the total DIC content (Fig. 6, discussed above) and alkalinity in the deep ocean, and these results are echoed to some extent in proxy studies. For example, Galbraith et al. (2007) documented a thorough ventilation of glacial deep waters in the North Pacific around 12600 B.C., which coincided with a 10 ppm increase in atmospheric CO_2 in the ice core record.

However, the replacement of glacial deep waters containing high levels of respired DIC with surface waters that have relatively low DIC and higher [CO_3^{2-}] (see Yu et al. (2010)) would have contributed further to a long term increase in atmospheric CO_2 by supporting more $CaCO_3$ sedimentation, thereby decreasing net ocean alkalinity (Galbraith et al. 2007).

While alkalinity-induced changes in the pCO_2 of the oceans are not possible in the CA transient setup (by definition), the differences between the FC HW and CO2rad HW experiments help quantify this effect. The only distinction between these two simulations is the radiative forcing of CO_2 imposed on the CO2rad HW experiment, although they yield quite different end results (Fig. 1a,5a). The FC HW run produced a slight increase in alkalinity between the LGM and the Holocene; carbonate compensation in favour of sediment burial is unable to outpace the weathering (alkalinity) inputs into the ocean until the late Holocene, contributing to the lower atmospheric CO_2 (~180-182 ppm) toward the end of the simulation. The CO2rad HW experiment showed the opposite trend, with a significant net decrease in alkalinity (40 μmol kg^{-1}, see Fig. 9a) and a pronounced increase in CO_2 to 215 ppm during the Holocene (Fig. 1a), outpacing the CO2rad CA simulation by 10 ppm by the mid-Holocene. This is aided by both a decrease in DIC content of the deep oceans due to greater ventilation (Fig. 6a-b) accompanied by a larger increase in precipitated calcite (Fig. 9c) from greater biological productivity (Fig. 8a).

The total difference between the end-result FC HW and CO2rad HW simulations is approximately 30-35 ppm, leading to 10 ppm more CO_2 in the atmosphere than the combined contribution of greater ventilation (related to reduced sea ice) and warming in the CO2rad CA experiment. The alkalinity of the CO2rad HW and FC HW simulations begins to diverge between 15000 B.C. and 14000 B.C. (Fig. 9a, purple line vs. orange line), coincident with the MOC recovery in the CO2rad simulations and reduced DIC storage in the deep Atlantic Ocean.

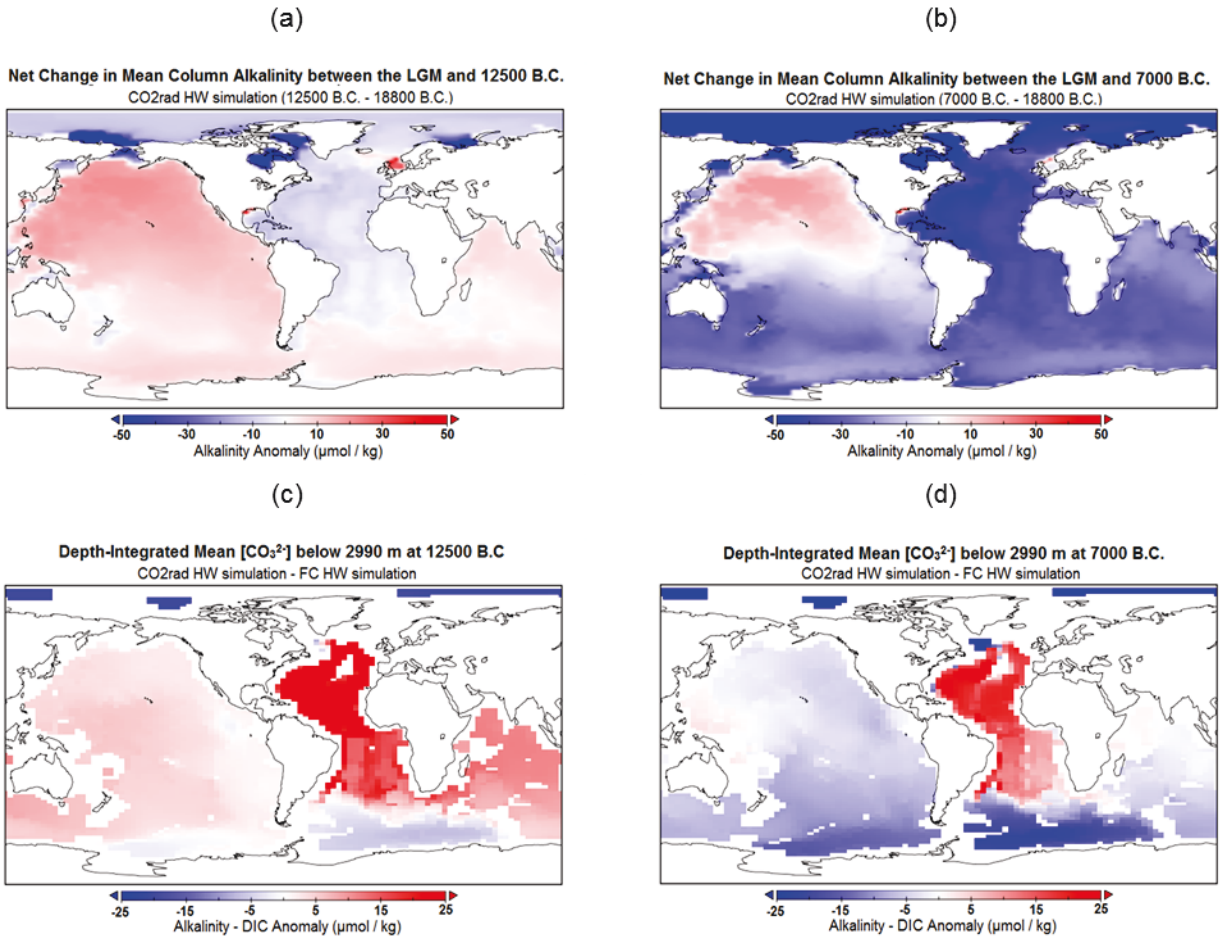

Fig. 10: The spatial distribution of alkalinity anomalies (a-b) since the LGM in the CO2rad HW simulation, and Alkalinity-DIC (~[CO_3^{2-}]) differences (c-d) between the CO2rad HW and FC HW simulations. In (a-b), the net change in the the total column mean alkalinity (average depth-integrated alkalinity for each gridcell) between the LGM and (a) 12500 B.C. and (b) 7000 B.C. is given. In (c-d), the column (depth-integrated mean) Alkalinity-DIC below 2900 m depth in the CO2rad HW simulation is subtracted from that of the FC HW simulation at (c) 12500 B.C. and (d) 7000 B.C.

This AMOC-induced change in alkalinity is portrayed by the column depth-integrated alkalinity averages in Fig. 10a-b, which shows Atlantic waters losing alkalinity with time. Proxies tend to relate changes in alkalinity more specifically to [CO_3^{2-}] (for example, Catabig et al. (1998); Yu et al. (2010); Rickaby et al. (2010), and references therein), and subtracting alkalinity (Alk) from DIC in the model's spatial output allows a rough approximation of this quantity. By 7000 B.C. (shown in Section 3.2.3), the CO2rad HW simulation provides Δ[Alk-

DIC] changes since the LGM below 2990 m of +26-42 μmol kg^{-1} in the North Atlantic (above current estimates), +5-10 μmol kg^{-1} in most of the Pacific (comparable to Yu et al. (2010)), little net change in the Southern Ocean, and -10 μmol kg^{-1} in the Weddell Sea (below current estimates). A decrease in [Alk-DIC] in intermediate waters was also produced in the Atlantic (not shown), as in Yu et al. (2010).

However, Fig. 10 shows that [CO_3^{2-}] during deglaciation (Fig. 10c) and the early interglacial (Fig. 10d) is also greater in the CO2rad HW simulation compared to the neo-glacial FC HW simulation in the Atlantic, with much smaller changes in the Pacific. The contrast between the CO2rad HW and FC HW in the North Atlantic (+20 to +25μmol kg^{-1}) are similar to the +20 μmol kg^{-1} LGM-to-Holocene change given in Yu et al. (2010), and the simulated change (-24 μmol kg^{-1}) in the deep Weddell Sea is comparable to that given in Rickaby et al. (2010) (-25 μmol kg^{-1}). Although the proxy record of glacial-interglacial changes in [CO_3^{2-}] at sufficient resolution is highly limited and prevents firm conclusions, the spatial distribution in Fig. 10c-d agrees qualitatively with the evidence available to date. By itself, the CO_2-ventilation feedback in our model appears to account for the pattern of proxy-derived [CO_3^{2-}] in the deep Atlantic and Weddell Sea (Yu et al. 2010; Rickaby et al. 2010).

In the case considered here, however, deep ocean DIC changes are more pronounced in the Atlantic and Southern Indian than they are in the Pacific (Fig. 4a), whereas Galbraith et al. (2007) documented a deglacial ventilation in the North Pacific around 12600 B.C. By contrast, the ventilation-alkalinity feedback illustrated in this paper seems to be largely driven by Atlantic DIC changes, with Pacific changes possibly providing an even greater net decrease in alkalinity and increase in CO_2 during a real-world deglaciation. The model did, in fact, slowly increase the circulation in CO2rad HW until a renewal of deep waters in the North Pacific was completed

between 6000 B.C. and 4000 B.C. in a manner similar to that illustrated in Chapter 4. The renewal of deep Pacific waters also allowed a continued reduction in ocean alkalinity (Fig. 9a). It is possible that the distribution of Antarctic marine ice shelves (the interpolated ICE-4G database) in the model favours a faster circulation in the Pacific at this time, and an earlier ice shelf transition might force a more accurate North Pacific flush of DIC, which would in turn permit an earlier alkalinity-induced increase in atmospheric CO_2 during the Holocene. The ice configuration around Antarctica merits further study in this regard in order to provide a more abrupt and earlier ventilation of the North Pacific as proxy evidence (Galbraith et al. 2007) suggests. A larger wind shift than that parameterized here may also produce the same effect. In particular, Huiskamp and Meissner (2012) showed that a vigorous deep meridional circulation in the North Pacific could be also be obtained with a prescribed 9° northward shift of the Southern Hemisphere Westerlies (from their present location), whereas the simulations presented here only imposed relatively small variations on the NCEP wind field according to the wind feedback mechanism (Weaver et al. 2001).

3.1.6: Sensitivity to Weathering and Carbonate Compensation

Another important contributor to ocean alkalinity (as well as a significant uncertainty in the glacial-interglacial climate debate) is the chemical weathering rate. Despite the model's inability to produce a deglacial increase in atmospheric CO_2 without CO_2 radiative forcing, it demonstrated significant sensitivity to the choice of weathering rate, which explains an approximately 10-15 ppm difference between the FC LW and HW FC simulations. Fig. 9a provides an illustration of the alkalinity changes for each simulation, with the lower weathering rate associated with a lowering of mean alkalinity (-33 μmol kg^{-1}) and the higher weathering rate providing a net increase in alkalinity (+10 μmol kg^{-1}). These results may seem rather intuitive,

but they demonstrate the relative importance of carbonate compensation, weathering, sedimentation flux, and ocean ventilation.

A closer look at the FC LW simulation reveals that the sedimentation rate increased with time and exceeded the weathering rate for the entire simulation after 17000 B.C. (Fig. 9c, thin light green line vs. thick dark green line), associated with an increase in calcifiers. Because sedimentation (an alkalinity sink) surpassed weathering (alkalinity source) for virtually the entire simulation, the greater removal of carbonate and bicarbonate in the surface ocean led to a downwelling of waters that have low [CO_3^{2-}], supporting a shallower lysocline and greater (oxic) dissolution of sediments and calcite rain. This is reflected in Fig. 9c, which shows that the FC LW sediment flux dipped below the FC CA sediment flux after 13000 B.C. (both simulations possessed equivalent marine productivity contributing to this flux—Fig. 8a). At the same time, carbonate compensation in favour of increasing dissolution still cannot fully offset the flux of calcite rain introduced by greater marine productivity, and thus the model ocean produced a net precipitation event and loss of alkalinity.

The limited impact of carbonate compensation for the lower weathering rate is also illustrated in Fig. 9d by changes in the CCD (defined here as the level where the rate of sedimentation equals the rate of dissolution, above which 99-100% of net sedimentation occurs). While the CCD was shallowest in the FC LW experiment compared to other runs, it still deepened during ventilations (a process favouring greater sedimentation, an ocean alkalinity sink) and did not rise above the original depth until 2500 B.C. The rapid shoaling in the late Holocene appears to be aided by the increasing prevalence of more corrosive, high DIC southern-sourced deep waters after the Antarctic marine ice shelf disappearance (4000 B.C.-3000 B.C.) in the interpolated land ice dataset (see Chapter 4 for more details). However, before this

transition, a comparison of Fig. 9c with Fig. 5c reveals that the CCD deepening in the simulation was stimulated by greater ventilation (i.e., a stronger alkalinity pump to the deep ocean via the NADW). Although the partial recovery of the NADW driven by land ice and orbital forcing is much more limited without the addition of CO_2 radiative forcing, the somewhat more intense downwelling of low-DIC, high-alkalinity North Atlantic surface waters appears to be sufficient to support a deepening of the CCD. Without these changes in the MOC, a CCD shoaling would be supported throughout the simulation based on carbonate compensation. Therefore, a combination of low weathering (low alkalinity input), more marine productivity (additional marine calcifiers to remove alkalinity from the ocean), and greater ventilation (which flushes deep DIC and lowers the CCD) may be able to overcome carbonate compensation effect for most of the simulation, driving down ocean alkalinity and increasing atmospheric CO_2.

The FC HW simulation (Fig. 9, purple line) shows a different pattern of carbonate compensation; from the beginning of the simulation to 9000 B.C., the sediment flux (Fig. 9c, light purple line) lies below the weathering rate (Fig. 9c, dark purple line), and the greatest deepening of the CCD was obtained during this time (Fig. 9d). In this case, the more intense ventilation after 14000 B.C. (Fig. 5c) and carbonate compensation (Fig. 9c) together favored a deepening of the CCD up to the beginning of the Holocene. This allowed for more sediment preservation and caused the sediment flux to drift above that of the FC CA simulation (Fig. 9b,c, blue line vs. purple line).Then after 9000 B.C. (approximately the beginning of the Holocene), the calcite flux to surpass the weathering rate, resulting in increasing dissolution with time by the mid-Holocene (in Fig. 9c, the light purple line re-approaches blue line), although the shoaling of the CCD associated with this effect (after 5000 B.C.) is nearly negligible (Fig. 9d). The deepening of the CCD accompanied by a larger sediment flux contributed to the decrease in

alkalinity during the Holocene in this simulation, although this change is not substantial enough to counter the increase in ocean alkalinity during the late Pleistocene associated with a greater alkalinity source (weathering) than sink (sedimentation).

By contrast, when CO_2 radiative forcing was added to HW experiment, in response to greater ventilation and nutrient availability at the surface, sediment flux surpassed the weathering flux much earlier (14500 B.C.) and exceeded it by a much greater quantity (57 Tg C yr^{-1}) than in the simulation without radiative forcing (17 Tg C yr^{-1}). Correspondingly, the greater dissolution supported after 14500 B.C. drove the sediment flux significantly below the constant alkalinity experiment (CO2rad CA) after 9000 B.C (Fig. 9c, light orange line vs. red line). Carbonate compensation in the CO2rad HW simulation should, in turn, support a more pronounced shoaling of the CCD than in the FC LW simulation (in which the sedimentation flux only surpassed weathering by a maximum of 29 Tg C yr^{-1}). However, the CCD in the CO2rad HW experiment remained below the original LGM level until 3000 B.C. and did not shoal above the FC LW CCD. The implication is that the greater ventilation stimulated by the CO_2-ventilation feedback, favouring the replacement of low-alkalinity, high-DIC deep waters with with higher-alkalinity, lower-DIC surface waters, significantly overpowered carbonate compensation for most of the simulation to decrease oceanic alkalinity and drive an increase in atmospheric CO_2. The deepening of the CCD associated with carbonate compensation and a smaller ventilation increase (related to ice sheet and orbital forcing changes) in the FC HW simulation is not able to bury enough sediment to overcome the effect of larger alkalinity inputs (weathering) to decrease CO_2. However, the much greater ventilation created by the CO_2 warming effect clearly has the capacity to overcome weathering and carbonate compensation to further increase atmospheric CO_2.

These results are generally consistent with the proxy data presented in Yu et al. (2010), which suggest that abyssal oceans demonstrate a decrease in deep-ocean DIC content and increase in [CO_3^{2-}] into the early Holocene in the deep Equatorial Pacific and North Atlantic in response to a ventilation of the deep ocean. Moreover, they confirm the conjecture in Rickaby et al. (2010) that, for a lower weathering rate for the LGM, an increase in sedimentation flux (due to a low CCD) can by itself work to decrease alkalinity and increase CO_2 (although the influence ofsedimentation and weathering rates in our model study is limited to the ~10 ppm difference between the FC HW and FC LW simulations). Our modeling results also suggest, however, that the same net effect (greater abyssal alkalinity and a deeper CCD) can be obtained from more ventilation of the deep ocean for both weathering rates, including in cases where carbonate compensation opposes the ventilation-induced alkalinity change.

A carbonate compensation supporting dissolution, stimulated by excess alkalinity removal from greater calcite rain associated with a ventilation event, may potentially explain why total sedimentary deposition and CCD depth may not have varied substantially since the LGM (Catubig et al. 1998). This is perhaps particularly relevant during the deglacial ventilation fluxes: in the Atlantic with recovery of the NADW at the end of Heinrich Event 1 (~13000 B.C.: McManus et al. 2004), Southern Ocean (~15000 B.C., Anderson et al. 2009), and the North Pacific around 12600 B.C. (Galbraith et al. 2007). Most of these major upwelling events predate early-interglacial weathering accelerations (Foster and Vance 2006) and may have prompted, through increased calcite rain, carbonate compensation in favour of greater dissolution (in spite of increased ventilation associated with the event itself).

In summary, weathering dominates ocean alkalinity changes, except for strong deep-ocean ventilations. Greater ocean ventilation, in turn, appears to dominate carbonate

compensation in the model, except for very long time scales (~15000-20000 years). While the simulations presented here explain a roughly 35 ppm difference in CO_2, the CCD changes in all experiments are relatively minor, with variations generally less than 150 m and well within the allowable range given by proxy evidence (as much as 1-1.5 km) (Catubig et al. 1998; Rickaby et al. 2010). The ability for nearly 40% of the magnitude of glacial-interglacial change in CO_2 to be explained by small changes in the CCD is encouraging and demonstrates that various conflicting factors can drive large differences in atmospheric CO_2 without substantially modifying the CCD. Greater ocean alkalinity in the HW simulation drives CO_2 (180-182 ppm) slightly below the CA simulation (183 ppm), whereas the relatively higher end-result CO_2 (195 ppm) obtained in the LW simulation appears to be determined by the reduction in ocean alkalinity due to lower alkalinity inputs, as slightly greater ventilation delayed the ability for carbonate compensation to raise the CCD above the original level to support more sediment dissolution. However, a similar-scale ventilation change (Fig. 5c) in the FC HW simulation is not able to overcome the greater alkalinity inputs into the ocean (due to greater weathering), hence the net increase in alkalinity in this simulation. Only the larger ventilation change in the CO2rad HW (with intensified calcite rain) can overcome a higher weathering rate to decrease alkalinity and increase atmospheric CO_2.

Given the enhanced ventilation of the CO_2 radiative forcing simulation, weathering would have to increase markedly for the oceans to be able to gain alkalinity as in the HW simulation. In particular, only a late Holocene weathering rate above 200 Pg C yr^{-1} (~16.7 Tmol yr^{-1}, determined by the light orange line in Fig. 9c) would be sufficient for ocean alkalinity sources (weathering and carbonate compensation) to exceed the intensified alkalinity sinks

(calcite rain and more carbonate in the deep ocean) to drive down CO_2 to initiate the next glacial cycle (in the absence of anthropogenic influence).

It should be emphasized that the weathering rates used in these experiments are reasonably close to the sedimentation flux calculated for the LGM equilibrium simulation (see Section 2), thus limiting the scope of the carbonate compensation response. A broader range of weathering rates could potentially produce a much larger effect on CO_2, although glacial-interglacial changes in chemical weathering are relatively poorly constrained and require further investigation. Using the CLIMBER-2 model, Brokvin et al. (2012) found that the weathering of continental shelf carbonates exposed above sea level during glacial times led to substantially greater alkalinity source to the ocean during the LGM, and this exerted significant control on changes in their ocean carbonate chemistry. The total weathering rates at the LGM in their study was (50 Tmol yr^{-1}), greater than the interglacial (36 -38 Tmol yr^{-1}) weathering rates due to carbonate weathering of shallow water sediments on exposed continental shelves.

In contrast to the small silicate weathering changes in Brovkin et al. (2012), Lupker et al. (2013) recently provided direct evidence from the Bay of Bengal that chemical weathering from the Tibetan plateau during the LGM may have been as much as 56-89% lower than in the past 2000 years, Foster and Vance (2006) used Pb isotope ratios (correlated to alkalinity fluxes from continental weathering into the ocean) to suggest that chemical weathering from the glaciated and periglacial continental interior (25% of the continental landmass) was 2.5±0.6 times lower during glacial periods, which rose to particularly high weathering rates during early interglacial climates due to warmer temperatures, meltwater, and fresh soil material. A higher-resolution record off the coast of Newfoundland (Crocket et al. 2012) also documented an decrease in chemical weathering (as inferred from the Pb isotope record) to the LGM, followed by an

increase from ~16000 B.C. to 5000 B.C., with large increases associated with Heinrich Event 1 and the Younger Dryas. Foster and Vance (2006) proposed that lower continental interior weathering rates during glacial periods essentially balance increases in continental shelf weathering, leading to little net change in ocean alkalinity from the weathering flux on glacial-interglacial timescales. Similarly, the abrupt increase in continental weathering (an ocean alkalinity source) during the early interglacial documented in Lupker et al. (2013) and Foster and Vance (2006) occurred at the same time as the greatest sea level rise (Broecker and Henderson 1998). While the sea level rise would support more shallow water sedimentation and the upslope growth of coral reefs (ocean alkalinity sinks), the reintensified weathering flux (poorly constrained in the current literature) may essentially cancel out or even eventually overwhelm (as conjectured in Rickaby et al. (2010)) the influence of shallow water sedimentation and coral reefs on interglacial ocean alkalinity. This may help explain why shallow water sedimentation has been unable to induce an increase in atmospheric CO_2 during most previous interglacials (Ruddiman et al. 2011). Thus, any increase in shallow water sedimentation that occurs prior to reintensified weathering should have the greatest net impact on ocean alkalinity; once better-defined this could be simply parameterized in modeling studies as a reduction of the weathering flux (in this case below 10.1 Tmol yr^{-1}).

While the current experiments with the UVic ESCM v. 2.9 do not include shallow water sedimentation, carbonate shelf weathering , or coral reef parameterizations, it is possible that changes in chemical weathering overwhelm these effects during the early and mid-Holocene and that the net alkalinity source to the oceans imposed by 'net weathering' (the increase in shallow water sedimentation subtracted from the increase in weathering) may be closer to the range considered in the present paper (10.1 to 12 Tmol yr^{-1}). Our results suggest that a lower

weathering rate (10.1 Tmol yr^{-1} or lower) continuing through the first stages of deglaciation (through the early Mystery Interval, as in Crocket et al. (2012) and Lupker et al. (2013)) may help maintain or propel higher atmospheric CO_2 until the ventilations of glacial deep water serve to decrease alkalinity further through a replacement of deep-ocean DIC and lowering of the CCD in some regions (CO2rad HW). The greater productivity of marine calcifiers in response to ocean ventilation and increasing SSTs accelerates sedimentation, while warming waters ensure that more organic material is respired in the upper ocean. Due to the slow nature of carbonate compensation, ocean alkalinity would continue to decline even under greater 'net weathering'; in particular, alkalinity would decrease in the CO2rad HW simulation for increases in weathering rate up to ~16.7 Tmol yr^{-1}.

Following the early interglacial increase in both weathering and shallow water sedimentation, weathering declined into the late interglacial (the late Holocene in Crocket et al., 2012), although sea level rise is virtually complete by this time (Broecker and Henderson 1998). Without an explicit global increase in nutrient upwelling, further increases in shallow water sedimentation are probably limited to coral reef expansion in the tropics (which reached maximum accumulation rates around 3000 B.C., according to Ridgwell et al. 2003). As the reduced weight load of ice sheets gradually brought some NH mid-latitude and high latitude shelves in high-productivity regions back above sea level, and coral reef accumulation waned somewhat in the late interglacial, a slow increase in 'net weathering' in the late interglacial might initiate the transition to the next glacial, as suggested in Rickaby et al. (2010). In our simulations, Fig. 9c suggests that the alkalinity of the oceans will continue to decrease in response to greater ventilation unless the 'net weathering' rate meets or exceeds ~200-220 Tg C or ~16-18 Tmol yr^{-1} (CO2rad CA simulation, red line and light orange lines), a plausible scenario given the scale of

weathering changes considered in the proxy evidence. While only represented by two data points (and thus highly aliased), Foster and Vance (2006, their Fig. 3) reveals that weathering rates during the present interglacial were perhaps less than previous interglacials in the North Atlantic, which would allow for a lower net weathering rate instead of a higher one. Although far from conclusively established on a global scale, a lower net weathering rate during the present interglacial in comparison to previous interglacials would permit the alkalinity removal related to deglacial ventilations and coral reefs to continue unabated into the Holocene until carbonate compensation reverses the effect (on a much longer 10000 year time scale, according to our model). With weathering being the most important long-term contributing factor to CO_2 changes, our study concurs with recent proxy and modeling evidence that further research into glacial-interglacial weathering changes may be the key to determining the full effect of ocean alkalinity on the deglacial rise in CO_2 (particularly for the Holocene).

3.1.7 The CO_2-Alkalinity Feedback Associated with Terrestrial Uptake

Concerning terrestrial impacts on ocean alkalinity, Broecker et al. (1999) proposed that terrestrial uptake during the early Holocene (boreal forests and expanded monsoonal vegetation) contributed to a deglacial-interglacial alkalinity change by sequestering CO_2 from the atmosphere and surface ocean, thus increasing the sea surface concentration of carbonate relative to dissolved CO_2. The downwelling of these low pCO_2, high [CO_3^{2-}] waters in the mid-Holocene would have deepened the CCD, allowing more sedimentation of falling $CaCO_3$ shells and ultimately reducing the [CO_3^{2-}] of the ocean. Broecker et al. (1999) documented the removal of alkalinity through the decrease in [CO_3^{2-}] from the size distribution of $CaCO_3$ shells in western tropical Atlantic and western tropical Pacific cores, which implied a late Holocene 11±2 μmol kg^{-1}decrease in [CO_3^{2-}] and over 20 ppm atmospheric CO_2 increase due to greater sedimentation

during the early and mid-Holocene. Subsequent modeling studies, however, do not reproduce the CO_2 increase suggested by Broecker et al. (1999). In particular, Joos et al. (2004) attributed 4-11 ppm of the Holocene CO_2 increase to an alkalinity decline in response to a sediment preservation event, forced primarily by greater CO_2 fertilization of the terrestrial biosphere. In more recent modelling studies, Kleinen et al. (2010) argued that there was no significant difference due to this effect from sensitivity simulations including and excluding terrestrial changes, whereas Menviel and Joos (2012) attributed about +5.3 ppm in response to terrestrial uptake during the Holocene.

Of the results presented in this study, PC HW simulation provides the best evaluation of this effect, as it imposed a decrease in atmospheric CO_2 (Supplementary Fig. 1a) between the early and mid-Holocene, as documented in the ice core record in Petit et al. (1999). This caused 125 Pg C to be extracted from the oceans (Supplementary Fig. 1b). However, the resulting total ocean alkalinity decrease of 4 μmol kg^{-1} (Fig. 11a, magenta line) could not account for the pace of the CO_2 increase after the mid-Holocene, requiring continued injections of carbon into the atmosphere in order to reproduce the late Holocene rise in CO_2. Fig. 11c-d show the change in the alkalinity and [Alk-DIC] patterns for the PC HW simulation between 7000 B.C and 3600 B.C., just prior to the Antarctic ice shelf transition (effectuated in the model at 3500 B.C.) and before renewed acidification from external CO_2 sources (Supplementary Fig. 1b). It shows the greatest alkalinity losses are in the Pacific Ocean (Fig. 11b), where deep Δ[Alk-DIC] is relatively high (Fig.11d), whereas a low [Alk-DIC] anomaly drove down deep ocean values in the Atlantic.

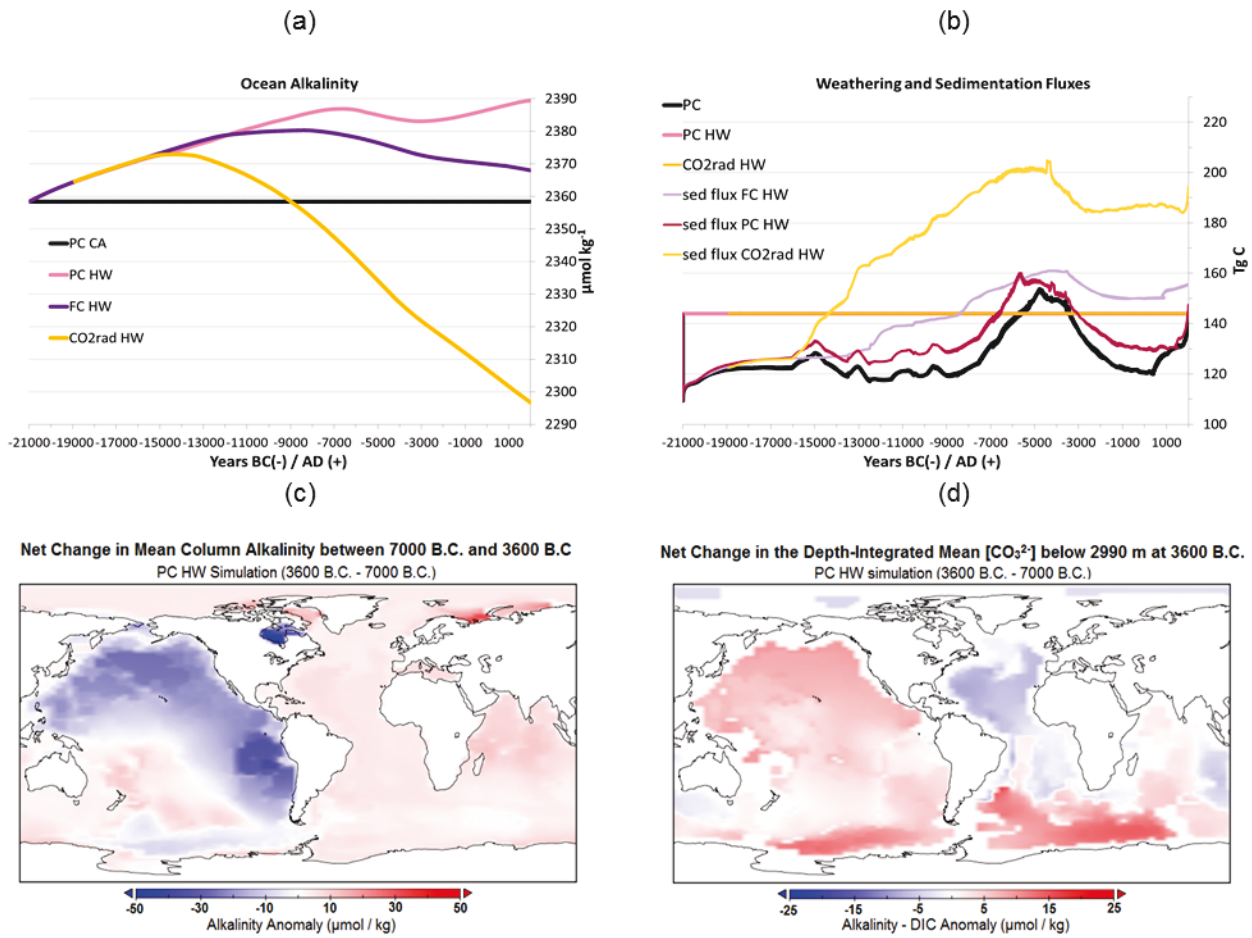

Fig. 11: On the same scale as Fig. 9a,d, the (a) ocean mean alkalinity and (b)weathering (thick lines) and sedimentation fluxes (thin lines) are given, but for the PC CA and PC HW simulations, with comparison to the FC HW and CO2rad HW simulations. For the PC HW simulation, in (c) the mean total column depth-integrated alkalinity change between 7000 B.C. and 3600 B.C. is given at each gridcell, whereas in (d) the net change in mean column depth-integrated[Alk-DIC] below 2990 m depth is provided for the same time interval.

The carbonate losses in the Atlantic had already begun by this date (-5 to -10 µmol kg^{-1}), whereas in the Pacific they had not yet been achieved (+5 µmol kg^{-1}). By 1000 B.C. (not shown), the low carbonate anomaly began to move to the Equatorial Pacific (-5 µmol kg^{-1}), whereas the Atlantic anomaly (-25 µmol kg^{-1}) was overestimated (due in part to the more prominent AABW after the ice shelf transition).

Fig. 11b helps illustrates the uncertainties surrounding the small alkalinity decrease (4 µmol kg^{-1}) computed by the model. It shows that one possibility for amplifying the alkalinity effect of the early Holocene decrease in the PC HW simulation would be to lower the net weathering rate (below the HW rate), which would lead to more total sedimentation on the time

scale of the late Holocene. Another would be to increase the sediment flux, assuming that late Pleistocene dissolution is too high in this simulation (Supplementary Fig. 1d). In particular, a closer look at Fig. 11b shows that the sediment flux (ocean alkalinity sink) in the PC HW simulation (magenta line) is substantially lower than the CO2rad HW simulation (light orange line). This is because the unforced ocean and terrestrial components of the model (represented by the FC HW simulation) are unable to account for a deglacial increase in atmospheric CO_2, so that carbon is added to the system (similar to a measured 'Volcanic' release) in order to balance the demands of these reservoirs and also allow atmospheric CO_2 to follow the ice core record. The introduction of external (non-oceanic) CO_2 into the system, however, acidified the oceans and increased sediment dissolution, leading to a much smaller net sedimentation flux than if ocean processes controlled most of the atmospheric CO_2 increase (the case for the CO2rad HW simulation). If the sedimentation flux for the PC HW simulation had mirrored that of the CO2rad HW simulation, more of the increased sediment flux (in response to the extraction of CO_2 from the atmosphere and ocean) would lie above the weathering rate, representing a larger alkalinity sink than in the PC HW simulation. However, if more sedimentation were to occur in the CO2rad HW simulation, carbonate compensation in favour of increasing dissolution would also oppose this alkalinity change to an even greater degree than in the original experiment.

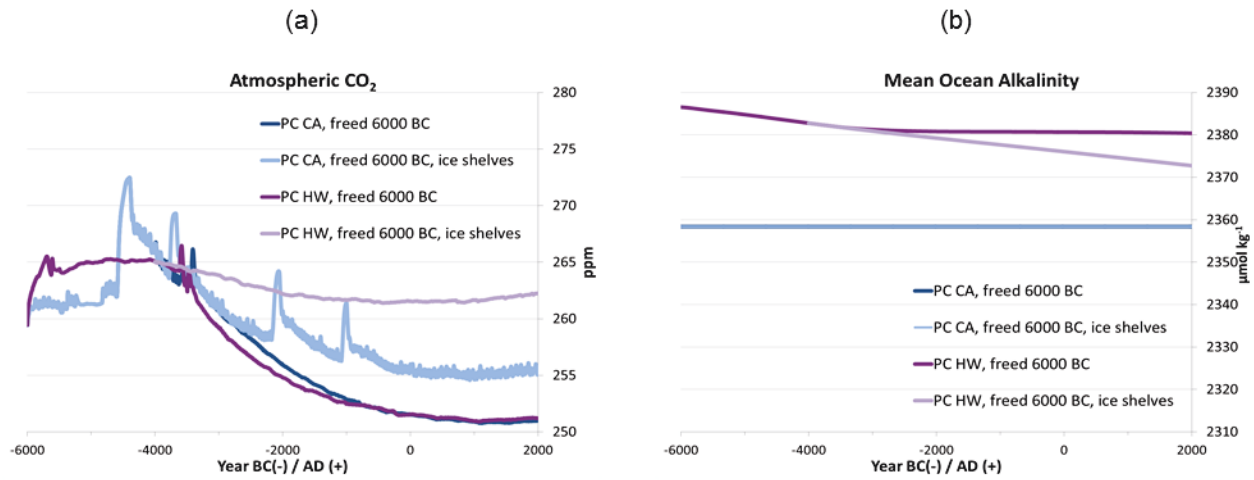

Fig. 12: The PC CA and PC HW simulations repeated with a freed carbon cycle after 6000 B.C., including different Antarctic marine ice shelf configurations. In the legend, "freed 6000 B.C." indicates that no further carbon was injected into the atmosphere (after 6000 B.C.), whereas "ice shelves" indicates a simulation where marine ice shelves in the interpolated ICE-4G dataset were held fixed after 4000 B.C., as in Chapter 4. Trends in (a) atmospheric CO_2 and (b) ocean alkalinity are portrayed for these simulations. Note that the time scale for both figures (6000 B.C. to 2000 A.D.) is different than in the other time series in this paper, and Fig. 12a has a different y-axis scale than in Fig. 1a and Supplementary Fig. 1a.

Another approach to evaluating terrestrial-alkalinity interactions as proposed by Broecker et al. (1999) is to free the carbon cycle in the PC simulations after 6000 B.C. (that is, to stop forcing the atmospheric carbon content to follow the ice core trend after 6000 B.C.). We did this for both the constant alkalinity experiment (PC CA, Fig. 12, dark blue line) and the higher weathering rate (PC HW, Fig. 12a, dark purple line). Fig. 12a shows that there is virtually no difference in the end-result atmospheric CO_2 concentrations for these two simulations (251.3 ppm). Furthermore, the alkalinity change following 6000 B.C. in the freed PC HW simulation (Fig. 12b, dark purple line) is small (5 µmol kg^{-1}), becoming roughly constant after 4000 B.C. Therefore, it appears that the greater downwelling of more corrosive Southern Ocean-generated waters in these simulations after 4000 B.C. exactly counterbalances the slowly decreasing alkalinity in response to DIC removal between 8000 and 6000 B.C., leading to unchanging alkalinity in the freed PC HW simulation. Redoing these two simulations (freed PC CA and freed PC HW) with more extensive ice shelves (Fig. 13, light blue and light purple line respectively) as in Chapter 4 led to less AABW formation and a more prominent NADW. As Fig. 12b reveals,

the more prominent NADW allowed alkalinity to continue decreasing during the late Holocene in the PC HW simulation, allowing atmospheric CO_2 to be 10 ppm higher than in the PC HW simulation without ice shelves and 7 ppm higher than the constant alkalinity experiment with the same more-extensive ice shelves. The significantly greater atmospheric CO_2 concentrations in the PC HW simulation with Antarctic marine ice shelves suggests that substantial NADW formation is required in order for ocean alkalinity to continue decreasing in response to the early Holocene terrestrial uptake. The mechanism proposed by Broecker et al. (1999) thus appears to be strongly dependent on the ocean circulation and proportion of AABW to NADW at depth in the model. The net effect in our PC HW experiment with ice shelves, however, accounts for only about 2 ppm of the net increase in atmospheric CO_2 (to 262 ppm) between the 6000 B.C. and the pre-industrial period instead of the 20 ppm increase seen in the ice core record.

Results from the FC simulations also suggest a limited impact of the terrestrial uptake on ocean alkalinity without the inclusion of more extensive Antarctic ice shelves. Ciais et al. (2012) scaled back the terrestrial uptake to ~300 Pg C between the LGM to the pre-industrial Holocene, which is only slightly greater than the ~200-250 Pg C terrestrial uptake between the early and late Holocene in our FC and CO2rad simulations. The FC HW simulation, which experienced a terrestrial uptake of ~130 Pg C between 12500 B.C. and 6000 B.C. (Fig. 1c), induced a slight decrease in alkalinity into the later Holocene (Fig. 9a, purple line), although a significant fraction of this signal seems to be associated with more ventilation (Fig. 5c) and calcite rain (Fig. 9c) during this time period. In any case, the combined effect of CCD deepening in response to both ventilation changes and terrestrial uptake is relatively modest, narrowing the difference between the FC CA and FC HW simulation from 5 ppm to 1 ppm. This combined effect

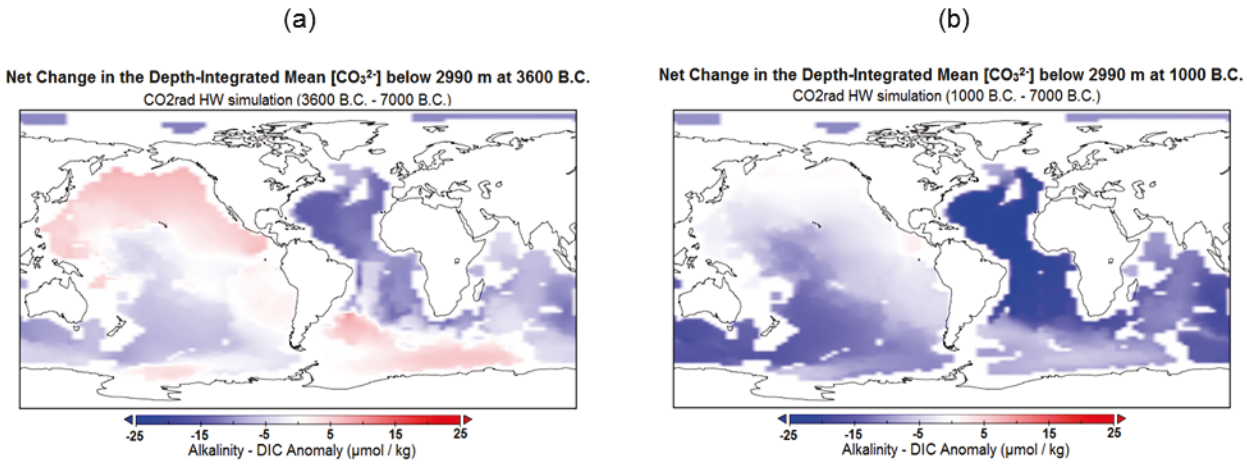

Fig. 13: The net change between 7000 B.C. and (a) 3600 B.C. and (b) 1000 B.C. in the depth-integrated column (gridcell) average Alk-DIC below 2990 m depth.

of 4 ppm, comparable to the lower-end estimate (4-10 ppm) provided by Joos et al. (2004), is unable to fully overcome the net alkalinity increase in this simulation in the late Pleistocene, hence maintaining atmospheric CO_2 that is 1 ppm lower in the FC HW simulation compared to the FC CA results during the late Holocene. It should also be noted that peatland processes are not included in these simulations, and that the 300 Pg C change between the LGM and the pre-industrial period may actually be the end-result of a significant terrestrial release during deglaciation (as argued in Section 3.2) compensated for by a large terrestrial uptake during the interglacial (afforded by peatlands, not represented in the model) rather than a slow increase in terrestrial carbon as provided in the FC and CO2rad experiments. In such a case, the CO_2-alkalinity feedback would be enhanced during the interglacial period, more in line with results from the freed PC HW and freed PC CA sensitivity simulations discussed above.

While terrestrial uptake in our simulations has a limited impact on interglacial alkalinity, the CO2rad results do provide for a substantial alkalinity-induced increase in atmospheric CO_2 during the Holocene in the CO2rad HW simulation from oceanic processes. Furthermore, this increase occurred in spite of decreased vegetation carbon storage between the LGM and the early Holocene. In particular, the terrestrial carbon storage in the CO2rad HW scenario (with higher

CO_2) only began to (slowly) surpass the FC HW simulation at ~7500 B.C. and was only 20 Pg C larger than the FC HW simulation at 6000 B.C., at which point (comparing the CO2rad CA and CO2rad HW trends in Fig. 1a) the alkalinity-induced increase in atmospheric CO_2 in the CO2rad HW simulation was already well underway. A general decrease in [CO_3^{2-}] over the course of the late Holocene was also obtained in this experiment (Fig. 13a,b), again perhaps somewhat overestimated due to the influence of the Antarctic ice shelf transition on AABW but also on the scale of the changes given in Broecker et al. (1999). This indicates that a vegetation uptake scenario as proposed in Broecker et al. (1999) is not required for a sediment preservation event (Fig. 9c) or a significant ocean chemistry-induced increase in interglacial atmospheric CO_2, although it is certainly possible that a slightly deeper CCD propelled by early-Holocene terrestrial uptake could have driven even more CO_2 into the atmosphere by the end of the simulation, especially with the inclusion of more extensive ice shelves.

The results from the CO2rad HW simulation may reflect this effect by stabilizing the CCD in the late Holocene (Fig. 9d), despite the fact that calcite sedimentation far exceeded the weathering flux in this simulation and should have promoted a shoaling of the CCD. In the simulations presented here, however, the alkalinity-induced CO_2 increase appeared to be controlling the terrestrial sequestration in the CO2rad HW simulation instead of terrestrial uptake forcing an alkalinity anomaly. In our results, the effects of the greater ocean ventilation of respired deep-ocean DIC (the CO_2-ventilation feedback) is the more prominent factor in promoting a decrease in ocean alkalinity.

3.2 A High Latitude Terrestrial Carbon Release

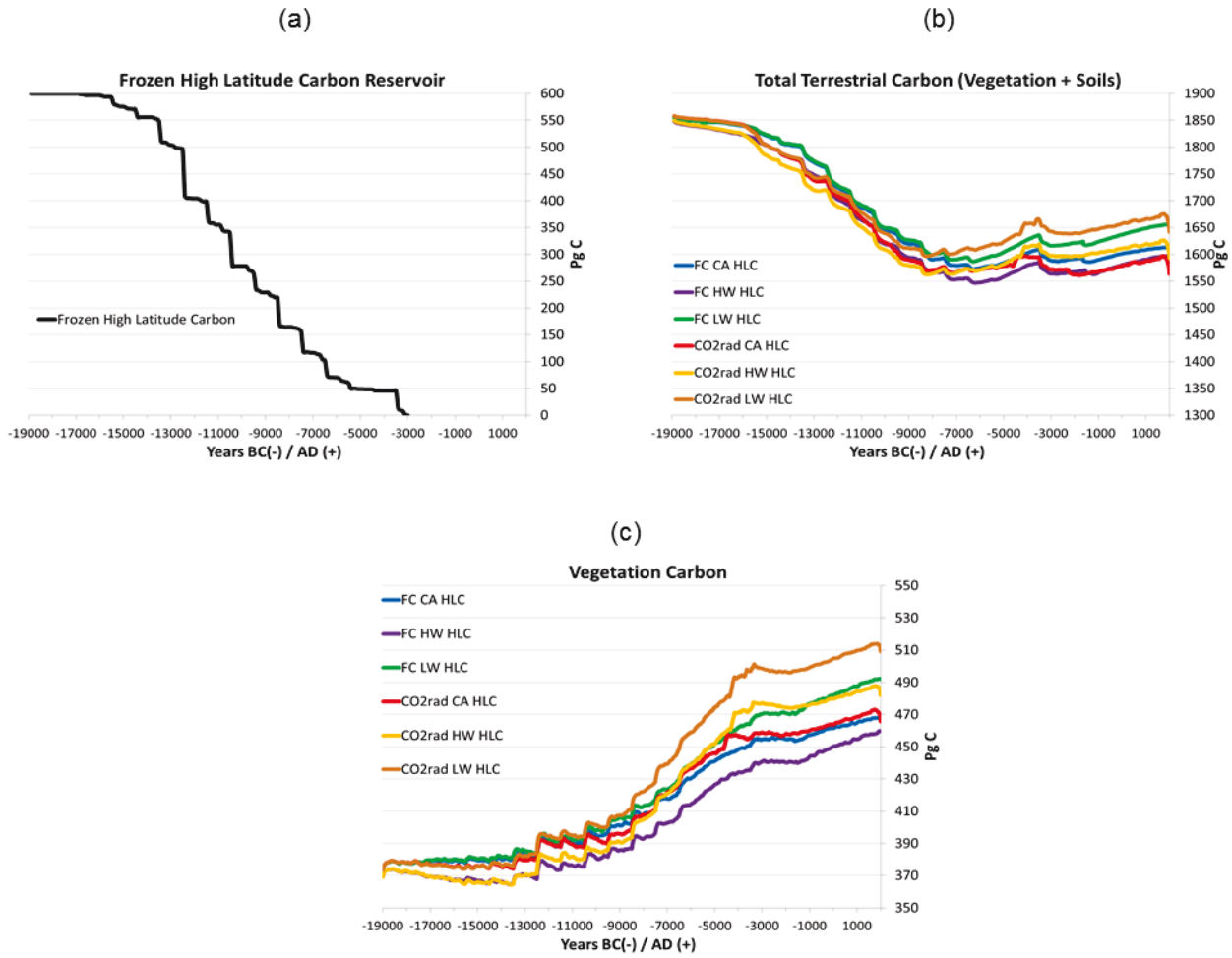

Fig. 14: The terrestrial carbon reservoir for the HLC (high latitude carbon) simulations. In (a), the paced removal of carbon from a frozen soil layer (with no respiration) to the actively-respiring soil layer is represented, whereas (b) portrays the total terrestrial carbon reservoir for the HLC experiments. In (c), the vegetation carbon reservoir (above-ground biomass) is depicted. The coloured lines describe the same simulations as in Fig. 1 repeated with the high latitude carbon reservoir. The additional CO2rad LW HLC simulation is portrayed by a brown line. The scale of (a) is the same as that in (b). In (c), the scale and y-axis range (350-550 Pg C) is different than in Figs. 1d and 3b.

In the high latitude carbon (HLC) experiments, as described in Section 2.4, a 600 Pg C reservoir is inserted into an inactive frozen soil carbon layer that is gradually returned to the active soil layer over the course of deglaciation. Because lower-latitude glaciated regions have gridcells with relatively larger surface areas, this led to reasonably large releases during the earlier part of deglaciation (Fig. 14a). The results indicate that the terrestrial carbon reservoir is unable to sequester the entire terrestrial release through the respiration of the high latitude carbon reservoir (due to the later timing of much of the release); approximately 200-300 Pg C goes into the atmosphere and the oceans (Fig 1b).

In reality, much of the net release projected by the model would have been sequestered by northern peatlands after ~9000 B.C. (not modeled in these experiments). However, it should be noted that most of the net release occurred prior to the period when peatlands were most relevant. After 9000 B.C. the HLC release was fully balanced by terrestrial re-sequestration in all simulations, as Fig. 14b demonstrates. In particular, while 68% of the paced high latitude carbon release occurred after 12000 B.C. (the Pleistocene-Holocene transition), virtually all of this high latitude carbon was reabsorbed by the (non-peatland) terrestrial reservoir represented in the model (Fig. 13b). This suggests that, according to our experiments, the only high latitude release of any consequence for the deglacial rise in CO_2 would have had to occur prior to 12000-11000 B.C., principally during the Mystery Interval. While this release (193 Pg C) only represents 32% of the total contribution of high latitude carbon during the simulations, it plays a much more significant role on atmospheric CO_2 due to less land availability for terrestrial regrowth (and presumably also peatland formation) at this time. This release is also sufficient to stimulate greater vegetation sequestration, which provides a profile of vegetation carbon reservoir that

remains stable during deglaciation (Fig. 14c). By contrast, there are strong losses as in the simulations without high latitude carbon (Fig. 1d and Section 3.1.2).

According to the observations of atmospheric $\delta^{13}C$ in ice cores, the Mystery Interval is also the most likely time for a substantial terrestrial release contributing to higher atmospheric CO_2. In particular, Schmitt et al. (2012) shows there was an abrupt decrease in atmospheric $\delta^{13}C$ between ~15000 B.C. and ~13000 B.C., followed by an interval of lower $\delta^{13}C$ (with smaller variations) between ~13000 B.C. and ~10000 B.C. and a steady increase between ~10000 B.C. and ~4000 B.C. (surpassing glacial values again around 7000 B.C.). The decrease during the Mystery Interval could thus be explained by either a terrestrial release or an upwelling of respired DIC from the ocean or both together (Schmitt et al. 2012; Zech 2012). The interpolation of the ice sheet dataset suggests that there was a significant disappearance at 12500 B.C. and release of high latitude carbon to respiration at this time (Fig. 14a), slightly after the largest drop in the compilation of $\delta^{13}C$ in Schmitt et al. (2012). Because the interpolation is abrupt, it is likely that much of respiration of high latitude carbon in the model at 12500 B.C. could explain part of the trend from Schmitt et al. (2012). For this reason (and uncertainties in the ice dataset), we propose that the modeled change in high latitude carbon storage prior to 12000 B.C. could potentially be relevant to the sharp decline in atmospheric $\delta^{13}C$ indicated in Schmitt et al. (2012).

3.2.1: Consequences for Atmospheric CO_2

Fig. 15a illustrates that the introduction of ~600 Pg C into the one-layer soil of the UVic Model has a varying impact atmospheric CO_2, depending on the weathering rate and presence or

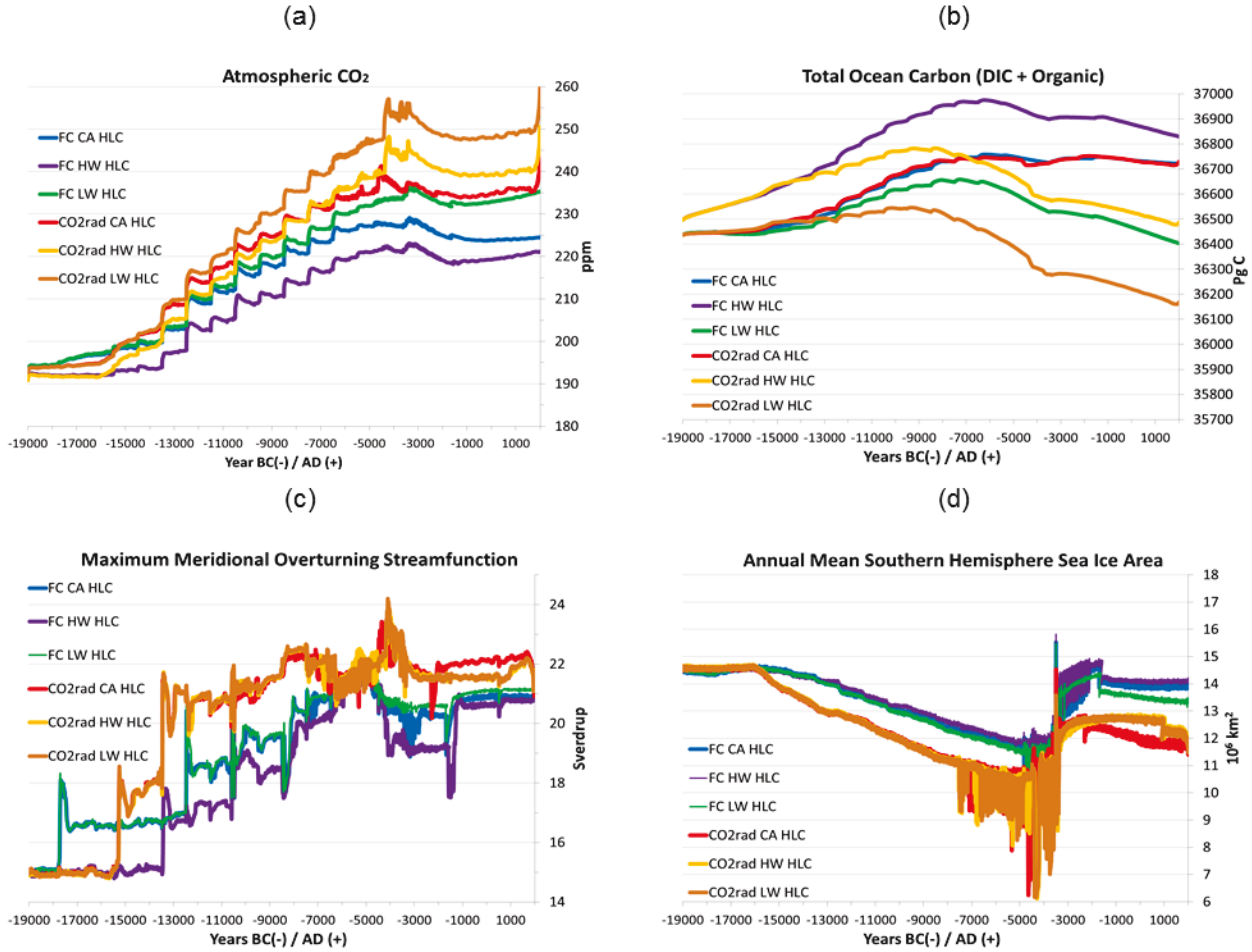

Fig. 15: High latitude carbon simulations represented as in Fig. 14, but portraying (a) atmospheric CO_2, (b) total ocean carbon storage (inorganic and organic), (c) the global maximum meridional overturning streamfunction in the oceans, and (d) the annual mean southern hemisphere sea ice area. In (a), the scale and range for the y-axis (180-260 ppm) is different than in Fig. 1a.

absence of CO_2 radiative forcing. The largest increases are 216 ppm (CO2rad LW HLC) and 214 ppm (CO2rad CA HLC) at 12500-12000 B.C., explaining more than half of the Mystery Interval increase in CO_2. Without the CO_2 warming/ventilation effect, a maximum atmospheric CO_2 of 220-235 ppm was obtained. The 25 ppm range between the FC HW HLC (a maximum of 222 ppm) and the CO2rad HW HLC experiment (maximum of 247 ppm) is slightly less than the 30 ppm difference in the simulations without high latitude carbon, due primarily to the greater acidification and higher alkalinity of the CO2rad HW HLC simulation (discussed further below in Section 3.2.2.). Also unlike the experiments in Section 3.1, the FC LW HLC simulation

achieves the same atmospheric concentrations as the CO2rad CA HLC simulation, suggesting that the low weathering rate's influence on decreasing ocean alkalinity allows for an equivalent contribution to atmospheric CO_2 levels as a more complete CO_2 outgassing (from CO_2 radiative forcing) with no alkalinity change. The massive terrestrial release was most significantly absorbed by the oceans in the FC HW HLC simulation, due to the comparatively high alkalinity of this simulation. The net effect of the terrestrial release was only a 7-10 ppm greater atmospheric CO_2 than the CO2rad HW simulation without a net terrestrial release (compare Fig. 14a with Fig. 1a).

The atmospheric CO_2 increase from the terrestrial pulse is understandably limited by the oceanic response (Fig. 15b). By 12000 B.C. (the period most relevant to the terrestrial release), the ocean carbon reservoir increased by 280 Pg C and 219 Pg C for the FC HW HLC and CO2rad HW HLC simulations (respectively), 145 Pg C for the two simulations with constant alkalinity, and 110 Pg C and 80 Pg C for the FC LW HLC and CO2rad LW HLC simulations (respectively). This represents an increase in carbon storage by 150-190 Pg C relative to the simulations without high latitude carbon from Section. 3.1 (Fig. 1b). Most striking is the small absorption (80 Pg C) implied in the simulation using the lower weathering rate with CO_2 radiative forcing (CO2rad LW HLC).

3.2.2: Alkalinity Impacts

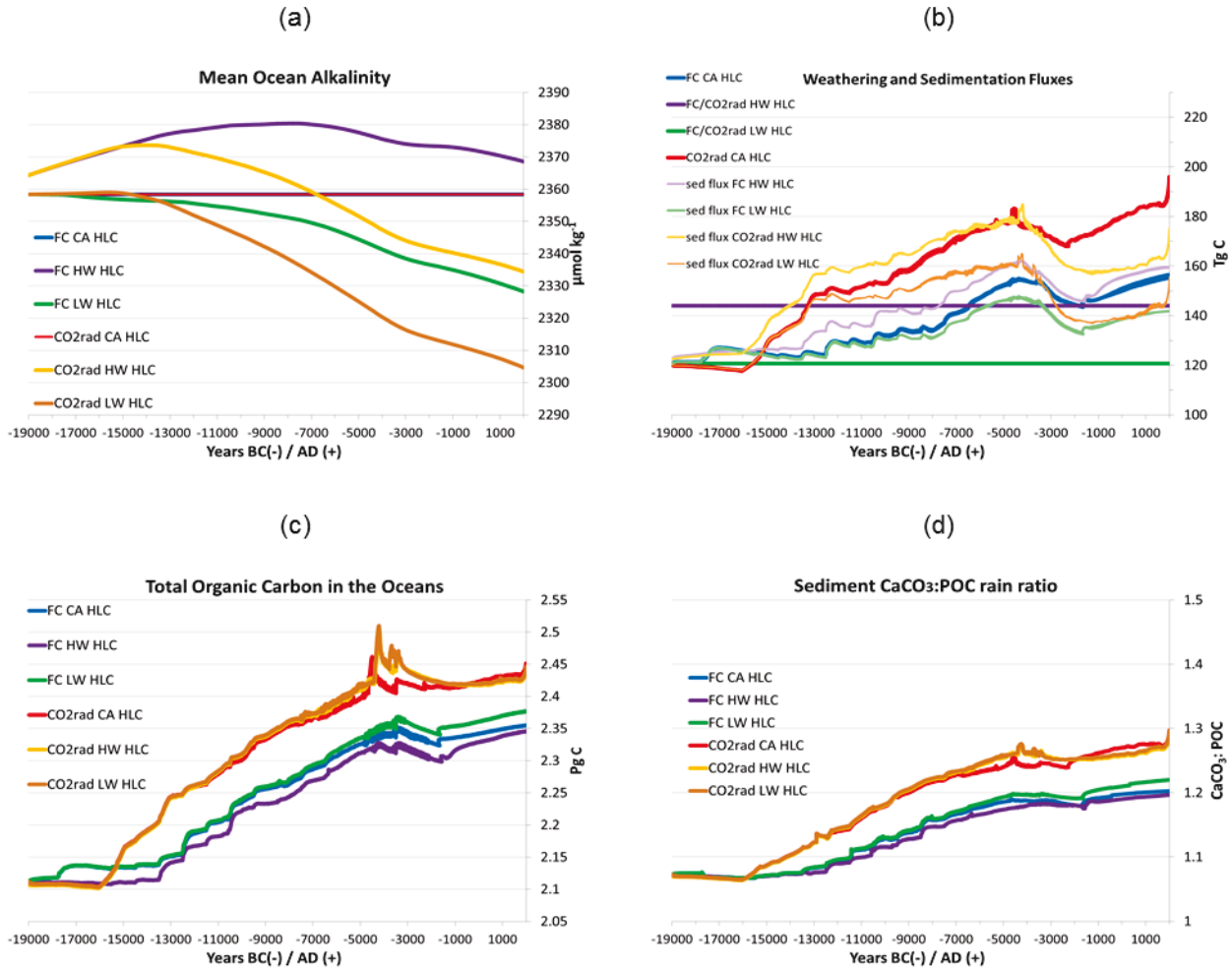

Fig. 16: As in Figs. 14-15, but for (a) the volume-weighted average ocean alkalinity, (b) weathering fluxes and sedimentation fluxes plotted together for comparison, (c) total organic carbon in the oceans (living biomass), and (d) the $CaCO_3$:POC rain ratio at the sediment level (a function of the temperature-dependent respiration of organic carbon before it reaches the sediment layer).

An analysis of Fig. 16a-b indicates that the differences between the FC HLC simulations and those without high latitude carbon is the influence of a terrestrial release on alkalinity. In general, increasing atmospheric CO_2 from a non-oceanic source acidifies the ocean, which lowers oceanic pH and causes further sediment dissolution, increasing the alkalinity and decreasing atmospheric CO_2 on long timescales. It thus seems reasonable to expect that the HLC simulations (Fig. 16a) would experience an increase in alkalinity over those without high latitude carbon (Fig. 9a), especially for the FC HW HLC simulation, which absorbs substantially more

carbon from the atmosphere (~145 Pg C more by 12000 B.C.) than the original FC HW simulation. However, a comparison of the FC HW HLC and FC LW HLC alkalinity profiles in Fig. 16a with the FC HW and FC LW in Fig. 9a shows very little difference (~1-3 μmol kg^{-1}) between the simulations with and without a high latitude carbon release. Thus, while there is a substantial pulse of CO_2 into the ocean (especially pronounced for the HW simulations), there is little increase in alkalinity over the course of the simulation relative to the experiments without high latitude carbon.

There are several contributing factors for the lack of an alkalinity increase due to acidification: (1) the higher CO_2 levels and greater CO_2 radiative forcing of the HLC simulations supports less sea ice extent in the Southern Ocean (Fig. 15d) and better ventilation (Fig. 15c) than in the original simulations; (2) the better ventilation stimulates more calcite rain than in the original experiments, leading to a greater flux of calcite to the deep ocean and sedimentation (Fig. 16b); (3) the warmer temperatures than the original simulation (from more CO_2 in the atmosphere) support higher rain ratios at the sediment level (Fig. 16d) and (slightly) more outgassing, and (4) a terrestrial release associated with a losses in tropical carbon reservoir (Section 3.1.2) is not produced in the simulations with high latitude carbon due to higher CO_2 levels. The impact of the release of high latitude carbon before 12000 B.C., then, is an ocean with substantially greater DIC (Fig. 15a) but virtually no difference in alkalinity between these simulations and those without high latitude carbon.

Of the interconnected contributors opposing a net change in alkalinity for the FC HLC experiments, greater ventilation appears to be the most important. This is demonstrated by the results for the CO2rad HW HLC experiment, which has a similar MOC profile with high latitude carbon (Fig. 14c, orange line) as without high latitude carbon (Fig. 5c, orange line). Here,

without a major difference in the ventilation of the ocean, the acidification from a high latitude carbon release appears to have a greater net effect. The sediment flux (alkalinity removal) is significantly lower in Fig. 16b (orange line) than in Fig. 9b (orange line), demonstrating greater sediment dissolution in the HLC simulation due to the acidification effect. Overall, whereas the CO2rad HW simulation produced a net decrease in ocean alkalinity (in response to greater ventilation) starting at 9000 B.C. (the beginning of the Holocene) (Fig. 9a), the corresponding simulation with high latitude carbon only resulted in an alkalinity decline starting at 7000 B.C. (Fig. 15c). Thus, the alkalinity-induced response is tempered and delayed in the simulation with high latitude carbon relative to the simulation without high latitude carbon for the CO2rad case.

However, these experiments do not include peatlands (which become important after 9000 B.C.) (Yu 2012). It is likely that the addition of a substantial peatland uptake starting in the early Holocene would cause the alkalinity of the CO2rad HW HLC simulation to decrease at a faster rate than that represented here (during the Holocene), promoting an oceanic stabilization of atmospheric CO_2 during the interglacial (as in the simulations without high latitude carbon). In other words, a high latitude terrestrial release would temper the ocean alkalinity response during the late Pleistocene for cases with a quick return to strong ventilation (the CO2rad simulations). However, the addition of peatland uptake (by driving down alkalinity further than that represented here) would allow ocean alkalinity to play a greater role in stabilizing the higher CO_2 concentrations afforded by the earlier terrestrial release during the Holocene. The combination of a low weathering rate and an early ventilation (both contributing to an early oceanic alkalinity decrease) allowed for relatively small oceanic absorption of the high latitude carbon release: ~80 Pg C by 12000 B.C., or 62% of the net terrestrial release (i.e., after terrestrial re-sequestration). The constant decline in alkalinity throughout the simulation allowed atmospheric CO_2 gains

afforded by the pre-11000 B.C. net terrestrial release to be maintained by an ocean that outgasses more with time.

To summarize, the HLC simulations do suggest a potentially important role for a terrestrial release in increasing atmospheric CO_2 during the early part of deglaciation (mainly prior to 12000 B.C.), with decreases in alkalinity during the interglacial period (in response to earlier ventilation changes) helping to sustain the higher atmospheric CO_2 levels initiated by the terrestrial release. In addition, weathering again appears to be the primary moderating factor on the amplitude of these changes, with the range of atmospheric CO_2 change between the FC HW HLC and FC LW HLC simulations being ~10-15 ppm. The results suggest that a weathering rate lower than the equilibrium weathering rate at the LGM (here 10.1 Tmol yr^{-1}), as proposed by Rickaby et al. (2010), would likely accomplish most of the rest of the Mystery Interval rise in atmospheric CO_2 not obtained through the high latitude terrestrial release. Additionally, with very little difference in the alkalinity profiles between the FC and FC HLC simulations, the higher CO_2 in the FC HLC compared to the original experiments (an increase of 37 ppm for the FC HW HLC simulation and by 42 ppm for the FC LW HLC simulation by the mid-Holocene) does not appear to be driven by changes in alkalinity sources and sinks in the ocean.

At the same time, while the FC simulations (without the full CO_2 radiative forcing of the Mystery Interval rise) do obtain an MOC overturning rate comparable to the CO_2 radiative simulations (~21 Sv, Fig. 15c), they do not achieve this until the mid-Holocene, thus limiting the influence of the ventilation-alkalinity feedback on atmospheric CO_2 as compared to the CO2rad simulations. An earlier deglacial ventilation is thus important. While the CO_2-ventilation feedback imposed by the prescribed terrestrial release in our experiments is just large enough to counter the acidification of the terrestrial release (leading to no net change in alkalinity compared

to the FC simulations without high latitude carbon), it cannot invoke a ventilation strong enough to initiate a significant deglacial ventilation-induced decrease in alkalinity. A larger early soil carbon release than that represented here could create the deglacial CO_2 rise during the Mystery Interval and thus provoke an earlier ventilation of the oceans. However, such a scenario would upset the balance between the ventilation-alkalinity feedback and ocean acidification and force the mean ocean alkalinity to increase, delaying the ventilation-induced alkalinity decrease to the mid Holocene (similar to the CO2rad HW HLC experiment). Thus, our results suggest that the abrupt ~30 ppm Mystery Interval CO_2 rise should have both terrestrial and oceanic contributions. While the full effect of a Mystery Interval upwelling event is not achieved in this study (likely due to a lower ocean DIC than that which represents the glacial period, as in Huiskamp and Meissner 2012), the added contribution from a greater ventilation of DIC through the Southern Ocean during the Mystery Interval could serve to decrease ocean alkalinity in the long term, helping to maintain the increase in atmospheric CO_2 initiated by a combined upwelling event and terrestrial release.

3.2.3 Implications for Observational Constraints

While the model configured for these simulations in this paper does not calculate $\delta^{13}C$ in the atmosphere and ocean, the results presented here could have potentially important implications for reconciling the $\delta^{13}C$ atmospheric and oceanic trends within the context of a major terrestrial release. In general, it is well established that glacial maxima have lower $\delta^{13}C$ in the oceans (Olivier et al. 2010), due most likely to an accumulation of respired carbon (Bradtmiller et al. 2010). Yu et al. (2010) also demonstrated that over the course of deglaciation, intermediate waters demonstrated abrupt decreases in $[CO_3^{2-}]$ and $\delta^{13}C$ (linked to an upwelling event in the Southern Ocean, as indicated by Anderson et al. (2009)). This was further coupled to

an increase in [CO_3^{2-}] in deep waters in several ocean basins, associated with the downwelling of high-alkalinity surface waters and especially prominent after the reinvigoration of the NADW. However, in the cores analyzed by Yu et al. (2010), the $\delta^{13}C$ of the deep ocean remained relatively constant until the late deglacial. Zech (2012) suggested that the decrease in [CO_3^{2-}] near the surface could be linked to an oceanic absorption of a large permafrost release rather than an upwelling of high DIC. However, given that downwelling in the North Atlantic virtually ceased (McManus et al. 2004) during Heinrich Event 1 and larger alkalinity inputs were supplied to this region (Crocket et al. 2012) and not to the primary sinking region in Southern Ocean, the [CO_3^{2-}] in deep waters would probably stabilize or decrease in this scenario instead of increase as documented in Yu et al. (2010). This explanation also does not explain the disappearance of a suboxic deep water mass during deglaciation (Bradtmiller et al. 2010).

Our results support a slightly different scenario that caters to both the terrestrial and oceanic release hypothesis and fits reasonably well within the framework offered by Rickaby et al. (2010). The CO2rad LW HLC simulation provides an example of a large terrestrial release with relatively little oceanic absorption. The small oceanic absorption is, in turn, determined by the low weathering rate (low alkalinity inputs into the ocean) coupled to a larger ventilation of the deep ocean between 14000 B.C. and 13000 B.C. The two work together to drive an early decrease in ocean alkalinity (Fig. 16a) and prevent a significant absorption of the terrestrial release (Fig. 15b). The LW weathering rate (10.1 Tmol yr^{-1}) is in equilibrium with the LGM sedimentation rate (19000 B.C.) in our simulations. Rickaby et al. (2010) suggested that the deeper CCD (high alkalinity) of LGM deep waters may have allowed for most

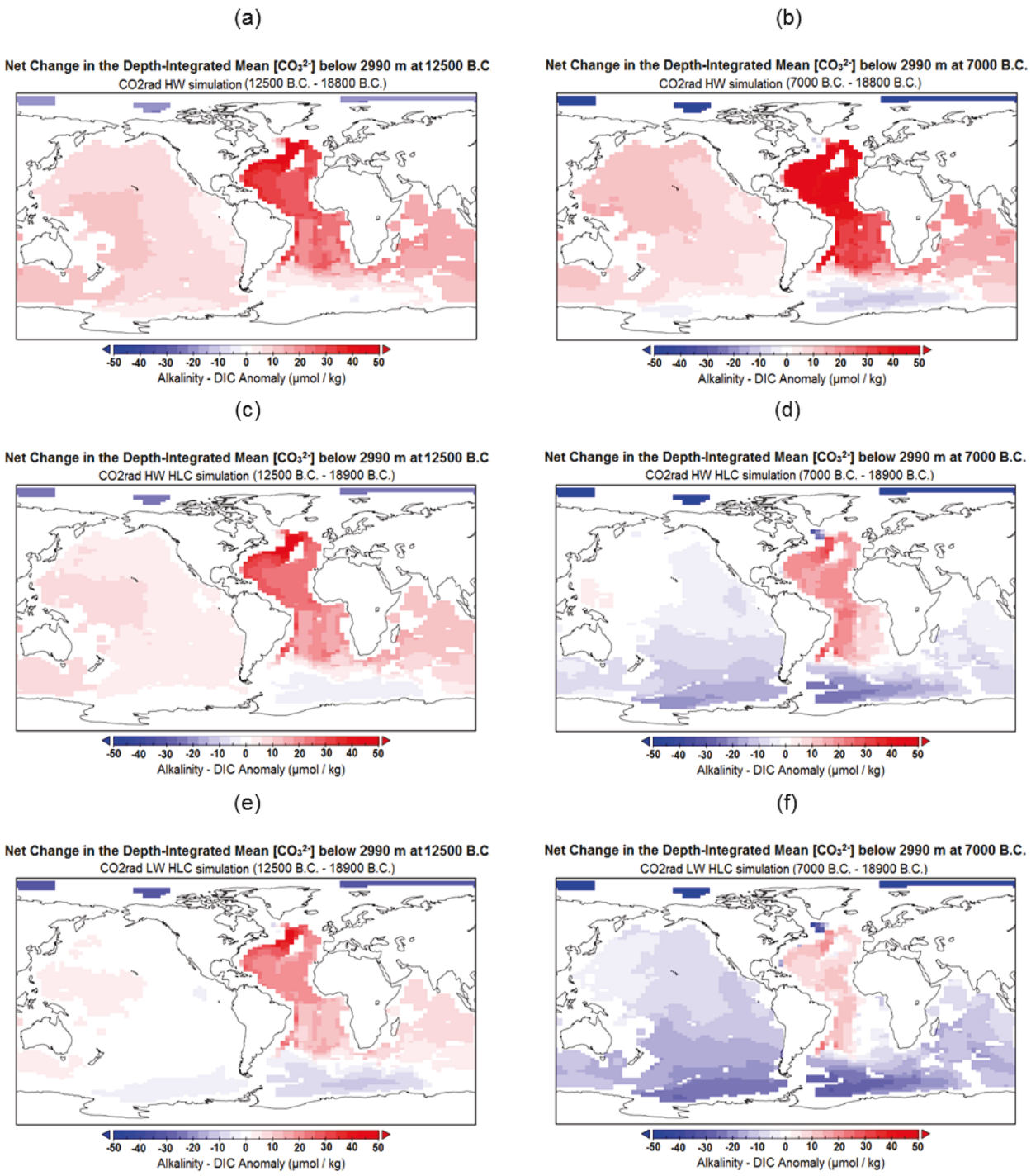

Fig. 17: Changes in the depth-integrated average Δ[Alk-DIC] below 2990 m depth since the LGM for (a-b) the CO2rad HW simulation, (c-d) the CO2rad HW HLC simulation and (e-f) the CO2rad LW HLC simulation. In (a,c,and e), the net change in [Alk-DIC] between the LGM and 12500 B.C. are portrayed, whereas in (b,d,and f) the net change in [Alk-DIC] between the LGM and 7000 B.C. are depicted for the respective simulations.

sedimentation occurring above the CCD, and thus that the sedimentation rate at the LGM was potentially much higher than the weathering rate. This would imply that the LW weathering rate (used in the CO2rad LW HLC simulation) is also too high. An even lower weathering rate than the LW case would lead to even less oceanic sequestration of the terrestrial release during the early deglacial and could potentially explain the entire Mystery Interval increase in CO_2. While this experiment is not presented here, the ~10-15 ppm sensitivity per 2 Tmol yr^{-1} difference in 'net weathering' suggests that a rate of 8-9 Tmol yr^{-1} with a terrestrial release should be sufficient to explain the Mystery Interval increase in CO_2 and thus reproduce the full early CO_2-ventilation feedback and ventilation-alkalinity feedback as described for the CO_2 radiative forcing experiments. Greater sediment dissolution (carbonate compensation) would oppose the increase, although several thousand years after the initial upwelling, by which point larger alkalinity inputs in the ocean (Foster and Vance 2006; Crocket et al. 2012) could reverse this process and contribute to carbonate compensation in the opposite sense (the observed sediment preservation event) during the early Holocene.

In addition to supporting the hypothesis of Rickaby et al. (2010), this scenario could also partially explain the proxy data from Yu et al. (2010). Yu et al. (2010) indicates that the deglacial period from ~12000 B.C. to ~8000 B.C. demonstrated a change of ~+20 μmol kg^{-1} in the deep North Atlantic and ~+10 μmol kg^{-1} in the abyssal Indo-Pacific and deep western tropical Pacific since the LGM. As discussed briefly in Section 3.1.5, the CO2rad HW simulation overestimated the change in the deep Atlantic (Fig. 17a-b) relative to Yu et al. (2010), producing an increase of +30-50 μmol kg^{-1} since the LGM across a large expanse of the Atlantic basin when values were likely closer to +20 μmol kg^{-1}. Similarly, Indian and western Pacific values are closer to 15-20 μmol kg^{-1}.The inclusion of a high latitude terrestrial release in the CO2rad simulations, however,

resulted in more realistic values in all three ocean basins. In particular, the Δ[Alk-DIC] in CO2rad LW HLC simulation fit the data better for 12500 B.C., and the CO2rad HW HLC simulation came closer to reality for 7000 B.C. (suggesting an increase in the net weathering rate over this time period).

While the poor-resolution of $[CO_3^{2-}]$ proxy data prevents firm conclusions, these results suggest that a significant carbon release from a non-oceanic source during the deglacial period could provide a better representation of deep-ocean deglacial $[CO_3^{2-}]$ changes than simulations without such a release. The scenario with an early-deglacial high latitude carbon release might start with a ventilation (implicit at 13000 B.C. in the CO2rad simulations) of deep waters during and after HE1, bringing low $[CO_3^{2-}]$ waters to the surface. These surface waters would increase in $\delta^{13}C$ due to the release of respired CO_2 to the atmosphere, followed by a gradual re-fertilization of surface waters by high-$\delta^{13}C$ permafrost carbon. The flux of this high latitude carbon into the ocean would be small (due to the lower weathering rate resulting in a lower alkalinity), and the (small) flux of high-$\delta^{13}C$ CO_2 into the oceans could help maintain the low $\delta^{13}C$ of downwelling surface waters in the reinvigorated post-HE1 NADW without overpowering the gradually increasing $[CO_3^{2-}]$ from greater weathering and terrestrial sequestration (Fig. 17d) in this region. Despite low weathering globally, greater weathering inputs locally in the North Atlantic during HE1 could contribute to high alkalinity surface waters in North Atlantic downwelling regions after the end of freshwater fluxes, filling much of the Atlantic and Indian Oceans (up to the tropical Pacific in our simulations) with high $[CO_3^{2-}]$, low $\delta^{13}C$ NADW. Ideally, these $\delta^{13}C$ and $[CO_3^{2-}]$ constraints could be used to determine the exact weathering rate (likely lower than the LW rate) that could support the proposed scenario, although this is beyond the scope of the simulations presented here.

3.3 Freshwater Forcing

These experiments apply freshwater forcing to the UVic model to simulate Heinrich Event 1 (HE1) (Liu et al. 2009), administered through the St. Lawrence drainage basin and the Mississippi Valley, and the Younger Dryas event, initiated by a flux through the St. Lawrence (Meissner 2007). Similar experiments have been performed with the UVic model by Meissner (2007) and Huiskamp and Meissner (2012), with more detailed analysis and proxy-model comparisons than the simulations presented here. However, the fluxes in Huiskamp and Meissner (2012) lasted for 500 years, while the freshwater fluxes used here were applied for a much longer period, starting at 17050 B.C. and ending at 12720 B.C. as in Liu et al. (2009). Our global maximum meridional overturning streamfunction (not shown) mimicks almost exactly the meridional overturning profile in Liu et al. (2009) during the flush itself—a two-stage decrease in the strength of overturning until a complete shutdown (2 Sv) by 15300 B.C. Liu et al. (2009) were able to produce a fast rebound in the MOC after the flush (~12600 B.C., as in nature), but the UVic ESCM demonstrates unrealistic hysteresis behavior, and the North Atlantic overturning never recovered from HE1. Thus, exchanges in the ocean after 15300 B.C. are primarily due to Southern Ocean-forced dynamics, an unrealistic scenario after 12700 B.C. Nevertheless, in the aftermath of HE1, the simulations reveal that the Southern Ocean is able to by itself provide a significant contribution to atmospheric CO_2 by forcing a more complete ventilation of the Pacific Ocean (through warming) than achieved in the simulations described in Sections 3.1 and 3.2.

3.3.1: Freshwater -Specific Features: Terrestrial Release and Deep Ocean Temperature

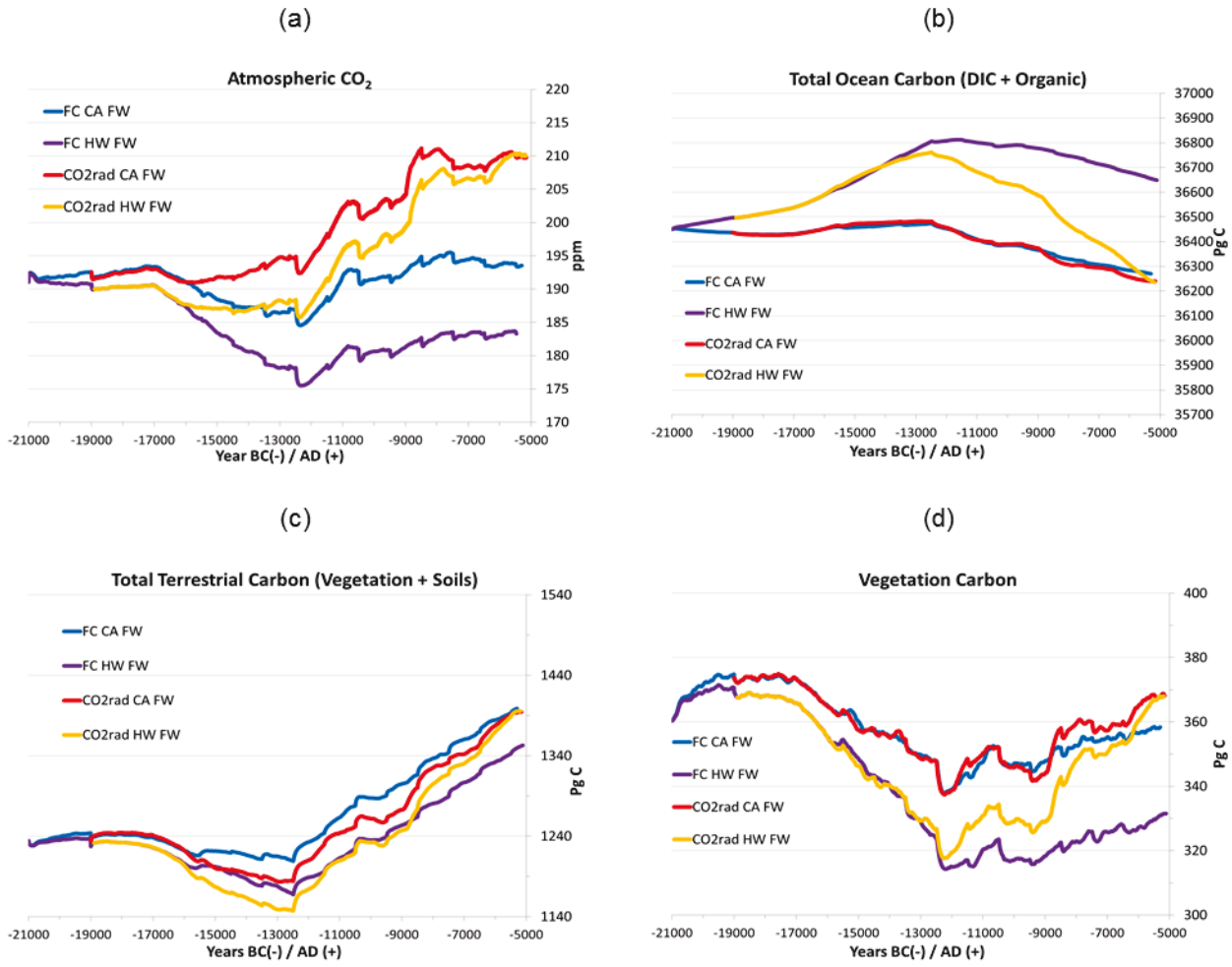

Fig. 18: Results for experiments with freshwater fluxes (Heinrich Event 1 and the Younger Dryas), including (a) atmospheric CO_2, (b) total ocean carbon (organic and inorganic) storage, (c) terrestrial carbon (including both vegetation and soils), and (d) above-ground vegetation biomass.

Unlike in several previous experiments with the model, the freshwater fluxes did not produce a rise in atmospheric CO_2 during HE1 in most experiments (Fig 18a). In fact, the freshwater fluxes themselves led to lower atmospheric CO_2 concentrations than the original experiments during this event. Some models (for example, Brovkin et al. (2012)) produce an increase in atmospheric CO_2 from freshwater flushes, whereas others modeling studies show no change or a decrease in atmospheric CO_2 from the oceanic response to freshwater fluxes (Obata

2007; Menviel et al. 2008b; Bozbiyik et al. 2011). The large range in model solutions reflects the uncertainties surrounding flux magnitude, flux duration, and the importance of different carbon cycle feedbacks during and after these freshwater fluxes (Bouttes et al. 2012).

In addition to a drawdown of atmospheric CO_2, the terrestrial biosphere experienced significant net losses during HE1 (Fig. 18c): 72 Pg C for the FC HW FW experiment and 86 Pg C for the CO2rad HW FW experiment. These losses are generally comparable in magnitude with those documented by Bozbiyik et al. (2011) for a shutdown of North Atlantic circulation (60 Pg C). The additional terrestrial release during HE1 in our results represents a net decrease of 35-40 Pg C in terrestrial carbon storage relative to the same simulations without freshwater fluxes (compare with Fig. 1c). The largest net losses appear to be in vegetation (Fig. 18d), with most of this carbon increasing the DIC content of the oceans (Fig. 18b). The constant alkalinity experiments showed much smaller net losses related to the freshwater flux (total flux of 23 Pg C, a 13 Pg C difference from the original simulations). This indicates that the strength of the terrestrial release during HE1 depends strongly on alkalinity changes in the ocean. The increasing ocean alkalinity during a freshwater flush (discussed below in Section 3.3.2) caused the oceans to sequester more CO_2 from the atmosphere in these simulations, which resulted in slower/less terrestrial regrowth. In Bozbiyik et al. (2011), the terrestrial releases associated with a shutdown in the AMOC were proposed as the mechanism for the 20 ppm increase in atmospheric CO_2 during the YD and HE1 (with the ocean acting as a net sink in that study). Our simulations, on the other hand, suggest that the ocean is a stronger sink of atmospheric CO_2 during the AMOC shutdown and overwhelms the effect of the additional terrestrial release.

The spatial pattern for biosphere carbon losses are shown in Fig. 19, which gives the change in terrestrial carbon storage between the LGM and the end of the freshwater fluxes

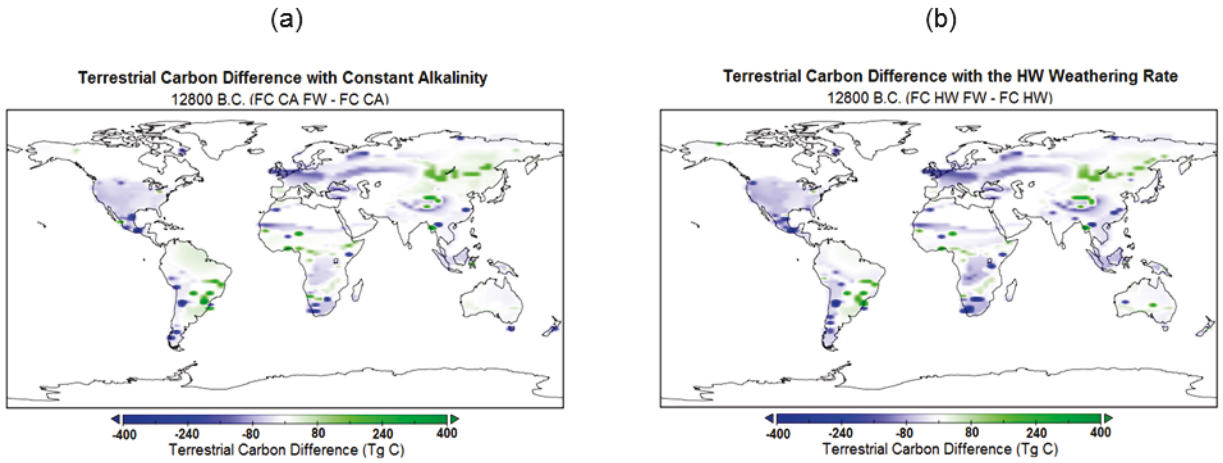

Fig. 19: The difference in terrestrial carbon storage (vegetation and soils) at 12800 B.C. between the simulations with and without freshwater fluxes are portrayed for (a) the FC CA FW simulation (FC CA FW – FC CA) and (b) the FC HW FW simulation (FC HW FW – FC HW). Blue shading indicates relative terrestrial releases to the atmosphere in the FW simulations, whereas green shading represents areas of relative terrestrial uptake in the FW simulations.

associated with HE1. There are some changes that are similar to those in Handiani et al. (2012a) (another study of vegetation dynamics during HE1 using the UVic ESCM), mainly the vegetation losses in the northern Sahel region and western Eurasia. The generally larger decrease in terrestrial carbon storage at mid-latitudes (where the temperature effects of the shutdown in NADW are strongest) are consistent with Bozbiyik et al. (2011), although the small changes in the wind field do not lead to the pronounced tropical losses in terrestrial carbon as suggested by Dupont et al. (2010), Bozbiyik et al. (2011), and Handiani et al (2012a,b) for HE1. However, terrestrial carbon losses (relative to the experiments with no freshwater fluxes) are a global phenomenon due to substantially reduced CO_2 fertilization from the atmosphere, leading to slower growth in the FW simulations. Fig. 19b indicates that the inclusion of alkalinity effect (i.e., greater alkalinity and oceanic uptake of CO_2) mainly amplified the terrestrial losses from the FC CA FW without changing the spatial distribution of these losses.

Fig. 18b also indicates that most of the terrestrial carbon absorbed by the oceans was flushed back to the atmosphere after HE1. However, the divergence between the FC HW FW

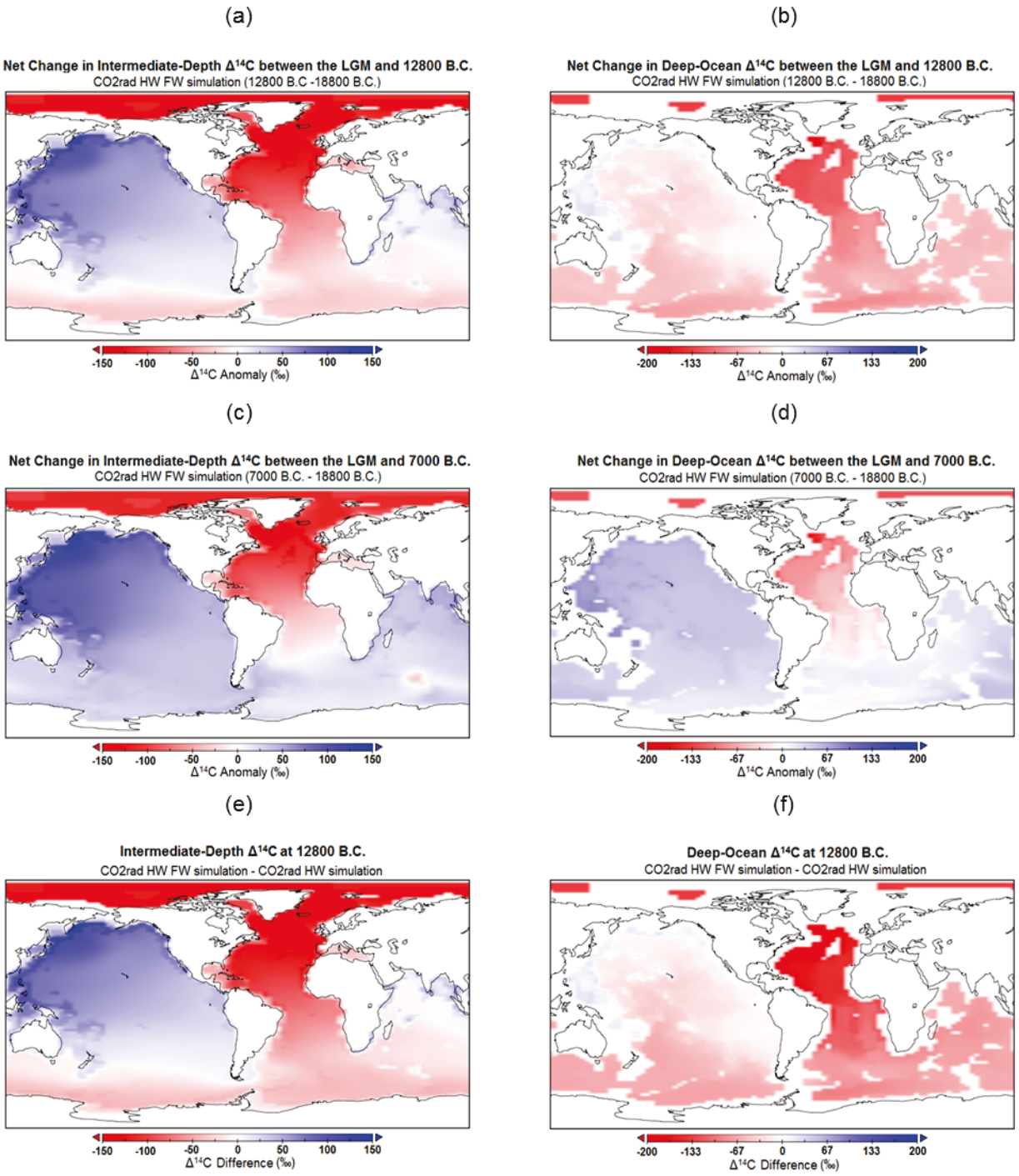

Fig. 19: Spatial patterns of depth-integrated mean $\Delta^{14}C$ changes in the intermediate (240 m – 2990 m depth) and deep (below 2990 m depth) ocean are portrayed. In (a-b), the net change in mean $\Delta^{14}C$ for (a) intermediate waters and (b) deep waters between the LGM and 12800 B.C. are given, and in (c-d) the net change in mean $\Delta^{14}C$ for (c) intermediate waters and (d) deep waters between the LGM (18800 B.C.) and 7000 B.C. are shown. In (e-f), the difference between the CO2rad HW FW simulation and the CO2rad HW simulation at 12800 B.C. is given for (e) intermediate waters and (f) deep waters. Red shading indicates regions where waters are more poorly-ventilated (higher $\Delta^{14}C$) in the CO2rad HW FW experiment, whereas blue shading indicates regions where waters are better-ventilated (lower $\Delta^{14}C$) in the CO2rad HW FW experiment.

(purple line) and CO2rad HW FW (orange line) simulations is of a similar magnitude (400-450 Pg C) by 5000 B.C. as in the simulations without freshwater fluxes (Fig. 1b). This indicates that the model produced a similar purge of deep-ocean DIC over the course of the late deglacial and early interglacial as the experiments described in Section 3.1, even without a recovery of the NADW. This ultimately led to the comparable atmospheric CO_2 levels and terrestrial sequestration between the experiments shown in Section 3.1 and those presented here with the freshwater fluxes (despite no AMOC recovery in the experiments in this section).

This suggests a reorganization of the pattern of deep water renewal (as determined by Southern Ocean dynamics) following HE1 that included flushes of deep DIC to the surface of equal magnitude to those generated by an intensification of the NADW. Spatial profiles of depth-integrated average $\Delta^{14}C$ in the deep and intermediate Pacific (Fig. 20) illustrate these ventilation changes. In the northwest Pacific, intermediate waters (defined here between 1000 m and 2990 m depth) increased in $\Delta^{14}C$ over the course of the HE1 flux due to greater convection in this region (starting approximately at 15500 B.C., after the complete shutdown of the NADW) (Fig. 20a). This convection, however, had limited reach, as the average deep-ocean $\Delta^{14}C$ (Fig. 20b) increased slightly in the Pacific over the period. This pattern appears to be consistent with Okazaki et al. (2010), who documented with a compilation of proxy data that North Pacific intermediate waters (above 3000 m depth) were well-ventilated, oxygen-rich, and nutrient depleted, due perhaps to an active overturning circulation in this region. Furthermore, our $\Delta^{14}C$ pattern for deep waters (Fig. 20b) also compares well to Galbraith et al. (2007), who showed that a ventilation of abyssal North Pacific waters post-dated HE1 (~12600 B.C.). The formation of a more prominent North Pacific circulation during HE1 is also consistent with another recent investigation of the Mystery Interval with the UVic model (Huiskamp and

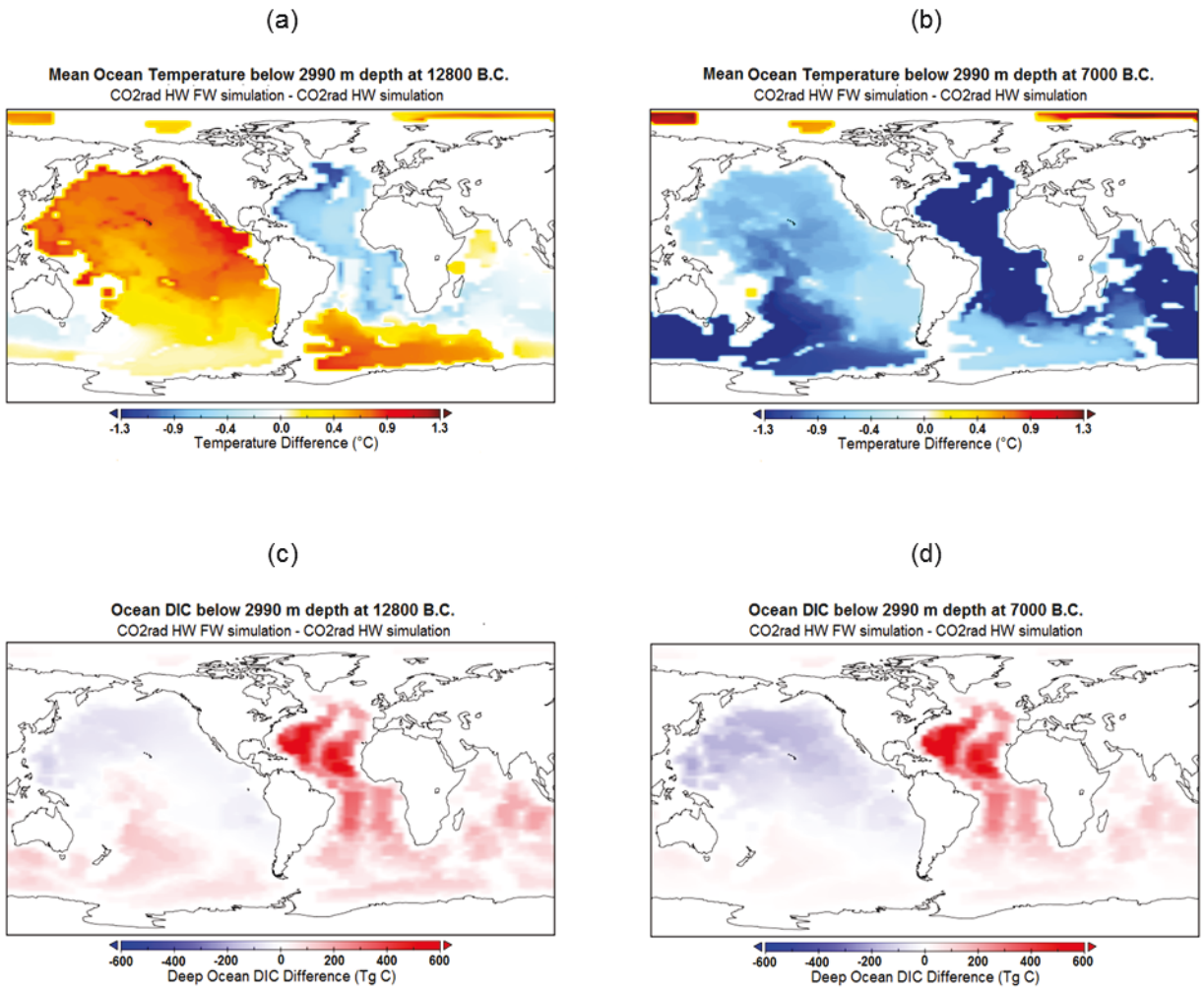

Fig. 20: Deep ocean temperature (°C) and deep ocean dissolved inorganic carbon (DIC) differences between the CO2rad HW FW and the CO2rad HW experiments (i.e., with and without freshwater forcing). This includes the depth-integrated mean temperature below 2990 m depth at (a) 12800 B.C. and (b) 7000 B.C. In (c-d), the total DIC content below 2990 m is provided at (a) 12800 B.C. and (b) 7000 B.C. Orange (red) shading indicates warmer temperatures (more DIC) in the freshwater flux experiment (CO2rad HW FW), whereas blue indicates colder temperatures (less DIC) in the freshwater flux experiment. In (c-d), the scale (-600 Tg C to +600 Tg C) is different than in Fig. 6.

Meissner 2012). Meanwhile, the Atlantic basin became the location of the most poorly-ventilated deep waters (Fig. 20b,d), while the Pacific and Southern Ocean gradually ventilated after HE1 (Fig. 20c-d).

This result is quite different from the original CO2rad HW simulation without freshwater fluxes (Fig. 6), which demonstrated no change or an accumulation of DIC in the North Pacific

between the LGM and 7000 B.C. (Fig. 6b), with a much later ventilation of the deep Pacific (likely due to Antarctic ice shelf changes) after 6000 B.C. From these results, it follows that the CO2rad HW FW simulation flushed North Pacific waters earlier (12700-10000 B.C.) than in the CO2rad HW simulation (6000-4000 B.C.). This earlier ventilation is also more consistent with the proxy data (Galbraith et al. 2007), which shows a change in deep-water properties in the North Pacific ~12600 B.C. shortly after the end of the freshwater fluxes prescribed in this simulation (12720 B.C.). However, in reality, the ventilation of the deep North Pacific was probably more abrupt than in the simulation described here (Galbraith et al. 2007). Furthermore, the continued formation of North Pacific Intermediate Water after HE1 (Fig. 20c), a symptom of the continuing lack of NADW formation in these simulations, is also unlike the proxy record (Okazaki et al. 2010).

Fig. 20, showing deep ocean temperature and DIC, suggests that buoyancy is perhaps the most important contributor to the ventilation of the Pacific by the end of HE1. In particular, relative to the original CO2rad HW simulation, the CO2rad HW FW simulation has notably warmer deep waters temperatures in the North Pacific (Fig. 20a). Because the freshwater fluxes continued over 4000 years, during which time the entire abyssal ocean became poorly ventilated (Fig. 19b,20a), the deep waters of the North Pacific were able to warm slowly through diffusion (as in Meissner et al. 2008). This subtle warming appears to be enhanced by the rigourous formation of North Pacific Intermediate Waters, which transferred surface heat (from rising near-surface temperatures associated with the CO_2 radiative forcing) to the deep ocean through mixing and diffusion around 3000 m depth. Enhanced convection in the North Pacific thus transfers heat to abyssal waters in this region, making them potentially unstable as a result of the freshwater fluxes in the Atlantic. The opposite occurred in the Atlantic, where the predominance

of Southern Ocean-generated waters and a lack of overturning led to a much colder deep ocean (and loss of buoyancy at greater depths). The end of the freshwater fluxes associated with HE1 (at 12720 B.C.) signal a period of increasing salinity in surface and intermediate waters (not shown), which allowed the warmer Pacific deep waters to be more readily convected/mixed to the surface. If the freshwater fluxes in the present experiments were unrealistically high (as suggested by J. McManus, personal communication, 2013), the strong ventilation of the Southern Ocean at 11800 B.C. (not shown) might occur at an earlier date (during the Mystery Interval) (15000-13000 B.C.). This Southern Ocean ventilation event was suggested by Anderson et al. (2009). Some of the greater ventilation in the Southern Ocean, however, can be explained by decreasing SH sea ice extent in response to increasing CO_2 during the Mystery Interval.

The reorganization of carbon storage associated with this ventilation pattern can be seen in Fig 20c-d, which shows that the North Pacific had begun losing DIC by 12800 B.C. and became DIC-deprived (relative to the simulation without freshwater fluxes) in the early Holocene. Without a recovery of the NADW, however, the Atlantic stored substantially more DIC than in the original simulation without freshwater fluxes. The end result is thus a slight net gain of CO_2 to the atmosphere due to the better ventilation of the Pacific and parts of the Southern Ocean (Fig. 17a). While our simulations do not produce a recovery of the NADW, an integration of the NADW-affected regions in Fig. 20c indicates that a reinvigoration of the NADW at the same magnitude as in the CO2rad HW simulation at 12800 B.C. would lead to an additional 300 Pg C decrease in deep-ocean DIC storage (mostly in the Atlantic, Indian, and South Pacific), representing a potentially significant source of atmospheric CO_2.

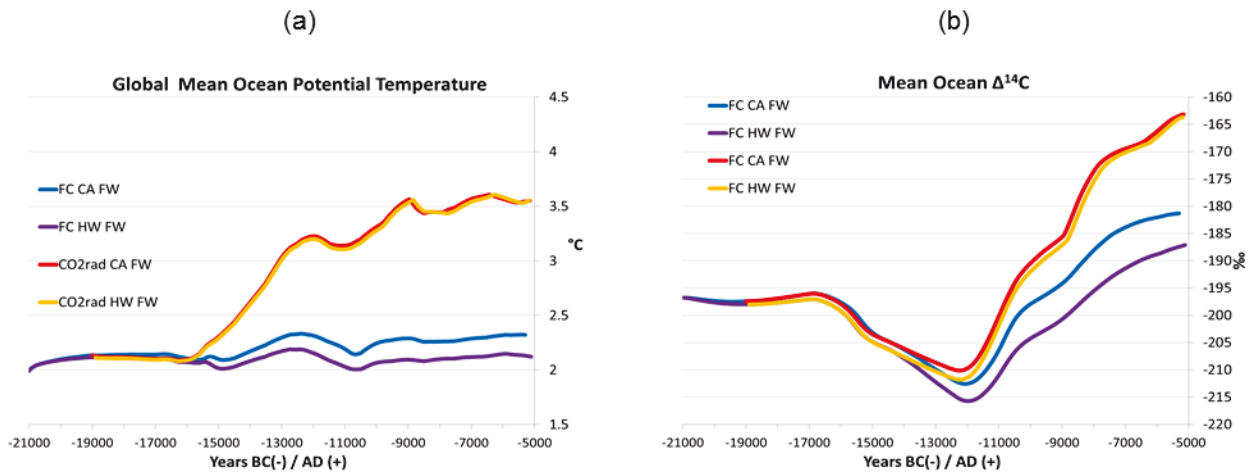

Fig. 21: As in Fig. 17, but for the (a) global mean depth-integrated ocean potential temperature and (b) the global volume-integrated mean ocean $\Delta^{14}C$ (with atmospheric $\Delta^{14}C$ set to a constant 0.0‰ as in all other simulations). The y-axis ranges in (a) and (b) are different than in Fig. 5b and 5d.

While our conclusions are limited by a lack of a post-HE1 recovery of the NADW, the increase in the buoyancy of abyssal North Pacific waters during HE1 may help explain why, in nature, abyssal waters in the North Pacific were possibly dislodged in the wake of a resurgent NADW (Galbraith et al. 2007). In our simulations, on the other hand, they were not ventilated (the case without freshwater fluxes) or slowly ventilated (the case with freshwater fluxes but no NADW recovery) at this time. In addition to providing a larger outgassing of respired CO_2, the depletion of DIC and replacement with more alkaline surface waters in both the Atlantic and Pacific would enhance the ventilation-alkalinity feedback (discussed in Section 3.1.5) as well as the long-term increase in atmospheric CO_2. By setting the stage for a more thorough depletion of respired CO_2 in deep waters globally, freshwater fluxes could explain the increase of $[CO_3^{2-}]$ between the early and late deglacial periods associated with the deep Pacific core in Yu et al. (2010).

The time series plot of depth-integrated mean ocean potential temperature (Fig. 21a) and mean-ocean $\Delta^{14}C$ (Fig. 21b) help define the broad relationship between increasing mean ocean temperature during freshwater fluxes and accelerated ventilation (after the addition of freshwater

fluxes). The buoyancy transfer mechanism through stagnation and slow heat diffusion (as in Meissner et al. 2008) and/or enhanced intermediate water formation in the North Pacific (Huiskamp and Meissner (2012) and the present simulations) provide a mechanism for accomplishing part of the deglacial atmospheric CO_2 trend. Furthermore, the large divergence in mean ocean $\Delta^{14}C$ between the simulations with and without CO_2 radiative forcing (Fig. 21b) is also striking. In particular, in the case of freshwater fluxes, the difference between the simulations with and without CO_2 radiative forcing (~15-22 per mil by 8000 B.C.) is larger than those without freshwater fluxes (Fig. 5b, ~9-10 per mil by 8000 B.C.). This suggests that the strong correlation between SH sea ice extent and CO_2 radiative forcing (introduced in Section 3.1.3) is particularly important when Southern Ocean processes dominate, as is the case during freshwater flushes in the North Atlantic. As a result, decreases in sea ice extent in the Southern Ocean during the Mystery Interval and the Younger Dryas may be especially important for the outgassing documented by ice cores at these times. We thus argue that the climate-carbon cycle feedbacks associated with SH sea ice extent were perhaps disproportionately important during AMOC shutdowns in the North Atlantic during HE1 and the Younger Dryas.

3.3.2: Alkalinity Response to Freshwater Fluxes

The drawdown in the CO_2 during HE1 in the FC HW FW and CO2rad HW FW simulations appears to be largely a result of alkalinity changes over the course of the prescribed freshwater flux. Fig. 22a demonstrates that alkalinity increases at an accelerated rate as compared to the original experiments without freshwater fluxes (Fig. 9a). Figs. 22b indicates, in turn, that the larger increase in alkalinity is related to a reduction in the sediment flux (alkalinity removal) to the ocean floor (and a decrease of living biomass at the surface, Fig. 22c). While

carbonate compensation would work against this increase in alkalinity, the full effect of carbonate compensation requires

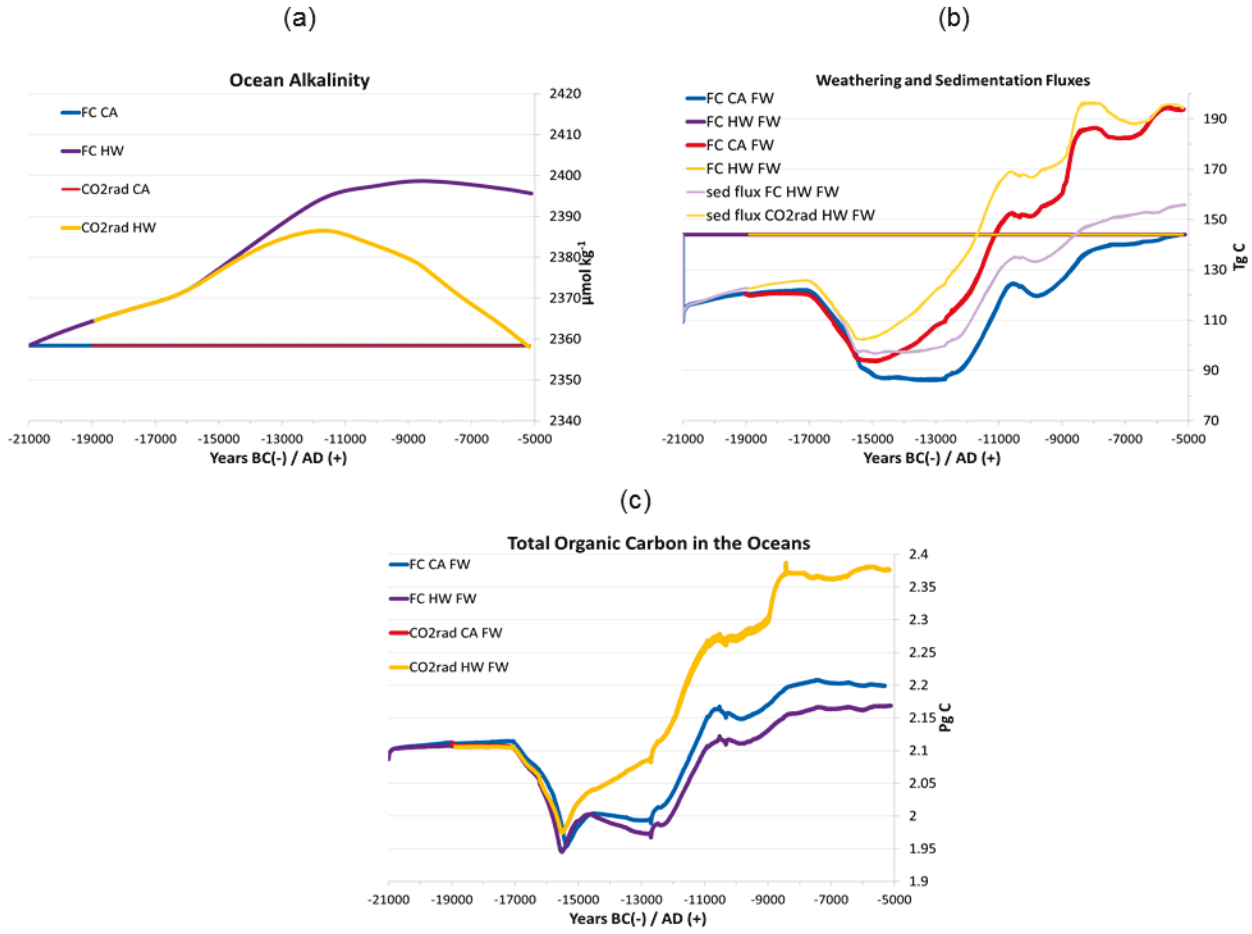

Fig. 22: As in Fig. 17, but for (a) volume-weighted mean ocean alkalinity, (b) weathering and sedimentation fluxes, and (c) total organic carbon (living biomass) in the oceans. The y-axis range used here are different than in Figs. 8-9.

5000-10000 years to complete, longer than the time scale of the Mystery Interval. In addition to a decrease in calcite rain on the ocean floor, higher respired CO_2 content of the slower-circulating deep waters generated in the Southern Ocean (Fig. 29c) also substantially decreased the $[CO_3^{2-}]$ of the entire Atlantic, Indian and Southern oceans (not shown), leading to greater sediment dissolution in these regions as compared to the LGM state.

Schmittner and Galbraith (2008) argued that atmospheric CO_2 should increase during glacial Dansgaard–Oeschger oscillations (AMOC shutdowns) due a weakening of the biological pump. As downwelling in the Southern Ocean generally removes unused (preformed) nutrients from the ocean surface, Schmittner and Galbraith (2008) used the UVic model to show that increasing deep water formation in the Southern Ocean during AMOC shutdowns indeed weakens the biological pump, allowing atmospheric CO_2 to eventually increase in response to reduced marine productivity. In the present study, however, a drawdown in atmospheric CO_2 and an increase in ocean carbon storage was tied to reduced sedimentation at the beginning of HE1.

The somewhat conflicting results between this paper and Schmittner and Galbraith (2008) reveal the highly complex nature of the carbon cycle changes related to freshwater fluxes and deserves further exploration. It should be noted that the time scale of the freshwater flux used here, as well as the initial conditions, are different than in Schmitter and Galbraith (2008). Furthermore, Schmittner and Galbraith (2008) used a version of the UVic ESCM without ocean sediments and did not consider alkalinity changes related to weathering. The HW weathering rate used here (12 Tmol yr^{-1}) is substantially greater than the sediment flux at the beginning of the simulation, and a waning of this flux caused, in turn, an increase of ocean alkalinity on millennial time scales due to the first-order effect of the stronger alkalinity source to the ocean and the slow nature of carbonate compensation to dampen these changes.

A much lower constant weathering rate (lower, in fact, than the LW weathering rate of 10 Tmol yr^{-1}) would be able to cause a decrease rather than an increase in ocean alkalinity over this time period. In this case, the reduction in calcite rain and decreasing alkalinity would work together to increase atmospheric CO_2 during the AMOC shutdown, as modeled by Schmittner and Galbraith (2008). Even so, it could also be argued that the weakening of the biological

pump discussed in Schmittner and Galbraith (2008) may be more relevant to glacial Heinrich events, when the soft tissue pump (non-calcifying diatoms) may play a more important role in the global carbon cycle. In such a case, a reduction in the biological pump would reduce the flux of respired CO_2 to the deep ocean, thus reducing sediment dissolution and enhancing alkalinity removal from the ocean on long time scales. In general, though, the results from the freshwater forcing experiments in this paper concur with the conjecture given in previous sections (for example, Section 3.2.3) and Rickaby et al. (2010), namely that a lower weathering rate than the two (HW and LW) considered here should characterize the early deglacial increase in atmospheric CO_2.

3.3.3: Freshwater Fluxes with a High Latitude Terrestrial Carbon Release

The combination of a high latitude terrestrial carbon release with freshwater fluxes returns slightly less CO_2 to the atmosphere (Fig. 23a) than in the simulations without freshwater fluxes described in Section 3.2. Some of this carbon is returned to the biosphere, as vegetation carbon (Fig. 23b) remains relatively stable and demonstrates smaller losses during HE1 (~20 Pg C or less) compared to the larger decreases documented in Section 3.3.1 above (i.e, without a high latitude carbon release). Regional terrestrial carbon losses (not shown) between the beginning and end of the HE1 freshwater flux were most pronounced in the Sahel and central Asia (as in Handiani et al. 2012a) as well as in parts of central America and the present-day southeastern United States. The reduction in calcite rain due to the freshwater fluxes (reducing the sedimentation flux and alkalinity sinks) with the acidification effect of the permafrost release caused the alkalinity of the deep oceans to increase more than in the earlier freshwater

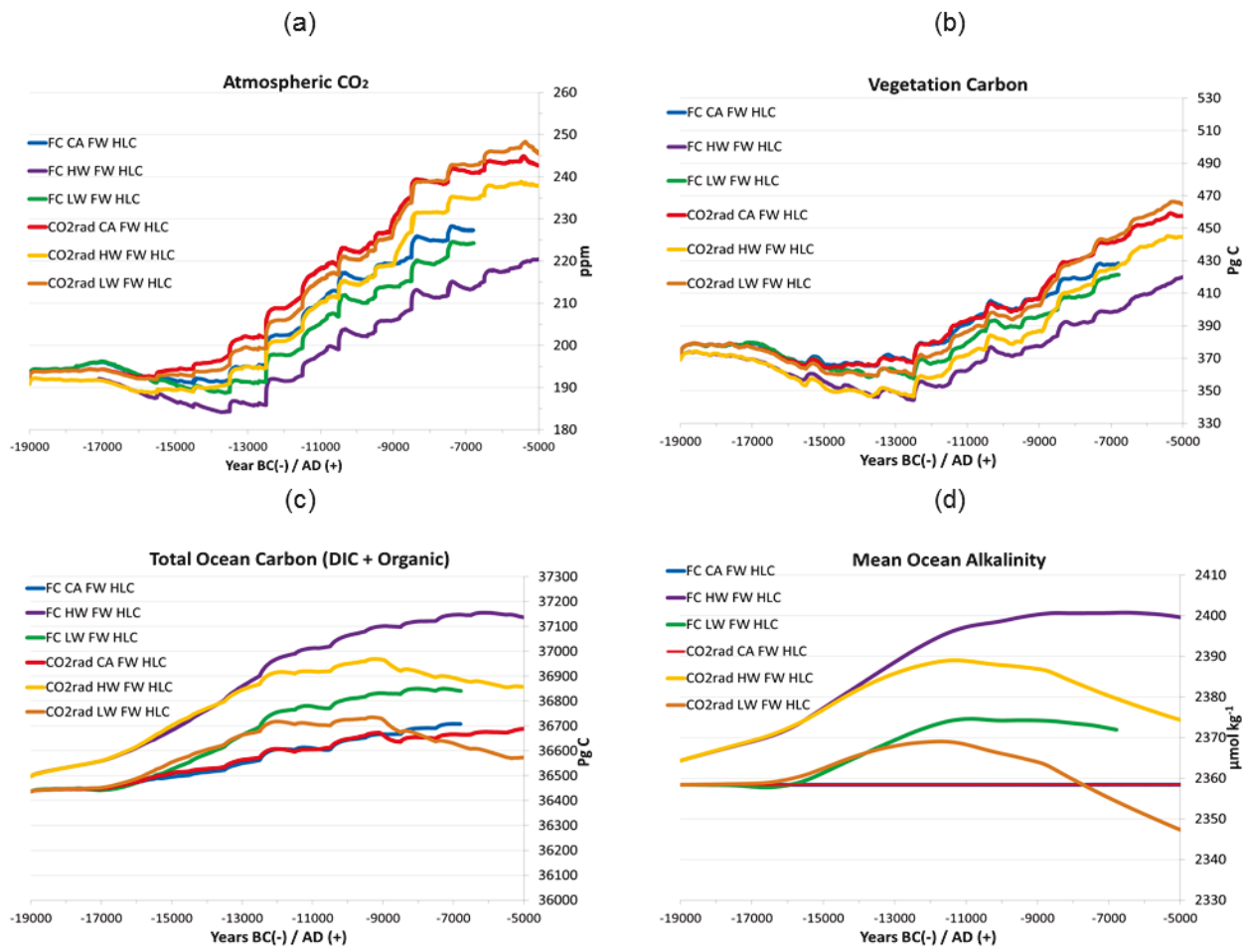

Fig. 23: Selected time series for (a) atmospheric CO_2, (b) vegetation carbon (above-ground biomass), (c) total ocean carbon (inorganic and organic carbon), and (d) average ocean alkalinity for simulations with freshwater forcing and a high latitude terrestrial carbon release. The y-axis ranges for (b),(c), and (d) are different than in Section 3.2 (Figs. 15-16), but the same y-axis scales are maintained.

simulations (Fig. 22a). Even the FC LW FW HLC and the CO2rad LW FW HLC experiments, characterized by decreasing alkalinity after the LGM when performed without freshwater fluxes, yielded a higher alkalinity than during the LGM for the entire deglacial period and early interglacial. The greater alkalinity during deglaciation in the LW simulations thus delays most of the atmospheric CO_2 increase due to terrestrial release until the early-mid Holocene, by which time peatland uptake (not represented in the model) would have been better able to counterbalance these releases. Therefore, in order to account for a more significant increase in atmospheric CO_2 during HE1, it may be possible that the deglacial net weathering rates were

lower than the LW rate considered here, especially during the early part of HE1 when the simulated calcite rain (and permanent sedimentation) was significantly lower than during the LGM. Furthermore, these simulations (more than the freshwater flux simulations without a high latitude carbon release) emphasize the importance of a reinvigoration of North Atlantic overturning to increasing atmospheric CO_2. The combination of a higher ocean alkalinity from reduced sedimentation and a pulse of CO_2 into the ocean (supporting sediment dissolution) caused the oceans to absorb and store a greater fraction of the CO_2 pulse from the terrestrial release. The greater carbon storage in the ocean increases the potential DIC flush associated with a reinvigoration of the NADW from 300 Pg C for the CO2rad HW FW simulation (Section 3.3.2) to 322 Pg C for the CO2rad HW FW HLC simulation. Therefore, it appears that the inclusion of a high latitude carbon release with freshwater fluxes appears to provide a somewhat greater role for the AMOC in the outgassing of deep ocean DIC.

4 Conclusions

In this paper, we presented a suite of simulations using the UVic ESCM v. 2.9 to test the model's transient response to land ice changes, orbital parameter changes, CO_2 radiative forcing, alkalinity (weathering rates), high latitude terrestrial carbon storage, and freshwater flushes from the LGM to the present. In the simulations without high latitude terrestrial carbon storage, we focused on important oceanic processes. These simulations failed to reproduce the full deglacial rise in atmospheric CO_2. Depending on the processes included, we simulated both a decline in atmospheric CO2 of ~10 ppm to an increase of up to 25 ppm. Modeling experiments with only Milankovitch and ice sheet forcing did not produce a full recovery in the Atlantic meridional overturning circulation, leading to higher oceanic carbon storage and the lowest values of atmospheric CO_2 (unchanged or lower than the LGM value, depending on the weathering rate).

Those modeling experiments that included CO_2 radiative forcing produced a more thorough ventilation of the deep ocean and outgassing through the Southern Ocean. This suggests that the warming effect provided by higher atmospheric CO_2 acts as a positive feedback on the deglacial rise in CO_2.

This CO_2-ventilation feedback occurred in the model in response to stronger overturning circulation in the North Atlantic and greater outgassing in the Southern Ocean, both enhanced by reduced sea ice extent. This ventilation of deep-ocean DIC allowed atmospheric CO_2 to increase by ~10 ppm. The corresponding ventilation-alkalinity feedback contributed an additional 10 ppm in our simulations, mostly during the interglacial period due to the downwelling of high-alkalinity, low-DIC waters in the North Atlantic. These circulation features are largely driven by a reorganization of the Atlantic and Indian oceans, where the NADW has greater influence in the model. However, in the freshwater forcing experiments, a substantial warming of the Pacific (through greater diffusive heat transfer to intermediate waters in the region) destabilized North Pacific deep waters following the freshwater flux and allowed them to ventilate earlier than in simulations without freshwater fluxes. This suggests that freshwater fluxes may help provide for a more thorough ventilation of the deep ocean. In terms of alkalinity changes, a comparison with simulations without CO_2 radiative forcing reveals that the CO_2-ventilation feedback in the model may by itself potentially explain deep ocean variations in $[CO_3^{2-}]$ on the order of those provided in Yu et al. (2010) and Rickaby et al. (2010) in the deep Atlantic and Weddell Sea.

The ocean alkalinity and atmospheric CO_2 during deglaciation are also strongly influenced by weathering (~10-15 ppm for the range of weathering rates considered here). When only ice sheets and Milankovitch forcing are prescribed, the total ocean alkalinity was largely driven by the weathering rate, with higher (lower) weathering rates leading to higher alkalinity

and lower (higher) atmospheric CO_2. Only the thorough, early ventilation of deep-ocean DIC that occurred in the CO_2 radiative forcing experiments were able to produce a net lowering of total ocean alkalinity under higher weathering rates. This alkalinity decrease occurred in response to a lower CCD in the Atlantic, Indian, and South Pacific basins in response to stronger NADW formation. The results suggest that an early ventilation event is important for stimulating a decrease in alkalinity during the deglacial and interglacial periods to maintain higher atmospheric CO_2. However, the constant weathering rates used for this experiment assume an equilibrium between weathering and sedimentation for two different points during the LGM (21000 B.C. and 19000 B.C.). Rickaby et al. (2010), on the other hand, suggested that the weathering rate may have been substantially lower than the sedimentation rate during the LGM. This would have resulted in an increased atmospheric CO_2 during the early deglacial period. While the present set of simulations do not model this differentiation in weathering and sedimentation rates during the LGM and early deglacial, they support this hypothesis in three ways:

(1) Lower weathering rates and greater deep ocean ventilation work together to oppose carbonate compensation to allow a net decrease in alkalinity. This provides increases in CO_2 under substantially lower weathering rates.

(2) The oceans in our simulation with a lower weathering rate, CO_2 radiative forcing, and a high latitude terrestrial carbon release absorb a relatively small fraction of the terrestrial carbon released in the simulations, allowing for the CO_2 to build up in the atmosphere (up to ~250-255 ppm for the Holocene).

(3) Less sedimentation during the freshwater forcing experiments led to less calcite rain on the ocean floor (the predominate process in the model to remove alkalinity from

the oceans). This promoted an increase in ocean alkalinity (and greater ocean uptake) and requires a lower weathering rate for this process to be reversed and alkalinity to decrease.

In summary, our results suggest that there are potential oceanic contributors to the atmospheric CO_2 rise during deglaciation:

(1) Lower weathering rates during the early deglacial maintain a slowly increasing atmospheric CO_2 (providing that the sedimentation rate exceeds the weathering rate).

(2) Ventilations of glacial deep water, the reinvigoration of the NADW, and stronger overturning support an outgassing of respired CO_2 from the deep ocean.

(3) Freshwater forcing leads to a diffusive warming of the deep Pacific, providing greater buoyancy to the deep waters in the North Pacific and allowing them to be dislodged more readily after freshwater forcing has ended and the surface ocean begins to become more saline again.

(4) The ventilation of high-CO_2 deep waters and replacement with surface waters with higher carbonate concentrations allows alkalinity to continue to decrease (through greater sedimentation) in the late deglacial and early interglacial period, maintaining the initial increases in CO_2 even as weathering rates increase.

While the four steps together do not account for the full deglacial rise in CO_2 in the simulations presented here, it is possible that our experimental setup does not account for several important processes. In particular, during our equilibrium simulation for the LGM, we removed 366 Pg C of terrestrial carbon from the pre-industrial spin-up that would have otherwise been transferred under the ice sheet. Reconfiguring the model to reapportion this carbon to the oceans and terrestrial biosphere (under fixed CO_2) during the equilibrium simulation would have

increased the DIC content of the oceans and enhanced the ventilation-alkalinity feedback during deglaciation. Furthermore, the downwelling of CO_2 would have increased sediment dissolution and provided an even lower equilibrium weathering rate than the HW and LW rates used here. Huiskamp and Meissner (2012) found that the upwelling of DIC in their simulations for the Mystery Interval could only explain ~58% of the CO_2 rise through ocean processes, perhaps also because of the lack of transfer of terrestrial carbon to the deep ocean in these experiments. A weakened biological pump during NADW shutdowns (with less calcite rain and sedimentation as a result) would also lead to an increase in alkalinity, and thus greater oceanic absorption of atmospheric CO_2. Therefore, the freshwater forcing experiments also require a lower weathering rate than those used here to support an increase in CO_2 during major freshwater purges. Our results thus indicate that a combination of a lower weathering rate and higher initial DIC content of the oceans could allow for a larger early deglacial increase in atmospheric CO_2 than in the present simulations.

Terrestrial processes also provided important contributions to the simulated deglacial and interglacial carbon cycle. Experiments with only CO_2 radiative forcing, ice sheet, and orbital changes produced modest (200-250 Pg C) increases in terrestrial carbon storage from the LGM to the present. Increasing land availability and warmer temperatures were not sufficient mechanisms to stimulate net gains in vegetation carbon, as the lower CO_2 levels (and limited fertilization) led to carbon losses in the tropics and subtropics that compensated for greater carbon sequestration at higher latitudes. Terrestrial releases were particularly pronounced during freshwater flushes. Simulations with prescribed CO_2, in which enough carbon was physically injected into the modeled Earth system to allow CO_2 to follow the ice core trend, produced an increase in terrestrial carbon storage of 600 Pg C, comparable to other recent modeling estimates

(Prentice et al. 2011). Therefore, our simulations suggest that CO_2 fertilization accounts for virtually all of the net vegetation carbon uptake since the LGM. Furthermore, this fertilization effect (when compared to the low fertilization simulations) provided a significant increase in temperatures (0.1-0.3°C) in the tropics and may have strengthened outgassing by warming important upwelling regions and increasing the baroclinic gradient (wind speeds) and coastal upwelling in the subtropics. The introduction of these temperature anomalies into a model with a three-dimensional atmosphere would go further in determining the importance of these fertilization-induced wind anomalies and would be a worthwhile endeavor for future work.

Simulations that included a high latitude terrestrial carbon release of 600 Pg C came much closer to reproducing the deglacial rise in CO_2 (240-250 ppm with CO_2 radiative forcing). Most of this release (300-400 Pg C) was reabsorbed into the (non-peatland) terrestrial biosphere represented in the model, with the rest remaining in the oceans and atmosphere. However, a high latitude carbon release reduced the ventilation-alkalinity feedback when CO_2 radiative forcing was included, and the full ventilation-alkalinity feedback in simulations without CO_2 radiative forcing was delayed until the mid-to-late Holocene. Because a decrease in alkalinity over the course of deglaciation and the Holocene is essential to maintaining increases in CO_2, our simulations suggest a modest early deglacial terrestrial contribution to the CO_2 rise (permafrost, wood burial in glaciers, glacial peatlands, and other forms of passive terrestrial carbon). The ocean (through increased DIC outgassing and low weathering rates) likely accounts for the rest of the Mystery Interval rise in atmospheric CO_2. An early release of terrestrial carbon from permafrost (Zech 2012) and buried wood (Zeng 2007) has been suggested in the literature, and our simulations show that they have significant potential for explaining deglacial increases in atmospheric CO_2. However, additional proxy evidence will be required to justify the timing of an

early release of these carbon reservoirs to the atmosphere during the Mystery Interval and early deglacial.

Supplementary Figures

(a)

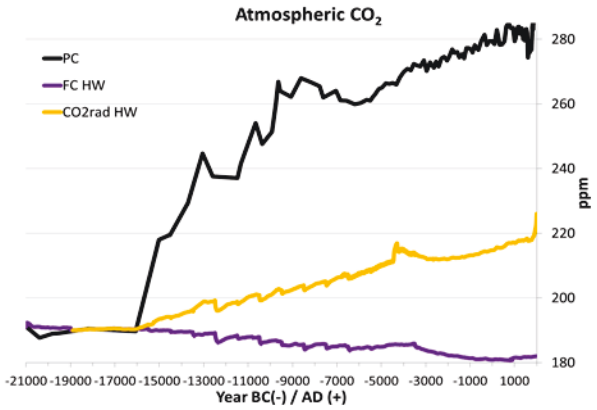

(b)

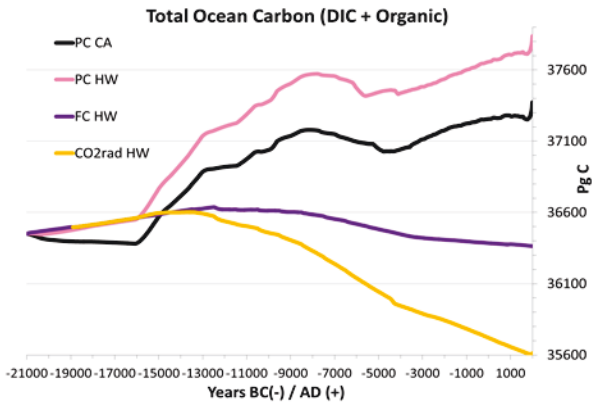

(c)

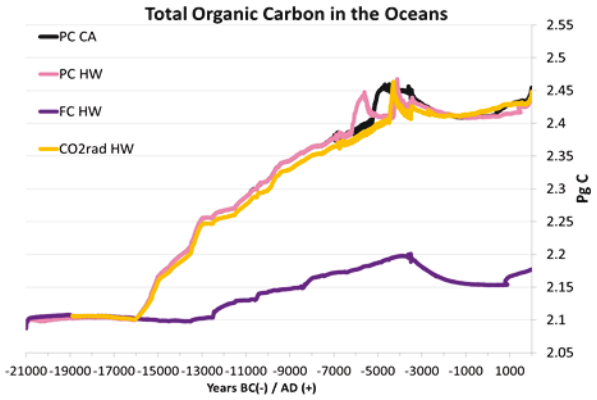

(d)

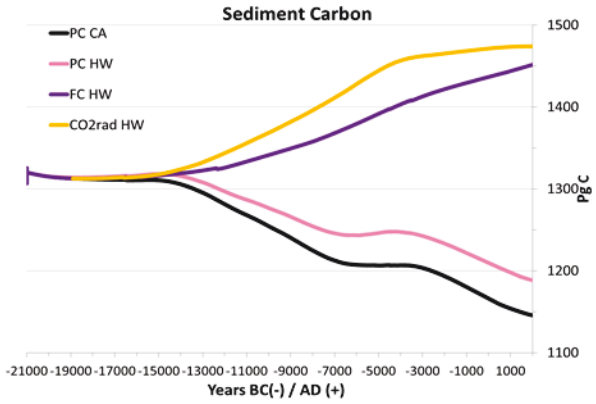

(e)

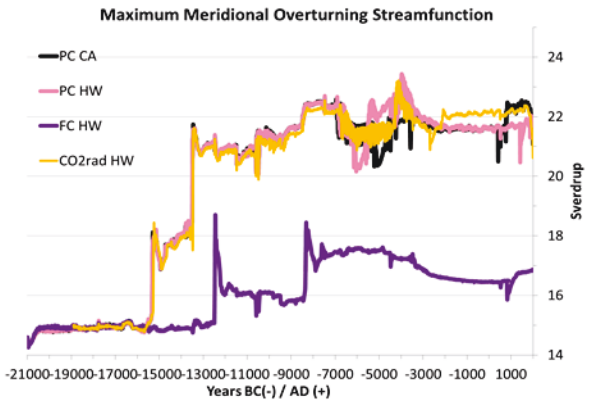

(f)

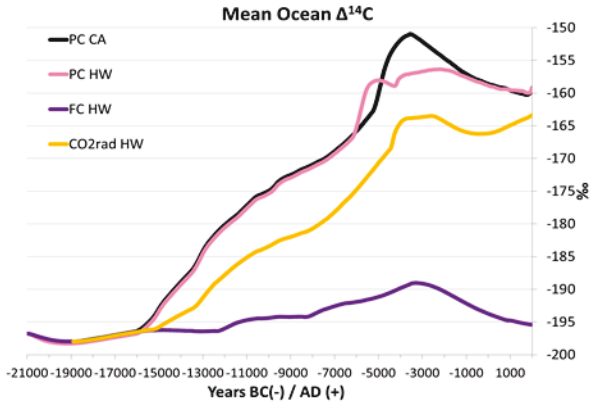

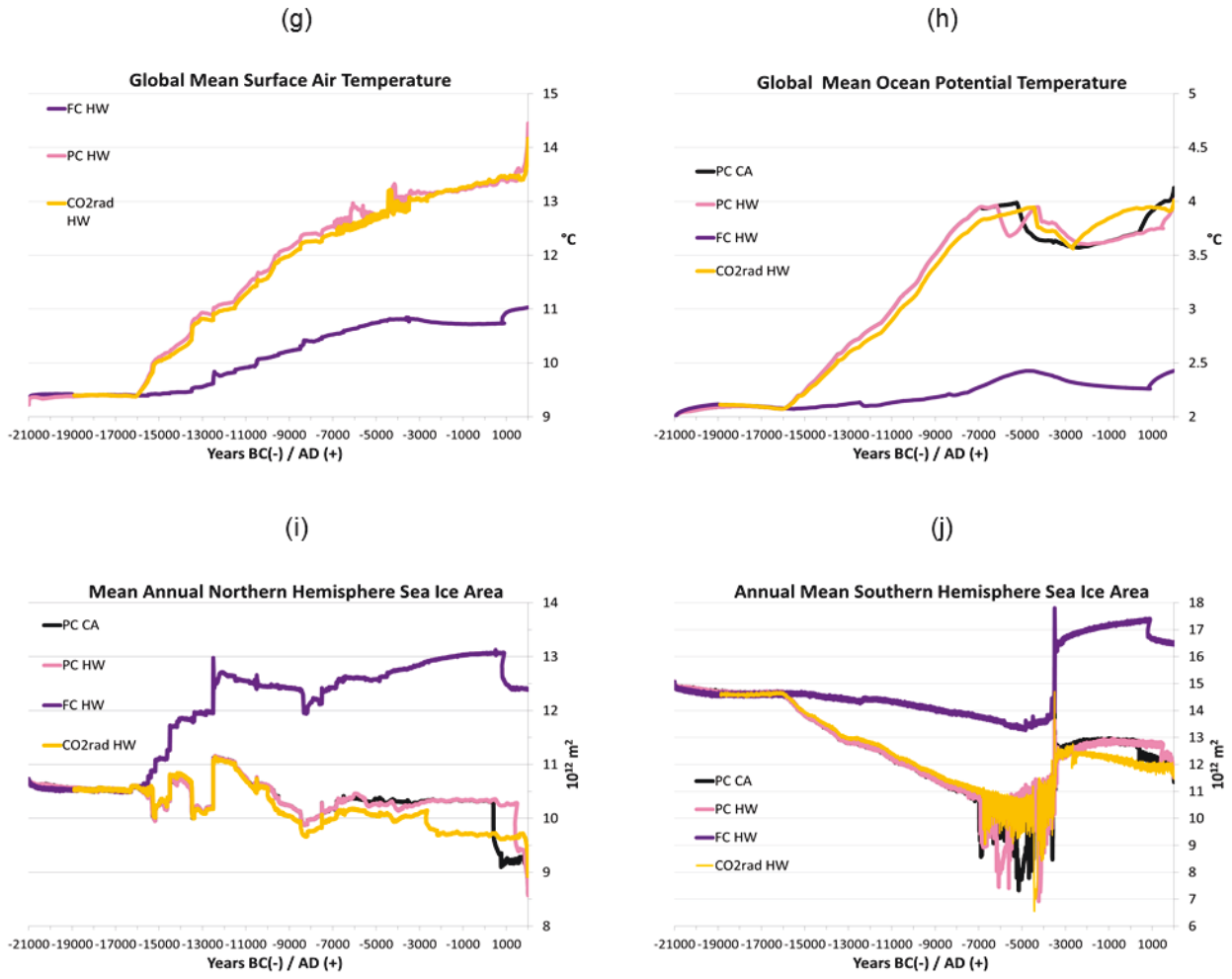

Supplementary Fig. 1: Time series results from the LGM to the present for Prescribed Carbon simulations (a 'Volcanic Release' scenario) PC CA (black line) and PC HW (pink line) set adjacent to the FC HW (purple line) and CO2rad HW (orange line) simulation for a scale comparison with Figs. 1, 5,and 9 in Section 3.1. The plots represent (a) atmospheric CO_2, (b) total ocean carbon, (c) organic ocean carbon (living biomass), (d) total sediment carbon, , (e) global maximum meridional overturning streamfunction, (f) $\Delta^{14}C$, (g) global mean surface air temperature, (h) ocean potential temperature, (i) northern hemisphere mean annual sea ice area, and (j) southern hemisphere mean annual sea ice area.

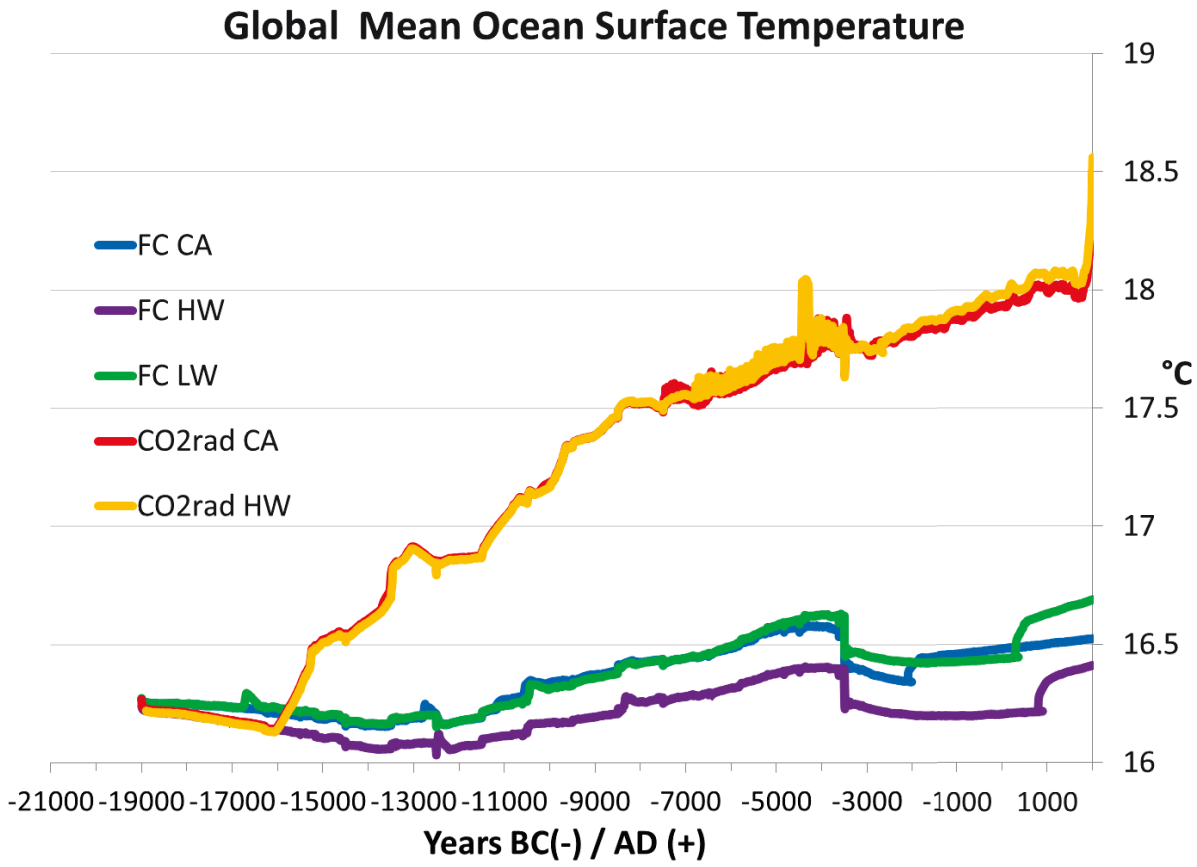

Supplementary Fig. 2: The time evolution of global annual mean ocean surface temperature (on a scale of 16 to 19°C) for the simulations without high latitude carbon.

Chapter 4: Investigation of the Natural Carbon Cycle since 6000 B.C. using an Intermediate Complexity Model: The Role of Southern Ocean Ventilation and Marine Ice Shelves

In addition to exploring the deglacial carbon cycle with the UVic ESCM, we also used the model to explore the climate feedbacks more exclusively associated with the middle and late Holocene. This article, published in the journal *Atmosphere-Ocean*, begins as a review paper synthesizing the Holocene carbon cycle debate and then presents our own modelling contributions to this discussion. These simulations attempted to address the evolution of the natural carbon cycle in response to the hypothesis in Ruddiman (2003) that atmospheric CO_2 should decrease during this period without external influences. Unlike the simulations from Chapter 3, here the mean ocean alkalinity is held constant for all simulations; however, the potential response of alkalinity can be diagnosed from the plotted time series of sediment carbon, with more sedimentation implying a greater alkalinity decrease. Also differing from the transient simulations in Chapter 3, which used an equilibrium simulation for the Last Glacial Maximum as initial conditions, the modeling experiments in this chapter use a different equilibrium simulation derived from constant climate forcing for 6000 B.C. Most of our transient experiments produced a decline in atmospheric CO_2 after 6000 B.C. (as proposed by Ruddiman), although these results demonstrated some sensitivity to the winds used (NCEP vs. wind feedback) and the initial conditions (the ventilation state of deep water in the North Pacific). Perhaps the most intriguing result was the model's significant sensitivity to the extent of Antarctic marine ice shelves, which represent an important contributor to higher late Holocene CO_2 levels.

Abstract

The mechanisms behind the 20 ppm pre-industrial rise in atmospheric CO_2 since 6000 B.C. have been the focus of considerable debate in recent years. Some studies suggest that natural processes, such as a decline in global forests, carbonate compensation, and warming ocean temperatures, can explain the increase in CO_2. Others have argued that, because the CO_2 increase did not occur during previous interglacial periods, it is an indication of an early human influence on the climate. In this paper, we investigate several facets of the natural carbon cycle of the past 8000 years related to ocean circulation patterns and ice shelf configuration using the University of Victoria Earth System Climate Model (v. 2.9), which includes a representation of the climate system with dynamic vegetation and an interactive carbon cycle. The fully simulated earth system for various freely evolving atmospheric carbon scenarios since 6000 B.C. failed to recreate the observed rise in CO_2 and consistently produced a decline in CO_2 throughout the Holocene, in keeping with projections related to previous interglacial periods. However, the extent and timing of the decline was strongly dependent on the initial state of the ocean's meridional overturning circulation and the location of marine ice shelves off the coast of Antarctica. For simulations with ice shelves, carbon-poor North Atlantic Deep Water (NADW) dominated the deep Atlantic basin, with less production of (relatively) carbon-rich deep water from the Southern Ocean. This setup led to lower net ocean carbon storage and thus elevated atmospheric CO_2 levels. These deep water distributions, which are relatively independent of orbital forcing and CO_2 concentrations but strongly dependent on Antarctic marine ice shelves, suggest that greater ice shelf extent during the Holocene relative to previous interglacial periods (Pollard & DeConto, 2009) may have contributed 5–6 ppm CO_2 to the atmosphere. The results from this study also indicate that multi-centennial scale changes in the meridional overturning

circulation on the order of 2–3 Sv may lead to quasi-periodic increases in atmospheric CO_2 concentrations (approximately 6 ppm) through an enhanced ventilation of Pacific deep waters.

1 Introduction: A review of the Holocene carbon cycle debate

In order to understand the response of the Earth's climate to past, present, and future atmospheric carbon dioxide (CO_2) and methane (CH_4) concentrations better, earth system scientists have made a concerted effort to quantify and model the global carbon cycle. Given the complex interplay of short and long time-scale processes and feedbacks between carbon and climate dynamics, it is important to interpret major influences on the carbon cycle adequately in order to evaluate present and future trends. Fortunately, Antarctic ice core records, such as those provided by the Vostok (Petit et al., 1999) and the European Project for Ice Coring in Antarctica (EPICA) Dome Concordia (C) ice cores (Loulergue et al., 2008; Lüthi et al., 2008), have made such an inquiry possible and have been the launching point for recent paleoclimatic studies of atmospheric CO_2 and CH_4 concentrations for the past 800,000 years. The objective of this paper is to evaluate natural controls on the carbon cycle since 6000 B.C. using an intermediate complexity model to help interpret the CO_2 trends in the ice core data.

On shorter time scales, the Taylor Dome Antarctic ice core first provided a higher-resolution reconstruction of CO_2 levels for the past 11,000 years (Indermühle et al., 1999), the period encompassing the Holocene. This record demonstrates a decrease in atmospheric CO_2 by 7–8 ppmv from 9000 to 6000 B.C., followed by an increase of 20–25 ppmv (henceforth ppm) from 6000 B.C. to the end of the pre-industrial era (Indermühle et al., 1999; the data from which are represented in the Prescribed Carbon (PC) simulation in Fig. 6a). Several hypotheses have been put forward to explain these features in the CO_2 record. Modelling and data studies (Indermühle et al. 1999; Joos et al. 2004; Yu 2011) tend to agree that the initial decrease in CO_2 during the early Holocene was a result of vegetation regrowth and peatland uptake over formerly

ice-covered areas. However, the mechanism causing the subsequent increase in atmospheric CO_2 from approximately 260 ppm at 6000 B.C. to the pre-industrial level of approximately 280 ppm is still not well understood (Ruddiman 2008, 2011).

1.1 The Debate over Contributions from Human Land Use

Much scientific debate has focused on the contribution of human land use to the 20 ppm increase in atmospheric CO_2. Ruddiman and Thompson (2001), Ruddiman (2003), and Ruddiman et al. (2011) introduced the idea that changing human subsistence strategies during the Holocene, accompanied by notable increases in population and a transformation of the landscape, have had a significant effect on both CO_2 and CH_4 levels during the middle and late Holocene. Putting together evidence from previous interglacial periods, during which a decrease in CO_2 was observed, Ruddiman (2003) concluded that CO_2 concentrations should have also declined from the early Holocene peak of 268 ppm to a value close to 240 ppm. More recently, Ruddiman et al. (2011) confirmed that the Holocene was unique relative to the previous eight interglacial periods (using both insolation and $\delta^{18}O$ excursion alignment methods) in terms of the substantial, continuous rise in CO_2 starting around 6000 B.C .

Using these analogues to eliminate natural variability as an explanation for the CO_2 increase during the Holocene, Ruddiman (2003) and Ruddiman et al. (2011) suggested human activity as the key contributor to the observed CO_2 increase (the "Early Anthropogenic Hypothesis"). To support this conjecture, Ruddiman (2003) cited pollen and archaeological evidence for forest clearing in China and the Fertile Crescent/Mediterranean basin by 6000 B.C. Because 80% of the CO_2 rise was achieved by the beginning of the Common Era (1 AD), Ruddiman (2003, 2007) also pointed to "great" deforestation by that time in southern and

eastern Asia and the Mediterranean basin, as discussed in Roman chronicles and seen in pollen and erosion records from formerly forested watersheds.

However, the ability of human agricultural activities to contribute substantially to the rise in CO_2 prior to 2000 years ago seems problematic given low global populations (5–250 million) during this period (Boyle et al., 2011). Another major challenge to the early anthropogenic hypothesis has come from the direct mechanistic modelling of human land use and the resulting net carbon release to the atmosphere. Olofsson and Hickler (2008) calculated that the atmospheric CO_2 level would have increased only a few parts per million as a result of a 26 Pg C (petagrams (10^{15} g) of Carbon) net release between 4000 B.C. and 1 A.D., not enough to account for the observed increase in CO_2 of nearly 16 ppm during the Holocene to that point. Using the HistorY Database of the global Environment (HYDE) v. 3.0 with pasture and agricultural land use for 1700 A.D. in the Lund-Potsdam-Jenna Dynamic Global Vegetation Model (LPJ-DGVM), Strassmann et al. (2008) obtained a carbon release of 45 Pg C between their land-use simulation and their spin-up run (potential natural vegetation), determining this to be the maximum pre-industrial release possible (resulting in a CO_2 increase of only a few parts per million when released gradually over the course of millennia). Further, Strassmann et al. (2008) emphasized the importance of enhanced CO_2 fertilization from forests as a negative feedback (a reduction of approximately 25%) to the land-use carbon flux to the atmosphere. Pongratz et al. (2008) developed another land-use database that took into account increased land-use efficiency with time from 800 A.D. to 1992 A.D., the part of the Holocene that witnessed the greatest growth in human population. This dataset was applied to the European Centre Hamburg Model (ECHAM5) atmosphere-ocean general circulation model (AOGCM), and the simulations (Pongratz et al. 2009) produced a 5–6 ppm increase between 800 A.D. and 1850 A.D. Their

extrapolation back in time suggests that early agriculture would have only contributed about 1 ppm of the observed 16 ppm rise in CO_2 between 6000 B.C. and 1 A.D.(Pongratz et al. 2009).

Each of these modelling studies assumes that land-use efficiency before 1 A.D. remained roughly constant or increased conservatively with time, often projecting more recent data from the Middle Ages and the present day back to 6000 B.C. (land-use efficiency at 0.16–1.3 ha per person). The Boserup Hypothesis (Boserup 1965), as elaborated in Ruddiman and Ellis (2009), challenges these low estimates of the contribution of human land use to the 20 ppm increase. In particular, low land-use efficiency during the neolithic period (4 ha per capita or greater land use) likely provided a greater per-person carbon flux to the atmosphere than modern agriculture (closer to 0.16 ha per person) as a result of the cruder technologies used in early farming.

In order to address this challenge, land-use scenarios adapted from HYDE 3.1 (Klein Goldewijk et al. 2011) were incorporated mechanistically into the Bern Carbon Cycle (CC) model (containing the LPJ-DVGM) in Stocker et al. (2011). Their results suggest that even extreme terrestrial releases would not have been significant enough to reproduce the Holocene atmospheric CO_2 trend, leading to a contribution of only 6 ppm by 1 A.D.. However, an alternative land use scenario of early Holocene populations summarized in Kaplan et al. (2011) places mid-Holocene land use efficiency between 5.5 and 8 ha per capita (depending on the region) with greater agriculture-related soil carbon depletion than applied in Stocker et al. (2011). This database applied to the LPJ -DVGM suggests much higher anthropogenic emissions (325–357 Pg C) than previous estimates (Kaplan et al. 2011). By constrast, Boyle et al. (2011) proposed a smaller neolithic land-use efficiency nearer to 1.96 ha per person (based on a combination of archaeological evidence and human dietary requirements). However, the authors further indicated that global population estimates during the neolithic period could have been an

order of magnitude greater (near 100 million) than that proposed by McEvedy and Jones (1978) (closer to 10 million) used as the basis for most human land-use databases, including some regions in Kaplan et al. (2011). In short, given the complexity and uncertainties in reconstructing pre-industrial human land use (both in terms of global population and land-use efficiency) and the wide range of emissions estimates (from 48 to 357 Pg C), the contribution of agricultural activities to the Holocene carbon cycle remains an open question (Ruddiman et al. 2011).

1.2 Natural Explanations of the Holocene Trend

Various hypotheses involving the natural carbon cycle, however, have also been put forward to explain the pre-industrial Holocene increase in CO_2. Indermühle et al. (1999) suggested a natural vegetation release of carbon associated with the drying of the Sahara and declining solar insolation in the northern hemisphere (see Claussen (2009) for a recent review). In their comprehensive model study of the Holocene, Schurgers et al. (2006) also attributed the CO_2 increase of 10 ppm to a terrestrial release. However, Wang et al. (2005) found that the flux of carbon to the atmosphere from North Africa was compensated for by the simulated growth of vegetation with increasing solar radiation in the southern hemisphere. Furthermore, several previous modelling studies (summarized in Joos et al. 2004) produced estimates ranging from a 90 Pg C release to a 370 Pg C uptake, indicating significant uncertainty in the role of natural vegetation.

Addressing the peatland question, Wang et al. (2009) incorporated the carbon accumulation of northern peatlands into the Green McGill Paleoclimate Model (MPM) and proposed that peatlands alone could account for a natural 160–280 Pg C terrestrial sink for the atmosphere since 6050 B.C. Since then, Yu et al. (2010) have provided a more exhaustive compilation of peat basal dates globally and “conservatively” estimated that northern peatlands

alone accumulated 547 Pg C during the Holocene, with tropical wetlands and Patagonian peatlands taking up 50 Pg C and 15 Pg C, respectively. Yu (2011) further calculated that a net accumulation of 267 Pg C should have led to a 19 ppm decrease in atmospheric CO_2 since approximately 6050 B.C. Furthermore, removal of carbon from the atmosphere was likely greater (87.9 Tg yr^{-1} from approximately 7000 to 6000 B.C.) during the early and mid-Holocene than during the late Holocene (16.3 TgC yr^{-1} from approximately 1000 B.C. to 1 A.D.) because of delayed decomposition of previously accumulated peat, perhaps helping to explain the accelerated decrease in CO_2 during the early Holocene as well as a gradually decreasing impact of peatlands on atmospheric CO_2 over thousands of years. This would thus allow atmospheric CO_2 to rise under the influence of other natural or anthropogenic contributors.

Another hypothesis proposes that an increase in mean oceanic sea surface temperature (SST) during the Holocene would have led to a release of CO_2 to the atmosphere. This interpretation was partly validated by Joos et al. (2004) who imposed a global SST warming of 0.6°C as a boundary condition in their model and obtained a 4–5 ppm increase in CO_2. Ruddiman et al. (2011) also attributes 9 ppm to the temperature–solubility relationship. However, proxy data based on near-coastal alkenone (Kim and Schneider 2004) suggest that the North Atlantic Ocean, an important region for transporting atmospheric CO_2 to the deep ocean, cooled with declining summer solar insolation in the late Holocene while other basins warmed. A modelling study using an AOGCM and an accelerated orbital forcing (Lorenz et al., 2006) yielded a similar trend in cooling (on the order of 1°–2°C) for the North Atlantic basin. Brovkin et al. (2008) also suggested that cooling in the critical North Atlantic region may have intensified overturning in this region, leading to faster uptake of CO_2 by the deep ocean in North Atlantic deep water (NADW). This regional cooling (stimulating greater CO_2 uptake) in the model is

stronger than the surface warming (associated with CO_2 release) in other basins and thus dominates the global carbon cycle, leading to a 1–6 ppm global net decrease (sink) of CO_2 rather than the net source postulated in Joos et al. (2004). However, Brovkin et al. (2008) did not address processes in the Southern Ocean, where Ruddiman (2007) and Vavrus et al. (2008) argue that the effects from mid-Holocene anthropogenic activities may have warmed the sea surface and reduced sea ice during the late Holocene, thereby increasing air–sea exchange with the atmosphere leading to a substantial CO_2 net release of 20–24 ppm. Whether anthropogenically or naturally induced, deuterium in ice core records suggests that the Antarctic climate was unusually warm during the Holocene compared with other interglacial periods, and this might have had important feedbacks on overturning in this region (Ruddiman et al. 2011).

Another interpretation of the positive CO_2 anomaly during the Holocene relates to ocean carbonate compensation and coral reef growth (Broecker et al., 1993; Archer and Maier-Reimer 1994; Broecker et al., 2001; Broecker and Clark, 2003; Broecker and Stocker 2006). Because the terrestrial biosphere (expanding forests and peatlands during deglaciation) extracts carbon from the sea surface, a deepening of the lysocline (associated with a downwelling of waters with less CO_2) should eventually lead to greater calcite deposition, reduced solubility of CO_2 in the oceans, and a corresponding recovery in atmospheric CO_2. Another way of achieving this chemical transformation of the ocean is through upslope tropical coral reef migration in response to postglacial sea level rises (Ridgwell et al. 2003).

A number of modelling studies also lend strong support to the ocean chemistry hypothesis (Brovkin et al. 2002; Joos et al. 2004; Ridgwell et al. 2003; Elsig et al. 2009; Kleinen et al. 2010), albeit with a fairly large uncertainty regarding the oceanic carbon release. According to the BERN CC simulations by Joos et al. (2004), carbonate compensation from terrestrial

sequestration may have accounted for a 4–10 ppm ocean release, which explains about 25 to 50% of the rising Holocene CO_2 levels. Similarly, Elsig et al. (2009) proposed that 6 ppm CO_2 came from carbonate compensation (associated with terrestrial uptake) and 5 ppm from coral reef growth. On the other hand, Kleinen et al. (2010) suggested that carbonate compensation has little impact on the Holocene trend, with a pre-industrial atmospheric CO_2 concentration of only 257 ppm when only carbonate compensation and atmosphere–vegetation (non-peatland) carbon exchanges are considered in the CLIMate and biosphERe Model- Lund-Potsdam-Jenna (CLIMBER-LPJ) model. However, even with peatlands (a net 105 Pg C uptake in their simulation), Kleinen et al. (2010) was able to approximate the Holocene carbon trend (to 278 ppm) with the inclusion of shallow water sediments (partly an approximation for coral reefs). However, Kleinen et al. (2010) also noted that the reduction in ocean alkalinity that produced this increase in CO_2 was much greater than that calculated by Broecker et al. (1999) and that a forced terrestrial release would be required to explain the model's divergence in $\delta^{13}C$ from the observed trend after approximately 550 B.C.

More recently, Goodwin et al. (2011) proposed that a reduction in the soft tissue (organic carbon) pump to the deep ocean, possibly in conjunction with a sedimentation event, could explain much of the Holocene carbon trend when taking into account $\delta^{13}C$ in both ice cores (representing atmospheric carbon isotope fractionation) and marine sediments (dissolved inorganic carbon in benthic foraminifera, documenting deep-ocean carbon isotope fractionation). In particular, a synthesis of data in Goodwin et al. (2011) from mostly western Pacific sources supports the idea that deep water $\delta^{13}C$ was increasing during the Holocene, which suggests that less organic carbon (strongly negative fractionations of $\delta^{13}C$) was being transported to the deep ocean. Correspondingly, Menviel and Joos (2012) showed that the Bern3D+C model can

reproduce the Holocene CO_2 increase and the $\delta^{13}C$ trend from Elsig et al. (2009) with shallow water sedimentation (4.8 ppm), SST warming (1.6 ppm), sediment interactions (ventilation-alkalinity feedbacks related to CO_2 radiative forcing following glacial termination) (~5 ppm), and CO_2-alkalinity feedbacks (10.3 ppm in response to terrestrial uptake since termination).

1.3 Arguments on the Holocene Carbon Cycle Based on $\delta^{13}C$

Many studies, including Goodwin et al. (2011), point to the small $\delta^{13}C$ excursions of 0.2 ‰ (ppt) in Taylor Dome (since 5000–6000 B.C.) and an even smaller 0.05 ‰ (since 4000 B.C.) decrease in the higher-resolution EPICA ice core (Indermühle et al. 1999; Elsig et al. 2009; Schmitt et al. 2012) as evidence that a major terrestrial release did not occur during the late Holocene. Because the biosphere generally prefers the ^{12}C over the ^{13}C carbon isotope, most vegetation carbon (and biological carbon generally) has a negative $\delta^{13}C$ fractionation, and a release of terrestrial carbon to the atmosphere would accordingly lead to a measurable decrease in $\delta^{13}C$ in the atmospheric CO_2 value obtained from ice cores. Based on this simple assumption, Joos et al. (2004) calculated that a decrease of 0.6 ‰ in $\delta^{13}C$ would be required for a 40 ppm human land-use contribution, well above the uncertainty in measured $\delta^{13}C$ fractionation of CO_2 in ice cores, suggesting that the carbon flux that led to the 20 ppm increase in atmospheric CO_2 during the Holocene came from an ocean source (with approximately 0.0 ‰ $\delta^{13}C$ fractionation).

Challenges to this interpretation, however, have come to light in recent studies on high-latitude carbon cycle dynamics. In particular, Zimov et al. (2009) noted that permafrost covered large parts of Siberia, North America, and Europe during the Last Glacial Maximum (LGM). As a result of slow cooling leading up to the LGM, more and more carbon litter was frozen into the permafrost layer over the course of 100,000 years (Zimov et al. 2009). With ice sheet retreat and warming, the permafrost disappeared in many areas or retreated to greater soil depths in others,

exposing large quantities of carbon to decomposition and a reduction of 36–46 kg C m^{-2} in the permafrost system. This implies a release of more than 1000 Pg C to the atmosphere (Zimov et al., 2009). Similarly, Ciais et al. (2012) compared fractionation of ^{16}O and ^{18}O in ice cores, which suggests global photosynthesis (GPP) approximately 57% of its pre-industrial value during the LGM; however, global carbon stocks (from $\delta^{13}C$ changes in ice cores and marine sediments) imply a terrestrial carbon reservoir during the LGM of only 330 Pg C (approximately 8%) less than during the pre-industrial period. The authors thus inferred that the non-photosynthizing fraction of biological carbon (approximately 700 Pg C) is likely dominated by inert storage in permafrost, which would have been released during deglaciation.

Within the context of a permafrost release, the $\delta^{13}C$ of dissolved inorganic carbon (DIC) in benthic foraminifera does not demonstrate a $\delta^{13}C$ decrease during the late Pleistocene or early Holocene (which would indicate a flux of organic carbon to the deep ocean via the atmosphere). In fact, an overview of data from several ocean basins in Oliver et al. (2009) indicates an increase of 0.4–1.0 ‰ from the LGM to 5000 B.C. in the Atlantic basin and an increase of 0.1–0.4 ‰ in the Pacific and Indian oceans, whereas Ciais et al. (2012) calculated a global marine (benthic) $\delta^{13}C$ increase of 0.34±0.13 ‰ from the LGM to the pre-industrial period. Zimov et al. (2009) thus assumed that a permafrost release may have been taken up by terrestrial vegetation, with the fraction absorbed by the ocean balanced by a reduction in the soft carbon pump (transfer of sea-surface biological carbon to the deep ocean) or faster ocean ventilation during the late Pleistocene and early Holocene than during the LGM. A gradual release of permafrost carbon over this period may have transferred more of this carbon from the permafrost to northward-expanding forests and peatlands (experiencing accelerated accumulation during the early Holocene) instead of into the ocean, leading to a lower net biosphere extraction of CO_2 from the

atmosphere–ocean carbon reservoir and reducing the role of carbonate compensation in the Holocene CO_2 increase (Kleinen et al. 2010; Ruddiman et al. 2011).

At the beginning of the Holocene, slowly increasing atmospheric $\delta^{13}C$ (approximately 0.2 ‰ SST-corrected $\delta^{13}C$ between 10000 B.C. and 4000 B.C. in Schmitt et al. (2012)) and marine $\delta^{13}C$ have been linked to terrestrial uptake, in concert with contributions from changes in ocean circulation and oceanic biological production (Schmitt et al. 2012). Later during the middle and late Holocene, the substantial terrestrial uptake of peat (extracting ^{12}C from the atmosphere) documented in Yu (2011) should have led to increasingly positive $\delta^{13}C$ in atmospheric CO_2 from ice core records instead of the slight decrease seen in Indermülhe et al. (1999) and Elsig et al. (2009). In assuming that a virtually constant $\delta^{13}C$ implies little release from the terrestrial biosphere, Joos et al. (2004) and Elsig et al. (2009) may have substantially underestimated the positive $\delta^{13}C$ contribution from peatland uptake (Yu 2011). Using the new peatland estimates established in Yu (2011), a terrestrial release on the order of 23–24 ppm (or 330 Pg C) would be needed to counterbalance the peat uptake and the $\delta^{13}C$-implied atmospheric CO_2 increase of 5 ppm from terrestrial sources, which likely stems from natural (monsoon weakening and retreat of boreal forests) or anthropogenic (human land use) causes (Ruddiman et al. 2011).

1.4 The Contribution of the UVic Model to the Holocene Carbon Cycle Debate

In this study, we use an intermediate complexity climate model to test the hypotheses involving terrestrial carbon release, sea surface temperature, and meridional overturning controls on the carbon cycle. We present simulations of the entire period of CO_2 increase (from 6000 B.C. to 1850 A.D.) using the University of Victoria Earth System Climate Model (UVic ESCM) version 2.9. The model includes a fully interactive terrestrial, atmospheric, and oceanic

(organic/inorganic/sediments) carbon cycle, which represents coupling and feedbacks that occur between the atmosphere, ocean, and biosphere. While the Holocene has been modelled with other intermediate-complexity models, this is the first time that this period has been extensively investigated using the UVic ESCM in continuous, fully interactive transient simulations. Furthermore, some previous studies of the Holocene climate (e.g., Renssen et al. 2005; Schurgers et al. 2006) assume unchanging pre-industrial land ice for the entire Holocene, whereas our simulations test the sensitivity of the climate system to changing ice sheets and in particular to marine ice shelves.

It is important to emphasize that these experiments only model the natural carbon cycle and potential natural vegetation changes (with no incorporated anthropogenic land use). Furthermore, the UVic ESCM does not presently include wetland or peatland processes or the upslope growth of coral reefs with increasing sea level. Without addressing these issues and their uncertainties, the UVic ESCM experiments provide mostly an investigation of carbon transport through physical ocean dynamics, a factor not investigated in studies such as Kleinen et al. (2010), and the effects of different ice shelf distributions. Our results suggest that the coupling between the carbon reservoirs changes substantially for different ocean thermohaline circulation states and land-ice configurations and that these would thus likely have a notable influence on how much CO_2 from human land-use emissions or other carbon sources remains in the atmosphere on millennial time scales.

The following sections are structured as follows. First, we give a description of the UVic model (Section 2), then we provide the experimental set-up (Section 3.1), results for the model spin-up for 6000 B.C. (Sections 3.1 and 3.2), and the set-up for transient simulations (Section 3.3). In Section 4.1, we evaluate the sensitivity of the carbon cycle to partial and complete

ventilations of stagnant North Pacific deep water, and in Section 4.2 we present the results of transient simulations in which the atmospheric carbon is allowed to evolve freely from 6000 B.C. to the end of the pre-industrial era. In Section 4.3, we compare the result of these experiments with transient runs in which atmospheric CO_2 is prescribed from observed ice core data, and in Section 4.4 we investigate the sensitivity of the vertical circulation of the oceans and deep ocean carbon storage to Antarctic ice shelf extent. Finally, Section 5 affords a discussion of the limitations of our model and methodology, and in Section 6 we present our major conclusions.

2 Model Description

The UVic ESCM 2.9, classified as an Earth system Model of Intermediate Complexity (EMIC) (Claussen et al., 2002), has been gradually built up from the original UVic model described in Weaver et al. (2001). Since its development, the UVic ESCM has been employed in a number of climate modelling efforts, including Fourth Assessment Report of the Intergovernmental Panel on Climate Change (IPCC) (Meehl et al., 2007) and the Coupled Climate-Carbon Cycle Intercomparison Project (C^4MIP) (Friedlingstein et al., 2006). Furthermore, the UVic model (and its incorporated Top-Down Representation of Foliage and Flora Including Dynamics (TRIFFID) dynamic global vegetation model) has also already been used previously to investigate land-use impacts on climate over the past three centuries (Matthews et al. 2004). They showed that the total effect of land-use change for the above period was an increase in global temperature of 0.15°C. The research presented in this paper extends the application of the UVic model to include most of the Holocene epoch (but without land use).

The core components of the model representing the atmosphere (a one-layer Energy Moisture Balance Model (EMBM) calculated every 15 hours) and the ocean (the 3D Modular Ocean Model general circulation model (GCM) v. 2.0, with 19 layers, calculated every 30 hours

for tracers and every 18.75 minutes for barotropic and baroclinic velocities) were coupled in Fanning and Weaver (1996) and refined in Weaver et al. (2001). Coupling between the atmosphere and the ocean occurs every five model days. Moisture advection in the model relies on prescribed winds, and in this study climatological winds from the National Centers for Environmental Prediction (NCEP; Kalnay et al., 1996) were used. However, in order to test the robustness of using twentieth century winds in our simulations, all experiments were repeated with the model's wind feedback mechanism, which adjusts the NCEP wind climatology according to the real-time model-generated air temperature field (Weaver et al., 2001). Isothermal land ice and thermodynamic–dynamic sea ice was also included in the original model (Weaver et al. 2001). Land ice was prescribed in the model according to ICE-4G in Peltier (1994); it contributes no freshwater pulse to the ocean as it melts, and where it extends over the ocean in the form of ice shelves, it simply acts as an insulating lid with no latent heat exchange with waters below or beside it.

To represent the terrestrial biosphere, the TRIFFID dynamic global vegetation model (Cox 2001) was adapted to the UVic Model (Meissner et al., 2003; Matthews et al., 2005). This module generates five plant functional types (PFTs), including broadleaf trees, needleleaf trees, C_3 (mid- and high-latitude) grasses, C_4 (mainly tropical) grasses, and shrubs (or small trees), which each grow under specified bioclimatic (temperature and precipitation) conditions. Where more than one PFT can grow, a dominance hierarchy (based on canopy height) prefers trees to shrubs and shrubs to grass, with grass types and tree types competing with each other (see Cox (2001) for more details). The TRIFFID model also includes a one-layer soil carbon model (depth 1 m) driven by biomass input and microbial respiration. Primary production and the resulting

carbon fluxes between the land and the atmosphere are calculated by a version of the Met Office Surface Exchanges Scheme (MOSES; Cox et al. 1999; Meissner et al. 2003). The oceanic

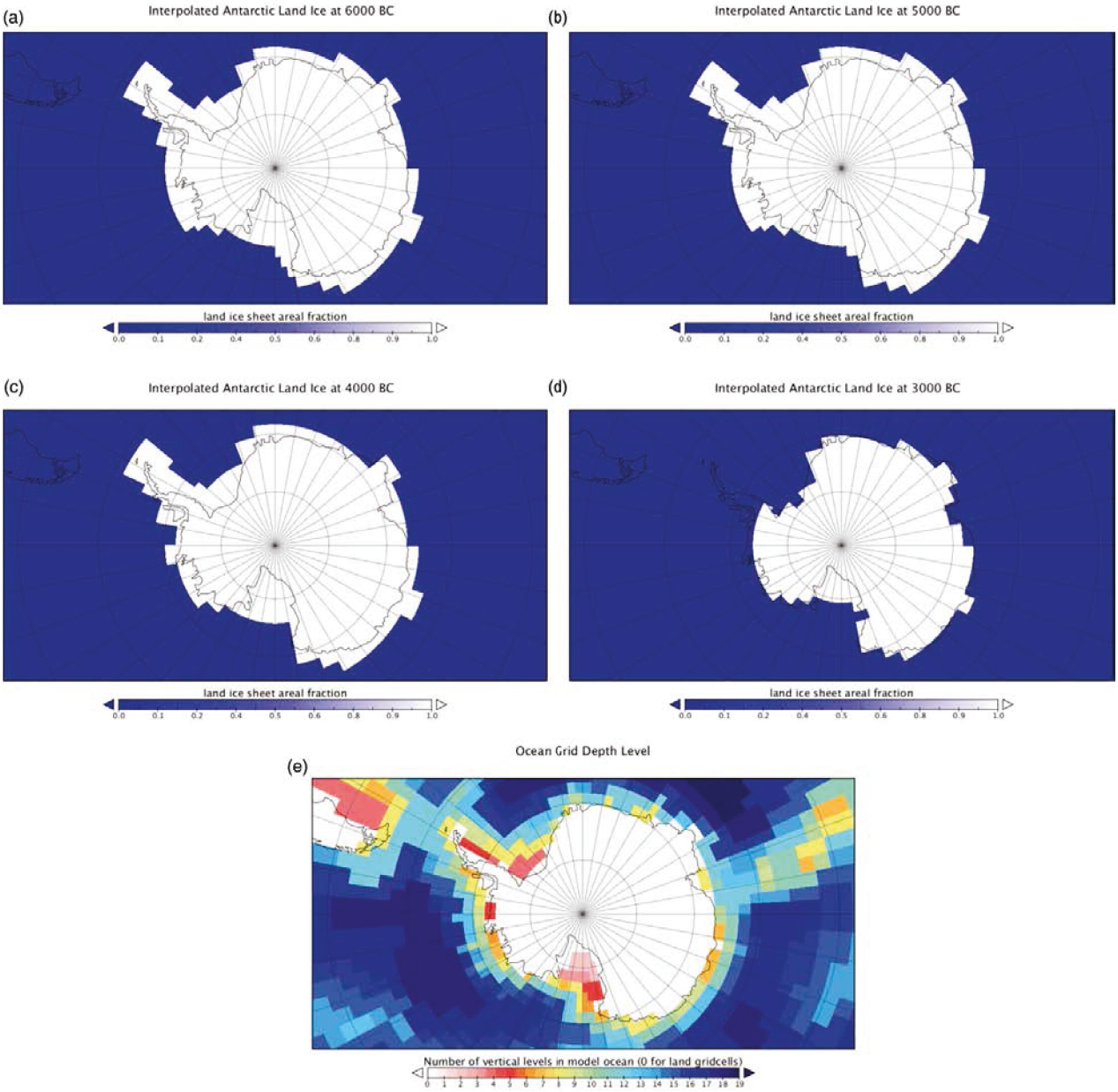

Fig. 1: Ice sheet distributions around Antarctica for (a) 6000 B.C., (b) 5000 B.C., (c) 4000 B.C., and (d) 3000 B.C. according to ICE-4G (Peltier et al. 1994) interpolated to the resolution of the UVic ESCM. The model's land–ocean boundaries around Antarctica are provided in (e).

carbon cycle module was added by Schmittner et al. (2005); this is a classic nitrate-phytoplankton- zooplankton-detritus (NPZD) model with dissolved organic matter and including

diazotrophs for nitrogen fixation (but lacking iron limitation). Inorganic carbon, ocean sediment deposition and dissolution, and the evolution of the lysocline occur as in the model developed in Archer (1996), which includes only the oxic respiration of sediments (Eby et al. 2009). Because there is no comprehensive weathering module in the model, the land-to-ocean weathering rate was diagnosed by the sediment burial flux for the simulations presented in this paper. This results in constant ocean alkalinity and no contribution from carbonate compensation in order to explore purely physical mechanisms leading to carbon cycle changes.

For all subcomponents, the model operates on a 1.8° x 3.6° (latitude-longitude) horizontal grid (Weaver et al. 2001). The model simulations presented here (see Table 1) are performed with the carbon cycle "online" with respect to the climate system, so that the two evolve interactively and the sum total of all feedbacks is considered.

3 Equilibrium simulations and transient simulation Set-up

3.1 The Model Spin-up for 6000 B.C.

To spin-up the model to an equilibrium state, the UVic ESCM 2.9 was run for more than 10,000 model years, forced with the ICE-4G land-ice configuration (e.g., Fig. 1a) (Peltier, 1994), orbital forcing (Berger, 1978), and carbon dioxide (260.2 ppm) (Indermühle et al. 1999) all fixed at their 6000 B.C. configuration. Moisture advection and wind stress over the ocean were determined by winds from the NCEP reanalysis climatology (Kalnay et al. 1996). This simulation will henceforth be called EQ_1 (see Table 1, which describes the other equilibrium and transient simulations discussed in this study). With all forcing mechanisms being time independent, a stable equilibrium was expected to evolve. However, even with the assigned parameters, the model never reached a steady state. Instead, the meridional overturning

circulation (MOC) weakened (by approximately 4–5 Sv (where 1 Sv = 10^6 m^3 s^{-1})) and rebounded in an oscillatory fashion as shown in Fig. 2a. Many other prognostic variables also

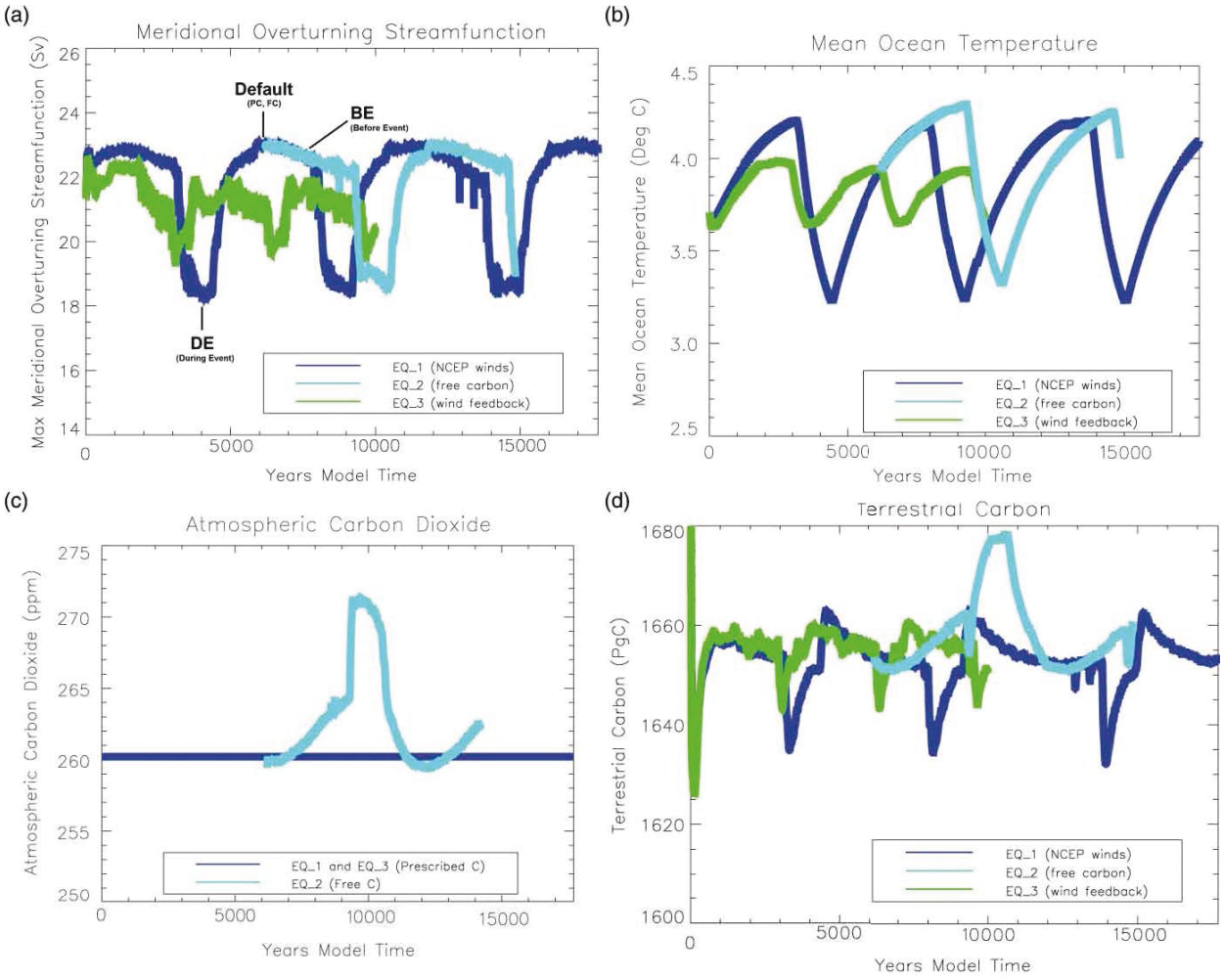

Fig. 2: Selected results from EQ_1 (spin-up for 6000 B.C., fixed atmospheric carbon), EQ_2 (spin-up for 6000 B.C., free atmospheric carbon), and EQ_3 (spin-up for 6000 B.C., fixed atmospheric carbon, wind feedback). In (a), the global maximum meridional overturning streamfunction (Sv) for the oceans is shown for all three simulations, and (b) illustrates mean depth-integrated ocean temperature (°C) for the same simulations. (c) shows the atmospheric carbon dioxide, and (d) illustrates the evolution of terrestrial carbon.

exhibited these multi-millennial oscillations (such as mean depth-integrated ocean temperature and terrestrial carbon (see Figs 2b and 2d)).

In order to determine the interactive exchange between the carbon cycle and the different thermohaline circulation states, another simulation (EQ_2), starting from Model Year 6200 of EQ_1, was performed with freely evolving atmospheric carbon but with land ice, winds, and

orbital forcing kept fixed as in EQ_1. Despite changing atmospheric CO_2, this new simulation also produced millennial-scale oscillations in the MOC, which resulted in a 12 ppm CO_2 fluctuation in the atmosphere over about 4000 years (Fig. 2c).

In EQ_2, a similar terrestrial carbon release (approximately 7 Pg C) occurred in the first hundred years of the flush, initially helping to propel atmospheric CO_2 concentrations upward. However, for the following 1000 years in EQ_2, the terrestrial carbon reservoir quickly rebounded and exceeded its original level by 15 Pg C. This indicates that the elevated atmospheric CO_2 for nearly 1000 years during the millennial-scale events in the equilibrium simulation were exclusively the consequence of a slow, thorough flushing of deep ocean carbon to the atmosphere, which in turn fertilized the biosphere.

3.2 A Conceptual Model of Southern Ocean Flushing Events

On running the UVic ESCM (v. 2.8), Meissner et al. (2008) discovered a similar intermillennial MOC oscillation in several equilibrium simulations under present-day forcing conditions. In their study, atmospheric CO_2 concentrations were kept constant for separate simulations, taking values between 360 ppm and 720 ppm. All simulations with fixed CO_2 levels over 400 ppm demonstrated these flushing events (total MOC weakening), with the periodicity of these deep-ocean ventilations dependent on the level of prescribed atmospheric CO_2. Furthermore, each flush was associated with deep water ventilation and a simultaneous decrease in sea-ice extent near Antarctica. This was subsequently followed by long periods of extensive sea ice and strong sea surface stratification, which served to prevent ventilation through the Southern Ocean. Changes in sea-ice extent, albeit on a shorter time scale, have been shown to be able to trigger changes in the thermohaline circulation in the North Atlantic Ocean on this order of magnitude (Mauritzen and Häkkinen, 1997).

Following the flushing events in Meissner et al. (2008) and in this study, the deep ocean warmed slowly over the course of a few thousand years through diffusion of heat, with Southern Ocean overturning by strong stratification as a result of more extensive seasonal sea ice. Eventually the deep ocean warmed to the point that it became temporarily unstable and another flushing event was initiated. Meissner et al. (2008) tested the sensitivity of these oscillations to the prescribed winds by carrying out several simulations with the model's wind feedback parameterization (see Weaver et al. 2001) turned on and off. The oscillations occurred even with the wind feedback (at a slightly different amplitude). Thus, the authors concluded that a CO_2 threshold near 400 ppm was probably responsible for the simulated millennial-scale phenomenon and might be a significant feature of a future climate with atmospheric CO_2 concentrations above 400 ppm.

In our study, a comparable flushing of the Southern Ocean and the North Pacific Ocean was produced by the model's oceanic general circulation model (OGCM). As in Meissner et al. (2008), this ventilation event occurred for a separate spin-up for 6000 B.C. (EQ_3) including the model's wind feedback mechanism, albeit producing flushes with a higher frequency and lower amplitude than simulations using the NCEP winds. The spatial output (not shown) from the fixed CO_2 (EQ_1 and EQ_3) spin-ups and the free carbon spin-ups (EQ_2) yielded a similar and relatively coherent picture of the ocean state, with a slow but comprehensive flushing of deep ocean carbon completed in the one thousand years following the initiation of an event. After each flushing event, the model ocean below 1 km was remarkably "newer" (evidenced by $\Delta^{14}C$ ages of deep-ocean water) and colder.

In summary, the flushing events produced in the three equilibrium simulations were associated with deep ventilation in the Southern Ocean and corresponded to the global

replacement of very deep waters, following the same pattern as in Meissner et al. (2008). However, the presence of these cycles in this paper's spin-up for 6000 B.C. affords a new perspective on the model's millennial-scale variability. Our equilibrium simulations (EQ_1 and EQ_2) under mid-Holocene conditions produced these events at much lower CO_2 concentrations (260 ppm) than the 400 ppm threshold proposed by Meissner et al. (2008). Because both our results and the results of Meissner et al. (2008) suggest that the wind feedback parameterization does not reduce or eliminate the occurrence of such oscillations, the nature of mid-Holocene solar forcing and land ice play a critical role in producing the millennial-scale oscillations during the equilibrium simulation.

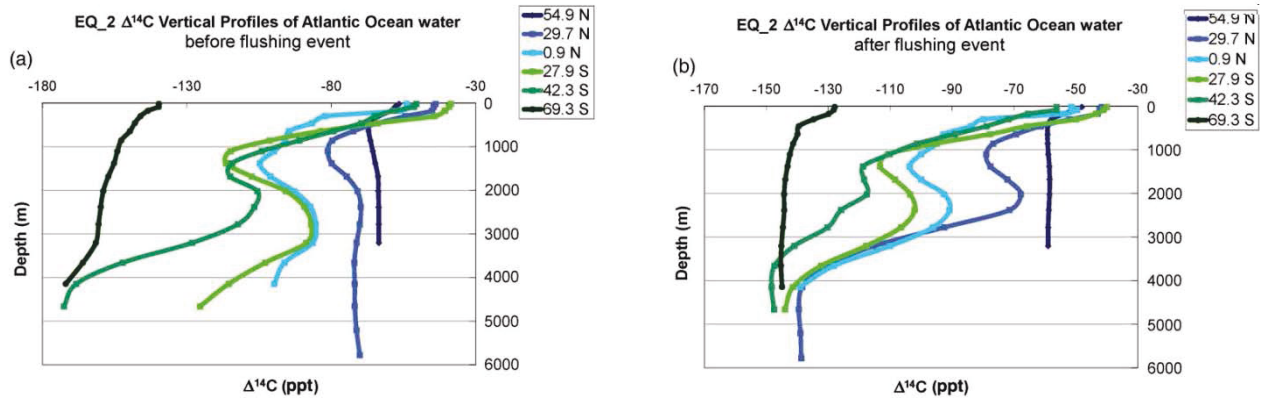

Fig. 3: Vertical profiles of $\Delta^{14}C$ at grid cells in the Atlantic basin (a) immediately before the flush in EQ_2 (year 9095 in the simulation) and (b) 1400 years later at the end of the flush event in the EQ_2 (year 10495 in the simulation). The blue lines represent profiles in the North Atlantic: 54.9°N, 41.4°W, 29.7°N, 55.8°W, 0.9°N, 23.4°W; the green lines represent profiles in the South Atlantic and Southern oceans: 29.7°S, 23.4°W, 42.3°S, 30.6°W, 69.3°S, 41.4°W.

Another prominent feature of these flushes was a change in deep water distribution globally before (Fig. 3a) and after the flush (Fig. 3b). Figure 3 provides $\Delta^{14}C$ profiles calculated by the model for the Atlantic basin in EQ_2, with lower $\Delta^{14}C$ values generally indicating stagnant, older deep waters and more positive values indicating newer deep waters recently exposed and well mixed with the atmosphere. As can be seen in both Fig. 3a and Fig. 3b, NADW

retains characteristically higher $\Delta^{14}C$ values, whereas $\Delta^{14}C$ in deep waters in the Southern Ocean tends to be much more negative. The scenario just before the flush in Fig. 3a indicates that Atlantic deep waters were strongly dominated by NADW, which is relatively carbon deprived (for further discussion see Section 4d). However, after the flush (Fig. 3b), the deep waters in much of the Atlantic Basin below 2000 m depth had a much more prominent Antarctic signature and were also more enriched in carbon than the NADW that it replaced.

In general, DIC, the dominant contributor to total deep ocean carbon, is directly correlated with $\Delta^{14}C$ in most regions in the model so that more negative $\Delta^{14}C$ deep waters generally accumulate and hold more DIC. By the time deep water distributions reached those from Fig. 3b in the EQ_2 simulation, atmospheric CO_2 was decreasing. This suggests that the cold, carbon-rich, abyssal Antarctic-generated waters, henceforth broadly referenced in this paper as Antarctic Bottom Water (AABW), were being buried in the Pacific and North Atlantic basins (outside the Southern Ocean) and were no longer being mixed as frequently to the surface. As NADW slowly retook the deep Atlantic basin in the lead up to the next flush (eventually returning to the state in Fig. 3a), Antarctic-generated waters retreated to the Southern Ocean, where they were mixed to the surface more frequently along the Antarctic Circumpolar Current (ACC). As a result, much of the excess carbon buried in the deep Atlantic basin was slowly returned to the atmosphere, helping produce the gradual increase in CO_2 just prior to the flush. Then the flush itself was characterized by a ventilation of the stagnant and even more carbon-rich deep water in the North Pacific (DWNP).

It is important to note that the MOC events produced in EQ_1, EQ_2, and EQ_3 are associated with an unrealistically stable forcing (time-independent land ice, CO_2, and orbital forcing for thousands of years). However, such a millennial-scale event in the Southern Ocean

has already been proposed by Ruddiman (2007) as a possible explanation for the consistent increase in atmospheric CO_2 during the late Holocene, and in nature it would represent a significant CO_2 release to the atmosphere on the order of 10 ppm. Schmittner et al. (2007b) and Ahn and Brook (2008) demonstrate similar, millennial-scale fluctuations in atmospheric CO_2 and Southern Ocean stratification, respectively, resulting from changes in regional overturning. Furthermore, it has also been argued that longer-term modes of meridional circulation in the Southern Ocean may be a crucial driving force in glacial-interglacial variations of atmospheric CO_2 (Stephens and Keeling 2000). Therefore, the thermohaline circulation is an important focus of investigation in this study.

3.3 Design of Transient Simulations

	Initial Conditions	Atmospheric CO_2	Land Ice	Orbital Forcing	Winds
Equilibrium Simulations					
EQ_1	Modern spin-up	Constant 6000 BC value	6000 BC configuration	6000 BC configuration	NCEP
EQ_2	Year 6200 in EQ_1	Free	6000 BC configuration	6000 BC configuration	NCEP
EQ_3	Modern spin-up	Constant 6000 BC value	6000 BC configuration	6000 BC configuration	Wind feedback
Transient Simulations					
PC	Year 6200 in EQ_1	Prescribed	Prescribed	Prescribed	NCEP
BE_PC	Before event	Prescribed	Prescribed	Prescribed	NCEP
DE_PC	During event	Prescribed	Prescribed	Prescribed	NCEP
FC	Year 6200 in EQ_1	Free	Prescribed	Prescribed	NCEP
BE_FC	Before event	Free	Prescribed	Prescribed	NCEP
DE_FC	During event	Free	Prescribed	Prescribed	NCEP

Table 1. Summary of simulations discussed in this paper. The modern spin-up referenced in the initial conditions is a climate state for 1800 A.D. used in Eby et al. (2009). "Free" atmospheric CO_2 refers to a model state wherein atmospheric CO_2 responds freely to the climate state and changes in other carbon reservoirs, without being forced to follow the observed value or trend in atmospheric CO_2 from Taylor or Law Dome ice cores.

Considering that it would be difficult to verify 4–5 Sv variations in the strength of the MOC using proxy data, given the limited temporal and spatial resolution of sediment cores, there is a great deal of uncertainty about what constitutes the actual state of the MOC starting at 6000 B.C. Given this ambiguity, any Southern Ocean ventilation state generated during the spin-up could be a valid starting point for transient simulations. The significant influence of the MOC on

the evolution of atmospheric carbon in EQ_2 (Fig. 2c) thus provides the motivation behind a series of sensitivity studies described below.

The "default" starting point for several reference simulations was selected at 6200 years following spin-up initiation in EQ_1, corresponding to maximum MOC strength (see Fig. 2a) and a deep water distribution between the two extremes in Fig. 3a and Fig. 3b. Other simulations were started during a flushing event (DE), at a time when the total MOC had stabilized at a low transport value in the spin-up and AABW constituted the dominant deep water below 3000 m depth in the oceans globally (see Figs 2a, 2b, and Fig. 3b). In addition, more experiments were started at about 200–300 years before the initiation of an event (BE) in the spin-up simulation, when warmer NADW constituted the dominant water mass in the deep Atlantic (see Fig. 3a). Altogether, these different initial conditions provided the launching points for transient simulations of the carbon cycle with prescribed and free atmospheric carbon, denoted PC and FC, respectively. The simulations summarized in Table 1 were then repeated with the model's wind feedback.

The transient forcing is provided by time dependent changes in orbital parameters (Berger 1978) and prescribed land ice (Fig. 1), which are interpolated for the model year. Sudden transitions (rather than interpolations) from land-ice area to potential vegetative area occur in the model at 5500 and 4500 B.C., which explains the instantaneous jumps evident in terrestrial carbon variables in the mid-Holocene as the last vestiges of the Laurentide ice sheet disappeared. The prescribed atmospheric carbon included in the model is based on Taylor Dome (Indermühle et al., 1999) from 6000 B.C. to 1006 A.D. and from Law Dome (Etheridge et al. 1996) from 1006 A.D. to the end of the simulation at 1850 A.D. In the prescribed carbon runs (PC, BE_PC, DE_PC), the model's atmospheric CO_2 followed the observed trend in Taylor and Law Dome

cores while all other components of the carbon cycle (including vegetation/soils, organic and inorganic ocean carbon, and ocean sediments) responded directly to the forced changes in the atmospheric carbon reservoir but were free to evolve without any other constraint. By contrast, the FC simulation allowed the model's atmospheric carbon content to respond freely to the evolution of the model's interactive representation of the Earth's natural carbon cycle and climate.

In summary, the equilibrium simulations suggest that two "extreme" solutions are equally plausible for 6000 B.C. deep-water distributions with (1) little AABW, stagnant DWNP in the Pacific Ocean, and dominant NADW in the deep north and south Atlantic Ocean as in Fig. 3a, and with (2) newly ventilated DWNP and dominant AABW in the North Pacific and Atlantic basins below 3000 m (Fig. 3b). Furthermore, a range of solutions are possible between these two extremes. The BE initial conditions represent a starting point for case (1); the DE initial conditions represent case (2), and the default initial conditions represent a deep-water distribution between these two extremes.

4 Results

4.1 Millennial-Scale Oscillations under Transient Forcing

As discussed in Section 3b, the presence of millennial-scale oscillations in the thermohaline circulation for the model's equilibrium simulations produced a venting of deep waters globally through the Southern Ocean and a temporary slowing of NADW formation. When atmospheric carbon was allowed to vary freely (EQ_2), this resulted in an increase in atmospheric CO_2 of 8–13 ppm, likely a result of carbon-rich deep waters from the North Pacific being ventilated at the surface (Fig. 4a) and a temporary slowing of CO_2 entrainment into the deep ocean in the North Atlantic. In Meissner et al. (2008), it was determined that a CO_2

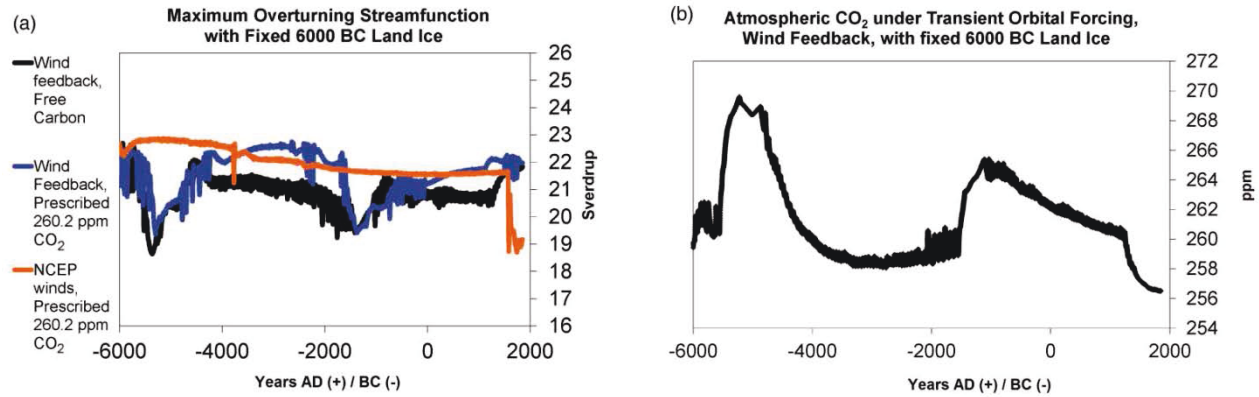

Fig. 4: Time series of (a) the global maximum meridional overturning streamfunction (Sv) and (b) atmospheric CO_2 for a transient simulation including the wind feedback for the Holocene (6000 B.C. to 1850 A.D.) with land ice fixed at its 6000 B.C. configuration.

concentration of 400 ppm was the critical threshold for such millennial-scale oscillations. However, with mid-Holocene land-ice and insolation forcing configurations, this threshold is clearly much lower (at least 260 ppm), and these oscillations continue to occur in sensitivity simulations when CO_2 (EQ_2) and winds (EQ_3) are allowed to vary. Considering their substantial impact on the carbon cycle, it is useful to identify which factor (insolation or land ice) is more important for their initiation and whether these millennial-scale oscillations can be present under transient (time-evolving) forcing conditions.

A number of sensitivity simulations were conducted with transient orbital forcing from 6000 B.C. to 1850 A.D. but with land ice fixed at 6000 B.C. (see Fig. 1a) for the entire run period. The simulations, summarized in Fig. 4, start from the default initial conditions defined in Section 3.3 and continue to produce millennial-scale flushes (with similar characteristics to EQ_2) during the late Holocene (Fig. 4). These repetitive millennial-scale oscillations do not explicitly occur in the other transient simulations described in Table 1, which are all forced with both transiently evolving land ice and orbital forcing. This suggests that the distribution of land-ice extent (particularly Antarctic land ice prescribed by ICE-4G) in the model, and not orbital forcing, is critical to producing these millennial-scale oscillations.

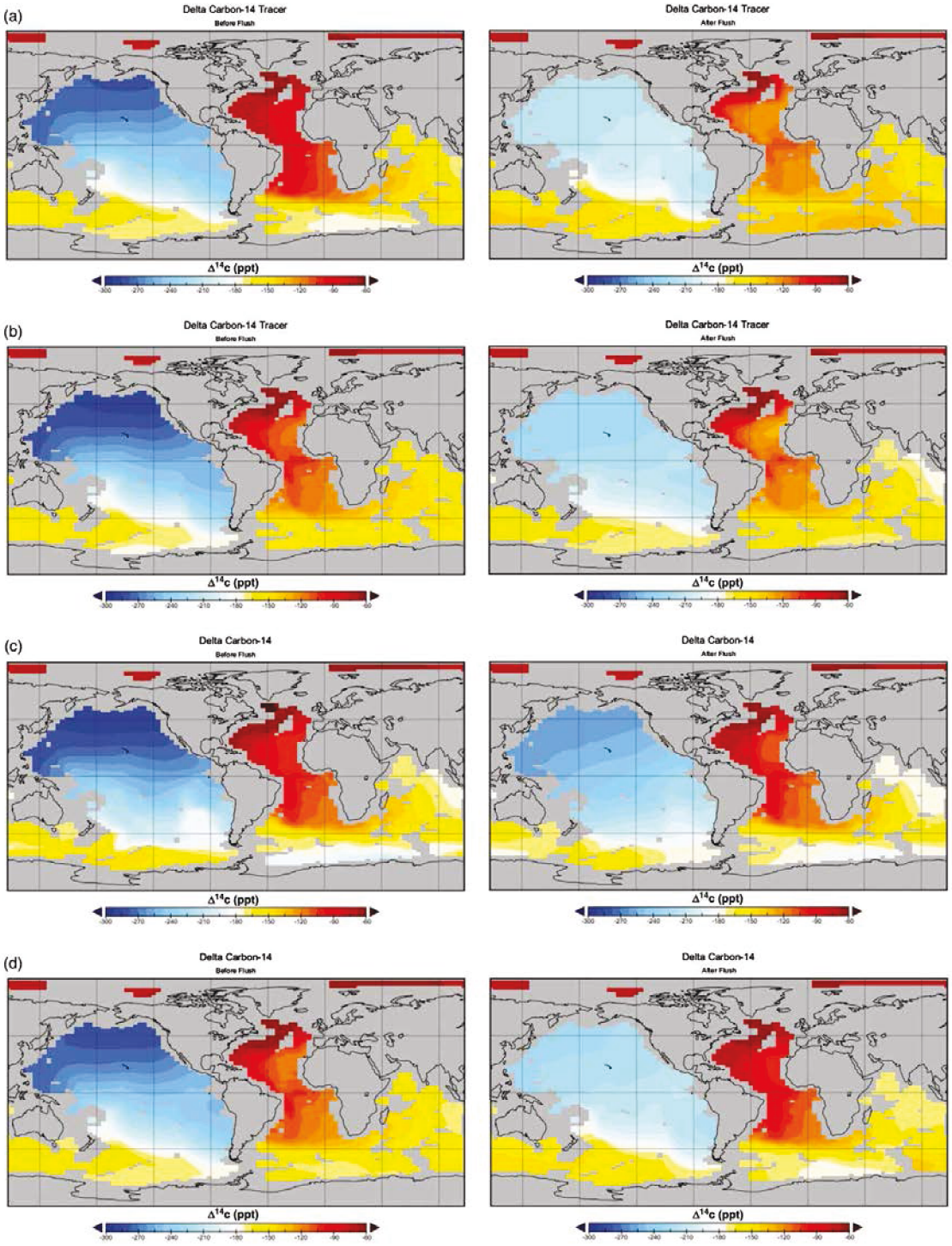

Fig. 5: Spatial distributions of $\Delta^{14}C$ (‰, orppt) at 3202 m depth before and after the ventilation of DWNP in several equilibrium and transient simulations. Shown in (a) are the results from EQ_2 year 9195 (left panel) and year 10195 (right panel), in (b) results from 5600 B.C. (left panel) and 4100 B.C. (right panel) in a simulation with transient orbital forcing, wind feedback, freely evolving atmospheric CO_2 and fixed 6000 B.C. land ice, in (c) results for 5100 B.C. (left panel) and 4100 B.C. (right panel) in the default FC simulation, and in (d) results for 5100 B.C. (left panel) and 4100 B.C. (right panel) in the Before Flush FC wind feedback simulation.

In a simulation with constant CO_2 at 260.2 ppm and NCEP winds, a millennial-scale flush does not occur until 1300 A.D. When the carbon cycle was freed at 1200 A.D. in this simulation (not shown), a 7.5 ppm jump in atmospheric CO_2 was produced within a decade as a ventilation of DWNP was initiated. Atmospheric CO_2 then stabilized at 268 ppm for 500 years before declining slowly back toward 260 ppm. In a similar simulation with land ice (Fig. 1a) and CO_2 (260.2 ppm) fixed at the 6000 B.C. configuration, but including the wind feedback adjustment to NCEP winds, two millennial-scale flushes occurred (amplitude of 4 Sv), one at 5500 B.C. and another at 1500 B.C. These oscillations continued with a 3000-year period (Fig. 4a), similar to the equilibrium simulation (EQ_3, Fig. 2a) which also incorporated the wind feedback. When this experiment was repeated with atmospheric CO_2 allowed to evolve freely (Figs 4a and 4b), the earlier oscillation (5500 B.C.) occurred at a slightly greater amplitude (4 Sv) than the flushing event at 1500 B.C. (2 Sv anomaly). Both events in this free-carbon simulation led to a slow flushing of DWNP, but the first event (Fig. 5b) produced a more thorough replacement of DWNP (evidenced by $\Delta^{14}C$) than in the second flush at 1500 B.C. Consequently, the carbon released to the atmosphere was greater during the first flush (a 10 ppm excursion comparable to the release in EQ_2) than in the second (a 6 ppm excursion).

The combined effect of both flushes in this simulation kept atmospheric CO_2 substantially higher (near or above 260 ppm) for a much longer interval than in the transient simulations from Table 1 (see Fig. 6a and discussion in Sections 4b and 4c). These oscillations, in turn, appear to be related to the presence of an extensive land ice shelf prescribed around the periphery of Antarctica (Fig. 1a). The flushing events were also associated with a more frequent ventilation of older, carbon-rich North Pacific deep water through the Southern Ocean and, as a consequence, higher atmospheric CO_2 concentrations near or above 260 ppm for much of the

simulated late Holocene climate. The results thus suggest that atmospheric CO_2 is highly sensitive to land-ice extent, and this was the motivation for further sensitivity experiments concerning ice shelves in Section 4.4.

Similar flushes of DWNP have been recorded by proxy evidence in nature. Galbraith et al. (2007) note that the ventilation of long-stagnant North Pacific deep waters occurred around 12650 B.C. and likely contributed to an abrupt 10 ppm increase in atmospheric CO_2, which was balanced, in part, by a strengthening NADW and greater CO_2 uptake through biological productivity in the surface ocean. The North Pacific Ocean thereafter became more estuarine following this event (with more frequent ventilation). The UVic model oscillations simply serve to circulate deep ocean carbon stored in the North Pacific, albeit in abrupt events that resemble the first major interglacial ventilation of DWNP at 12650 B.C. in the proxy data. While a flush of the same magnitude as at 12650 B.C. has not been documented since 6000 B.C., periodic, partial ventilations of DWNP could well be a feature of the Holocene MOC.

The simulations with transiently evolving land ice elaborate on this idea of partial DWNP ventilations. None of the fully transient simulations summarized in Table 1 (see Fig. 6), with and without the model's wind feedback, produced a millennial-scale oscillation on the same scale as in the equilibrium simulations EQ_1 and EQ_2 or the experiments with land ice fixed at the 6000 B.C. configuration (Fig. 4). However, DWNP was still ventilated in all free carbon simulations, except with DE initial conditions, in which the DWNP had already been flushed at the start of the transient simulation. Furthermore, both the default and BE transient simulations replaced these deep waters in an event around 5000 B.C. (Fig. 6c) that produced a notable loss in global ocean carbon (Fig. 6d). More dramatically, the BE IC simulation with freely varying atmospheric carbon and a wind feedback demonstrated a multi-centennial-scale weakening in the MOC near

5000 B.C. (Fig. 6b), which was accompanied by a more gradual and thorough (Fig. 6d) flushing of DWNP (according to δ^{14} C ages) and greater oceanic carbon loss (Fig. 6d) than any other simulation.

4.2 Results from Free CO_2 Experiments

4.2.1 Atmospheric CO_2

` From the transient runs summarized in Table 1, the marked contrast in the atmospheric CO_2 concentration in the FC experiment (Fig 6a, light blue line) compared to the observed atmospheric carbon from ice cores (Fig. 6a, dark blue line) may provide important implications for the early anthropogenic hypothesis. In all simulations, atmospheric CO_2 decreased to values between 245 ppm and 255 ppm by the Industrial Revolution, well below the 280 ppm observed value and in-line with the analogue prediction of decreasing Holocene CO_2 in Ruddiman (2003) and Ruddiman et al. (2011).

Initially, atmospheric CO_2 increased in the FC experiment, nearly reproducing the observed trend through natural processes (without the intervention of peatlands, coral reefs, or human land use) until about 4000 B.C. In the BE simulation including the wind feedback, the divergence between the model-simulated carbon cycle and the natural carbon cycle does not occur until even later (3000 B.C.). This suggests that the initial CO_2 increase during the mid-Holocene might be explained by natural processes represented in the model, delaying the date at which an external source of carbon would be required to recreate the Holocene carbon trend. A later date of divergence between the Holocene's natural potential carbon cycle and the observed cycle in the proxy record may theoretically lend more weight to the revised Anthropogenic Hypothesis (Ruddiman and Ellis, 2009), because the late neolithic period was characterized by not only low land-use efficiency but also much higher human populations

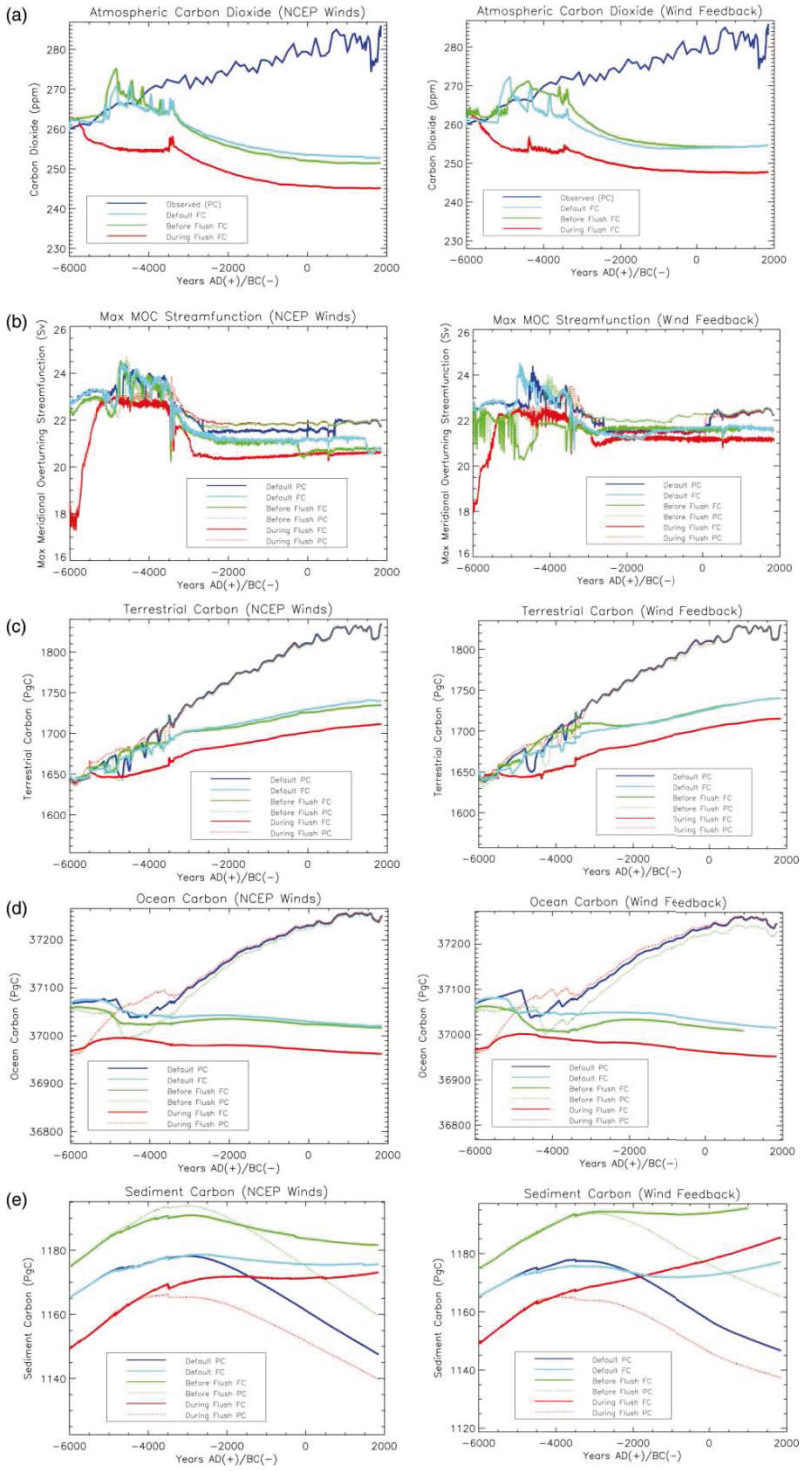

Fig. 6: Time series of (a) atmospheric CO_2 (ppm), (b) global maximum meridional overturning streamfunction (Sv), (c) terrestrial carbon (Pg C), (d) ocean carbon (Pg C), and (e) sediment carbon (Pg C). The results from simulations with prescribed NCEP winds for the entire simulation (as in Table 1) are given in the left panels, and the results using the wind feedback for the same initial conditions are given in the right panels. The dark blue line represents the prescribed CO_2 (PC) simulation using default initial conditions, whereas the cyan (light blue) line shows free CO_2 (FC) evolving from the same default initial conditions. The green line represents before flushing event (BE) initial conditions for free CO_2 (solid line) and prescribed CO_2 (dashed line). The red curves represent during flushing event (DE) initial conditions with free CO_2 (solid line) and prescribed CO_2 (dashed line).

following several millennia of horticultural, agricultural, and pastoral subsistence. With global populations nearing 100 million by 4000–3000 B.C. by some estimates (Boyle et al. 2011), it can be speculated from previous studies summarized in Section 2.2 that the human transformation of the landscape began to have a measurable impact on global CO_2 concentrations (see Chapter 5 for a quantification of this effect).

On closer examination of the CO_2 trend lines in Fig. 6a anomalies (spikes) in the simulated CO_2 curve between 5000 and 4000 B.C. can be seen. These appear to be initiated by changes in the MOC (Fig. 6b, light blue line), which take the form of periods of deeper ventilation off the western Antarctic coast, south of Australia. However, these brief multidecadal-scale events tend to mix AABW and Antarctic Circumpolar waters locally in the Southern Ocean and do not have the same spatial and temporal scale as those observed in EQ_1 and EQ_2 (which ventilate DWNP). As a consequence, they do not appear to have the same broad influence on deep ocean temperatures and deep water carbon storage.

4.2.2 Terrestrial Carbon

The terrestrial carbon (vegetation and soil carbon) time series plotted in Fig. 6c indicate that vegetation carbon constantly increased over the course of the Holocene simulation, with a total terrestrial uptake over the period ranging from 70–100 Pg C for the FC simulations. This led to net removal of carbon from the atmosphere–ocean system over the 8000 simulated years and is consistent with the results of Kleinen et al. (2010) and Goodwin et al. (2011), which also suggested similar net increases in terrestrial carbon of approximately 100 Pg C over the course of the Holocene. However, the CLIMBER-LPJ model in Kleinen et al. (2010) simulated no net change in terrestrial carbon without peatlands: decreasing boreal vegetation during the late Holocene (carbon loss in living biomass) led simply to a transfer of carbon to litter (carbon gain

to colder soils) as the tree line shifted south. Only in simulations including peatlands does the terrestrial carbon (soils and biomass) in Kleinen et al. (2010) increase by 105 Pg C. The UVic ESCM 2.9 does not include an estimate of peatland accumulation but does similarly transfer shrub and tree carbon to soils during the late Holocene in the FC simulations associated with an insolation-induced southward retreat in the boreal forest line after 4000 B.C. (not shown). The high latitude C_3 grasses that replaced trees and shrubs continued to accumulate soil carbon to produce the same net effect as the peatlands in Kleinen et al. (2010). The PC simulations, with steadily increasing temperature and greater biosphere CO_2 fertilization, produced instead a northward advance of the boreal forests during the late Holocene.

The results also indicate that the increase in terrestrial carbon is greatest from 6000 B.C. to 4000 B.C. as boreal vegetation expanded rapidly northward in Eurasia during the mid-Holocene climatic optimum and new land became available in North America as the last remnants of the Laurentian ice sheet disappeared. Because the Sahara region remained mostly bare ground in the equilibrium simulations, even when incorporating the wind feedback, the model does not capture the terrestrial release in this region as proposed by Intermühle et al. (1999). However, as boreal vegetation began to retreat southward around 4000 B.C. in the FC simulations, total terrestrial carbon continued to increase. This increase is primarily associated with a slowly increasing storage of carbon in high-latitude soils below sub-Arctic C_3 grasses, which are not parameterized to imitate peatland dynamics.

In an approximate analogy to prairie grasses, model C_3 grasses store a significant proportion (approximately 40%) of their carbon in the soil. As in areas with persistent permafrost, this storage is more pronounced at high latitudes and at high altitudes where respiration rates are low because of cold temperatures and a short summer season. Because the model shrubs do not

store as much soil carbon, when shrubs advance northward and replace grass in the northern "tundra C_3" region, soil respiration quickly overtakes biomass input. As a consequence, the carbon stored in the former high-latitude grass soils, which slowly accumulate carbon with time, is released to the atmosphere when overtaken by shrubs and small trees.

The tundra (not shown) nearly disappeared in pulses from 6000 B.C. to 4000 B.C. with northern hemisphere warming, then expanded southward after 4000 B.C. in the FC simulations as boreal forests retreated to the south in response to solar insolation changes. Clearly the accumulation in high-latitude soils more than compensated for the loss of terrestrial carbon resulting from retreating boreal vegetation, leading to a steady net increase in terrestrial carbon between 4000 B.C. and 1850 A.D.

The brief flushes in the transient simulations were associated with net terrestrial carbon releases of the order of 10 Pg C (the dips in Fig. 6c), which help drive the atmospheric CO_2 concentration upward, followed by a return of this carbon to the terrestrial biosphere a few decades later. The largest such release occurred when the DWNP waters were ventilated and ocean carbon was released around 5000 B.C. Most of these brief releases occurred in high latitude regions of Eurasia and North America, where tundra carbon was being released to the atmosphere.

4.2.3 Ocean and Sediment Carbon

The ocean carbon reservoir (Fig. 6d) also played a critical role in the simulated Holocene carbon cycle. Between 5000 B.C. and 3500 B.C., sediments gradually absorbed about 6 Pg C (Fig. 6e, light blue line) before levelling off. However, this does not account for the 35 Pg C decline in total ocean carbon (DWNP ventilation), most of which occurred between 5500 B.C. and 4500 B.C. (Fig. 6d, light blue line). Following this pronounced loss early in the simulation,

ocean carbon remained virtually constant or in slow decline thereafter (with no substantial aging of DWNP during the late Holocene). The relatively stable, declining ocean carbon in the FC simulations is in contrast to the PC simulations, which showed an increase in ocean carbon in response to the forced increase in atmospheric carbon (Fig. 6d). The contrast between the FC and PC simulations clearly indicates that the ocean carbon in the prescribed runs primarily responded to atmospheric carbon and was not forced by the internal ocean chemistry.

Furthermore, a comparison of Fig. 6a with Fig. 6d suggests that the substantial increase in atmospheric CO_2 around 6000 B.C., on the order of approximately 8 ppm (excluding the additive effect from terrestrial carbon), is associated first and foremost with a release of carbon from DWNP to the atmosphere. However, different ocean carbon losses between the simulations suggest differing degrees of "thoroughness" and rapidity (as discussed in Section 4a) in the flushing of DWNP. It is further interesting that each simulation with default and BE initial conditions produced some kind of DWNP ventilation around 5000 B.C, which is surprising considering that one would expect an earlier ventilation from the BE initial conditions and a much more delayed event from the default (FC) initial conditions. This suggests that the orientation and transient evolution of marine ice shelves (for further discussion see Section 4.4) is more important for the initiation of these DWNP flushing events than initial temperature and salinity of the deep water.

However, initial conditions and winds can clearly influence the thoroughness of the flushes of DWNP (and thus the quantity and duration of the carbon release to the atmosphere). The BE initial conditions with the wind feedback produced the most thorough ventilation of DWNP and the longest period of elevated CO_2 in the atmosphere. Default initial conditions resulted in a less thorough ventilation of DWNP (as evidenced by model $\Delta^{14}C$ ages) and a

shorter period of elevated atmospheric CO_2. These peaks to 270 ppm by 5000 B.C. appear quite pronounced compared to the smooth, gradual increase in atmospheric CO_2 suggested by ice core records. However, if considering the source data for these proxies, ice in Antarctica must be given time to compact under newer layers of slowly accumulating snow above it to form isolated ice bubbles from which paleo-CO_2 concentrations can be extracted. Thus, the proxy data do not represent one single year (as do the model data) but rather decades if not centuries of mixed air bubbles, depending on the accumulation rate at the core site. A comparable running average of yearly data of the events produced in our model (not shown) produced lower-amplitude "humps" than is presented in Fig. 6a. This is more in keeping with the observed CO_2 trend from ice sheets, as humps (periods of accelerated CO_2 increases over a thousand years of approximately 5 ppm, followed by decreases on the order of 2–3 ppm) are visible in EPICA Dome C between approximately 3571 and 2787 B.C. and between approximately 968 B.C. and 198 A.D. Millennial-scale flushes of DWNP of a smaller magnitude than EQ_2 (periodic, incomplete ventilations on millennial time scales) thus may be embedded in the observed ice core data with other processes leading to the net increase in atmospheric CO_2 over the course of the Holocene.

The ocean carbon reservoir also interacts with centennial-scale changes in ventilation. During the periods when the Southern Ocean ventilation was locally active (characterized by dips in the maximum MOC streamfunction in Fig. 6b), relatively carbon-rich deep waters in the Southern Ocean were circulated to the surface and NADW uptake slowed. The brief loss of carbon from the ocean to the atmosphere during these events was minimal under NCEP winds but pronounced for the wind feedback simulations (see the zig-zag pattern in Fig. 6d). These centennial events occurred with relative frequency and are associated with elevated CO_2, higher Antarctic temperatures, and much greater Antarctic precipitation rates.

After 4000 B.C., the observed and simulated natural atmospheric carbon diverged (Fig. 6a), with atmospheric carbon dropping rapidly between 4000 B.C. and 2000 B.C. The most significant decline in atmospheric CO_2 concentration in the FC simulation occurred during and 1000 years after a permanent 2–3 Sv reduction in the global maximum overturning streamfunction (Fig. 6b). Over this period, the cycles in Southern Ocean ventilation and Antarctic sea ice essentially stopped and mean-annual sea ice remains virtually unchanged for thousands of years.

The restabilization of the model MOC appears to be related to the disappearance of a major fraction of the Antarctic Ice Shelf at 3500 B.C. (interpolation between Fig. 1c and Fig. 1d), which corresponds to the single greatest loss of southern hemisphere land ice area during the 19000 B.C. to 2000 A.D. period in the interpolated ICE-4G dataset (it should be reinforced that the model does not experience this event as a freshwater pulse). At first, a large portion of the Weddell Sea was free of ice, which initially stimulated intense ventilation between 3500 B.C. and 3400 B.C. and a corresponding spike in atmospheric CO_2. Following this event, however, annual Southern Ocean sea ice expanded and reached a steady equilibrium, with areal coverage of sea ice (and thus winter production rates of sea ice in the Southern Ocean) changing little during the following millennia. Accordingly, virtually no periods of intense Southern Ocean ventilation were experienced for the rest of the Holocene simulation. Furthermore, with no additional abrupt DWNP ventilations, atmospheric CO_2 fell quickly to adjust to the lowered ocean carbon content (from 2000 years previously) as the MOC approached a new equilibrium in the transient simulation.

Following the stabilization of the MOC between 3000 B.C. and 2000 B.C., simulated atmospheric CO_2 continued to drop slowly, approaching a limit of 252 ppm at the end of the pre-

industrial era. The BE_FC simulation levelled out at a similar value (251 ppm) and the DE_FC simulation stabilized near 245 ppm. These values are significantly (approximately 25–35 ppm) lower than the ice core record of atmospheric CO_2 concentrations but are above the 240 ppm value projected by Ruddiman (2003) and used in the GCM studies of Vavrus et al. (2008) and Kutzbach et al. (2009). The range of 245–251 ppm by 1800 A.D. are, however, close to the average decrease (just below 250 ppm) of the six previous interglacial periods aligned by their ($\delta^{18}O$-determined) start date (Ruddiman et al. 2011).

The decline of atmospheric carbon appears to respond to the continuous uptake of carbon by the terrestrial biosphere. This increase is dominated by soil uptake as the high-latitude C_3 grasses begin to expand southward, in part, as a result of declining northern hemisphere solar insolation after 4000 B.C. However, the terrestrial uptake of approximately 30 Pg C only accounts for the relatively small net 8 Pg C (3 ppm) decline in atmospheric CO_2 from 2000 B.C. to 1850 A.D., approximately equivalent to the contribution of terrestrial release to the atmosphere from human land use proposed in Pongratz et al. (2009). Figure 6 reveals that much of the carbon gains in the biosphere during this stable MOC period after 2000 B.C. appear to be more or less balanced by a corresponding slow loss in ocean carbon.

4.3 Comparison of Free Carbon Results with Prescribed Carbon Runs

As described above, a series of experiments, labelled PC, DE_PC, and BE_PC scenarios, were performed with prescribed atmospheric carbon, and the results are also summarized in Figs 6a to 6e. We have noted that the PC and FC carbon experiments yielded similar results for the first 1500–2000 years of both simulations; however, after 4000 B.C. a pronounced divergence is evident. Furthermore, we established in Sections 4.1 and 4.2 that the MOC state plays a particularly crucial role in the evolution of atmospheric carbon. On the surface, the evolution of

the MOC (Fig. 2b) seems quite similar in the FC and PC runs, although the greatest variations between the two appear during times of greater ice shelf extent between 6000 and 3000 B.C.

This suggests that emissions of carbon to the atmosphere might feed back to the MOC at times when Southern Ocean ventilation is more variable and net downwelling of Antarctic-generated waters is reduced. Small differences in atmospheric CO_2 between the individual PC and FC simulations has the largest impact on the MOC strength during this period of greater Antarctic ice shelf extent. When Antarctic ice shelves retreated after 3400–3300 B.C., the MOC states between the PC and the FC simulations approximately converged. We thus infer that some other effect (such as the 3500 B.C. Antarctic ice shelf disappearance) and not CO_2 was driving MOC variability and deep water distributions. It is also clear from a comparison of the FC and PC simulations that the increasingly large divergence of atmospheric CO_2 (and the corresponding radiative forcing) between the two experiments had virtually no effect on the stabilized MOC after 3500 B.C. In summary, our results suggest that the MOC is only notably altered by the CO_2 difference between the PC and FC simulations during periods when ice shelves are more extensive.

Our model results therefore indicate that the greatest impact resulting from small perturbations in CO_2 (such as those associated with terrestrial releases as proposed by Ruddiman (2007)) would have occurred before 3300 B.C., the date of final MOC stabilization in all simulations. Although this date is very early in human agricultural history, it also may have been a time of low-efficiency (greater per-capita) land use related to the cruder technologies of the neolithic Period (Ruddiman and Ellis, 2009). Furthermore, this period (before the disappearance of Antarctic marine ice shelves) is characterized by low-efficiency ocean uptake of carbon

resulting from faster local circulation of Antarctic-generated deep waters to the surface and thus reduced long-term carbon storage in these waters.

However, it is not clear whether the multi-millennial steadiness obtained for the model MOC after 3300 B.C. is accurate (see Section 4d). In particular, proxy evidence of $\delta^{15}N$ off the coast of Chile (Robinson et al., 2007), taken as a measure of the stratification of Southern Ocean surface waters (e.g., Ahn and Brook, 2008), shows variations during the Holocene that are nearly on the same order as those during Heinrich events earlier in the proxy record. Also, abundances of penguin rookeries described in Baroni and Orombelli (1994) and Emslie et al. (2003) suggest that 2000–1000 B.C. and 700–1400 A.D. were periods of low Antarctic sea-ice extent, interspersed with more extensive sea ice (for example, during the period from 1000 B.C. to 1 A.D.). Furthermore, our modelling results suggest that Antarctic warming and cooling are closely coupled to Southern Ocean ventilation, and abrupt warmings and coolings during the Holocene have been documented in Antarctic proxies (for example, Kulbe et al. 2001; Shevenell et al. 2011).

The proxy evidence for significant variability in sea ice (and probably Southern Ocean overturning) implies that the production of sea ice off the coast of Antarctica following 3300 B.C. was not as steady as indicated by our results. Furthermore, the MOC naturally undergoes oscillations on the same order of magnitude and temporal scale as those seen in the FC and PC simulations between 5300 B.C. and 3300 B.C., making circumspect the near constancy of the MOC for thousands of years after 3300 B.C. Therefore, it is quite plausible that Southern Ocean ventilation continued to be locally active in the Southern Ocean during the late Holocene, and correspondingly the increasing extent of human land use with time might have mildly influenced the net terrestrial carbon release to the atmosphere observed for these events. The potential

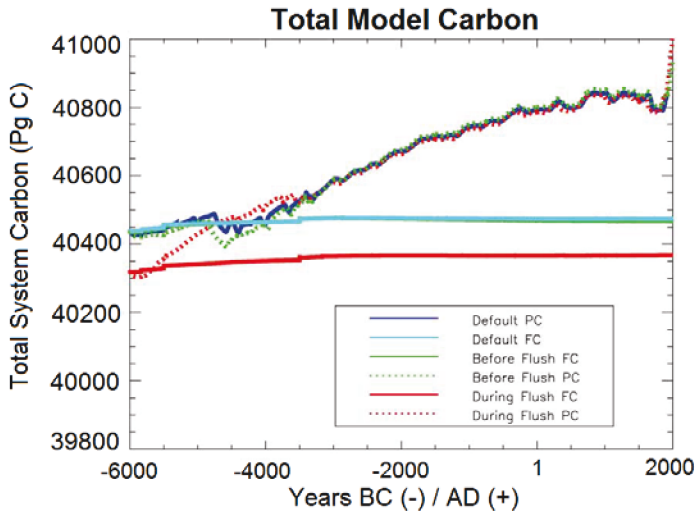

Fig. 7: The total carbon stored in the atmosphere, ocean, sediments, and terrestrial biosphere/soils for all simulations in Table 1, from 6000 B.C. to 2000 A.D.

magnitude of these contributions were investigated by UVic simulations for different land-use scenarios using adaptations of HYDE 3.1 (Klein Goldewijk 2001; Klein Goldewijk et al. 2011) in Chapter 5.

The most compelling evidence for some kind of external carbon forcing not represented in the model, and potentially provided by human land use, carbonate compensation, and/or coral reef regrowth, is demonstrated in Fig. 7. As seen in all the FC simulations, total earth system carbon is generally conserved by the UVic ESCM 2.9 when the carbon cycle is allowed to evolve freely. It is also approximately conserved for the PC and BE_PC simulations for the first 2000 years.

However, after 4000 B.C., total system carbon began to increase in these two PC experiments. A comparison with Fig. 6d reveals that much of this carbon is stored in the ocean so the atmosphere is clearly forcing the ocean carbon to increase in the prescribed runs. Furthermore, Fig. 6c reveals that terrestrial carbon also increased as did atmospheric CO_2 during the PC simulations as a result of greater CO_2 fertilization and more large (needleleaf) trees in subpolar regions replacing small trees (shrubs). The combined warming and fertilization effect

from higher CO_2 concentrations enhanced carbon storage in the terrestrial biosphere much more than the greater soil carbon storage in high-latitude C_3 grasses from the FC simulations (Figs 6c and 8c), which conversely responded to both decreasing CO_2 levels (cooling) and decreasing insolation after 4000 B.C.

Therefore, some external forcing to the model's climate system is clearly necessary in order to reproduce the observed increasing atmospheric carbon trend shown in Indermühle et al. (1999) and Lüthi et al. (2008). This unaccounted-for input into the climate system, which increases with time, may be determined by the model's sediment and ocean chemistry initial conditions (see the limitations described in Section 5) or unaccounted-for volcanic activity. Peatlands (a sink for atmospheric estimated to be as great as 35 ppm by Frolking and Roulet (2007) and slightly less by Yu (2011)) and coral reef-related carbonate compensation (a source of atmospheric CO_2 estimated to be as much as 40 ppm by Ridgwell et al. (2003) and approximately 28 ppm by Kleinen et al. (2010)) are also not represented in the model. Although these two carbon pools might have balanced each other during previous interglacial periods, leading to little net influence on the atmospheric carbon concentrations, a slight lag or imbalance between the two during the Holocene could also be responsible for some of the increase in total system carbon. It is also worth noting that this increase in earth system carbon in the PC simulation exceeds 400 Pg C, which is considerably larger than many estimates of the potential carbon flux to the atmosphere associated with early agriculture (Stocker et al. 2011) but not far from the emissions estimates (as high as 327–357 Pg C) associated with crop rotations in Kaplan et al. (2011).

4.4 Sensitivity of the Simulated Holocene Climate to Land-Ice Configuration

As established in Section 4.1, the model's ability to ventilate relatively stagnant, carbon-rich DWNP is dependent on the land-ice configuration between 6000 and 5000 B.C. Although this purging of deep ocean waters in the Pacific Ocean led to higher atmospheric CO_2 (largely between 258 to 270 ppm in transient simulations), it failed to explain the permanent increase in CO_2 to 280 ppm during the Holocene. However, these millennial-scale flushes kept atmospheric CO_2 near or above 260 ppm for the entire late Holocene, as opposed to 245–252 ppm in model simulations without comparable flushes. Therefore, we might speculate that a greater transfer of DWNP carbon to the atmosphere, associated with MOC sensitivity to land-ice extent, might explain part of the trend during the Holocene.

Furthermore, the results (Sections 4.2 and 4.3) from transient simulations in Fig. 6 suggest that the land-ice transition between 4000 and 3000 B.C. led to a sudden stabilization of the MOC for the remainder of the simulated late Holocene, regardless of the initial conditions of the simulation or adjustments to the model winds. Comparing Fig. 1c with Fig. 1d indicates that this transition coincided with the complete disappearance of large ice shelves off the coast of Antarctica in the ICE-4G dataset; this land ice had only been melting slowly between previous time slices.

Because an abrupt and permanent stabilization of the model's MOC and climate state may not represent the reality of the Holocene; the transient simulations in Table 1 (with and without the wind feedback) were repeated by eliminating this transition. This was done very simply by fixing the land-ice configuration after 4000 B.C. to the configuration in Fig 1c. The motivation for these simulations is that the interpolation of ICE-4G to the model grid cell eliminates nearly all marine ice shelves (Fig. 1d compared with Fig. 1e), and in particular, the

prominent Ross and Ronne-Filchner ice shelves in the Ross and Weddell Seas, respectively, as well as extensive marine ice shelves off Graham Land (Antarctic Peninsula) and Queen Maud Land (east of Weddell sea) that still exist today (Vaughan 2008, their Fig.1). Because sea ice, temperature, and ventilation depth are particularly variable in these regions during the modelled millennial- and centennial-scale flushes in the Southern Ocean (Sections 4a and 4b), these new experiments test the sensitivity of the global carbon cycle to the presence of Antarctic marine ice shelves during the late Holocene.

Prescribed ice shelves in the UVic ESCM 2.9 essentially act as a lid over the ocean grid cells below, cutting off fluxes (heat, moisture, carbon, and tracer) between the ocean and the atmosphere. As evident in a comparison of Figs 1a to 1d with Fig. 1e, grid cells are either open ocean or marine ice shelf (with no partial ice shelf coverage). With these ice sheets prescribed above the sea surface, grounding (marine ice shelves extending to the seafloor along continental shelves) is not represented. The open ocean grid cells adjacent to ice shelf margins are influenced by the albedo of the nearby ice sheet, which affects regional surface temperature and, correspondingly, precipitation and runoff to the ocean. In addition, the presence of the ice sheet raises the elevation of the grid cell (which also feeds back to regional temperature, precipitation, and runoff) and cuts off the ocean from overlying winds (which will in turn influence overturning). However, there is no exchange of latent heat between the ice sheet and the nearby or underlying ocean waters (which would serve to intensify convection along ice shelf margins), and the retreat of ice shelves does not contribute to a freshwater pulse to the ocean. Additionally, because ice shelves are only represented as a lid, ocean convection and circulation can continue beneath them.

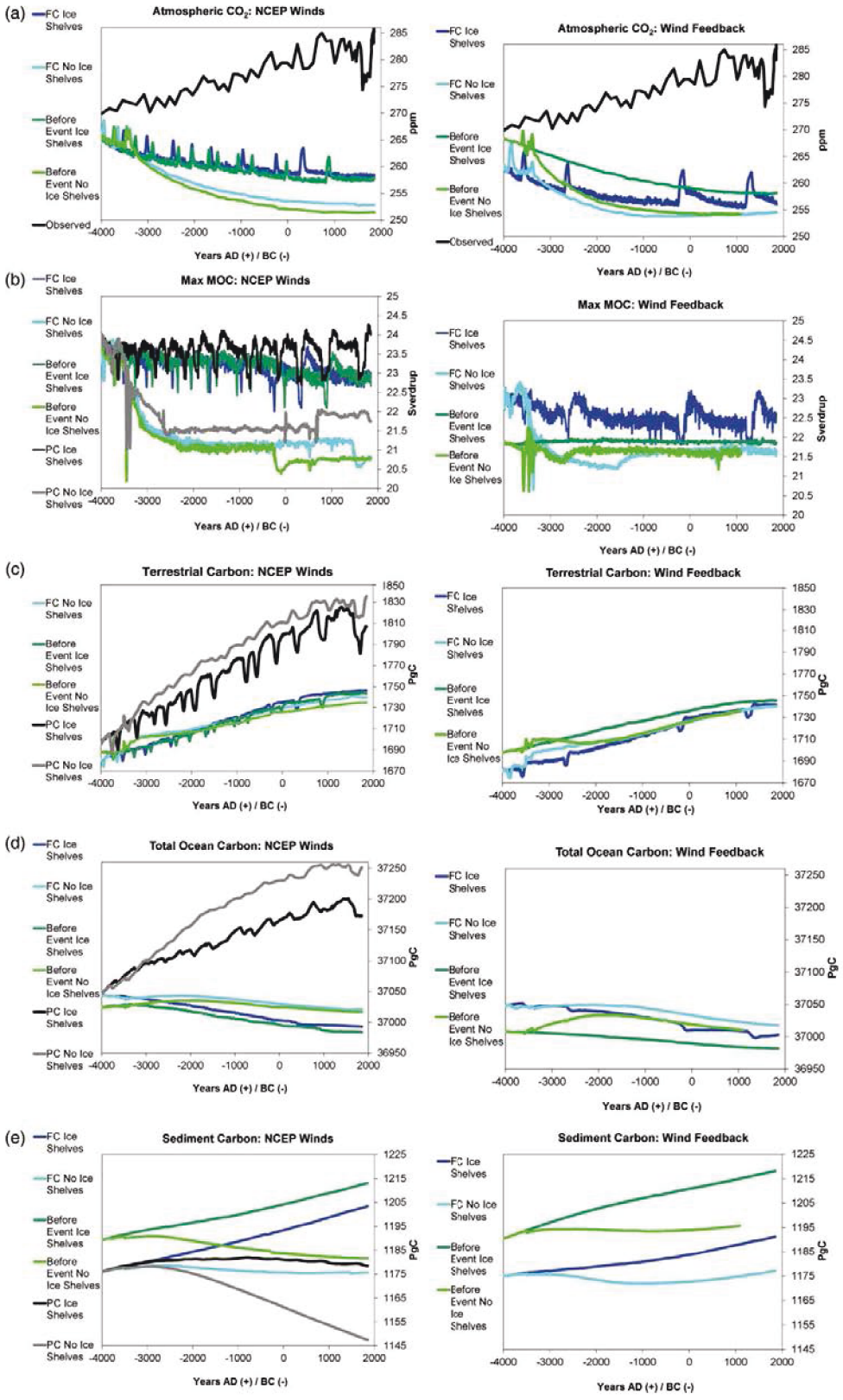

Fig. 8: As in Fig. 6, but with results for simulations (dashed lines) when Antarctic ice shelves are kept in the model (unchanging land-ice configuration after 4000 B.C.).

Taking these considerations into account, Fig. 8 indicates there is a non-negligible difference in the carbon cycle dynamics between the simulations without ice shelves after 3000 B.C. (as for all the simulations represented in Fig. 6) and those with ice shelves (unchanging land ice after 4000 B.C.). Atmospheric CO_2 was notably higher for simulations with the ice shelves (Fig. 8a), yielding a pre-industrial value approaching 258 ppm with BF initial conditions, approximately 5–6 ppm higher than the same simulations without ice shelves. This increase was smaller (2–3 ppm) with the wind feedback because atmospheric CO_2 was already 1–2 ppm higher with the wind feedback in the no-ice-shelf experiments (Fig. 6a). Furthermore, Fig. 8b shows a divergence in MOC strength between the Default PC and Default FC simulations with ice shelves. This indicates that changing CO_2 forcing may influence the MOC, but only when marine ice shelves are present in the model (refer to Section 4.3). This excess carbon in the atmosphere cannot be associated with a terrestrial release, because the biosphere and soils actually held more carbon (approximately 10 Pg C) in the simulations with ice shelves (Fig. 8c). Furthermore, North Atlantic overturning was slightly stronger (Fig. 8b) for the simulations with ice shelves, which would normally suggest a greater CO_2 uptake efficiency and reduced atmospheric CO_2. However, a more substantial net loss of carbon in the ocean (Figs 8d and 8e) explained the increased atmospheric CO_2 concentrations for the simulations with ice shelves.

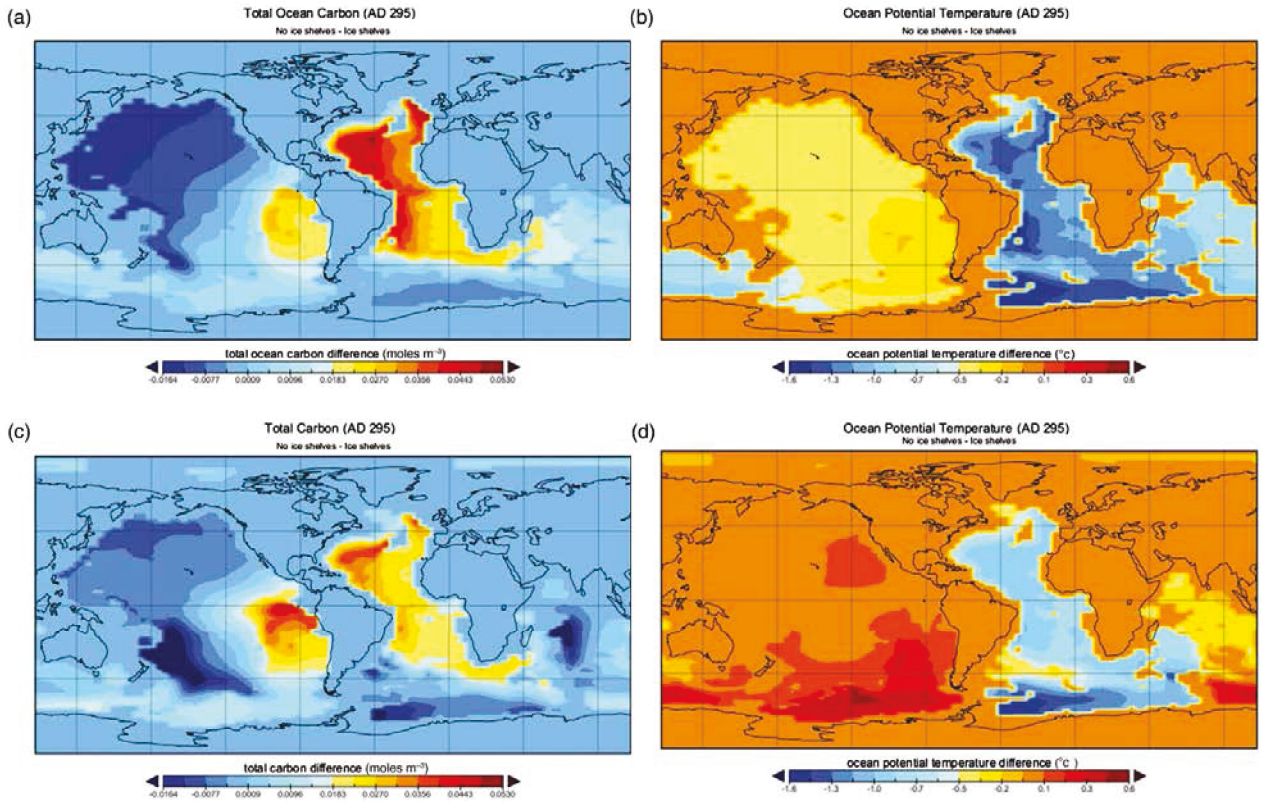

Fig. 9: The difference (BE_FC without Antarctic ice shelves - BE_FC with Antarctic ice shelves) at 295 A.D. and 3202 m depth of the spatial fields for (a) total ocean carbon concentration and (b) temperature. Similar difference fields appear in (c) and (d) but with results from the Default initial conditions PC simulations.

The model's spatial output further revealed that this loss was most pronounced in the deep ocean, particularly in the Atlantic basin between 2500 and 5500 m depth. Figure 9 compares temperature and total ocean carbon at the vertical layer with a 3202 m depth for the BE simulation (NCEP winds) initial conditions with and without ice shelves, and it indicates that deep waters in the Atlantic were significantly (1.5ºC) colder and held substantially more carbon in the simulation without marine ice shelves. However, the simulation with ice shelves had a more stagnant DWNP and thus greater carbon storage in the North Pacific Ocean (Fig. 9a). As a result, in the simulation with ice shelves, the net loss of ocean carbon from a zonally averaged perspective (not shown) was in deep waters south of the equator, concentrated in the tropical and subtropical South Atlantic Ocean.

The PC simulation (with default initial conditions) was repeated with constant ice shelves after 4000 B.C., and a similar profile was produced (Fig. 9c and Fig. 9d). This suggests that the difference in the distribution of water masses between the two simulations was dependent on ice sheet configuration (not CO_2 concentration) for the range of CO_2 values (245–280 ppm) considered in this study. Furthermore, the MOC states (as implied in Fig. 8b) and characteristics of water masses, both with and without ice shelves, were relatively stable over time, and thus this pattern changed little with increasing southern hemisphere insolation during the late Holocene.

Figure 10 further clarifies the change in water mass characteristics at depth between the two simulations. As discussed in Section 3.2, the NADW is characterized by more positive $\Delta^{14}C$ values and is generally more oxygenated, whereas deep waters in the Southern Ocean are less oxygenated and have more negative $\Delta^{14}C$ values. However, Fig. 10 indicates that waters with NADW characteristics extended much deeper (3000–5000 m) in the North and South Atlantic ocean basins for the simulation with ice shelves. However, without ice shelves, the tongue of NADW was much narrower in the Atlantic Ocean and remained mostly above 3000 m depth, with more extensive colder, carbon-rich, oxygen-deprived AABW at depth. Taken together, this evidence suggests that AABW is much more prominent in both the North and South Atlantic Ocean basins when ice shelves are not present in the model. More AABW formation in the Weddell Sea would also help explain the slightly faster replacement of DWNP in the simulations without ice shelves (Fig. 9a). When Antarctic ice shelves are kept in the simulation, AABW was limited mostly to the southern hemisphere and deep trenches in the North Atlantic Ocean, and warmer, newer, carbon-poor NADW appeared dominant between 2500 and 3500 m depth. The characteristics of deep water masses in the model simulations with ice shelves thus closely resemble today's deep water distributions.

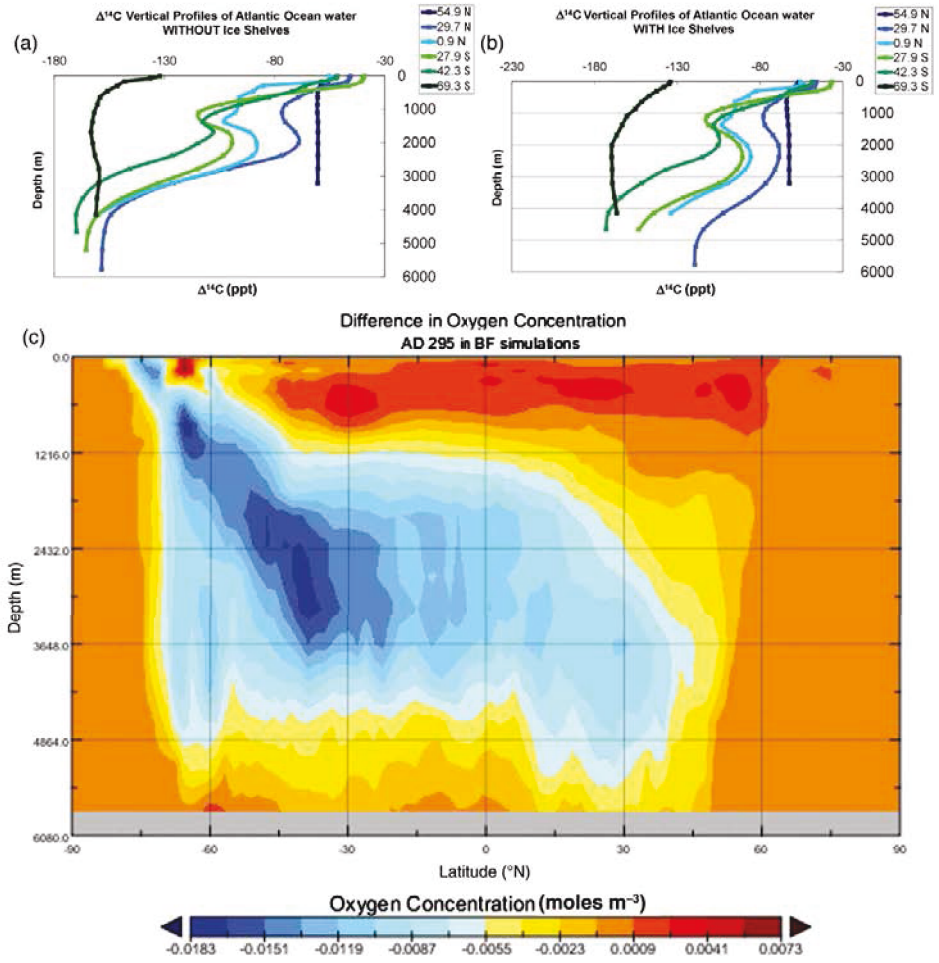

Fig. 10: The 295 A.D. vertical profiles of $\Delta^{14}C$ at grid cells in the Atlantic basin (a) in the transient BE_FC simulation without ice shelves after 3000 B.C. and (b) in the BE_FC with ice shelves (unchanging land-ice configuration after 4000 B.C.). The blue lines represent profiles in the North Atlantic Ocean: 54.9°N, 41.4°W; 29.7°N, 55.8°W; 0.9°N, 23.4°W; the green lines represent profiles in the South Atlantic and Southern oceans: 29.7°S, 23.4°W; 42.3°S, 30.6°W; 69.3°S, 41.4°W. In (c), the field difference (BE_FC without Antarctic ice shelves - BE_FC with Antarctic ice shelves) is represented at 295 A.D. for latitudinal averages of oxygen (O_2) concentration with depth.

Greater AABW formation and burial for the no-shelf experiments can be linked to greater sea-ice production and greater sea surface salinity. Although underemphasized in the model's NCEP winds, in reality the shifting the open ocean closer to the Antarctic continent also allows a greater influence of downsloping Antarctic winds. When model ice shelves were more extensive in the simulations, overlying winds (and associated heat and moisture fluxes) were weaker, less

sea ice was produced (and is generally more variable), and sinking was initiated at lower latitudes. This resulted in a less extensive AABW, a more uniform Antarctic circumpolar water mass, and dominant NADW at depth in much of the Atlantic basin. Because NADW holds less carbon than other water masses, its prominence during the simulation with ice shelves lowers ocean-wide DIC, which may further lead to a long-term increase in the pCO_2 in the global ocean and thus decreased oceanic CO_2 solubility, following Galbraith et al. (2007).

Another interesting feature in the simulations with ice shelves is the more stagnant DWNP and greater build-up of carbon in the North Pacific Ocean. This deep water was never flushed over the course of these simulations and has the potential to increase atmospheric CO_2 substantially if it were to be ventilated, as in EQ_2 and transient simulations with land ice fixed at the 6000 B.C. configuration (Fig. 4). The land ice at this earlier date (Fig. 1a) was slightly more extensive than land ice at 4000 B.C. (Fig. 1c), further restricting AABW formation to even lower latitudes with less influence from continental downsloping Antarctic winds. Therefore, with very little AABW being generated, the DWNP remained even more stagnant and isolated and warmed slowly through diffusion until it could be ventilated (through the Southern Ocean and equatorial upwelling) in a millennial-scale flushing event. With waters in both the Atlantic and North Pacific basins now newer and carbon-deprived, ocean DIC was even lower in this experiment than the simulations with ice shelves fixed at 4000 B.C., and oceanic CO_2 solubility should be reduced even more on longer time scales.

This change in deep water distribution for varying Antarctic ice shelf extents may be significant for carbon cycle comparisons between different interglacial periods. Huybrechts (2002) suggested that the edge of the Eemian (approximately 118000 B.C.) Ronne-Filchner ice sheet was 50–150 km further south than today. Taking into account sea level changes, insolation,

and $\delta^{18}O$ proxies, Pollard and Deconto (2009) used a combined ice sheet–ice shelf model to reconstruct changes in Antarctic marine ice sheets during the past five million years. Their results indicate that there were much less extensive marine ice sheets during the last three interglacial periods, during which the Ross and Ronne-Filchner ice sheets virtually disappeared (their reconstruction also correctly reproduced the present more extensive Ross and Ronne-Filchner ice sheets during the Holocene interglacial period).

Our results on deep water distribution, which are independent of orbital forcing changes and CO_2 concentrations but strongly dependent on prescribed ice shelf extent, suggest that this is one potential contributing factor to the higher atmospheric CO_2 values during the late Holocene. Indeed, the model estimate of 5–6 ppm through the ice shelf mechanism by itself (without accounting for alkalinity changes) would almost entirely account for the 8 ppm contribution that Ruddiman et al. (2011) attribute to the Southern Ocean, and other evidence suggests that marine ice shelves during the Holocene were, and remain, unusually extensive relative to many previous interglacial periods.

5 Limitations and Subsequent Work

It is necessary to underscore the limitations of our model and the methodology that we employed. Our modelling experiments lack representations of coral reefs and peatlands, both of which changed substantially and likely played critical roles in the natural carbon cycle over the course of the Holocene. As for the appropriate spin-up state to use, this has no unique answer because the Earth's climate system was not likely in steady state with orbital, CO_2, and land-ice forcing fixed at 6000 B.C., especially given the climate system's abrupt reaction to the approximately 6200 B.C. (8.2 kyr before present) cooling event/thermohaline weakening prior to this date. This is also especially true for ocean sediments (Fig. 6e), which at 6000 B.C. had likely

been responding to decreasing atmospheric CO_2 since the early Holocene CO_2 maximum (268 ppm) (Broecker et al. 1993). Thus, in order to evaluate the full response of the ocean sediments to carbonate compensation, a starting point from the post-glacial CO_2 maximum (or earlier) would be the more appropriate choice.

However, regardless of changes in ocean chemistry, the results presented here do suggest that changes in the ocean carbon reservoir depend strongly on vertical overturning in the ocean. Regarding the MOC itself, the inability of low-resolution OGCMs (in this study 1.8° latitude x 3.6° longitude) to capture downsloping currents may provide a further limitation to the interpretation of sea-ice induced instabilities in the thermohaline circulation (Winton et al. 1998).

In all of the simulations described above, the wind forcing (important for ocean surface wind stress and moisture advection) followed the seasonal cycle of the modern climatology. This is a significant caveat in the interpretation of our results, because the wind forcing from 1958 to 1998 is clearly not representative of the actual winds for the entire Holocene. For this reason, the model was unable to generate (for example) a green Sahara or a green Arabian Peninsula during the mid-Holocene. Although GCM time-slice winds have been produced for different periods of the Holocene, because these periods have climate states that do not correspond exactly to those in our model, we tested our results with NCEP winds using the wind parameterization feedback available in the UVic ESCM (Weaver et al. 2001). Sensitivity studies (Figs 6 and 8, right panels) suggest that the wind feedback (for all initial conditions) only leads to a net 1–2 ppm increase in atmospheric CO_2 compared to the NCEP climatology simulations, mostly after 1 A.D. as a result of increasing overturning in the Southern Ocean.

6 Conclusions

We used the UVic ESCM v. 2.9 to investigate various aspects of the natural carbon cycle from 6000 B.C. to the pre-industrial period. Because the spin-up (EQ_1) did not reach a steady climate state but instead produced millennial-scale oscillations in the thermohaline circulation, we used different meridional overturning conditions (default, before a flushing event (BE), and during a flushing event (DE)) as initial conditions for transient simulations. These different initial conditions explore the possibility of different deep water mass distributions (Section 3.3), with BE initial conditions representing a dominant NADW in the deep Atlantic basin while DE initial conditions start from a state with extensive, newly produced AABW dominating the deep Atlantic basin.

We performed several experiments with atmospheric CO_2 prescribed to observed values (PC simulations), whereas in others the carbon cycle was allowed to freely evolve (FC). For all transient simulations, terrestrial carbon storage increased continuously during the Holocene, placing this model's output in a league with studies such as Kaplan et al. (2002) and Kleinen et al. (2010), which showed an increase in natural terrestrial carbon storage during the Holocene. In general, the values we obtained (approximately 100 Pg C) are in the positive part of the -90 to +370 Pg C range of terrestrial carbon uptake summarized in Joos et al. (2004).

Under a steady MOC with the Southern Ocean capped by sea ice and no Antarctic ice shelves, terrestrial carbon sequestration continued during the late Holocene with a corresponding decrease in ocean carbon storage, leading to little net change (on the order of a few parts per million) in atmospheric CO_2. This relatively constant MOC and atmospheric CO_2 is a feature of every UVic free carbon simulation for the late Holocene with and without ice shelves after 4000

B.C. This long-term stabilization occurs largely as an indirect consequence of an unchanging land ice configuration and, consequently, a steady pattern of deep-water distribution.

As discussed in Section 4.4, the presence of ice shelves off the coast of Antarctica led to less Antarctic deep water formation, slower circulation of deep waters in the North Pacific, and the dominance of newer, carbon-poor NADW in the Atlantic basin. Significant AABW formation occurred mostly during the centennial-scale ventilation events (the dips in Fig. 6b associated with brief southward retreats in the sea-ice margin), and AABW otherwise remained largely constrained to the Southern and abyssal oceans. At the same time, atmospheric CO_2 increases during these periods of short-term ventilation in response to ocean carbon losses (mostly from the deep Southern Ocean) and also to climatically induced releases of terrestrial carbon at high latitudes associated with these events. During periods of more localized deep circulation in the Southern Ocean, atmospheric CO_2 tended to increase while oceanic carbon decreased slightly.

The net effect is that the relatively carbon-rich AABW was regionally constrained and better locally-ventilated in the transient simulations described in Table 1 before the disappearance of marine ice shelves in the model between 4000 and 3000 B.C. Correspondingly, with less high-carbon AABW in the deep Atlantic, atmospheric CO_2 stabilized at a higher value (257–259 ppm). This suggests that, for more extensive ice shelves and a distribution of deep water masses comparable to their known orientations today, the natural carbon cycle as simulated by the UVic ESCM produced little net change in atmospheric CO_2 after 4000 B.C.

On the other hand, the transient simulations without ice shelves after 3500 B.C. produced more carbon-rich Antarctic deep water that spread globally through the deep ocean. This led to a slightly better-circulated North Pacific (with less deep-water carbon storage in this region) but

significantly greater carbon storage in the deep Atlantic basin. Because more carbon remained in the deep ocean globally as a result of the greater prevalence of deep Antarctic-generated waters, this caused CO_2 to stabilize at lower values near 251–252 ppm for the FC and BE_FC simulations. This deep water orientation and carbon storage pattern stayed relatively unchanged during the late Holocene, regardless of the evolution of insolation. Furthermore, the prescribed carbon (PC) simulation without ice shelves after 3500 B.C. had significantly more AABW formation than a PC simulation with ice shelves (Figs 9c to 9d), suggesting that the deep water distribution is not sensitive to the range of CO_2 values during the Holocene. With the "ice shelf effect" on the global thermohaline circulation being relatively independent of both CO_2 and orbital forcing, we speculate that the Holocene's more extensive Antarctic ice shelves compared to the three previous interglacial periods (Pollard and Deconto 2009) may be a contributing factor to the higher observed CO_2 concentrations.

Furthermore, the Holocene transient simulation with fixed ice after 6000 B.C. (in the case of slightly more extensive Antarctic ice shelves from Fig. 1a) produced AABW that was even more local in scale. In this case, deep water in the North Pacific (DWNP) stagnated, accumulated carbon and warmed diffusively, while even the mid-latitude South Atlantic Ocean retained a deep and prominent NADW signature. This led to a diffusive warming of the DWNP, which was eventually flushed out through the equatorial Pacific and Southern oceans when it became vertically unstable in millennial-scale flushing events. Thus, the more localized centennial-scale flushes were replaced with a deep flush of carbon to the atmosphere on 1000-year time scales, which raised atmospheric CO_2 values for more than a millennium.

Although not sensitive to insolation, EQ_3, EQ_2 and Section 4.1 demonstrate that the periodicity of these millennial-scale events, as well as the "thoroughness" of the flushing of the

North Pacific's deep carbon reservoir to the atmosphere, is sensitive to the winds used. In particular, the use of NCEP winds led to longer periods with less frequent flushes, whereas the wind feedback adjustment to the climate state suggests more frequent, moderate flushes of DWNP carbon during the late and mid-Holocene. For the transient simulations with transiently evolving ice shelves, the thoroughness of DWNP ventilation around 5000 B.C. appeared to be dependent both on winds (with the wind feedback leading to more thorough flushes) as well as to some extent on initial conditions (with BE initial conditions producing the most complete ventilation of DWNP). In turn, the much lower deep-ocean DIC in both the North Pacific and the Atlantic Ocean basins for more thorough DWNP ventilations would help reduce ocean CO_2 solubility globally on long time-scales, potentially contributing to an increase in atmospheric CO_2. Therefore, the physical dynamics of the MOC and the source region characteristics of deep water masses highlighted in this study likely feed back to other processes controlling CO_2 solubility in the oceans (such as carbonate compensation, shallow water sediments, and temperature changes).

Previous studies have also noted that the efficiency of carbonate compensation, SST changes, and human terrestrial release mechanisms might have depended on the thermohaline circulation (Ruddiman 2007; Broeker and Ellis 2007). The results presented here indicate that the millennial-scale fluctuations in the MOC, which may only have an amplitude of 2–3 Sv globally but are associated with significantly different distributions of water masses, control atmospheric CO_2 concentrations during the Holocene to a non-negligible degree. Such patterns influence both the release of oceanic and terrestrial carbon to the atmosphere as well as the long-term oceanic absorption of atmospheric CO_2. Schmittner et al. (2007b) also highlighted the importance of

similar Southern Ocean ventilation patterns in controlling global atmospheric CO_2 levels, although on a much longer time scale than that considered here.

This strong sensitivity to ocean circulation and paleo-ice conditions is a factor not considered in previous simulations using present-day ice, such as in Schurgers et al. (2006), and thus requires further exploration using the UVic ESCM and other models. Our results also underscore the fact that millennial-scale variability and data assimilation of proxy evidence (land ice in this case), two major sources of uncertainty in modelling studies (Crucifix et al. 2005), may have played a critical role during the Holocene carbon cycle.

However, with all the simulations considered, the model only produced no net change (approximately 260 ppm) in atmospheric CO_2 since 6000 B.C. Therefore, regardless of the initial conditions used or Antarctic ice-sheet extent, no simulations allowed for a permanent increase in CO_2 over the course of the Holocene as in the observed record. Figure 7 suggests that an external release of 400 Pg C into the earth system would be required to reproduce the increasing CO_2 levels (to 280 ppm) during the Holocene. Thus, the inability of the model to conserve carbon for the prescribed CO_2 simulations suggests that some kind of external forcing not represented in the model's carbon cycle after 4000–3000 B.C., such as human land use and coral reefs, may be responsible for much of the Holocene's observed CO_2 increase.

Chapter 5: Historical Land Cover Change during the Holocene: An Application of the UVic ESCM

Having established a potentially important sensivitiy of the carbon cycle to Antarctic marine ice shelves when only natural processes are considered, we also studied the model's evolution in response to anthropogenic land cover change. This was done by adding together both cropland and pasture data from the HYDE 3.1 database (Klein Goldewijk et al. 2011) and introducing them into the model as agricultural fractions, which prevent trees and shrubs from growing in a portion of each gridcell where land use is assigned. The unmodified HYDE 3.1 database is broadly seen as underestimating early agricultural fractions, as early horticulture and agriculture used cruder technologies and required more land use per person than today's more intensive agriculture (Ruddiman and Ellis 2009; Kaplan et al. 2011). However, both historical human populations and land use per person are poorly-constrained, representing a high degree of uncertainty in modelling studies (Boyle et al. 2011; Kaplan et al. 2011). To address these issues, we designed two scenarios that scaled HYDE 3.1 data to represent greater land use during the early agricultural era (up to 8 hectares per person). In addition, these experiments were repeated with a basic parameterization of soil erosion as agricultural activities intensified. For the modelling experiments presented here, as for most of those in Chapter 3, the original ICE-4G configuration was maintained. As in Chapter 4, the alkalinity of the oceans was kept constant to isolate the physical contributions of deforestation to atmospheric CO_2.

Abstract

The University of Victoria Earth System Climate Model v. 2.9 (UVic ESCM) is used in this study to examine the role of anthropogenic land cover change (ALCC) in the Holocene carbon cycle. Three ALCC scenarios were developed by scaling data from Hyde 3.1 (Klein Goldewijk et al 2011). Additionally, we introduced a new parameterization of soil management and erosion associated with increased tillage and agricultural intensity into the model. The transient simulations, covering the period from 6000 B.C. to 2000 A.D., indicate that even very high anthropogenic land use fractions during the Neolithic and Bronze ages led to a small (3-5 ppm) contribution to atmospheric CO_2 concentrations by 1 A.D., with a larger 10 ppm atmospheric CO_2 increase obtained in the ALCC scenarios by the beginning of the Industrial Era. While only able to explain a small fraction of the pre-industrial CO_2 trend, these figures are higher than in some previous studies. In addition, certain ALCC scenarios with lower per-capita land use in the mid-to-late Holocene had greater sedimentation than a simulation without ALCC, implying that more moderate deforestation scenarios could potentially stimulate a decrease in ocean alkalinity (through model feedbacks with ocean circulation) rather than the expected increase. In addition, our results with the original Hyde 3.1 database suggest that lower per-capita land use could stimulate greater deep water formation in the North Atlantic and a relatively large (+0.10°C) increase in global temperatures by 1 A.D. This process reduced oceanic uptake of atmospheric CO_2 in our simulations. Overall, however, all simulations indicate that an increase in sediment precipitationfrom other processes would be necessary to reduce the oceanic sink for the ALCC release and to promote an increase in atmospheric CO_2 during the mid-to-late Holocene.

1 Introduction

The contribution of deforestation to the Holocene rise of atmospheric CO_2 has been a subject of intense debate in recent years, as evidenced by the Special Issue of *The Holocene* in 2011 dedicated to the topic. The idea that horticultural, pastoral, and agricultural activities (human land use) might provide non-negligible contributions to the atmospheric CO_2 rise was eloquently proposed in Ruddiman and Thompson (2001) and Ruddiman (2003) as the "Early Anthropogenic Hypothesis." Ruddiman noted that the Holocene experienced a 20 ppm increase in atmospheric CO_2 since 6000 B.C., whereas the previous three interglacials were characterized by declines in atmospheric CO_2 due to greater terrestrial uptake. Because of the deviation from previous interglacials, Ruddiman (2003, 2007) and Ruddiman et al. (2011) argued that human land use during the Holocene might help explain the 'unnatural' increase in atmospheric CO_2. Ruddiman (2003) originally proposed that this anthropogenic forcing could account for as much as 40 ppm atmospheric CO_2 by the pre-industrial period, although subsequent work (Ruddiman 2007; Ruddiman et al. 2011) has scaled back this estimate to ~7 ppm.

A significant challenge to the Early Anthropogenic Hypothesis comes from both $\delta^{13}C$ observations and Earth system modeling efforts. As photosynthesis generally prefers ^{12}C to ^{13}C, a decrease in $\delta^{13}C$ (i.e., an increase in ^{12}C content of the atmosphere) would be expected from a major terrestrial release. However, Elsig et al. (2009) documented very little change in atmospheric $\delta^{13}C$ in ice cores (a decrease of 0.05‰ after ~4000 B.C.), somewhat less than the 0.2‰ from the lower-resolution Taylor Dome core (Indermühle et al. 1999). Elsig et al. (2009) argued that the Holocene rise in CO_2 could thus not be explained by anthropogenic land use and attributed 6 ppm to carbonate compensation in response to terrestrial uptake, 3 ppm to a net 50 Pg C terrestrial release, and proposed that the remaining rise could be caused by coral reefs (5-8

ppm). Similarly, Goodwin et al. (2011) calculated that the best fit to $\delta^{13}C$, temperature, and carbonate proxy data for the mid-to-late Holocene would be a 100 Pg C reduction of the soft tissue pump and a 350 Pg C sedimentation. Ruddiman et al. (2011), however, proposed that an relatively unchanging $\delta^{13}C$ could also be accounted for by peatland uptake (which would increase $\delta^{13}C$) balancing the effect of deforestation (decreasing $\delta^{13}C$). In other words, a terrestrial release of 350-360 Pg C (Kaplan et al. 2011; Olsen et al. 1983) could be balanced by peatlands, which extract more ^{12}C than other forms of vegetation and thus may have a greater influence on atmospheric $\delta^{13}C$ than terrestrial release related to land use.

However, beyond the observational constraints related to $\delta^{13}C$, Earth-system modeling efforts have also been unable to produce the Holocene CO_2 increase from the effects of deforestation. Olofsson and Hickler (2008) developed a land use database distinguishing between shifting and permanent cultivation for the past 6000 years but found only a 114 Pg C net terrestrial carbon release from agriculture during the pre-industrial period, with just 24 Pg C of this release occurring before 1 A.D. They also found that their simulated emissions were enhanced (35% greater) with the inclusion of slash-and-burn agriculture over permanent agriculture. A database for anthropogenic land cover change since 800 A.D. was also developed by Pongratz et al. (2008) and applied to an AOGCM in Pongratz et al. (2009). Their simulation revealed that much of the carbon released from land use activities was re-sequestered by the terrestrial biosphere, leading only to a small increase in atmospheric CO_2 (11.5-13.4 Pg C, or 5-6 ppm) between 800 A.D. and 1850 A.D. Furthermore, Pongratz et al. (2009) estimated (through extrapolation) an even smaller contribution (0.5-1 ppm) from agriculture prior to 800 A.D. Similarly, Strassman et al. (2008) determined that the terrestrial biosphere provided an important buffer against terrestrial releases by re-absorbing 25% of the anthropogenic land use emissions.

In response to these low figures, Ruddiman and Ellis (2009) countered by reviving the Boserup hypothesis (Boserup 1965), which poses that land area-per-person was significantly less in the industrial age than during the early agricultural era due to cruder technology. Several land use reconstructions (e.g., Ramankutty and Foley (1999) and Klein Goldewijk et al. (2011)), however, assume that per capita land use in moderns times was comparable to historical figures. Ruddiman and Ellis (2009) argue that the less-developed technologies and crop rotations during the Neolithic period required relatively larger per-capita land use in order to support the human populations of the time, which might have allowed for a greater deforestation during the mid-Holocene than previously thought. Ruddiman and Ellis (2009) cite a figure of 4 hectares (ha) per-capita (from Gregg (1988)), whereas Kaplan et al. (2011) assign anthropogenic land use as high as 7-8 ha per-capita in their database for parts of Asia. Furthermore, Boyle et al. (2011) also suggest that the population figures traditionally used to create historical land use reconstructions (McEvedy and Jones 1978) could underestimate human populations by as much as an order of magnitude.

Stocker et al. (2011) adapted the Hyde 3.1 database (Klein Goldewijk et al. 2011) to address the Boserup hypothesis by scaling land use fractions (as high as 9.5 hectares per person) for simulations with the BernCC model. This comprehensive modeling study found that the increase in atmospheric CO_2 varied between 2-7 ppm (without soil management/tillage) to 3-10 ppm with soil management (i.e., with the litter flux to the soils reduced by 13%) between 12000 B.C. and 1700 A.D. Stocker et al. (2011) also found that re-fertilization of the biosphere sequestered 20-30% of the original release. Furthermore, their simulation with 9.5 ha/person land use efficiency gave only a 3.5 ppm rise by 1 A.D. Similarly, in an extreme scenario in which CO_2 re-fertilization was suppressed, atmospheric CO_2 increased by only 8 ppm between 6000

B.C. and 2005 A.D. The authors also discovered that earlier land use change provided ample time for the dissolution of ocean sediments (in response to a CO_2 pulse into the ocean from the deforestation release) to increase alkalinity, causing the oceans to take up more of the terrestrial release (and leading to lower end-result atmospheric CO_2).

Most of the modeling studies cited above (Olofsson and Hickler 2008; Strassman et al. 2008; Stocker et al. 2011; Kaplan et al. 2011) evaluate the impact of anthropogenic deforestation on CO_2 using the Lund-Potsdam-Jena Dynamical Global Vegetation Model (LPJ DGVM). Pongratz et al. (2009) used a different vegetation model (JSBACH from Raddatz et al. (2007)) but only directly evaluated anthropogenic land cover change (ALCC) since the Medieval period. Thus, in order to provide an independent estimate from a different model than the LPJ DGVM used for most studies of Holocene deforestation, we include Holocene ALCC in the University of Victoria Earth System Climate Model (UVic ESCM, or simply the UVic model) v. 2.9. The UVic ESCM includes a different DGVM: the Top-Down Representation of Interactive Foliage and Flora Including Dynamics model (TRIFFID) (Cox 2001) coupled to the Met Office Surface Exchange Scheme (MOSES) soil module (Cox et al. 1999). As in Stocker et al. (2011), we scale the Hyde 3.1 data for different assumptions of land use efficiency (land area per person). This includes the original HYDE database, a scenario slightly modified from Ruddiman and Ellis (2009) with land use efficiency decreasing linearly from 4.5 ha/person to the original Hyde resolution at 2005 A.D. of ~1 ha/person, and a scenario with much higher Neolithic land use at ~7.5-8 ha/person before 1000 B.C. and a linear decrease to ~1ha/person between 1000 B.C. and 2005 A.D.

We also present a suite of simulations to test the effects of soil management (tillage and soil erosion). In general, shifting cultivating (which dominated early forms of agriculture, as in

Olofsson and Hickler 2008) requires little to no tillage, whereas permanent agriculture tends to apply more advanced and intensive tillage techniques (Lal 1989). The effect of tillage on soil organic carbon content varies considerably depending on soil type and other environmental factors; in general, these effects are largest on the soil organic carbon content of the upper soil layer. West and Post (2002) suggested that tillage agriculture increased carbon storage by as much as 570 kg C ha^{-1} yr^{-1} (mostly above 30 cm depth). Similarly, Blanco-Canqui and Lal (2008) indicated that no-tillage soils retained 21-50% more soil organic carbon in the upper 60 cm soil layer than plow-tillage soils. Given these results, the slow transformation from low-tillage (shifting) agriculture to plow-tillage agriculture might be associated with a significant decrease in the carbon content of cultivated soils. For this reason, unlike Stocker et al. (2011), in which fixed reductions of the carbon flux from vegetation to soils were used, we applied a linearly-increasing respiration of the litter soil flux to the atmosphere for tillage.

2 Model Description and ALCC Scenarios

2.1The Uvic ESCM and TRIFFID DGVM

The UVic ESCM (v. 2.9) is an Earth system Model of Intermediate Complexity (EMIC) (Claussen et al. 2002) and has been used to investigate the natural carbon cycle (without deforestation) during the Holocene in a previous study (Chapter 4). All components operate on a 1.8° lat x 3.6° lon resolution. The model's core component is an ocean general circulation model, the Modular Ocean Model v. 2.0, with 19 vertical levels (Pacanowski 1995). Due to the general coarseness of the ocean model resolution, eddies are parameterized according to Gent and McWilliams (1990). The model includes both inorganic (Ewen et al. 2004) and organic (Schmittner et al. 2008) ocean carbon, the latter treated by a Nutrient-Phytoplankton-Zooplankton-Detritus (NPZD) model. New to version 2.9 of the model is an oxic-only sediment

module (Archer et al. 1996), which allows for ocean-sediment interactions to influence ocean alkalinity but does not include a parameterization of coral reefs or shallow water sedimentation. The simulations presented here set the weathering rate to follow the sedimentation rate, which maintains a constant alkalinity profile, thus allowing us to isolate the impact of deforestation from other changes in the ocean carbon reservoir.

The atmosphere of the UVic model is a two-dimensional energy-moisture balance model (the EMBM), described in Fanning and Weaver (1996) and Weaver et al. (2001). Atmospheric temperature is modulated by local radiative forcings from longwave (greenhouse gases) and shortwave (insolation) radiation as well as the diffusion of heat between grid cells. Atmospheric moisture, which can be both diffused and advected, is calculated through evaporation minus precipitation. Precipitation occurs when relative humidity in a grid cell exceeds 85%. Evapotranspiration and the advection of atmospheric moisture, as well as surface wind stress on the ocean and the movement of sea ice, require a prescribed wind field. For this, we applied the model's (v. 2.9) internal wind feedback, which perturbs NCEP winds (Kalnay et al. 1996) with a thermal wind calculated from the model-generated spatial temperature gradient (Weaver et al. 2001).

The terrestrial scheme of the model uses the Top-Down Representation of Interactive Foliage and Flora Including Dynamics (TRIFFID) model (Cox 2001) with a simplified hydrology, coupled to the Met Office Surface Exchange Scheme (MOSES) with a 1 m surface soil layer with microbial respiration (Cox et al. 1999). More details on the integration of these components into the terrestrial biosphere can be found in Meissner et al. (2003). The TRIFFID module defines five plant functional types (PFTs) that characterize global vegetation distributions: broadleaf trees (deciduous and tropical forests), needleleaf trees (coniferous and

boreal forests), C_4 (mostly arid tropical) grasses, C_3 (mostly prairie and tundra) grasses, and shrubs (small trees and bushes representing semi-arid tropical and subtropical vegetation as well as high latitude boreal-tundra transition regions). Northern peatlands are not included in the current model setup. Every land grid cell maintains a tiny land fraction (0.01) for each PFT so that any individual vegetation type has the potential to thrive if climatic (temperature and moisture) conditions turn favourable. Many regions can support more than one PFT, and in these areas a dominance hierarchy is established by the model in which higher-canopy trees can take over more of the grid cell fraction at the expense of shrubs and grasses, and shrubs can in turn out-compete grasses if conditions for growth are favourable. Grasses thus only replace trees if the tree fraction (and hence tree NPP) decreases in a given grid cell. In grid cells where conditions for C_3 and C_4 grasses or needleleaf trees and broadleaf trees are both favourable, the two tree or grass types compete and the tree or grass-type with the highest grid-cell canopy predominates. Due to application of Lotka-Volterra equations in the TRIFFID model, one vegetation type tends to dominate each land point.

The growth of each PFT depends primarily on climatic conditions favourable to growth (namely, soil moisture and air temperature). For example, broadleaf trees, shrubs, and C_3 grasses can only photosynthesize between 0°C and 36°C, broadleaf trees between -5°C and 31°C, and C_4 between 13°C to 45°C. The seasonality of photosynthesis, in turn, affects net primary productivity (NPP) for each PFT. In high and mid-latitude regions, needleleaf trees can photosynthesize for a substantially greater fraction of the year than broadleaf trees. If both trees are present without moisture stress, the NPP of needleleaf trees in these regions is naturally greater than broadleaf trees. NPP in turn drives the density (represented by leaf area index, or LAI) and fractional grid cell coverage of that PFT. Once a PFT has a large NPP but a small

fractional coverage (that is, a large LAI), more of the NPP is dedicated to PFT spreading, i.e., increasing the grid cell fraction of that PFT. The length of the growing season (controlled largely by temperature) is not the only constraint to NPP in the TRIFFID model. NPP is defined as respiration subtracted from gross primary productivity, and gross primary productivity decreases to zero as soil moisture approaches the PFT-specific wilting soil moisture concentration. The above-ground biomass of needleleaf trees, broadleaf trees, and shrubs is generally always greater than that of grasses. However, net terrestrial carbon storage can increase where shrubs are replaced by grasses, especially in cold regions (such as northern Eurasia) where soil carbon accumulation is much larger for grasses than for shrubs (Chapter 4). Nitrogen-cycle limitations to growth and CO_2 fertilization are not included in the version of the model used here.

Pastoral and agricultural areas are defined by ALCC fraction of each land model grid cell, ranging from 0.0 (no anthropogenic land use) to 1.0 (the entire grid cell is used for agriculture and pastoral activities). There is currently no distinction in the UVic ESCM v. 2.9 between crops and pasture, and both types of land use are treated in the same manner. Crop/pasture types are parameterized as C_3 and C_4 grasses, and there are neither behavioral differences between crop grasses and natural ones nor specialized treatment of slash-and-burn agriculture. Where an ALCC fraction is greater than zero, the model reserves a corresponding areal fraction of the grid cell for C_3 and C_4 grasses only. If C_3 and C_4 are already naturally occurring in these grid cells, the natural grasses are counted as part of the crop area. All other PFTs in the fractional area are cut down, with all vegetation carbon burned directly to the atmosphere. This only has an influence on vegetation and soil carbon storage for grid cells where shrubs, needleleaf trees, and broadleaf trees are present or could be present. In regions where bare ground or grasses are naturally simulated, there is no change in PFT coverage or carbon storage when an ALCC

fraction is assigned (except for soil management simulations in the latter case, discussed in Section 2.3). This tends to limit contributions of agricultural release in in the Arabian peninsula (Mesopotamia), parts of northern Africa, and the region between the Black and Caspian seas, which the TRIFFID model tends to simulate as bare ground (e.g., Handiani et al. (2012a) and Chapter 4).

2.2 ALCC scenarios

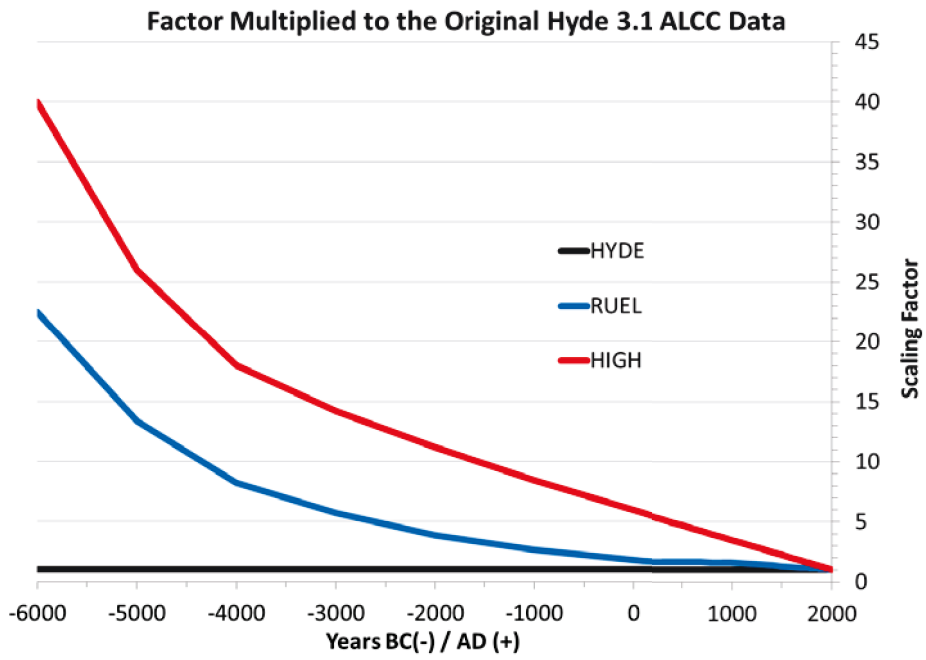

Fig. 1: The scaling factor, a constant multiplied to the original Hyde 3.1 anthropogenic land use fraction (after interpolation to the UVic model grid and the addition of the respective fractions of crops and pasture) at each grid cell, for the three ALCC scenarios presented in this study.

The land use scenarios applied in this study were created by scaling land use fractions from the Hyde 3.1 database (Klein Goldewijk et al. 2011). The Hyde 3.1 land use fractions were first interpolated to the UVic model's resolution using the MASK_LONLATTIME interpolation scheme developed for IDL (Stone 2011). After processing both pasture and croplands from the Hyde 3.1 database, the two fractions (crops and pasture) were added together for each grid cell to

produce a total ALCC distribution from the Hyde 3.1 dataset. The ALCC distributions were then scaled (multiplied) by a constant factor for different time periods to simulate different land use per-capita. The scaling factors for each time step are given in Fig. 1, and the scenarios are characterized as follows:

(1) HYDE: The original Hyde 3.1 land use fractions, which likely underestimates ALCC for the Neolithic period (Kaplan et al. 2011).

(2) RUEL: a configuration analogous to Ruddiman and Ellis (2009), with roughly 4.5 ha/person land use at 6000 B.C., decreasing linearly to the Hyde 3.1 land use efficiency at 2005 A.D. (~1 ha/person).

(3) HIGH: a simulation inspired by low land use efficiencies described in Kaplan et al. (2011), starting with very high land area per person (~8 ha/person) between 6000 B.C. and 1000 B.C., followed by linearly-increasing land use efficiency (from ~8 ha/person to ~1 ha/person) between 1000 B.C. and 2005 A.D. This scenario most closely resembles the "OS" sensitivity simulation from Stocker et al. (2011), although it assumes a relatively fast technology-based transition starting at 1000 B.C., allowing for reforestation in some areas during the late Iron Age.

The model's continental configuration (Weaver et al. 2001), however, is different from that provided in the original land use database, which results in some interpolated ALCC fractions being over ocean grid cells. Furthermore, the RUEL and HIGH scenarios have land use fractions greater than one for certain regions and time steps. To address both problems, a scheme was developed to reapportion crop fractions to the nearest available land grid cells not already fully consumed by land use. For ALCC fractions over ocean grid cells, we reassigned the excess ALCC area as far as three model grid points away from the original ocean cell (allowing

land grid cells to have an ALCC fraction greater than one during this reallocation). Once this redistribution was applied, for grid cells with ALCC fractions over land greater than one, the excess land use area (excess land use fraction multiplied by grid cell area) was reapportioned as far as seven grid cells away from the original land point; however most ALCC fractions could be redistributed one grid point away from the original cell, with very few redistributions extending beyond a radius of three grid points.

In more detail, this reallocation scheme was accomplished by first calculating the available non-ALCC land area in the eight cells (including corner cells) that bracketed the original grid cell (i.e., at a radius of one grid cell from the original grid point). This was followed by reapportioning the excess ALCC area equally between the available land grid cells within this radius. Where some grid points had less non-ALCC land area than others, each available grid cell was allocated with the minimum available area (determined by the grid point with smallest available land area) first before the remaining excess land use area was reapportioned equally to the other available cells. Where there were no surrounding grid cells over land, no surrounding land points with ALCC fractions less than one, or excess ALCC remaining after the first stage of redistribution, the same reapportionment formula was applied at a radius of two grid points away from the original cell, and then three grid points away from the original cell, etc., until the total excess crop area from the original cell had been redistributed. For ALCC over ocean grid points, the fractional areas not reapportioned within three grid cells from the original ocean cell were simply deleted. Similarly, for excess

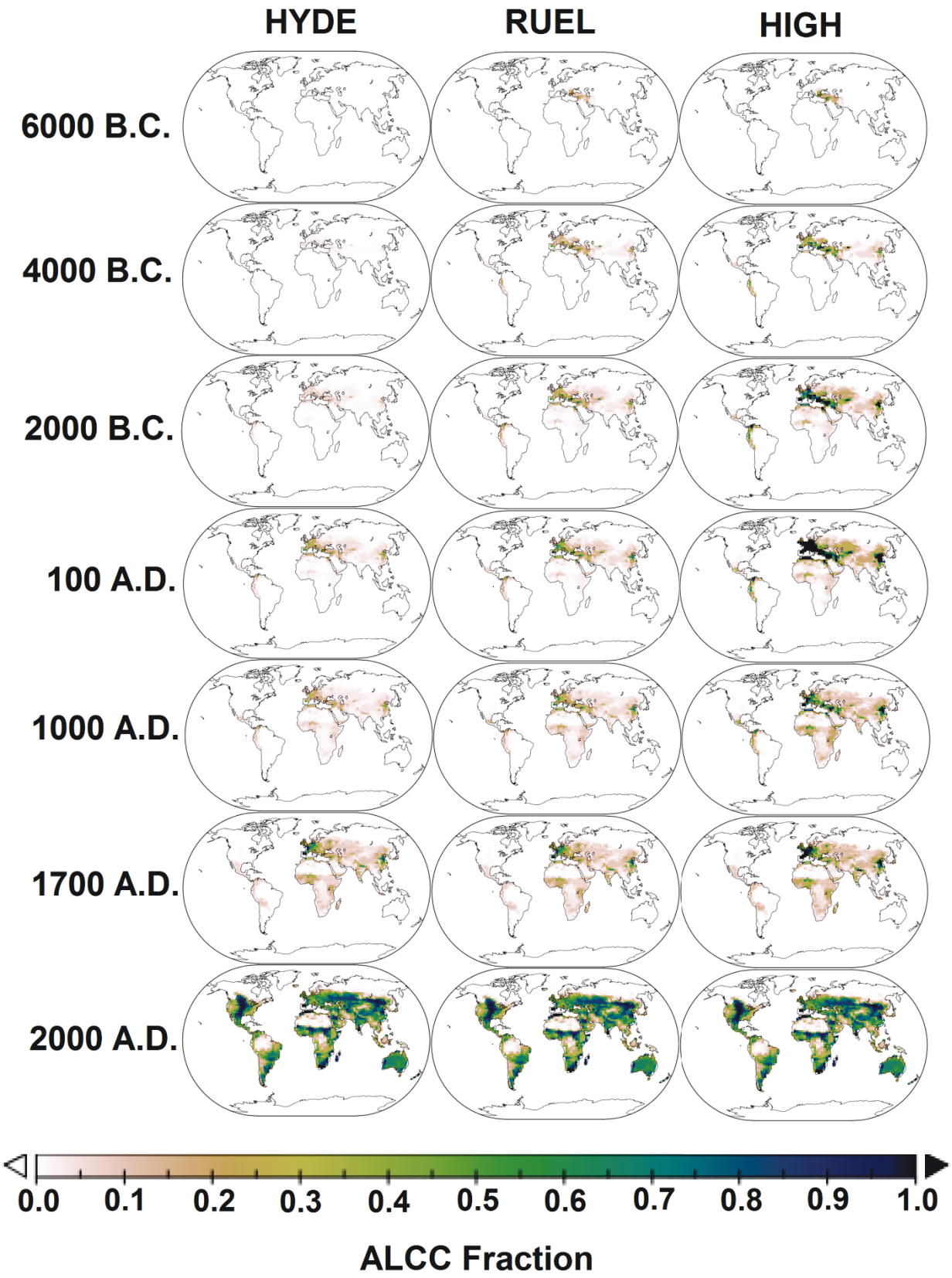

Fig. 2: The anthropogenic land use fractions for the HYDE (left column), RUEL (centre column) and HIGH (right column) scenarios described in Section 2.2. The ALCC fractions are given at selected dates (from top to bottom) for 6000 B.C. (first row), 4000 B.C. (second row), 2000 B.C. (third row), 100 A.D. (fourth row), 1000 A.D. (fifth row), 1700 A.D. (sixth row), and 2000 A.D. (seventh (bottom) row).

ALCC reapportionment over land not accomplished within seven grid cells away from the original data point (very rare), the remaining excess ALCC fractional area was removed. The goal of this reallocation of ALCC areas was to represent all possible human land use on land grid points (due to the model's simplified continental configuration). This method helped reapportion ALCC fractions from large land areas not represented in the model, such as the island of Cuba and parts of Indonesia, to nearby land areas with similar biomes. This interpolation strategy, however, is quite unlike Stocker et al. (2011), who cut off ALCC fractions at the edges of continents after interpolating to model resolution so as not to misrepresent the original land area fraction. Stocker et al. (2011) conceded that their method of interpolation might underestimate global ALCC fractions by eliminating ALCC beyond their model's continental configuration. By contrast, our methods likely overestimate them, especially for coastal grid points (e.g., the Iberian peninsula). The simulations here should thus be interpreted as a maximum impact scenario for the Hyde 3.1 land use configuration (and associated scaling scenarios RUEL and HIGH) as applied in the UVic ESCM. Land use fractions for each scenario for select dates are given in Fig. 2.

2.3 Soil Management

The simulations described above in Section 2.2 do not provide specialized treatment of croplands (i.e., no increase in soil erosion or microbial respiration in ALCC-affected regions). In these experiments, crop C_3 and C_4 grasses behave exactly as natural C_3 and C_4 grasses in the model. This may underestimate the contribution of deforestation, particularly in the upper mid-latitudes where shrublands are converted to grasslands, the latter having a generally higher parameterized soil carbon storage in the MOSES/TRIFFID module. However, greater soil erosion and/or respiration associated with tillage agriculture likely removes some of this carbon

from the near-surface soil layers. Thus, the three modeling experiments described above (HYDE, RUEL, and HIGH) were repeated with a simple soil management scheme designed to parameterize an increasing intensity of tillage agriculture with time.

This was accomplished by requiring that a set fraction, the soil management fraction, of the ALCC-assigned area (including both pasture and croplands) be converted into bare ground, which has no vegetation. Thus, all vegetation carbon within the soil management fractional area is released to the atmosphere and the remaining soil carbon continues to respire naturally (with no further soil carbon inputs). However, in grid points that already have a bare ground fraction greater than zero, this bare ground fraction is subtracted from the initial soil management fractional area for that particular cell, with only the remaining fractional area leading to a release of carbon to the atmosphere. Early horticulture (slash-and-burn agriculture) required relatively little tillage, and vegetation carbon as well as soil carbon is also removed in this simple parameterization. For these reasons, we assumed that the soil management fraction was relatively low for the Neolithic period, staring at 5% of the ALCC fraction in each grid cell at 6000 B.C. This percentage, which defines the soil management fractional area, was linearly increased to 30% at the end of the simulation (2005 A.D.) to reflect studies of relatively-intense tillage agriculture at present (e.g., Blanco-Canqui and Lal 2008). Not all studies agree that soil carbon reduction near the surface actually increases the respiration of this carbon to the atmosphere, with some suggesting that decomposition rates may actually decrease when the eroded soil is sedimented into valleys, lake beds and wetlands (Quinton et al. 2010). For this reason (and for the elimination of vegetation in the soil management fraction as well as the application of the same soil management fraction to both pasture and cropland in the current model configuration), the results presented here likely overestimate the increase in tillage-induced changes to soil carbon

storage. It should be noted that, in the present simulations, soil management does not influence the land erosion weathering rate (which is prescribed to follow the net sedimentation rate).

2.4 Simulations Setup

Initial conditions for the simulations presented in this study were taken from a transient simulation forced from 21000 B.C. to 6000 B.C. with time-evolving prescribed land ice (ICE-4G from Peltier 2002), orbital forcing (Berger 1978), and atmospheric CO_2 following the ice core record in Petit et al. (1999). This simulation is described in Chapter 3 as the PC CA simulation (i.e., prescribed atmospheric carbon content with constant alkalinity). The carbon cycle was then freed at 6000 B.C., allowing atmospheric CO_2 and other carbon reservoirs to evolve without being forced to follow the ice core trend; however, a constant ocean alkalinity was maintained. These transient simulations continued to include the prescribed forcing from continental ice sheets from the interpolated ICE-4G dataset (Peltier 2002) and Milankovitch forcing (Berger 1978). A simulation without ALCC fractions, denoted "FNCC" for "free natural carbon cycle," was run from 6000 B.C. to 2000 A.D. to illustrate the evolution of the model's natural carbon cycle without anthropogenic forcing. The results from the HYDE, RUEL, and HIGH simulations are presented in Section 3 as deviations from this natural carbon cycle (the FNCC simulation) in order to isolate the impacts of ALCC on the model's carbon reservoirs.

3 Results and Discussion

3.1 Soil Management Simulations

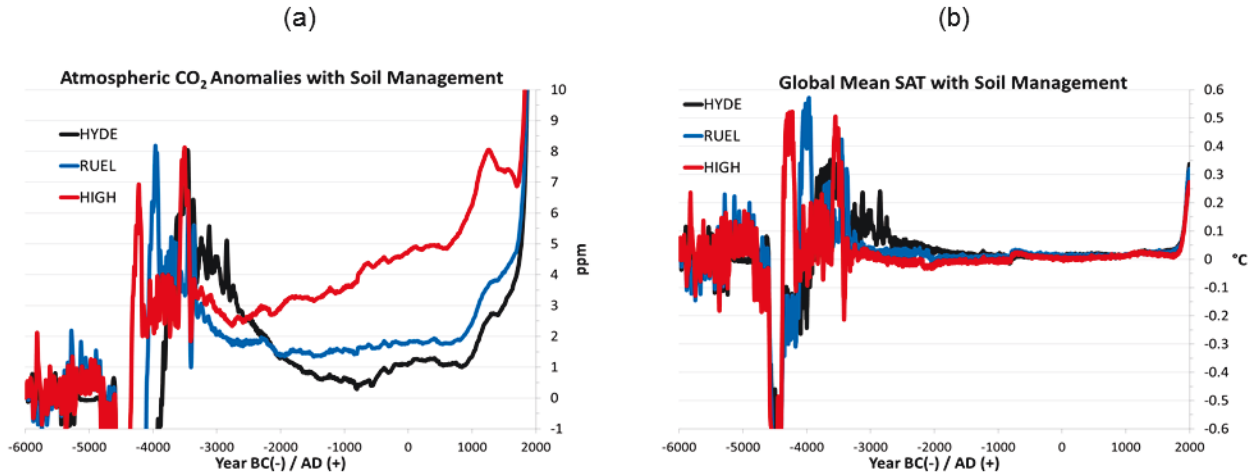

Fig. 3: The HYDE (black line), RUEL (blue line), and HIGH (red line) simulations with soil management minus the FNCC simulation (transient simulation without ALCC) each year for (a) atmospheric CO_2 (ppmv) and (b) the global mean surface air temperature.

Fig. 3 shows the results for atmospheric CO_2 (Fig. 3a) and global surface air temperature (Fig. 3b) for the soil management scenarios (defined in Section 2.2). In the early part of the simulation (the Neolithic period or Stone Age, referred to broadly ~6000 B.C. to ~2500 B.C. in this study), there are large variations from the natural carbon cycle simulation (FNCC), which are on the order of 10 ppm for CO_2 and 0.5°C for air temperature. These variations are largely superficial and occur because of slightly different timing in of a flush of deep waters in the North Pacific to the atmosphere (similar to those described in Chapter 4). These flushes cause CO_2 to rise abruptly by nearly 10 ppm in all simulations, although they are delayed slightly in the ALCC simulations. Because these variations are mostly due to slight differences in the MOC, it is difficult to isolate the effects of ALCC change on atmospheric CO_2 until the stabilization of the meridional overturning circulation after 3000 B.C. (when there are no more changes in the Antarctic Marine ice sheets, as described in Chapter 4, Fig. 1). Between 3000 B.C. and 1000

A.D., the atmospheric CO_2 for the HYDE (black line) and HIGH (red line) simulations diverged. By 1 A.D., atmospheric CO_2 reached ~5 ppm in the HIGH simulation, whereas the HYDE and RUEL experiments only showed a ~1 ppm and ~2 ppm increase in atmospheric CO_2, respectively. These contributions to atmospheric CO_2 (1-5 ppm) are significantly lower than the 40 ppm originally predicted by Ruddiman et al. (2003).

These results suggest that ALCC combined with soil management is not sufficient to produce the observed 16 ppm rise in atmospheric CO_2 by the Iron Age (~1200 B.C. to ~500 A.D.). As argued in Ruddiman and Ellis (2009), higher land use fractions during the Stone and Bronze (~2500 B.C. to 1200 B.C.) ages appear to have a disproportionate impact on atmospheric CO_2 (RUEL does not diverge significantly from HYDE, but HIGH provides a significantly greater contribution to atmospheric CO_2). However, at the same time, the biogeophysical effect of the soil management simulations, which produce more bare ground as we have parameterized it (Section 2.2), cancelled much of the biogeochemical impact of these early releases. As Fig. 3b demonstrates, there is virtually no change in temperature (0.001-0.02°C) between the non-ALCC simulations and ALCC experiments before 1700 A.D. After this date, the temperature changed substantially by 0.27-0.34 °C, largely due to the warming effect of increasing CO_2. The HIGH experiment demonstrated the smallest end-result warming due to the higher albedo associated with more crops and bare ground in this simulation.

Despite the small impact during the early part of the simulation, the effect of deforestation accelerated into the Middle Ages, reaching 8 ppm for the HIGH simulation by 1200 A.D. After that, the curves for the tree simulations begin to merge (as land use efficiency approaches that of the original HYDE 3.1 database), and the CO_2 concentrations accelerated

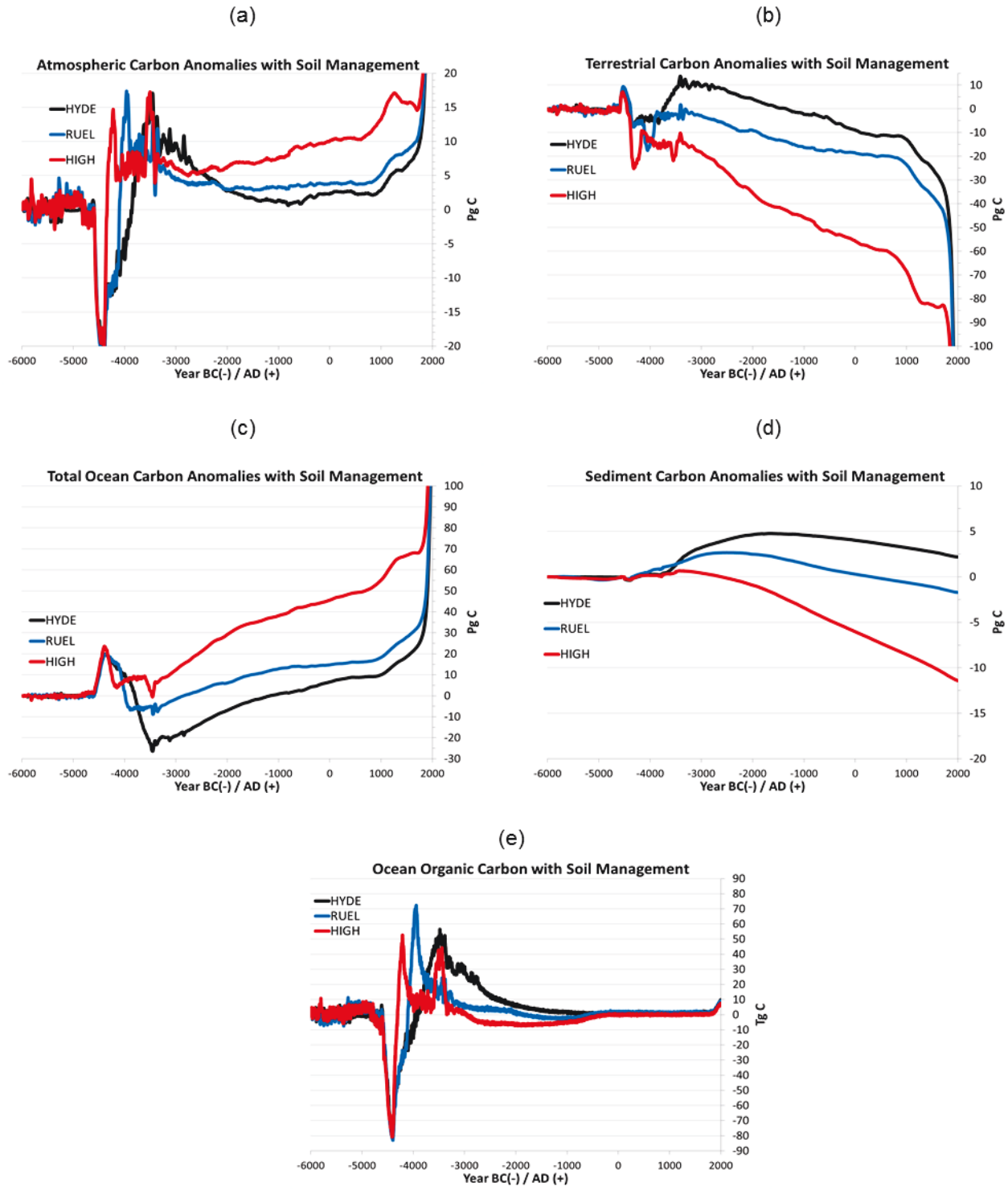

Fig. 4: The HYDE (black line), RUEL (blue line), and HIGH (red line) simulations with soil management minus the FNCC simulation (transient simulation without ALCC) each year for (a) atmospheric carbon content (Pg C), (b) terrestrial carbon (vegetation and soils) (Pg C), (c) total ocean carbon (organic and inorganic) (Pg C), (d) sediment carbon (Pg C), (e) and total organic carbon (living biomass, including phytoplankton, zooplankton, diazotrophs, and detritus) in the oceans (Tg C)

further, reaching 261 ppm, 10 ppm above the FNCC run, by 1825 A.D. The increase in atmospheric CO_2 concentrations between 800 A.D and 1825 A.D. (4-9 ppm) for these simulations is similar to the 5-6 ppm increase found in Pongratz et al. (2009). The Industrial Era (not shown) witnessed a more substantial increase in CO_2 to 313.7 in the HYDE simulation, to 312.4 in the RUEL experiment, and to 307.6 in the HIGH simulation by 2000 A.D., which amounts to 62.7 ppm, 61.4 ppm, and 56.6 ppm more CO_2 than in the FNCC simulation (with an end-result of 251 ppm). While the total rise (a net 50 ppm increase after 6000 B.C., with a 44-54 ppm rise after 1850 B.C.) seems excessive and is greater than that obtained by Matthews et al. (2004) (26 ppm after 1850 A.D.), Brovkin et al. (2004) (18 ppm), and Pongratz et al. (2009) (20 ppm), it also falls well below the total CO_2 increase during the Industrial Era (from ~280 ppm to ~364 ppm in 2000 A.D.) Thus, only a slightly lower soil management fraction (approaching 20% rather than the 30% used here), or the adjustment of the model to treat different types of ALCC (pasture vs. croplands) differently may provide a better solution for recreating Industrial-Era land use emissions.

A closer look at the time series for the model's four carbon reservoirs (Fig. 4) provides the context for the relatively small changes in atmospheric carbon content (Fig. 4a) before the Medieval period. Fig. 4b, which shows the net terrestrial emissions in terrestrial carbon including resquestration (Fig. 4c), indicates that terrestrial losses are substantially greater for the HIGH simulation (56 Pg C by 1 A.D.). The ocean (Fig. 4c) reabsorbs most of the carbon (~40 Pg C), leading to a small net gain for the the atmosphere. Fig. 4c also shows that, in the absence of a change in alkalinity, ocean carbon storage increased in concert with the net terrestrial release from ALCC. These simulations do include orbital forcing but do not appear to lead to an oceanic release associated with increasing southern hemisphere insolation. The warming effect of the

CO_2 radiative forcing related to the mid-to-late Holocene CO_2 rise could lead to a small additional oceanic outgassing of CO_2 that is not represented here (as the modelled pre-industrial CO_2 levels remain between 252-258 ppm at 1000 A.D.). Other simulations of the period (not shown here) with ALCC and prescribed atmospheric CO_2 radiative forcing produced a global ocean sea surface temperature rise of 0.3°C, which could lead to a ~3 ppm increase in CO_2 from this effect. In general, though, in order for (1) the CO_2 uptake efficiency of the oceans to decrease, and (2) deforestation to play a larger role in the global carbon budget for the period, a decrease in alkalinity or an increase in outgassing from CO_2 radiative forcing would be required.

Alkalinity was not allowed to change in the simulations presented here in order to isolate the physical effects of ALCC on atmospheric CO_2. In order to keep alkalinity fixed, the weathering rate in the model is changed so that the weathering flux (alkalinity source to the ocean) balances the sedimentation flux (the ocean alkalinity sink in the model). However, if weathering were to be assumed relatively constant over the period, Fig. 4d (sediment carbon) demonstrates the general sense of alkalinity changes that would occur in response to ALCC. For the HYDE and RUEL simulations, sedimentation is actually slightly greater for most of the simulation (3-5 Pg C greater than the non-ALCC run). A slight increase in the alkalinity sink would support a minor decrease in alkalinity. However, the HIGH simulation, with more substantial ocean absorption of the terrestrial release of carbon (Fig. 4b-c), produced a decrease in sediment carbon (due to in part to increase sediment dissolution). Fig. 4e, which shows the living biomass in the ocean, indicates that organic carbon is slightly less in this simulation (and this is accompanied by a reduction of phosphate at the surface, not shown). While these observations do not diagnose changes in the efficiency of the biological pump, a decrease in the biological activity may be a possible contributor to the Holocene CO_2 increase (Goodwin et al.

2011). However, any accompanying decrease in the calcite flux to the sediments (as modeled here) may oppose these changes on longer timescales. The combination of both a slight decrease in sedimentation and a pulse of CO_2 into the oceans (supporting dissolution) leads to a decrease in sediment carbon (already 6 Pg C less by 1 A.D.). The increase in ocean alkalinity in the HIGH simulation afforded by greater sediment dissolution would gradually allow the ocean to take up more CO_2 from the atmosphere than it does in the other ALCC simulations (Fig. 4c, red line). The time scale of sediment response (thousands of years) to CO_2 inputs into the ocean, however, does not allow major changes during the Industrial period due to changes in oceanic uptake efficiency related to alkalinity.

These results for the HIGH simulation are consistent with those of Stocker et al. (2011) in the sense that ocean-sediment interactions have time to work against the enhanced Neolithic terrestrial releases that occur in the HIGH simulation. Including the corresponding alkalinity changes would reduce the net effect on atmospheric CO_2 by 1 A.D. (5 ppm) discussed above. However, at the same time, the HYDE and RUEL simulations, which have slightly greater sedimentation (Fig. 4d, black and blue lines), imply the possibility of a slight decrease in alkalinity for the Neolithic and Bronze Age in response to the imposed ALCC fractions, which would allow slightly less oceanic absorption of the terrestrial release than that simulated here (Fig 4c, black and blue lines). Overall, Fig. 4d suggests that the inclusion of alkalinity changes in response to the terrestrial release would narrow the difference between the HYDE/RUEL simulations and the HIGH simulation. As such, it is possible that greater per-capita land use during the early agricultural period, as suggested by Ruddiman and Ellis (2009) and Kaplan et al. (2011), may lead to a similar increase in atmospheric CO_2 as less extensive deforestation. Understanding the response of marine productivity to deforestation (perhaps representing an

unresolved feedback as proposed in Ruddiman (2007) and Ruddiman et al. (2011)) could be important in isolating the oceanic response to the terrestrial release. Our simulations suggest that sediment-ocean interactions may enhance the terrestrial release in some cases and work against it in others, with a large early terrestrial release associated with greater sediment dissolution that is capable of reducing atmospheric CO_2 changes in the late Holocene.

In general, there are several model-specific factors that could lead to an underestimation of deforestation in certain regions. For example, the simulation of bare ground as the dominant land cover type in northern Africa and the Black Sea region provide a significant limitation to early agricultural releases. Furthermore, the lack of nitrogen limitation for vegetation growth may cause terrestrial re-sequestration to be over-represented on centennial time scales. Similarly, the assumption that all agriculture in our model is permanent (without providing for a differential treatment for regions where shifting agriculture was predominant) could underestimate the terrestrial release, especially prior to the Middle Ages, as suggested in Olofsson and Hickler (2008). On the other hand, other factors in this study such as the redistribution of excess land use areal fractions to nearby gridcells (Section 2.2), the application of soil management to both pasture and croplands, and our assumption that all terrestrial carbon in the soil management fraction is returned to the atmosphere (Section 2.3) may conversely overestimate the impacts of deforestation. Regarding the oceans, the assumption of a constant alkalinity profile (~2358.4 $\mu mol\ kg^{-1}$) is likely unrealistic, as alkalinity may be lower or decreasing at this time due to an expansion of coral reefs (Ridgwell et al. 2003), declining weathering rates (Crocket et al. 2012), peatland and terrestrial uptake (Broecker et al. 1999), more extensive marine ice shelves (Chapter 4), or a higher sedimentation flux (HYDE, this study). Putting aside $\delta^{13}C$ constraints (which may be dominated by contributions from northern peatlands), the ability of deforestation-

related terrestrial releases to leave an imprint on atmospheric CO_2 ultimately lies with ocean processes and requires a feedback not resolved in this study or in Stocker et al. (2011). As established in Chapter 3 for a high latitude terrestrial release during the deglacial period, decreasing ocean alkalinity allows more of the terrestrial release to remain in the atmosphere, promoting an increase in atmospheric CO_2. Within this context, modeling ALCC during a period of decreasing alkalinity during the Holocene may allow deforestation to better balance peatlands (Ruddiman et al. 2011), allowing CO_2 to increase in response to a combination of other oceanic processes related to alkalinity and the soft tissue pump (coral reefs, shallow water sedimentation, lower weathering rates, sea surface warming, a reduction in the biological pump). Including some of these natural processes, the (Bern3D+C) modelling study of Menviel and Joos (2012) was unable to reproduce the Holocene CO_2 trend for higher-end peatland uptake estimates, suggesting that the deforestation may play a compensating role.

3.2 Zero-Tillage Land Use

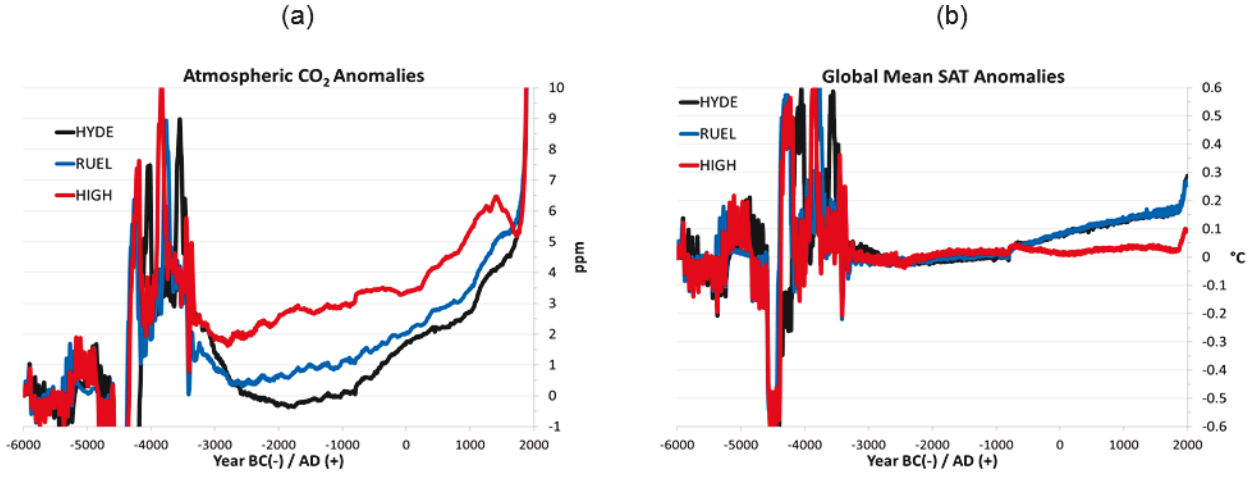

Fig. 5: (a) Atmospheric CO_2 anomalies and (b) Global Mean SAT anomalies, as in Fig. 3 but for simulations without soil management.

The same experiments repeated without tillage simply reserve the ALCC fraction for C_3 and C_4 grasses without imposing a bare soil fraction. Fig. 5 illustrates the results for these

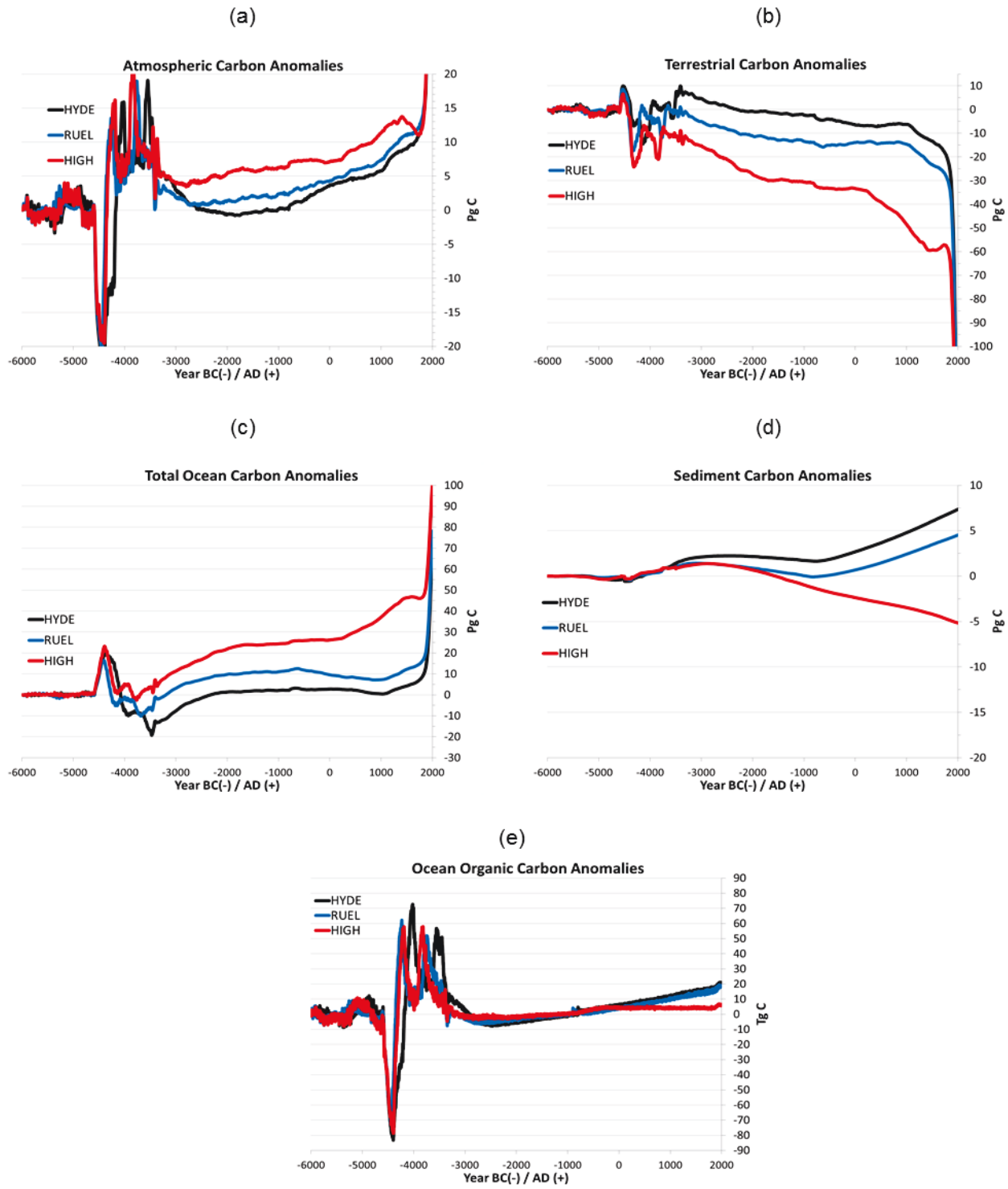

Fig. 6: (a) Atmospheric Carbon Anomalies, (b) terrestrial carbon anomalies, (c) total ocean (inorganic and organic) carbon anomalies, (d) sediment carbon anomalies, and (e) organic ocean carbon anomalies, as in Fig. 4 but for simulations without soil management.

simulations in the same manner as in Fig. 3. The changes in atmospheric CO_2 (Fig. 5a) by 1 A.D. are notably smaller than the original experiment for the HIGH simulation (3.4 ppm increase by 1 A.D.), comparable for the RUEL experiment (2 ppm) but slightly higher for the HYDE experiment (1.7 ppm increase). Surprisingly the HYDE scenario produced a slight net decrease in atmospheric CO_2 relative to the non-ALCC experiment between 2400 B.C. and 1000 B.C. This occurred due to virtually no net releases from the terrestrial biosphere, indicating that for smaller-scale deforestation (which the HYDE experiment without soil management represents), terrestrial re-sequestration is able to fully counter the deforestation release (while the ocean acts as a slight sink). Thereafter, however, the oceanic uptake efficiency decreased in the HYDE simulation over the Iron Age, absorbing only 0.2 Pg C (Fig. 6c, black line), while terrestrial releases accelerated (Fig. 6c, black line), allowing for atmospheric CO_2 concentrations to increase over the soil management simulations (Fig. 6a, black line).

These results identify an important response that exists in the simulations without soil management that allow lower land use efficiency scenarios (HYDE and RUEL) to achieve higher-than-expected CO_2 levels. This effect appears to be related to the balance of biogeochemical and biogeophysical processes evident in Fig. 5b. The deforestation appears to be large enough in the HIGH simulation that the biogeophysical effect on temperature (albedo increase) almost fully counters the biogeochemical effect, leading to little net increase (0.016°C at 1 A.D.). However, the HYDE and RUEL experiments show a notable increase in global surface air temperature of nearly +0.1°C by 1 A.D., an order of magnitude greater than the warming in the HIGH simulation as well as the HYDE and RUEL simulations with soil management. This steady increase is interesting in that it is of similar magnitude to the net

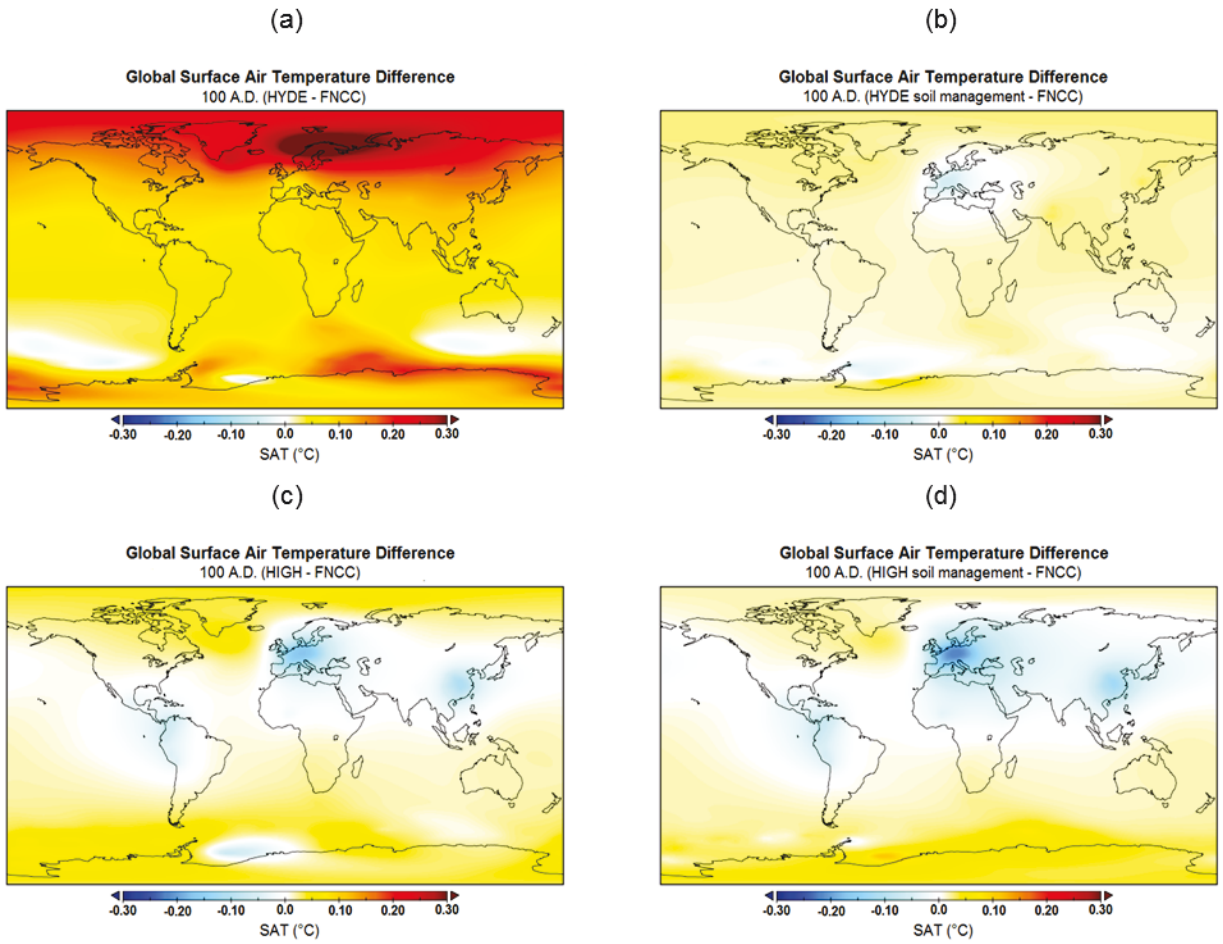

Fig. 7: The spatial pattern of surface air temperature differences at 100 A.D. for (a) HYDE minus FNCC, (b) HYDE soil management minus FNCC, (c) HIGH minus FNCC, and (d) HIGH soil management minus FNCC). Blue areas indicate regions of net cooling, whereas yellow, orange, and red indicate regions of net warming relative to the natural carbon cycle simulation.

warming effect (0.15°C) found in Matthews et al. (2004) associated with historical land cover change from 1700 A.D. to 2000 A.D.

Fig. 7a provides the spatial distribution of the HYDE warming relative to other simulations with more extensive deforestation (Fig. 7b,c,d). The warming epicenter north of Scandinavia was stimulated by decreased sea ice (not shown), which provided for a deeper North Atlantic overturning, better ventilation (9‰ greater $\Delta^{14}C$ below 3000 m depth in the North Atlantic), and less DIC storage (not shown). More extensive European deforestation afforded

greater regional cooling (Fig. 7b,c,d) that did not allow for the threshold decrease in sea ice as in the HYDE simulation, allowing for more AABW as shown in Chapter 4. This suggests that there may be a threshold in the degree of land clearing (somewhere between the HIGH and RUEL scenarios) in which biogeochemical effects (higher CO_2, less sea ice) dominate over biogeophysical effects (increased albedo, more sea ice, greater runoff), with consequences for the global distribution of North Atlantic Deep Water (NADW). The greater warming in the HYDE/RUEL simulations may, in turn, decrease the solubility of CO_2 in the oceans and provide an additional small contribution (~0.5-1 ppm) to the CO_2 increase (assuming an average 9 ppm outgassing per 1°C change) in addition to decreasing DIC storage in the deep Atlantic.

Another notable difference between the simulations with and without tillage is the influence of the sedimentation flux on ocean alkalinity. For the zero-tillage simulations in this section, greater sedimentation occurs (Fig. 6d) relative to the natural carbon cycle run prior to 2000 B.C. After 1000 B.C., the HYDE and RUEL simulations diverge from the HIGH simulation, the latter being the only simulation with a net sediment dissolution provoked by deforestation. While alkalinity is held constant in these simulations (as in the soil management modelling experiments discussed above), greater sedimentation in all but the most extreme experiment suggests that deforestation could contribute to a small decrease in alkalinity rather than the expected increase. In fact, with less North Atlantic sea ice and a more extensive low-DIC, high [CO_3^{2-}] NADW, sedimentation (and the potential alkalinity decrease) began to accelerate in the RUEL and HYDE simulation after 500 B.C. Only the most extreme scenario (HIGH) provoked greater sediment dissolution (which would result in an increase in alkalinity). This net dissolution for the HIGH scenario (compare Fig. 4d with Fig 6d, red line) is of a smaller

amplitude than in the simulations without soil management due to the smaller terrestrial flux to the atmosphere.

4 Conclusions

In this study, we used the UVic ESCM v. 2.9 to explore changes in climate and the carbon cycle due to anthropogenic land cover change (ALCC) for the period from 6000 B.C. to 2000 A.D. This paper represents one of the few modelling studies addressing this topic not using the LPJ-DGVM and also provides a special focus on the oceanic response to deforestation. Three different ALCC scenarios (described in Figs. 1-2) were developed by scaling the HYDE database. One (HYDE) used the original Hyde 3.1 (Klein Goldewijk et al. 2011) data in the model; RUEL scaled this data to obtain linearly decreasing land use efficiency from ~4.5 ha/person to ~1 ha/person from 6000 B.C. to 2000 A.D. (as suggested by Ruddiman and Ellis 2009); and HIGH introduced a ~8 ha/person land use efficiency from 6000 B.C. to 1000 B.C. and linearly decreasing land use efficiency thereafter from ~8 ha/person to ~1 ha/person. These land use scenarios were then applied to the UVic model without and with a simple soil management parameterization (to simulate increasing agricultural intensity and greater soil erosion/respiration with time), which cleared a fraction of the vegetation and soil carbon within the ALCC fraction and released it to the atmosphere. This soil management fraction increased linearly from 5% of the ALCC at 6000 B.C. to 30% of the ALCC fraction at 2000 A.D. as a rough approximation of increasing tillage intensity. The results from these modelling experiments were presented in the paper as anomalies from a simulation without ALCC, representing the model's natural carbon cycle evolution.

From our modelling results, we presented some surprising discoveries. The atmospheric CO_2 increase due to anthropogenic land use and soil management was only a fraction (1-5 ppm)

of the observed 16 ppm increase in CO_2 between 6000 B.C. to 1 A.D., as biosphere re-sequestration and oceanic uptake provided sinks able to absorb most of the deforestation emissions prior to the Industrial Period. However, the simulations with soil management yielded greater contributions during the Medieval period, resulting in an atmospheric CO_2 increase as high as 10 ppm between 6000 B.C. to 1825 A.D. for all land use scenarios. During the Industrial Era (and excluding fossil fuel emissions), atmospheric CO_2 concentrations as high as 313 ppm by 2000 A.D. were calculated by the model. Matthews et al. (2004) also modelled the period from 1700 A.D. to 2000 A.D. with historical land cover change and fossil fuel emissions but obtained atmospheric CO_2 concentrations 12 ppm below the observed trend. Our results suggest that some degree of soil management or greater soil respiration may be able to account for the rest of the atmospheric CO_2 increase (12 ppm). Overall, the UVic model was not able to capture increases in atmospheric CO_2 when deforestation was included and ocean alkalinity was held constant (by adjusting the weathering rate to match the sedimentation rate). This suggests that alkalinity changes are vital to producing the Holocene increase in atmospheric CO_2.

Several sensitivity simulations, however, revealed surprising case-specific positive feedbacks provided by the ALCC scenarios that may have allowed CO_2 to increase further in response to the initial deforestation pulse. While alkalinity was kept constant, the sediment module was kept online with respect to changes in the modelled climate and carbon cycle evolution, and several sensitivity studies suggest that smaller terrestrial releases may have been associated with greater sedimentation (~5 Pg C), which would contribute (slightly) to an alkalinity decrease and propelled to a slightly higher CO_2 concentration. Only the extreme deforestation (HIGH) scenario resulted in a notable net sediment dissolution (which would have increased alkalinity and led to a drawdown in atmospheric CO_2). Though some of these

feedbacks may prove to be model-specific, these results suggest thatgreater deforestation (low land use efficiency in the HIGH simulation) during the early agricultural period could have led to lower atmospheric CO_2 than that shown in response to greater longterm sediment dissolution. Conversely, the HYDE and RUEL experiments might have slightly greater atmospheric CO_2 than that shown with the inclusion of alkalinity effects. This would narrow the divergence between the trend lines, indicating that a very large early deforestation scenario would have led to little net gain in atmospheric CO_2 prior to the Middle Ages over more moderate deforestation cases (HYDE and RUEL).

In addition, a surprising effect was discovered in the model for the HYDE scenario without soil management. Stronger cooling (and greater freshwater runoff) in the other deforestation scenarios in Europe maintained a quasi-steady climate state, but the weaker regional cooling (and slightly higher atmospheric CO_2) in the HYDE simulation accompanied a significant reduction in sea ice in the North Atlantic, along with extensive NADW formation in the deep North Atlantic and reduced deep ocean DIC storage in this region. This series of events stimulated a disproportionate increase in global temperature (+0.1°C by 1 A.D.), reducing oceanic uptake efficiency and overwhelming the biogeophysical cooling associated with anthropogenic land use. The potential for positive feedbacks, related either to physical changes in the ocean circulation or sediment response to ALCC , suggest that smaller changes in deforestation (including those on the scale proposed in Ruddiman and Ellis 2009) may provide similar contributions to atmospheric CO_2 as higher release scenarios. However, our results indicate that a decrease in ocean alkalinity, provided by coral reef-related sedimentation (Ridgwell et al. 2003), greater Antarctic ice shelf extent (Chapter 3, Section 4.1.7), terrestrial uptake (Broecker et al. 1999; Yu 2012) or lower weathering (Foster and Vance 2006; Crocket et

al. 2012) would be needed in order for more of the deforestation carbon release to remain in the atmosphere. This carbon could then counterbalance a greater fraction of the peatland uptake (Yu 2012, not modelled here) and permit CO_2 to rise through oceanic processes.

Chapter 6: Conclusions

The University of Victoria Earth System Climate Model (UVic ESCM) v. 2.9 was used in this thesis to investigate carbon cycle dynamics since the Last Glacial Maximum. The core component of the UVic ESCM is a three-dimensional ocean model, coupled to a dynamic-thermodynamic sea ice model, a dynamic global vegetation model, an ocean sediments module, and an interactive carbon cycle. The ocean sediments module (Archer et al. 1996) is a new addition to v. 2.9 that allows (for the first time) sediment processes to alter alkalinity changes in the ocean. Two equilibrium simulations (with constant time-independent forcing) were obtained for both 21000 B.C. and 6000 B.C. and were used as the initial conditions for transient simulations forced by time-evolving Milankovitch forcing and ice sheet changes. Other sensitivity simulations were conducted with prescribed time-evolving CO_2 radiative forcing (from 19004 B.C.), prescribed CO_2 (from ice cores), a high latitude terrestrial carbon reservoir, freshwater fluxes, and anthropogenic land use scenarios. A more detailed summary of our primary results from these simulations are given in each of the individual articles: Chapter 3 (Section 4), Chapter 4 (Section 6), and Chapter 5 (Section 4).

In Chapter 3, a series of modelling experiments were conducted that covered the period from the Last Glacial Maximum (LGM) to the present (2000 A.D). Simulations including only prescribed Milankovitch forcing and land ice changes failed to produce an increase in atmospheric CO_2 for this time interval. However, the amplitude of atmospheric CO_2 changes demonstrated significant sensitivity (10-15 ppm) to small variations (1.9 Tmol yr^{-1}) in the weathering rate. Simulations incorporating the CO_2 radiative forcing starting at the LGM, however, resulted in significantly higher CO_2 (an increase of ~20 ppm) due to a stronger

meridional overturning circulation and reduced oceanic CO_2 uptake. These changes were related to a strong relationship in the model between sea ice extent and CO_2-related warming. The more complete ventilation of the deep ocean when CO_2 radiative forcing was included also caused a larger decrease in ocean alkalinity for the late deglacial and interglacial, even for higher weathering rates, permitting modelled atmospheric CO_2 to increase by an additional 10 ppm during the late deglacial and interglacial.

The addition of a high latitude terrestrial carbon reservoir provided a net release of carbon to the atmosphere (~200 Pg C) during the early deglacial when biospheric re-sequestration of the initial release was more limited by less land being available for additional growth. Most of the high latitude release (from the Pleistocene-Holocene transition onward) was reabsorbed by the terrestrial biosphere. The effect of the early deglacial net release produced atmospheric CO_2 concentrations closer to reality (240-250 ppm) when the greater ocean ventilation and related alkalinity changes stimulated by CO_2 radiative forcing were included. While the terrestrial release moderated changes in ocean alkalinity, carbonate concentrations in the model's deep ocean were in better agreement with the scale of changes suggested by proxy data since the LGM (Yu et al. 2010).

The inclusion of freshwater fluxes due to ice sheet melt in the Northern Hemisphere illustrated the complexity of carbon cycle interactions during these events. The simulations failed to produce a recovery in the Atlantic Meridional Overturning Circulation, thus providing emphasis on contributions from Southern Ocean dynamics (particularly during Heinrich Event 1). Unlike in Schmittner and Galbraith (2008), the reduction in calcite rain on the ocean floor allowed ocean alkalinity to increase to a greater degree than in the simulations without freshwater fluxes. These results thus put greater emphasis on the importance of a lower

weathering rate during the LGM and the early interglacial (Rickaby et al. 2010) in order to allow atmospheric CO_2 to increase. Furthermore, deep waters in the North Pacific were slightly warmer and dislodged earlier after the end of Heinrich Event 1, indicating that deep waters in the North Pacific may become more positively buoyant during Atlantic overturning shutdowns.

In Chapter 4, our results for the natural evolution of the Holocene carbon cycle indicate that atmospheric CO_2 tends to decrease between 6000 B.C. and 2000 A.D. without an external forcing. The magnitude of the decrease (8-15 ppm), however, depended strongly on the initial ocean circulation state. Furthermore, these Holocene modelling experiments revealed an important sensitivity to the extent of Antarctic marine ice shelves. The application of more extensive marine ice shelves during the Holocene increased modelled atmospheric CO_2 levels by ~5 ppm from a purely physical reduction in deep-ocean DIC associated with a more extensive distribution of North Atlantic Deep Water. This sensitivity increases to 7-10 ppm when alkalinity changes or different ocean circulation states are considered. These results together provide a new mechanism (more extensive marine ice shelves) to explain part of the Holocene increase in atmospheric CO_2 concentrations. Proxy-model reconstructions of Antarctic marine ice shelves (Pollard and DeConto 2009) indicate that ice shelf extent during the Holocene was indeed likely greater than during most other interglacials. These results indicate that future modelling studies should provide more attention to the distribution and treatment of marine ice shelves.

In Chapter 5, we applied three anthropogenic land use scenarios to the Holocene carbon cycle. The effects of anthropogenic deforestation are unable to explain the Holocene rise in CO_2 (maximum: 5 ppm before 1 A.D., only a third of the ~16 ppm rise to this time) through purely physical mechanisms (constant alkalinity). Surprisingly, however, we show that some deforestation scenarios actually lead to greater sedimentation (an alkalinity sink for the oceans),

whereas more extensive deforestation during the Neolithic and Bronze ages produced more sediment dissolution (an alkalinity source). The implication of these results is that greater land use efficiency (less land use area per person) could provide similar contributions to atmospheric CO_2 as larger land use area per person due to these effects, although the alkalinity-induced response to deforestation merits further investigation. Overall, the inclusion of deforestation in the modeled Holocene carbon cycle indicates that external mechanisms leading to a decrease in alkalinity during the Holocene (such as declining weathering rates, more extensive marine ice shelves, terrestrial uptake, more calcifiers, coral reef expansion, etc.) may prevent the ocean from absorbing as much of the anthropogenic terrestrial release. This would cause the deforestation flux to balance a greater fraction of the uptake from northern peatlands (Ruddiman et al. 2011), allowing atmospheric CO_2 to increase from oceanic processes (alkalinity decreases from coral reefs, terrestrial uptake, Antarctic marine ice shelves, and reduced weathering) that might have been overcompensated for by northern peatlands during previous interglacials.

References

Adkins JF, McIntyre K, Schrag DP (2002). The salinity, temperature, and $\delta^{18}O$ of the glacial deep ocean. *Science*, 298: 1769-1773.

Ahn J, Wahlen M, Deck BL, Brook EJ, Mayewski PA, Taylor KC, White JWC (2004) A record of atmospheric CO2 during the last 40,000 years from the Siple Dome, Antarctica ice core. *Journal of Geophysical Research: Atmospheres*, 109, doi: 10.1029/2003JD004415.

Ahn J, Brook EJ (2008) Atmospheric CO_2 and climate on millennial time scales during the last glacial period. *Science*, 322: 83-85.

Anderson RF, Ali S, Bradtmiller LI, Nielsen SHH, Fleisher MQ, Anderson BE, Burckle LH (2009) Wind-driven upwelling in the Southern Ocean and the deglacial rise in atmospheric CO_2. *Science*, 323: 1443-1448.

Archer DE (1996) A data-driven model of the global calcite lysocline. *Global Biogeochemical Cycles*, 10: 511-526.

Archer DE, Maier-Reimer E (1994) Effect of deep-sea sedimentary calcite preservation on atmospheric CO_2 concentration. *Nature*, 367: 260-268

Armstrong RA, Lee C, Hedges JI, Honjo S, Wakeham SG (2002) A new, mechanistic model for organic carbon fluxes in the ocean based on the quantitative association of POC with ballast minerals. *Deep-Sea Research II*, 49: 219-236.

Baroni C, Orombelli G (1994) Abandoned penguin rookeries as Holocene paleoclimatic indicators in Antarctica. *Geology*, 22: 23-26.

Berger A (1978) Long-term variations of daily insolation and quaternary climatic changes. *Journal of Atmospheric Science*, 35: 2362-2367.

Biermann A, Engel A (2010) Effect of CO_2 on the properties and sinking velocity of aggregates of the coccolithophore *Emiliana huxleyi*. *Biogeosciences*, 7: 1017-1029.

Blanco-Canqui H, Lal R (2008) No-tillage and soil-profile carbon sequestration: An on-farm assessment. *Soil Science Society of America Journal*, 72: 693-701.

Bopp L, Kohfeld KE, Le Quéré C, Aumont O (2003) Dust impact on marine biota and atmospheric CO_2 during glacial periods. *Paleoceanography*, 18: 1046, doi:10.1029/2002PA000810.

Boserup E (1965) *The conditions of agricultural growth: The economics of agrarian change under population pressure*. Chicago: Aldine.

Bouttes N, Roche DM, Paillard D (2012) Systematic study of the impact of fresh water fluxes on the glacial carbon cycle, *Climate of the Past*, 8: 589-607, doi:10.5194/cp-8-589-2012.

Bouttes N, Paillard D, Roche D M, Brovkin V, Bopp L (2011). Last Glacial Maximum CO_2 and $\delta^{13}C$ successfully reconciled.*Geophysical Research Letters*, 38: L02705, doi:10.1029/2010gl044499.

Boyle JF, Gaillard M-J, Kaplan JO, Dearing JA (2011) Modelling prehistoric land use and carbon budgets: A critical review. *The Holocene*, 21: 715, doi: 10.1177/0959683610386984.

Bozbiyik A, Steinacher M, Joos F, Stocker TF, Menviel L (2011) Fingerprints of changes in the terrestrial carbon cycle in response to large reorganizations in ocean circulation. *Climate of the Past*, 7: 319-338.

Bradtmiller LI, Anderson RF, Sachs JP, Fleisher MQ (2010) A deeper respired carbon pool in the glacial equatorial Pacific Ocean. *Earth and Planetary Science Letters*, 299: 417-425.

Bradtmiller LI, Anderson RF, Fleisher MQ, Burckle LH (2007) Opal burial in the equatorial Atlantic Ocean over the last 30 ka: Implications for glacial-interglacial changes in the ocean silicon cycle. *Paleoceanography*, 22: PA4216, doi:10.1029/2007PA001443.

Broecker WS, Clark E (2010) Search for a glacial-age ^{14}C-depleted ocean reservoir. *Geophysical Research Letters*, 37: L13606, doi:10.1029/2010GL043969.

Broecker WS, Clark E, Barker S (2008) Near constancy of the Pacific Ocean surface to mid-depth radiocarbon-age difference over the last 20kyr. *Earth and Planetary Science Letters*, 274: 322-326.

Broecker WS, Barker S (2007) A 190‰ drop in atmosphere's $\Delta^{14}C$ during the "Mystery Interval" (17.5 to 14.5 kyr). *Earth and Planetary Science Letters*, 356: 90-99.

Broecker WS, Ellis E (2007) Is the magnitude of the carbonate ion decrease in the abyssal ocean over the last 8 kyr consistent with the 20 ppm rise in atmospheric CO_2 content? *Paleooceanography*, 22, doi;10.1029/2006PA001311.

Broecker WS, Stocker TL (2006) The Holocene CO_2 rise: Anthropogenic or natural? *EOS Transactions*, American Geophysical Union, 87: 27

Broecker WS, Clark E (2003) Holocene atmospheric CO_2 increase as viewed from the seafloor, *Global Biogeochemical Cycles*, 17: 1052

Broecker WS, Lynch-Stieglitz J, Clark E, Hadjas I, Bonani G (2001) What caused the atmosphere's CO_2 content to rise during the last 8000 years? *Geochemistry Geophysics, Geosystems*, 2: 1062

Broecker WS, Clark E, McCorkle DC, Peng T-H, Hajdas I, Bonani G (1999) Evidence for a reduction in the carbonate ion content of the deep sea during the course of the Holocene. *Paleoceanography*, 14: 744-752.

Broecker WS, Henderson GM (1998) The sequence of events surrounding Termination II and their implications for the cause of glacial-interglacial CO_2 changes. *Paleoceanography*, 13: 352-364.

Broecker WS, Lao Y, Klas M, Clark E, Bonani G, Ivy S, Chen C (1993) A search for an early Holocene $CaCO_3$ preservational event. *Paleoceanography*, 8: 333-339.

Broecker WS (1982) Glacial to Interglacial changes in ocean chemistry. *Progress in Oceanography*, 11: 151-197.

Brovkin V, Ganopolski A, Archer D, Munhoven G (2012) Glacial CO_2 cycle as a succession of key physical and biogeochemical processes. *Climate of the Past*, 8: 251-264.

Brovkin V, Kim J-H, Hofmann M, Schneider R (2008) A lowering effect of reconstructed Holocene changes in sea surface temperatures on the atmospheric CO_2 concentration. *Global Biogeochemical Cycles*, 22, doi:10.1029/2006GB002885.

Brovkin V, Sitch S, von Bloh W, Claussen M, Bauer E, Cramer W (2004) Role of land cover changes for atmospheric CO_2 increase and climate change during the last 150 years. *Global Change Biology*, 10: 1253–1266.

Brovkin V, Bendtsen J, Claussen M, Ganopolski A, Kubatzki C, Petoukhov V, Andreev A (2002) Carbon cycle, vegetation, and climate dynamics in the Holocene: Experiments with the CLIMBER-2 model, *Global Biogeochemical Cycles*, 16: 1139-1159.

Bryan SP, Marchitto TM, Lehman SJ (2010) The release of ^{14}C-depleted carbon from the deep ocean during the last deglaciation: Evidence from the Arabian Sea. *Earth and Planetary Science Letters*, 208: 244-254.

Brzezinski MA, Pride CJ, Franck VM, Sigman DM, Sarmiento JL, Matsumoto K, Gruber N, Rau GH, Coale KH (2002) A switch from $Si(OH)_4$ to NO_3^- depletion in the glacial Southern Ocean. *Geophysical Research Letters*, 29: 1564, doi:10.1029/2001GL014349.

Burke A, Robinson LF (2012). The Southern Ocean's role in carbon exchange during the last deglaciation. *Science*, 335: 557-561.

Carlson AE, Clark PU, Haley BA, Klinkhammer GP, Simmons K, Brook EJ, Meissner KJ (2007) Geochemical proxies of North American freshwater routing during the Younger Dryas cold event. *Proceedings of the National Academy of Sciences*, 104: 6556-6561.

Catubig NR, Archer DE, Francois R, deMonocal P, Howard W, Yu E-F (1998) Global deep-sea burial rate of calcium carbonate during the last glacial maximum. *Paleoceanography*, 13: 298-310.

Ciais P, Tagliabue A, Cuntz M, Bopp L, Scholze M, Hoffmann G, Lourantou A, Harrison SP, Prentice IC, Kelley DI, Koven C, Piao SL (2012) Large inert carbon pool in the terrestrial biosphere during the Last Glacial Maximum. *Nature Geoscience*, 5: 74-79.

Chickamoto MO, Abe-Ouchi A, Oka A, Ohgaito R, Timmermann A (2012) Quantifying the ocean's role in glacial CO_2 reductions. *Climate of the Past*, 8: 545-563.

Claussen M (2009) Late Quaternary vegetation feedbacks. *Climate of the Past*, 5: 203-216.

Claussen M, Mysak LA, Weaver AJ, Crucifix M, Fichefet T, Loutre MF, Weber SL, Alcamo J, Alexeev VA, Berger A, Calov R, Ganopolski A, Goosse H, Lohmann G, Lunkeit F, Mokhov II, Petoukhov V, Stone P, Wang Z (2002) Earth system models of intermediate complexity: Closing the gap in the spectrum of climate system models. *Climate Dynamics*, 18: 579-586.

Cortese G, Gersonde R, Maschner K, Medley P (2012) Glacial-interglacial size variability in the diatom *Fragilariopsis kerguelensis*: Possible iron/dust controls? *Paleoceanography*, 27: PA1208, doi:10.1029/2011PA002187.

Cox PM (2001) Description of the 'TRIFFID' dynamic global vegetation model. Hadley Centre Technical Note 24 pp. 1-16. Berks, UK: UK Met Office.

Cox PM, Betts RA, Bunton CB, Essery RLH, Rowntree PR, Smith J (1999) The impact of new land surface physics on the GCM simulation of climate and climate sensitivity. *Climate Dynamics*, 15**:** 183–203.

Crocket KC, Vance D, Foster GL, Richards DA, Tranter M (2012) Continental weathering fluxes during the last glacial/interglacial cycle: Insights from the marine sedimentary Pb isotope record at Orphan Knoll, NW Atlantic. *Quaternary Science Reviews*, 38: 89-99.

Crucifix M, Loutre F, Berger A (2005) Commentary on "the anthropogenic greenhouse era began thousands of years ago." *Climatic Change*, 69, 419-426.

Curry WB, Oppo DW (2005) Glacial water mass geometry and the distribution of $\delta^{13}C$ of ΣCO_2 in the western Atlantic Ocean. *Paleoceanography*, 20: PA1017, doi:10.1029/2004/PA001021.

Denton GH, Heusser CJ, Lowell TV, Moreno PI, Andersen BG, Heusser LE, Schluchter C, Marchant DR (1999) Interhemispheric linkage of paleoclimate during the last glaciation, *Geografiska Annaler Series A: Physical* Geography, 81A: 107–153.

De Pol-Holz R, Keigwin L, Southon J, Hebbeln D, Mohtadi M (2010) No signature of abyssal carbon in intermediate waters off Chile during deglaciation. *Nature Geoscience*, 3: 192-195.

D'Orgeville M, Sijp WP, England MH, Meissner KJ (2010) On the control of glacial-interglacial atmospheric CO_2 variations by the Southern Hemisphere westerlies. *Geophysical Research Letters*, 37: L21703, doi:10.1029/2010GL045261.

Dorschel B, Hebbeln D, Rüggeberg A, Dullo W-C, Freiwald A (2005). Growth and erosion of a cold-water coral covered carbonate mound in the Northeast Atlantic during the Late Pleistocene and Holocene. *Earth and Planetary Science Letters*, 233: 33-44.

Duplessy J-C, Labeyrie L, Waelbroeck C (2002) Constraints on the ocean oxygen isotopic enrichment between the Last Glacial Maximum and the Holocene: Paleoceanographic implications. *Quaternary Science Reviews*, 21: 315-330.

Dupont LM, Schluetz F, Ewah CT, Jennerjahn TC, Paul A, Behling H (2010) Two-step vegetation response to enhanced precipitation in Northeast Brazil during Heinrich event 1. *Global Change Biology*, 16: 1647-1660.

Eby M, Zickfeld K, Montenegro A, Archer D, Meissner KJ, Weaver AJ (2009) Lifetime of anthropogenic climate change: Millennial time scales of potential CO_2 and surface temperature perturbations. *Journal of Climate*, 22: 2501-2511.

Elsig J, Schmitt J, Leuenberger D, Schneider R, Eyer M, Leuenberger M, Joos F, Fischer H, Stocker TF (2009) Stable isotope constraints on Holocene carbon cycle changes from an Antarctic ice core. *Nature*, 461: 507-510.

Emslie SD, Berkman PA, Ainley DG, Coats L, and Polito M (2003) Late-Holocene initiation of ice-free ecosystems in the southern Ross Sea, Antarctica *Marine Ecology Progress Series*, 262: 19-25.

Etheridge, DM, Steele, LP, Langenfelds, RL, Francey, RJ, Barnola, JM, and Morgan, VI. (1996) Natural and anthropogenic changes in atmospheric CO_2 over the last 1000 years from air in Antarctic ice and firn. Journal of Geophysical Research, 101: 4115–4128.

Eugster O, Gruber N, Deutsch C, Jaccard SL, Payne MR (2013) The dynamics of the marine nitrogen cycle across the last deglaciation. *Paleoceanography*, 28: doi:10.1002/palo.20020.

Ewen TL, Weaver AJ, Eby M (2004) Sensitivity of the inorganic ocean carbon cycle to future climate warming in the UVic coupled model. *Atmosphere Ocean*, 42: 23-42.

Fanning AE, Weaver AJ (1996) An atmospheric energy-moisture balance model: Climatology, interpentadal climate change, and coupling to an ocean general circulation model. *Journal of Geophysical Research*, 101: 15111-15128.

Fletcher SEM, Gruber N, Jacobson AR, Gloor M, Doney SC, Dutkiewicz S, Gerber M, Follows M, Joos F, Lindsay K, Menemenlis D, Mouchet A, Müller SA, Sarmiento JL (2007) Inverse estimates of the oceanic sources and sinks of natural CO2 and the implied oceanic transport. *Global Biogeochemical Cycles*, 21: GB1010, doi:10.1029/2006GB002751.

Foster GL, Vance D (2006) Negligible glacial-interglacial variation in continental chemical weathering rates. *Nature*, 444: 918-921.

Friedlingstein P, Cox P, Betts R, Bopp L, von Bloh W, Brovkin V, Cadule P, Doney S., Eby M, Fung I, Bala G, John J, Jones C, Joos F, Kato T, Kawamiya M, Knorr W, Lindsay K, Matthews HD, Raddatz T, Rayner P, Reick C, Roeckner E, Schnitzler K-G, Schnur R, Strassmann K, Weaver AJ, Yoshikawa C, Zeng N (2006) Climate-carbon cycle feedback analysis: results from the C^4MIP model intercomparison. *Journal of Climate*, 19: 3337-3353.

Frolking S, Roulet NT (2007) Holocene radiative forcing impact of northern peatland carbon accumulation and methane emissions. *Global Change Biology*, 13: 1079-1088.

Galbraith ED, Jaccard SL, Pedersen TF, Sigman DM, Haug GH, Cook M, Southon JR, Francois R (2007) Carbon dioxide release from the North Pacific abyss during the last deglaciation. *Nature*, 449: 890-893.

Ganopolski A, Ramstorf S (2001) Rapid changes of glacial climate simulated in a coupled climate model. *Nature*, 309: 153-158.

Gent PR, McWilliams JC (1990) Isopycnal mixing in ocean circulation models. *Journal of Physical Oceanography*, 20: 150– 155.

Gersonde R, Crosta X, Abelmann A, Armand L (2005) Sea-surface temperature and sea ice distribution of the Southern Ocean at the EPILOG Last Glacial Maximum—a circum-Antarctic view based on siliceous microfossil records. *Quaternary Science Reviews*, 24: 869-896.

Goodwin P, Oliver KIC, Lenton TM (2011) Observational constraints on the causes of Holocene CO_2 change. *Global Biogeochemical Cycles*, 25: GB3011, doi: 10.1029/2010GB003888.

Gregg SA (1988) Foragers and Farmers: Population Interaction and Agricultural Expansion in Pre-historic Europe. Chicago: University of Chicago Press.

Hain MP, Sigman DM, Haug GH (2011) Shortcomings of the isolated abyssal reservoir model for deglacial radiocarbon changes in the mid-depth Indo-Pacific Ocean. *Geophysical Research Letters*, 38: L04604, doi:10.1029/2010GL046158.

Handiani D, Paul A, Dupont L (2012a) Tropical climate and vegetation changes during Heinrich Event 1: a model-data comparison. *Climate of the Past*, 8: 37-57.

Handiani D, Paul A, Zhang X, Prang M, Merkel U, Dupont L (2012b) Tropical vegetation response to Heinrich Event 1 as simulated with the UVic ESCM and CCSM3. *Climate of the Past Discussions*: 8, 5359-5387.

He F, Shakun JD, Clark PU, Carlson AE, Liu Z, Otto-Bliesner BL, Kutzbach JE (2013) Northern Hemisphere forcing of Southern Hemisphere climate during the last deglaciation. *Nature*, 494: 81-85.

Hensons, SA, Sanders R, Madsen E (2012) Global patterns in efficiency of particulate organic carbon export and transfer to the deep ocean. *Global Biogeochemical Cycles*, 26: GB1028, doi:10.1029/2011GB004099.

Hesse T, Butzin M, Bickert T, Lohmann G (2011) A model-data comparison of $\delta^{13}C$ in the glacial Atlantic Ocean. *Paleoceanography*, 26: PA3220, doi:10.1029/2010PA002085.

Hodell DA, Venz KA, Charles CD, Ninnemann US (2003) Pleistocene vertical carbon isotope and carbonate gradients in the South Atlantic sector of the Southern Ocean. *Geochemistry, Geophysics, Geosystems*, 4: 1004, doi:10.1029/2002GC000367.

Huiskamp WN, Meissner KJ (2012) Oceanic carbon and water masses during the Mystery Interval: A model-data comparison study. *Paleoceanography*, 27, PA4206, doi:10.1029/2012PA002368.

Huybrechts P (2002) Sea-level changes at the LGM from ice-dynamic reconstructions of the Greenland and Antarctic ice sheets during the glacial cycles. *Quaternary Science Reviews*, 21: 203-231.

Huybers P, Langmuir C (2009) Feedback between deglaciation, volcanism, and atmospheric CO_2. *Earth and Planetary Science Letters*, 286: 479-491.

Indermühle A, Stocker TF, Joos F, Fischer H, Smith H, Wahlen M, Deck B, Mastroianni D, Tschumi J, Blunier T, Meyer R, Stauffer B (1999) Holocene carbon-cycle dynamics based on CO_2 trapped in ice at Taylor Dome, Antarctica. *Nature*, 398: 121-126.

Jaccard SL, Galbraith ED, Sigman DM, Huag GH, Francois R, Pedersen TF, Dulski P, Thierstein HR (2009) Subarctic Pacific evidence for a glacial deepening of the oceanic respired carbon pool. *Earth and Planetary Science Letters*, 277: 156-166.

Jolly D, Haxeltine A (1997) Effect of low glacial atmospheric CO_2 on tropical African montane vegetation. *Science*, 276:786-788.

Joos, F, Gerber, S, and Prentice, IC (2004) Transient simulations of Holocene atmospheric carbon dioxide and terrestrial carbon since the Last Glacial Maximum. *Global*

Biogeochemical Cycles, 18, doi:10.1029/2003GB002156.

Justino F, Peltier WR, Barbosa HA (2010) Atmospheric susceptibility to wildfire occurrence during the Last Glacial Maximum and mid-Holocene. *Paleogeography, Paleoclimatology, Paleoecology*, 295: 76-88.

Kalnay E, Kanamitsu M, Kistler R, Collins W, Deaven D, Gandin L, Iredell M, Saha S, White G, Woollen J, Zhu Y, Chelliah M, Ebisuzaki W, Higgins W, Janowiak J, Mo KC, Ropelewski C, Wang J, Leetma A, Reynolds R, Jenne R, Joseph D (1996) The NCEP/NCAR 40-year reanalysis project. *Bulletin of the American Meteorological Society*, 77: 437-471.

Kaplan JO, Krumhardt KM, Ellis EC, Ruddiman WR, Lemmen C and Klein Goldwijk K (2011) Holocene carbon emissions as a result of anthropogenic land cover change. *The Holocene*, 21: 775-791.

Kaplan JO, Prentice IC, Knorr W, Valdes PJ (2002) Modeling the dynamics of terrestrial carbon storage since the Last Glacial Maximum. *Geophysical Research Letters*, 29: 2074, doi: 10.1029/2002GL015230.

Keigwin LD, Lehman SJ, Cook MS (2006) Radiocarbon evidence for a benthic front near 3 km in the Glacial Pacific Ocean. Eos Transactions. AGU 87 (52) Fall Meeting Abstract PP44A-07.

Kim J.-H, and Schneider RR (2004) GHOST global database for alkenone-derived Holocene sea-surface temperature records, Retrieved from http://www.pangaea.de/Projects/GHOST/Holocene

Klaas C, Archer DE (2002) Association of sinking organic matter with various types of mineral ballast in the deep sea: Implications for the rain ratio. *Global Biogeochemical Cycles*, 16: 1116, doi:10.1029/2001GB001765.

Klein Goldewijk K, Beusen A, de Vos M, van Drecht G (2011) The HYDE 3.1 spatially explicit database of human induced land use change over the past 12,000 years. *Global Ecology and Biogeography,* 20: 73-86.

Klein Goldewijk K (2001) Estimating global land use change over the past 300 years: The HYDE database. *Global Biogeochemical Cycles*, 15: 417-433.

Kleinen T, Brovkin V, von Bloh W, Archer D, Munhoven G (2010) Holocene carbon cycle dynamics, *Geophysical Research Letters*, 37, L02705, doi:10.1029/2009GL041391.

Kohfeld KE, Ridgwell A (2009) Glacial-interglacial variability in atmospheric CO_2. In *Surface Ocean-Lower Atmosphere Processes*, Geophysical Research Series 37, Washington DC: American Geophysical Union, p.251–286, doi: 10.1029/2008GM000845.

Kohfeld KE, Le Quéré C, Harrison SP, Anderson RF (2005) Role of marine biology in glacial-interglacial CO_2 cycles. *Science*, 308: 74-78.

Kulbe T, Melles M, Verkulich SR, Pushina ZV (2001) East Antarctic climate and environmental variability over the last 9400 years inferred from marine sediments of the Bunger Oasis. *Arctic, Antarctic Alpine Research*, 33: 223-230.

Kutterolf S, Jegen M, Mitrovica JX, Kwasnitschka T, Freundt A, Huybers PJ (2013) A detection of Milankovitch frequencies in global volcanic activity. *Geology*, 41: 227-230.

Kutzbach JE, Ruddiman WF, Vavrus SJ, Philippon G (2009) Climate model simulation of anthropogenic influence on greenhouse-induced climate change (early agriculture to modern): The role of ocean feedbacks. *Climatic Change*, 99: 351-381.

Kwon EY, Sarmiento JL, Toggweiler JR, DeVries T (2011) The control of atmospheric pCO2 by oceanic ventilation change: The effect of the oceanic storage of biogenic carbon. *Global Biogeochemical Cycles*, 25: GB3026, doi:10.1029/2011GB004059.

Kwon EY, Primeau F, Sarmiento JL (2009) The impact of remineralization depth on the air-sea carbon balance. *Nature Geoscience*, 2: 630-635.

Lal R (1989) Conservation tillage for sustainable agriculture: tropics versus temperate environments. *Advances in Agronomy*, 42: 86-105.

Lambert F, Delmonte B., Petit JR, Bigler M, Kaufmann PR, Hutterli MA, Stocker TF, Ruth U, Steffensen JP, Maggi V (2008) Dust-climate couplings over the past 800,000 years from the EPICA Dome C ice core. *Nature*, 452: 616-619.

Lamy F, Kilian R, Arz HW, Francois J-P, Kaiser J, Prang M, Steinke T (2010) Holocene changes in the position of the southern westerly wind belt. *Nature Geoscience*, 3: 695-699.

Lamy F, Hebbeln D, Röhl U, Wefer G (2001) Holocene rainfall variability in southern Chile: A marine record of latitudinal shifts of the Southern Westerlies. *Earth and Planetary Science Letters*, 18: 369-382.

Liu Z, Otto-Bliesner L, He F, Brady EC, Tomas R, Clark PU, Carlson AE, Lynch-Stieglitz J, Curry W, Brook E, Erickson D, Jacob R, Kutzbach J, Cheng J (2009) Transient simulation of last deglaciation with a new mechanism for Bølling-Allerød warming. *Science*, 325: 310-314.

Lorenz SJ, Kim J-H, Rimbu N, Schneider RR, Lohmann G (2006) Orbitally driven insolation forcing on Holocene climate trends: Evidence from alkenone data and climate modeling. *Paleoceanography*, 21, doi:10.1029/2005PA001152.

Loulergue L, Schilt A, Spahni R, Masson-Delmotte V, Blunier T, Lemieux B, Barnola JM, Raynaud D, Stocker T, Chappellaz J (2008) Orbital and millennial-scale features of atmospheric CH_4 over the past 800,000 years. *Nature*, 453: 383-386.

Lund DC, Adkins JF, Ferrari R (2011) Abyssal Atlantic circulation during the Last Glacial Maximum: Constraining the ratio between transport and vertical mixing. *Paleoceanography*, 26, PA1213, doi:10.1029/2010PA001938.

Lupker M, France-Lanord C, Galy V, Lavé J, Kudrass H (2013) Increasing chemical weathering in the Himalayan system since the Last Glacial Maximum. *Earth and Planetary Science Letters*, 365: 243-252.

Lüthi D, Le Floch M, Bereiter B, Blunier T, Barnola J-M, Siegenthaler U, Raynaud D, Jouzel J, Fischer H, Kawamura K, Stocker TF (2008) High-resolution carbon dioxide concentration record 650,000–800,000 years before present. *Nature*, 453: 379-382.

Marchal O, Curry WB (2008) On the abyssal circulation in the glacial Atlantic. *Journal of Physical Oceanography*, 38: 2014-2037.

Marchitto TM, Lehman SJ, Ortiz JD, Flückiger J, van Geen A (2007) Marine radiocarbon evidence for the mechanism of deglacial atmospheric CO_2 rise. *Science*, 316: 1456-1459.

Martin JH, Gordon MR, Fitzwater SE (1990) Iron in Antarctic waters. *Nature*, 345: 156-158.

Matsumoto K, Sarmiento JL, Brzezinski MA (2002) Silicic acid leakage from the Southern Ocean: A possible explanation for glacial atmospheric pCO_2. *Global Biogeochemical Cycles*, 16: doi:10.1029/2001GB001442.

Matthews HD, Weaver AJ, Meissner KJ (2005) Terrestrial carbon cycle dynamics under recent and future climate change. *Journal of Climate*, 18: 1609-1628.

Matthews HD, Weaver AJ, Meissner KJ, Gillett NP, Eby M (2004) Natural and anthropogenic climate change: Incorporating historical land cover change, vegetation dynamics and the global carbon cycle. *Climate Dynamics*, 22: 461-479.

Mauritzen C, Häkkinen S (1997) Influence of sea ice on the thermohaline circulation in the North Atlantic Ocean. *Geophysical Research Letters*, 24: 3257-3260.

Mayr C, Wille M, Haberzettl T, Fey M, Janssen S, Lücke A, Ohlendorf C, Oliva G, Schäbitz F, Schleser GH, Zolitschka B (2007) Holocene variability of the Southern Hemisphere westerlies in Argentinean Patagonia (52°S). *Quaternary Science Reviews*, 26: 579-584.

McEvedy C, Jones R (1978) *Atlas of World Population History*. London: Penguin.

McManus JF, Francois R, Gherardi JM, Keigwin LD, Brown-Leger S (2004) Collapse and rapid resumption of Atlantic meridional circulation linked to deglacial climate changes. *Nature*, 428: 834-837.

Meehl, GA, Stocker TF, Collins WD, Friedlingstein P, Gaye AT, Gregory JM, Kitoh A, Knutti R, Murphy JM, Noda A, Raper SCB, Watterson IG,Weaver AJ, Zhao Z-C (2007) Global climate projections. In: *Climate Change 2007: The Physical Science Basis. Contribution of Working Group I to the Fourth Assessment Report of the Intergovernmental Panel on Climate Change* (Solomon, S., D. Qin, M. Manning, Z. Chen, M. Marquis, K.B. Averyt, M.Tignor and H.L. Miller (eds.)). Cambridge University Press, Cambridge, UK.

Meissner KJ, Eby M, Weaver AJ, Saenko OA (2008) CO_2 threshold for millennial-scale oscillations in the climate system: Implications for global warming scenarios. *Climate Dynamics*, 30: 161-174.

Meissner KJ (2007) Younger Dryas: A data to model comparison to constrain the strength of the overturning circulation. *Geophysical Research Letters*, 34, L21705, doi:10.1029/2007GL031304.

Meissner KJ, Weaver AJ, Matthews HD, Cox PM (2003a) The role of land-surface dynamics in glacial inception: A study with the UVic Earth System Model. *Climate Dynamics*, 21: 515-537.

Meissner KJ, Schmittner A, Weaver AJ, Adkins JF (2003b) Ventilation of the North Atlantic Ocean during the Last Glacial Maximum: A comparison between simulated and observed radiocarbon ages. *Paleoceanography*, 18, 1023, doi:10.1029/2002PA000762*,* 2.

Menviel L, Joos F (2012) Toward explaining the Holocene carbon dioxide and carbon isotope records: Results from transient ocean carbon cycle-climate simulations. *Paleoceanography*, 27: PA1207, doi:10.1029/2011PA002224.

Menviel L, Joos F, Ritz SP (2012) Simulating atmospheric CO_2, ^{13}C and the marine carbon cycle during the Last Glacial-Interglacial cycle: possible role for a deepening of the mean remineralization depth and an increase in the oceanic nutrient inventory. *Quaternary Science Reviews*, 56: 46-68.

Menviel L, Timmermann A, Elison Timm O, Mouchet A (2011) Deconstructing the Last Glacial termination: the role of millennial and orbital-scale forcings. *Quaternary Science Reviews*, 30: 1155-1172.

Menviel L, Timmermann A, Mouchet A, Timm O (2008a) Climate and marine carbon cycle response to changes in the strength of the Southern Hemispheric westerlies. *Paleoceanography*, 23: PA4201, doi:10.1029/2008PA001604.

Menviel L, Timmermann A, Mouchet A, Timm O (2008b) Meridional reorganizations of marine and terrestrial productivity during Heinrich events. *Paleoceanography*, 23: PA1203, doi:10.1029/2007PA001445.

Mohtadi M, Rossel P, Lange C, Pantoja S, Böning P, Repeta DJ, Grunwald M, Lamy F, Hebbeln D, Brumsack H-J (2008) Deglacial pattern of circulation and marine productivity in the upwelling region off central-south Chile. *Earth and Planetary Science Letters*, 272: 221-230.

Monnin E, Indermühle A, Dallenbach A, Flückiger J, Stauffer B, Stocker TF, Raynaud D, Barnola, J-M (2001) Atmospheric concentrations over the Last Glacial Termination. *Science*, 291: 112-114.

Montenegro A, Eby M, Kaplan JO, Meissner KJ, Weaver AJ (2006) Carbon storage on exposed continental shelves during the glacial-interglacial transition. *Geophysical Research Letters*, 33: L08703, doi:10.1029/2005GL025480.

Munhoven G (2010) The Rain Ratio Hypothesis: Can it be rescued? Geophysical Research Abstracts, vol. 12. General Assembly Abstract EGU20120-5595.

Munhoven G (2007) Glacial-interglacial rain ratio changes: Implications for atmospheric CO_2 and ocean-sediment interaction. *Deep-Sea Research II*, 54: 722-746.

Negre C, Rainer Z, Thomas AL, Masqué P, Henderson GM, Martínez-Méndez G, Hall IR, Mas JL (2010) Reversed flow of Atlantic deep water during the Last Glacial Maximum. *Nature*, 468: 84-89.

Obata A (2007) Climate–carbon cycle model response to freshwater discharge into the North Atlantic. *Journal of Climate*, 20: 5962–5976.

Okazaki Y, Timmermann A, Menviel L, Harada N, Abe-Ouchi A, Chikamoto MO, Mouchet A, Asahi H (2010) Deepwater formation in the North Pacific during the last glacial termination. *Science*, 329: 200-204.

Oliver KIC, Hoogakker BAA, Crowhurst S, Henderson GM, Rickaby REM, Edwards, NR, Elderfield H (2009) A synthesis of marine sediment core $\delta^{13}C$ data over the last 150 000 years. *Climate of the Past Discussions*, 5, 2497-2554.

Oliver KIC, Edwards NR (2008) Location of potential energy sources and the export of dense water from the Atlantic Ocean. *Geophysical Research Letters*, 35: L22604, doi:10.1029/2008GL035537.

Olofsson J, Hickler T (2008) Effects of human land-use on the global carbon cycle during the last 6,000 years. *Vegetation History and Archaeobotany*, 17: 605-615.

Olsen JS, Watts JA and Allison J (1983) *Carbon in Live Vegetation of Major World Ecosystems.* TN 37830 DOE/NBB Report TR004. Oak Ridge TN: Oak Ridge National Laboratory.

Pacanowski RC (1995) MOM 2 documentation, user's guide and reference manual. *GFDL Ocean Group Technical. Rep*ort, Princeton, NJ: NOAA, GFDL.

Parekh P*,* Joos F, Müller SA (2008) A modeling assessment of the interplay between aeolian iron fluxes and iron-binding ligands in controlling carbon dioxide fluctuations during Antarctic warm events*.* *Paleoceanography*, 23: PA4202*,* doi:10.1029/2007PA001531.

Peltier WR (2002) Global glacial isostatic adjustment: Palaeogeodetic and space-geodetic tests of the ICE-4G (VM2) model. *Journal of Quaternary Science*, 17: 491-510.

Peltier RW (1994) Ice age paleotopography. *Science*, 265: 195-201.

Petit JR, Jouzel J, Raynaud D, Barkov NI, Barnola J-M, Basile I, Bender M, Chappellaz J, Davis M, Delaygue G, Delmotte M, Kotlyakov VM, Lipenkov V, Lorius C, Pepin L, Ritz C, Saltzman E, Stievenard M (1999) Climate and atmospheric history of the last 420,000 Years from the Vostok ice core, Antarctica. *Nature*, 399: 429-436.

Pollard D, DeConto RM (2009) Modelling west Antarctic ice sheet growth and collapse through the past five million years. *Nature*, 458: 329-332.

Pongratz J, Reick, CH, Raddatz T, Claussen M (2009) Effects of anthropogenic land cover change on the carbon cycle of the last millennium. *Global Biogeochemical Cycles*, 23, doi:10.1029/2009GB003488.

Pongratz J, Reick C, Raddatz T, Claussen M (2008) A reconstruction of global agricultural areas and land cover for the last millennium. *Global Biogeochemical Cycles*, 22, doi:10.1029/2007GB003153.

Prentice IC, Harrison SP, Bartlein PJ (2011) Global vegetation and terrestrial carbon cycle changes after the last ice age. *New Phytologist*, 189: 988-998.

Prentice IC, Harrison SP (2009) Ecosystem effects of CO_2 concentration: Evidence from past climates. *Climate of the Past*, 5: 297-307.

Prentice IC, Jolly D, BIOME 6000 participants (2000) Mid-Holocene and glacial-maximum vegetation geography of the northern continents and Africa. *Journal of Biogeography*, 27: 507-519.

Putnam AE, Denton GH, Schaefer JM, Barrell DJA, Andersen BG, Finkel RC, Schwartz R, Doughty AM, Kaplan MR (2010) Glacier advance in southern middle-latitudes during the Antarctic Cold Reversal*.* *Nature Geoscience*, 3: 700-704.

Quinton JN, Gerard C, van Oost K, Bardgett RD (2010) The impact of agricultural soil erosion on biogeochemical cycling. *Nature Geoscience*, 3: 311-314.

Raddatz TJ, Reick CH, Knorr W, Kattge J, Roeckner E, Schnur R, Schnitzler K-G, Wetzel P, Jungclaus J (2007) Will the tropical land biosphere dominate the climate-carbon cycle feedback during the twenty-first century? *Climate Dynamics*, 29: 565-574.

Rahmstorf S, Crucifix M, Ganopolski A, Goosse H, Kamenkovich I, Knutti R, Lohmann G, Marsh R, Mysak LA, Wang Z, Weaver AJ (2005) Thermohaline circulation hysteresis: A model intercomparison. *Geophysical Research Letters*, 32: L23605, doi: 10.1029/2005GL023655.

Ragueneau O, Schultes S, Bidle K, Claquin P, Moriceau B (2006) Si and C interactions in the world ocean: Importance of ecological processes and implications for the role of diatoms in the biological pump. *Global Biogeochemical Cycles*, 20: GB4S02, doi: 10.1029/2006GB002688.

Ramankutty N, Foley JA (1999) Estimating historical changes in global land cover: Croplands from 1700 to 1992. *Global Biogeochemical Cycles*, 13: 997-1027.

Renssen H, Goosse H, Fichefet T, Masson-Delmotte V, Koç N (2005) Holocene climate evolution in the high-latitude Southern Hemisphere simulated by a coupled atmosphere-sea ice-ocean-vegetation model. *The Holocene*, 15, 951-964.

Richaud M, Loubere P, Pichat S, Francois R (2007) Changes in opal flux and the raion ratio during the last 50,000 years in the equatorial Pacific. *Deep-Sea Research II*, 54: 762-771.

Rickaby RE, Elderfield H, Roberts N, Hillenbrand C-D, Mackensen A (2010) Evidence for elevated alkalinity in the glacial Southern Ocean. *Paleoceanography*, 25, PA1209, doi:10.1029/2009PA001762.

Ridgwell AJ, Maslin M, Kaplan JO (2012) Flooding of the continental shelves as a contributor to deglacial CH4 rise. *Journal of Quaternary Science*, 27: 800-806.

Ridgwell AJ, Zeebe RE (2005) The role of the global carbonate cycle in the regulation and evolution of the Earth system. *Earth and Planetary Science Letters*, 234: 299-315.

Ridgwell AJ, Watson AJ, Maslin MA, Kaplan J (2003) Implications of coral reef buildup for the controls on atmospheric CO_2 since the Last Glacial Maximum. *Paleoceanography*, 18, doi:10.1029/2003PA000893.

Ridgwell AJ (2003) An end to the "rain ratio" reign? *Geochemistry, Geophysics, Geosystems*, 4, doi:10.1029/2003GC000512.

Rippeth TP, Scourse JD, Uehara K, McKeown S (2008) Impact of sea-level rise over the last deglacial transition on the strength of the continental shelf CO_2 pump. *Geophysical Research Letters*, 35: L24604, doi:10.1029/2008GL035880.

Robinson RS, Mix A, Martinez P (2007) Southern Ocean control on the extent of denitrification in the southeast Pacific over the last 70 ka. *Quaternary Science Reviews*, 26: 201-212.

Roche DM, Crosta X, Renssen H (2012) Evaluating Southern Ocean sea-ice for the Last Glacial Maximum and pre-industrial climates: PMIP-2 models and data evidence. *Quaternary Science Reviews*, 56: 99-106.

Rojas M, Moreno P, Kageyama M, Crucifix M, Hewitt C, Abe-Ouchi A, Ohgaito R, Brady EC, Hope P (2009) The southern westerlies during the last glacial maximum in PMIP2 simulations. *Climate Dynamics*, 32: 525-548.

Rose KA, Sikes EL, Guilderson TP, Shane P, Hill TM, Zahn R, Spero HJ (2010) Upper-ocean-to-atmosphere radiocarbon offsets imply fast deglacial carbon dioxide release. *Nature*, 466: 1093-1097.

Roth, R, Joos F (2012) Model limits on the role of volcanic carbon emissions in regulating glacial–interglacial CO_2 variations. *Earth and Planetary Science Letters*, 329, 141-149.

Ruddiman WF, Kutzbach JE, Vavrus SJ (2011) Can natural or anthropogenic explanations of late-Holocene CO_2 and CH_4 increases be falsified? *The Holocene*, 21, 865-887.

Ruddiman WF, Ellis EC (2009) Effect of per-capita land use changes on Holocene forest clearance and CO_2 emissions. *Quaternary Science Reviews*, 28: 3011-3015.

Ruddiman WF (2008) The challenge of modeling interglacial CO_2 and CH_4 trends. *Quaternary Science Reviews*, 27: 445-448.

Ruddiman WF (2007) The early anthropogenic hypothesis: Challenges and responses. *Reviews of Geophysics*, 45, doi:10.1029/2006RG000207.

Ruddiman WF (2003) The anthropogenic greenhouse era began thousands of years ago. *Climatic Change*, 61: 261-293.

Ruddiman WF, Thomson JS (2001) The case for human causes of increased atmospheric CH_4 over the last 5000 years. *Quaternary Science Review*, 20: 1769-1777.

Sarmiento, JLS, Gruber N (2006) Ocean Biogeochemical Dynamics. Princeton, N. J.: Princton Univ. Press.

Schartau M, Oschlies A (2003) Simultaneous data-based optimization of a 1d-ecosystem model at three locations in the North Atlantic: I. Method and parameter estimates. *Journal of Marine Research*, 61: 765–793.

Schmitt J, Schneider R, Elsig J, Leuenberger D, Lourantou A, Chappellaz J, Köhler P, Joos F, Stocker T, Leuenberger M, Fischer H (2012) Carbon isotope constraints on the deglacial CO_2 rise from ice cores. *Science*, 336: 711-714.

Schmittner A, Oschlies A, Matthews HD, Galbraith ED (2008) Future changes in climate, ocean circulation, ecosystems, and biogeochemical cycling simulated for a business-as-usual CO2 emission scenario until year 4000 AD. *Global Biogeochemical Cycles*, 22: GB1013, doi:10.1029/2007GB002953.

Schmittner A, Galbraith ED (2008) Glacial greenhouse-gas fluctuations controlled by ocean circulation changes. *Nature*, 456: 373-376.

Schmittner A, Galbraith ED, Hostetler SW, Pederson TF, Zhang R (2007a) Large fluctuations of dissolved oxygen in the Indian and Pacific oceans during Dansgaard-Oeschger oscillations caused by variations of North Atlantic Deep Water subduction. *Paleoceanography*, 22: PA3207, doi:10.1029/2006PA001384.

Schmittner A, Brook E, Ahn J (2007b) Impact of the ocean's overturning circulation on atmospheric CO_2. In *Ocean Circulation: Mechanisms and Impacts,* AGU Geophysical Monograph Series, vol. 173, eds. by A. Schmittner, J. Chiang, and S. Hemming, pp. 209-246, Washington, DC: American Geophysical Union.

Schmittner A, Oschlies A, Giraud X, Eby M, Simmons HL (2005) A global model of the marine ecosystem for long-term simulations: Sensitivity to ocean mixing, buoyancy forcing, particle sinking, and dissolved organic matter cycling. *Global Biogeochemical Cycles*, 19: GB3004:1-17.

Schmittner A, Yoshimori M, Weaver AJ (2002) Instability of Glacial Climate in a Model of the Ocean-Atmosphere-Cryosphere System. *Science*, 295: 1489-1493.

Schurgers G, Mikolajewicz U, Gröger M, Maier-Reimer E, Vizcaíno M, Winguth A (2006) Dynamics of the terrestrial biosphere, climate and atmospheric CO_2 concentration during interglacials: A comparison between Eemian and Holocene. *Climate of the Past*, 2: 205–220.

Skinner LC, Fallon S, Waelbroeck C, Michel E, Barker S (2010) Ventilation of the deep Southern Ocean and deglacial CO_2 rise. *Science*, 328: 1147-1151.

Shevenell AE, Ingalls AE, Domack EW, Kelly C (2011) Holocene Southern Ocean surface temperature variability west of the Antarctic Peninsula. *Nature*, 470: 250-254.

Sigman DM, Hain MP, Huag GH (2010) The polar ocean and glacial cycles in atmospheric CO_2 concentration. *Nature*, 466: 47-55.

Sigman DM, Boyle EA (2000) Glacial/interglacial variations in atmospheric carbon dioxide. *Nature*, 407: 859-869.

Sikes EL, Samson CR, Guilderson TP, Howard WR (2000) Old radiocarbon ages in the southwest Pacific Ocean during the last glacial period and deglaciation. *Nature*, 405: 555–559.

Simmons CT, Mysak LA, Matthews HD (2013) Investigation of the natural carbon cycle since 6000 BC using an intermediate complexity model: The role of Southern Ocean ventilation and marine ice shelves. *Atmosphere-Ocean*, 51: 187-212.

Smith DE, Harrison S, Firth CR, Jordan JT (2011) The early Holocene sea level rise. *Quaternary Science Reviews*, 30: 1846-1860.

Spero HJ, Lea DW (2002) The cause of carbon isotope minimum events on glacial terminations. *Science*, 296: 522-525.

Stephens BB, Keeling RF (2000) The influence of Antarctic sea ice on glacial-interglacial variations. *Nature*, 404: 171-174.

Stocker B, Strassmann, K, Joos F (2011) Sensitivity of Holocene atmospheric CO_2 and the modern carbon budget to early human land use: Analyses with a process-based model. *Biogeosciences*, 8: 69-88.

Stone DA (2011) mask_lonlattime.pro. Available 1 August 2013. From http://www.csag.uct.ac.za/~daithi/idl_lib/pro/mask_lonlattime.pro

Stott L, Timmermann A (2011) Hypothesized link between glacial/interglacial atmospheric CO_2 cycles and storage/release of CO_2-rich fluids from deep-sea sediments. In *Understanding the Causes, Mechanisms and Extent of Abrupt Climate Change,* Geophysical. Monograph Series*,* vol. 193*,* Eds Rashid H*,* Polyak L*,* E. Mosley-Thompson E*,* pp. 123–138*, AGU,* Washington, D. C.

Stott L, Southon J, Timmermann A, Koutavas A (2009) Radiocarbon age anomaly at intermediate water depth in the Pacific Ocean during the last deglaciation. *Paleoceanography*, 24: PA2223, doi:10.1029/2008PA001690.

Strassmann KM, Joos F, Fischer G (2008) Simulating effects of land use changes on carbon fluxes: Past contributions to atmospheric CO_2 increases and future commitments due to losses of terrestrial sink capacity. *Tellus (B)*, 60: 583-603.

Street-Perrot FA, Huang Y, Perrott RA, Eglinton G, Barker P, Khelifa LB, Harkness DD, Olago DO (1997) Impact of lower atmospheric carbon dioxide on tropical mountain ecosystem.

Tamburini F, Föllmi K (2009). Phosphorus burial in the ocean over glacial-interglacial time scales. *Biogeosciences*, 6: 501-513.

Thornalley DJR, Barker S, Broecker WS, Elderfield H, McCave IN (2011) The deglacial evolution of North Atlantic deep convection. *Science*, 331: 202-205.

Thompson LG, Davis ME, Mosley-Thompson E, Sowers TA, Henderson KA, Zagorodnov S, Lin P-N, Mikhalenko VN, Campen RK, Bolzan JF, Cole-Dai J, Francou B (1998) A 25,000-year tropical climate history from Bolivian ice cores. *Science*, 282: 1858-1864.

Toggweiller JR, Russell JL, Carson SR (2006) Midlatitude westerlies, atmospheric CO_2, and climate change during the ice ages. *Paleoceanography*, 21: PA2005, doi:10.1029/2005PA001154.

Tschumi T, Joos F, Gehlen M, Heinze C (2011) Deep ocean ventilation, carbon isotopes, marine sedimentation and the deglacial CO_2 rise. *Climate of the Past*, 7: 771-800.

Tschumi T, Joos F, Parekh P (2008) How important are Southern Hemisphere wind changes for low glacial carbon dioxide? A model study. *Paleoceanography*, 23: PA4208, doi: 10.1029/2008PA001592.

Tsunogai S, Watanabe S, Sago T (1999) Is there a ‘‘continental shelf pump’’ for the absorption of atmospheric CO_2? *Tellus*, 51B: 701– 712.

Ushie H, Matsumoto K (2012) The role of shelf nutrients on glacial-interglacial CO_2: A negative feedback. *Global Biogeochemical Cycles*, 26: GB2039: doi:10.1029/2011GB004147.

Vaughan, DG (2008) West Antarctic ice sheet collapse—the fall and rise of a paradigm. *Climatic Change*, 91: 65-79.

Vavrus SJ, Ruddiman WF, Kutzbach JE (2008) Climate model tests of the anthropogenic influence on greenhouse-induced climate change: The role of early human agriculture, industrialization, and vegetation feedbacks. *Quaternary Science Review*, 27: 1410-1425.

Wang Y, Roulet N, Frolking S, Mysak LA (2009) The importance of northern peatlands in the global carbon systems during the Holocene. *Climate of the Past*, 5 :1231-1258.

Wang Y, Mysak LA, Wang Z, Brovkin V (2005) The greening of the McGill paleoclimate model. Part II: simulation of Holocene millennial-Scale natural climate changes. *Climate Dynamics*, 24: 481-496.

Watson AJ, Naveira Garabato (2006) The role of Southern Ocean mixing and upwelling in glacial-interglacial atmospheric CO_2 change. *Tellus*, 58B, 73-87.

Watson AJ, Bakker DCE, Ridgwell AJ, Boyd PW, Law CS (2000) Effect of iron supply on Southern Ocean CO_2 uptake and implications for glacial atmospheric CO_2. *Nature*, 407: 730-733.

Weaver AJ, Eby M, Wiebe EC, Bitz CM, Duffy PB, Ewen TL, Fanning AF, Holland MM, MacFadyen A, Matthews HD, Meissner KJ, Saenko O, Schmittner A, Wang H, Yoshimori M (2001) The UVic Earth System Climate Model: Model description, climatology, and applications to past, present and future climates. *Atmosphere-Ocean*, 39: 361-428.

Weber SL, Drijfhout SS, Abe-Ouchi A, Crucifix M, Eby M, Ganopolski A, Murakami S, Otto-Bliesner B, Peltier WR (2007). The modern and glacial overturning circulation in the Atlantic ocean in PMIP coupled model simulations. *Climate of the Past*, 3: 51-64.

West TO, Post WM (2002) Soil organic carbon sequestration rates by tillage and crop rotation. *Soil Science Society of America Journal*, 66: 1930-1946.

Winckler G, Anderson RF, Fleisher MQ, McGee D, Mahowald N (2008) Covariant glacial-interglacial dust fluxes in the Equatorial Pacific and Antarctica. *Science*, 320: 93-96.

Winton M, Hallberg R, Gnanadesikan A (1998) Simulation of density-driven frictional downslope flow in z-coordinate ocean models. *Journal of Physical Oceanography*, 28: 2163-2174.

Yu J, Broecker WS, Elderfield H, Jin Z, McManus J, Zhang F (2010). Loss of carbon from the deep sea since the Last Glacial Maximum. *Science,* 330:1084-1087.

Yu ZC (2012) Northern peatland carbon stocks and dynamics: A review. *Biogeosciences*, 9: 4071-4085.

Yu ZC, Loisel J, Brosseau DP, Beilman DW, Hunt SJ (2010) Global peatland dynamics since the Last Glacial Maximum, *Geophysical Research Letters*, 37, L13402, doi:10.1029/2010GL043584

Yu ZC (2011) Holocene carbon flux histories of the world's peatlands: Global carbon cycle implications. *The Holocene*, 21:761-774.

Zimov SA, Zimov NS, Chapin FS III (2012) The past and future of the mammoth steppe ecosystem. In *Paleontology in Ecology and Conservation*, p. 193-225, doi: 10.1007/978-3-642-25038-5_10.

Zimov NS, Zimov SA, Zimova AE, Zimova GM, Chuprynin VI, FSC III (2009) Carbon storage in permafrost and soils of the mammoth tundra-steppe biome: Role in the global carbon budget. *Geophysical Research Letters*, 36: L02502, doi: 10.1029/2008GL036332.

Zimov NS, Edward, Schuur EAG, Chapin FS III (2006) Permafrost and the Global Carbon Budget. *Science*, 312: 1612-1613.

Zeng N (2007) Quasi-100 ky glacial-interglacial cycles triggered by subglacial burial carbon release. *Climate of the Past*, 3: 135-153.

Zeng N (2003). Glacial-Interglacial atmospheric CO_2 change—The glacial burial hypothesis. *Advances in Atmospheric Sciences*, 20:677-693.

Zech R (2012) A permafrost glacial hypothesis – Permafrost carbon might help explaining the Pleistocene ice ages, *Quaternary Science Journal*, 61 : 84–92.